Multiline CN Observations of Star Forming Regions

Inaugural–Dissertation
zur
Erlangung des Doktorgrades
der Mathematisch-Naturwissenschaftlichen Fakultät
der Universität zu Köln

vorgelegt von

Robert Simon
aus Rüsselsheim

Köln 1997

Berichterstatter: Prof. Dr. G. Winnewisser
Prof. Dr. H. Heintzmann

Tag der mündlichen Prüfung: 3. Dezember 1997

Meinen Eltern

If you think education is expensive, try ignorance.
Andy McIntyre

Somewhere, something incredible is waiting to be known.
Carl Edward Sagan

Contents

Stars. . . did they just happen or was they made?
Huckleberry Finn in *The Adventures of Huckleberry Finn*
Mark Twain

Chapter 1. Zusammenfassung

In der hier vorliegenden Arbeit wurde eine umfassende Studie der Emission aus ausgewählten Galaktischen Quellen in den unteren drei Rotationsübergängen des CN Radikales und seiner selteneren Isotopomere ^{13}CN und C^{15}N bei mm und submm Wellenlängen durchgeführt. Es werden detaillierte Ergebnisse für die Molekülwolken, assoziiert mit den HII Regionen Orion A und B, vorgestellt und diskutiert, während Karten der molekularen Emissionsverteilung und Beispielspektren für die übrigen Quellen im Anhang gezeigt werden. Einige der Quellen wurden erstmals in Rotationsübergängen von CN beobachtet.
Die Frequenzen der Rotationsübergänge von CN liegen nahe an denen der meist beobachteten interstellaren Spezies CO und sind aus diesem Grunde von den Standardempfänger-Systemen der mm und submm Observatorien überdeckt, sowie innerhalb der gleichen atmosphärischen Fenster zugänglich. Wann immer es möglich war, wurde CN parallel zu anderen molekularen Übergangen, haupsächlich von CS, beobachtet, entweder simultan mit den zur Verfügung stehenden Empfängern oder in beiden Seitenbändern des gleichen Empfängers, was die einmalige Gelegenheit eröffnete Unsicherheiten in der Positionierungsgenauigkeit des Teleskopes zu minimieren oder gar gänzlich zu vermeiden. Großräumige Kartierungen, gewonnen am KOSMA 3m Teleskop, stellten die Grundlage für detaillierte Beobachtungen am SEST 15m, IRAM 30m und JCMT 15m Teleskop dar, welche die zur Zeit höchste räumliche Auflösung, bezogen auf Einzelantennen im mm und submm Wellenlängenbereich, ermöglichen. Simultane CN N=1$\rightarrow$0 und mm Staub-Kontinuum Beobachtungen am Plateau de Bure Interferometer in Richtung eines ausgewählten Bereiches in NGC 2024 lieferten die höchste in dieser Arbeit erreichte räumliche Auflösung.
Die ursprüngliche Motivation für eine Studie der CN Emission bei Radiowellenlängen liegt in der Tatsache begründet, daß die simultan beobachtbaren Fein- und Hyperfeinstrukturlinien dieser häufig vorkommenden und hohe Dichte anzeigenden interstellaren Spezies es erlauben, optische Tiefen der Übergänge direkt aus den beobachteten Linienverhältnissen zu bestimmen. Darüber hinaus sind Übergänge aus den ersten drei Rotationsniveaus, welche unter den häufigsten interstellaren Bedingungen einen großen Anteil der totalen molekularen Säulendichte in sich vereinen, ein wichtiger Indikator für die Anregungsbedingungen. Zusammen mit einer Behandlung des spektroskopischen Hintergrundes für CN und seine Isotopomere, wird das Verfahren zur Bestimmung physikalischer Parameter aus den beobachteten Spektren in Anwesenheit von Fein- und Hyperfeinstrukturaufspaltung geschildert. Um physikalische Größen wie Gasdichten, Säulendichten und Häufigkeiten relativ zu H_2 abzuschätzen, werden Parameter, resultierend aus *least square* Fitprozeduren angewendet auf die beobachteten Spektren, in Rotationsdiagrammen und Strahlungstransport-Modellen der Photonen-Entweichwahrscheinlichkeit verwendet.

Das seltene C^{15}N Isotopomer, zuvor weder im interstellaren Raum noch im Labor beobachtet, wurde mit dem KOSMA 3m Teleskop durch die Identifizierung der N=2$\rightarrow$1 Hyperfeinstruktur in der Orion Molekülwolke-1 (**OMC-1**) entdeckt. Dieser Erstnachweis wurde anschließend durch Messungen der N=1$\rightarrow$0 und N=2$\rightarrow$1 Übergänge am IRAM 30m Teleskop bestätigt. Beobachtungen des Hauptisotopomers in OMC-1 ergaben signifikante Variationen in der CN Häufigkeit entlang des Nord-Süd orientierten molekularen Gases mit einem Minimum in Richtung der

bekannten Quelle IRc2. Dieses Ergebnis wird mit chemischem Abbau von CN zugunsten stabilerer Moleküle, hauptsächlich HCN, in der unmittelbaren Umgebung dieser heißen und dichten Region erklärt. Desweiteren wurden die ersten überhaupt beobachteten Karten in ^{13}CN Rotationslinien in der Orion Region durchgeführt. Häufigkeitsverhältnisse von CN und ^{13}CN entlang der Hauptachse der Molekülwolke weisen auf großräumige chemische Fraktionierung zugunsten der selteneren Spezies in einer von UV Photonen geprägten Wolke hin.

Das CN Molekül zog neue Aufmerksamkeit auf sich, als aktuelle Modelle photonendominierter Chemie eine Überhäufigkeit im Verhältnis zu anderen Molekülen, wie etwa CO oder CS, in den warmen und dichten Oberflächenschichten von UV beschienenen Klumpen vorhersagten. In nahe genug zur Erde gelegenen photonendominierten Regionen (PDR), und unter bestimmten geometrischen Voraussetzungen, ist zu erwarten, eine so resultierende geschichtete Verteilung von Molekülen bei hoher räumlicher Auflösung, und speziell bei höheren Frequenzen, beobachten zu können, da die Anregungsbedingungen in den warmen und dichten Wolkenschichten die Population der höher liegenden Rotationsniveaus begünstigen. Gleichzeitige Beobachtungen von CN N=3$\rightarrow$2 und CS J=7$\rightarrow$6 aus dieser Arbeit zeigen in der Tat eine geschichtete Verteilung beider molekularer Spezies in der **Orion Bar** Region, einer prototypischen PDR. Es wird gezeigt, daß dieses Phänomen nicht mit Anregungsargumenten zu erklären ist, sondern im Zusammenhang mit chemischen Häufigkeitsvariationen in einer von UV Photonen dominierten Umgebung interpretiert werden muß und so die Vorhersagen der chemischen Modelle bestätigt. Die beobachtete räumliche Separation der molekularen Emissionsmaxima wird, zusammen mit Resultaten der chemischen Modelle gerechnet für einen weiten Dichtebereich, benutzt, um die Dichte und Ausdehnung der emittierenden Schicht entlang der Sichtlinie zu bestimmen. Sorgfältige Untersuchungen anderer auffälliger photonendominierter Regionen in OMC-1 und NGC 2024 legen die Vermutung nahe, daß diese Art von Schichtung, obwohl hier erstmals für die Moleküle CN und CS berichtet, ein durchaus übliches interstellares Phänomen darstellt.

Die Interpretation von mm und submm Staub-Kontinuum Emissionsmaxima in verschiedenen Quellen als sehr dichte und kalte protostellare Kondensationen, löste eine kontroverse Diskussion, die tatsächlichen Eigenschaften dieser Objekte betreffend, aus. Eines der Hauptthemen in diesem Zusammenhang ist die Frage, ob Moleküle in der unmittelbaren Umgebung dieser Quellen auf Staubkörnern ausfrieren. Im Hinblick auf diese Fragestellung wurde im Rahmen dieser Arbeit spezielles Augenmerk auf Beobachtungen eventueller Korrelationen der CN Emission mit den Verteilungen anderer molekularer Spezies und des Staub-Kontinuums bei hoher räumlicher Auflösung gelegt. Im Gegensatz zu anderen Molekülen erwies sich CN Emission als ausgesprochen gut korreliert mit dem mm/submm Staub-Kontinuum, mit der Ausnahme von sehr dichten und heißen Umgebungen um neu entstandene Sterne, in denen es zugunsten von stabileren Molekülen chemisch umgewandelt wird.
Speziell für die dichten Kondensationen, assoziiert mit **NGC 2024**, liefern die in dieser Arbeit gewonnenen kombinierten CN und CS Beobachtungen neue zusätzliche Belege dafür, daß die Quellen in der Tat weiter entwickelt sein könnten als es für Protosterne zu erwarten wäre, und von außen geheizt werden, obgleich sogar eingebettete Heizquellen nicht ausgeschlossen sind. Diese Schlußfolgerung ist sowohl motiviert durch die ausgeprägte morphologische Übereinstimmung

zwischen warmem und dichtem Gas, besonders auffällig in energetisch höher liegenden Rotationsübergängen von CN und CS, und der Staub-Kontinuum Emission, als auch durch den hohen Grad von Aktivität (*Outflows*, Infrarotquellen und Maser), der in einigen der dichten Kondensationen beobachtet wird. Darüber hinaus zeigen die hergeleiteten CN Säulendichten und relativen Häufigkeiten keine Anzeichen von signifikanter chemischer Verarmung dieser Spezies in Richtung der Kondensationen. Die Korrelation von CN und Staub-Kontinuum Emission wurde parallel hierzu auf sehr kleinen räumlichen Skalen für eine ausgewählte Region mit dem Plateau de Bure Interferometer untersucht und die dort gewonnenen Resultate unterstützen die oben getroffenen Schlußfolgerungen.

Einige fundamentale Veränderungen im KOSMA Observatorium machten die Entwicklung eines neuen Hard- und Software Konzeptes für das Breitband Kontinuum Backend (**COBAC**) notwendig, was als technischer Teil im Rahmen dieser Arbeit realisiert wurde.

Chapter 2. Summary

In this thesis, a detailed study of emission from selected Galactic star forming regions in the lowest three rotational transitions of the CN radical and the rarer isotopomers ^{13}CN and C^{15}N at mm and submm wave lengths is performed. Detailed results are presented and discussed for the molecular clouds associated with the Orion A and B HII regions, namely OMC-1, the Orion Bar and NGC 2024, while maps of the molecular emission distribution and sample spectra for the other sources are given in the Appendix. Some of the sources have been observed in rotational transitions of CN for the first time.
The rotational transition frequencies of CN are similar to those of the most commonly studied interstellar species CO, and hence covered by the standard receiver systems at mm and submm observatories and are accessible through the same atmospheric windows. Whenever it was feasible, CN was observed in parallel to other molecular transitions of interest, mainly of CS, either simultaneously with the available receivers or in two sidebands of the same receiver, thus offering the unique opportunity to minimize or even avoid pointing uncertainties of the telescope between the different spectral line maps. Large scale observations obtained at the KOSMA 3m telescope constituted the basis for detailed observations at the SEST 15m, the IRAM 30m and JCMT 15m telescopes which at present supply the highest angular resolution of single-dish antennas at mm and submm wave lengths. Simultaneous CN N=1$\rightarrow$0 and mm dust continuum Plateau de Bure Interferometer observations toward a selected field in NGC 2024 provided the highest angular resolution obtained in this thesis.

The initial motivation for a study of CN emission at radio wave lengths stems from the fact that the simultaneously observable fine and hyperfine structure lines of this abundant, high density tracing interstellar species allow to directly derive the optical depth of the transition from the observed line ratios. In addition, observations of transitions from the first three rotational levels, which under most interstellar conditions comprise a large amount of the total molecular column density, are important probes of the excitation conditions. Together with a treatment of the spectroscopic background for CN and its isotopomers, the procedure to derive physical parameters from the observed spectra in the presence of fine and hyperfine splitting is outlined. In order to evaluate physical quantities like gas densities, column densities and abundances relative to H_2, parameters resulting from a least square fit procedure to the observed spectra are employed in rotation diagram and radiative transfer escape probability techniques.

The rare C^{15}N isotopomer, which has been observed neither in the interstellar medium nor in the laboratory before, was discovered in the Orion Molecular Cloud-1 (**OMC-1**) with the KOSMA 3m telescope via its N=2$\rightarrow$1 hyperfine pattern. This first detection was subsequently confirmed with the IRAM 30m telescope in the N=1$\rightarrow$0 and N=2$\rightarrow$1 transitions. Observations of the main isotopomer in OMC-1 reveal significant variation in the CN abundance along the north-south oriented molecular ridge with a minimum toward the prominent source IRc2. This finding is explained by chemical depletion of CN in favor of more stable molecules, in particular HCN, in the immediate vicinity of this very hot and dense environment. In addition, the first ever observed spectral line maps of ^{13}CN were obtained toward the Orion molecular ridge. Abundance ratios of CN and ^{13}CN along the main axis of the cloud indicate large scale chemical fractionation in a

UV influenced cloud in favor of the rarer species.

The CN molecule attracted new attention since recently developed models for photon dominated chemistry predicted it to be chemically enhanced with respect to other species like CO or CS in the warm and dense surface layers of UV irradiated clumps. In photon dominated regions (PDR) close enough to the Earth and under certain geometrical conditions, the resulting stratified distribution of molecules is expected to be observable at high angular resolution and in particular at higher frequencies, where the excitation conditions in the warm and dense cloud layers favor the population of the higher lying rotational levels. Simultaneous observations of CN N=3$\rightarrow$2 and CS J=7$\rightarrow$6 obtained in this work indeed show a stratified distribution of both molecular species in the **Orion Bar** region, a prototypical PDR. It is shown that this finding can not be explained by means of excitation but has to be interpreted in terms of chemical abundance variations in a UV photon dominated environment, thus confirming the predictions from the chemical models. The observed spatial separation of the molecular emission peaks is used in conjunction with results from the models, calculated for a wide range of densities, to derive the density and line of sight thickness of the emitting layer. Careful inspection of other less prominent photon dominated regions in OMC-1 and NGC 2024 suggests that this kind of stratification, although reported in detail for the first time for CN and CS in the Orion Bar, is a common interstellar phenomenon.

The interpretation of mm and submm dust continuum emission maxima found in several sources as very dense and cold protostellar condensations, initiated a controversial discussion on the nature of these objects. One of the major topics in this context is whether molecules freeze out onto dust grains in the immediate vicinity of these sources. With regard to this subject, particular emphasis in this thesis was attributed to an observational study of the correspondence of CN emission with the distribution of other molecular tracers and the mm dust continuum at high angular resolution. Unlike other molecular tracers, CN emission proved to correlate fairly well with mm/submm dust continuum emission, with the exception of very dense and hot environments around newly formed stars, where it is depleted in favor of more stable molecules. Especially for the dense condensations associated with the molecular ridge in **NGC 2024**, combined CN and CS observations, obtained within the scope of this thesis, provide new additional evidence that the sources in fact may be more evolved than expected for protostars, and externally heated, although even additional embedded heating sources are not excluded. This conclusion is motivated by the close morphological correlation of warm and dense gas, as traced particularly by the energetically higher rotational transitions of CN and CS, with the dust continuum emission, as well as by the high degree of activity (outflows, infrared sources and masers) associated with the condensations. Moreover, the derived CN molecular column densities and relative abundances show no signatures of significant depletion of this species toward them. The correlation of CN molecular line and mm dust continuum emission was investigated in parallel on very small angular scales for a selected field in NGC 2024 with the Plateau de Bure Interferometer and the results further support the above drawn conclusions.

Several recent fundamental changes at the KOSMA observatory required the development of a new hard- and software concept for a broadband continuum backend (**COBAC**) which was realized as a technical part of this thesis.

Chapter 3. Introduction

Since the discovery of interstellar molecules at radio wavelengths (e.g. OH by Weinreb et al. 1963, NH_3 by Cheung et al. 1968 as the first interstellar polyatomic molecule and CO by Wilson, Jefferts & Penzias 1970), continuum and spectroscopic observations in the various atmospheric radio windows together with theoretical modeling have substantially contributed to increase and consolidate our knowledge on the structure, composition, and the physical processes in the interstellar medium.

99% of the interstellar matter building up molecular clouds is comprised in molecules and atoms in the gas phase, but the remaining 1% dust plays a very important role since it serves as catalyst for the formation of many chemical species, including the most abundant interstellar molecule H_2. In addition, dust shields the molecules against ionizing and dissociating UV radiation from the stars. Molecular clouds contain H_2 masses of up to 10^6 $M_\odot$ at temperatures typically ranging from 10 to several 100 K and densities from several 100 to 10^6 cm^{-3}. Most of the low lying energy levels of important interstellar molecules, atoms and ions are preferentially populated under these conditions. Many of the resulting rotational and fine structure transitions fall into atmospheric windows accessible by ground based radio telescopes or they are observable from air or space borne observatories.

The H_2 molecule is difficult to observe since it has no permanent electric dipole moment. The quadrupole rotational and vibrational transitions require high energies for excitation and are only observable in the very dense and shock influenced environments around young stellar objects at near infrared wavelengths. For this reason, the second most abundant molecule CO became the most important tool to investigate the properties of molecular clouds. Due to the small dipole moment, CO is readily detected even in the lower density regions. Other linear molecules with higher values of the dipole moment like CS, HCN, and CN are especially useful as tracers of higher density gas. More complex molecules like H_2CO or the symmetric top molecules CH_3CN and NH_3 serve as good probes for temperature determinations in the clouds. In this context, observations toward the hot and dense environments of ongoing high-mass star formation, so called *hot cores*, gain importance since complex molecules are enriched here due to evaporation of ice mantles on the surfaces of dust particles.

Observations collected during the past 25 years revealed that the material in molecular clouds is not distributed homogeneously. Moreover, the clumpy and filamentary appearance of molecular clouds, observed on almost all size scales, suggests a hierarchical or fractal structure as a common phenomenon (see e.g. Scalo 1990).

Results obtained by combining radio data with observations in other spectral regions, from the infrared to the shortest wavelengths, helped to establish the generally accepted picture that high- and low-mass stars are born in the dense cores of molecular cloud fragments. Recently, a great number of protoplanetary disks (*proplyds*), which are believed to be the sites of current star and planetary system formation, have been observed directly with the Hubble Space Telescope in the optical (O'Dell et al. 1993). Earth based high resolution spectroscopy led to the discovery of the first extrasolar planets around evolved stars (see e.g. Marcy et al. 1997). The massive stars in turn, besides the fact that they reprocess the material out of which they have once formed,

have a strong influence on the evolution of the parental cloud. They heat gas and dust, dissociate and ionize the atoms and molecules of the interstellar medium and create HII regions of ionized hydrogen in their immediate environment. Further star formation is triggered by stellar winds, radiation and shocks.

The ionizing UV radiation from high-mass stars creates so called Photon Dominated Regions (PDRs), the transition zones from ionized to atomic and molecular material, on the surfaces of the individual clumps. These PDRs are of particular interest in terms of interstellar chemistry. They show bright emission in their most important cooling lines, namely (in sequence according to the distance from the clump edge toward the clump interior) fluorescent vibrational H_2, the atomic fine structure lines of ionized carbon [CII] and neutral oxygen [OI], and atomic carbon [CI], as well as rotational emission lines of CO and other molecular species from the clump core. Chemical models predict a CN abundance enhancement close to the clump surface facing the UV photon source. The CN radical thus serves not only as a high density but also as a PDR tracer.

The cyanide radical was first discovered in the laboratory at optical wavelengths (Kistiakowsky & Gershinowitz 1933; White 1940) and subsequently detected in the interstellar medium (Adams 1941; Meyer et al. 1989) as one of the first interstellar molecules together with CH and CH^+. The observed absorption spectra of transitions from the first electronic excited state in the ground state, arising in translucent clouds towards luminous background stars, indicated an unusual excitation mechanism for the lower rotational levels. After the discovery of the Cosmic Background radiation by Penzias & Wilson (1965), it became clear that the energetically lowest rotational levels of CN in such radiation dominated sources are in equilibrium with the 3 K black body radiation. This means the lower rotational levels of CN are populated by Cosmic Background photons and not, as presumed for a long time before, by local excitation processes in the cloud. Since then, the electronic transitions of CN have been used to determine the temperature of the Cosmic Background radiation, e.g. Meyer & Jura (1985) derived a value of 2.70 ± 0.04 K.
A detailed discussion of this subject is given by Winnewisser & Herbst (1993).

Although interstellar CN had already been discovered quite early in the optical spectral range, it was not until 1970 that it was detected via the pure rotational transitions at radio frequencies by Jefferts et al. (1970). They observed two hyperfine components of the CN N=1$\rightarrow$0 transition towards the molecular clouds associated with Orion A and W51. The first fairly precise determination of the rotational molecular constants arose from astronomical observations of the N=1$\rightarrow$0 transition in Orion A by Penzias et al. (1974). The extremely reactive nature of the CN radical prevented its radio spectrum from being observed in the laboratory until 1977, when Dixon & Woods detected the microwave absorption spectrum of CN N=1$\rightarrow$0, $v = 0$ and 1 in the electronic ground state. Within the scope of the present thesis, the $C^{15}N$ isotopomer could be observed for the first time via its N=1$\rightarrow$0 and N=2$\rightarrow$1 rotational transitions in several Galactic sources. These new data are used together with laboratory data on CN and ^{13}CN reported in the literature to reveal a deviation from the Born Oppenheimer approximation (for details see Saleck et al. 1994a). CN thus serves as one example where interstellar molecular line detections have led to the deduction of molecular parameters not previously obtained by laboratory spectroscopy.

The observations obtained to date show that CN is readily detected towards the warm and active

molecular cloud environment, but is depleted in very hot and dense regions like the Orion hot core. The deficient excitation conditions in the cold and quiescent molecular phase make it difficult to observe CN in dark and cold interstellar clouds. Observational studies of interstellar CN at radio wavelengths are motivated by a number of attractive features:

- CN has a high abundance in the interstellar medium ($CN/H_2 \sim 10^{-8} - 10^{-9}$).
- The rotational transitions of CN are easy accessible through atmospheric windows with available receiver technology.
- Since CN is a radical with simultaneously observable hyperfine structure, optical depths are determined without ambiguities due to trapping.
- The high dipole moment of 1.45 Debye makes it a high density tracer and chemical models predict CN to be a PDR tracer as well.
- CN emission in conjunction with dust continuum and emission from other molecular species yields important information on the morphology, kinematics and chemistry in the cloud.
- Observations of several rotational transitions allow, in conjunction with radiative transfer models, the determination of the excitation conditions and the physical parameters of the clouds.
- Observations of the rarer isotopomers are an additional tool to determine isotopic ratios and to study fractionation effects.

In the following chapters, a detailed summary of the theoretical treatment concerning spectroscopic features and radiative transfer for CN will be given, followed by the presentation of results for the first three rotational transitions of CN, the N=1$\rightarrow$0 and N=2$\rightarrow$1 transitions of ^{13}CN and C^{15}N together with observations of other molecular species. As some highlights, the present thesis contains the first detection of C^{15}N, the first ever published maps of CN N=3$\rightarrow$2 (obtained in several sources) and ^{13}CN N=1$\rightarrow$0 and N=2$\rightarrow$1 (Orion A).

Chapter 4. The Cyanide Radical

4.1 Introduction

The electronic ground state of CN is $X^2\Sigma^+$ and the pure rotational energy levels of the CN radical resemble closely those of the most important polar interstellar species CO since both molecules have comparable masses and bond lengths and hence similar rotational constants. For CN, the spin of the unpaired electron $(\mathrm{S} = 1/2)$ and the nuclear spin of $^{14}\mathrm{N}$ $(\mathrm{I} = 1)$ lead to additional fine- and hyperfine splitting of the rotational levels. The quantity of the splitting is determined by the coupling of the different angular momenta and the values of the molecular coupling constants. Hund's coupling cases give approximations to the actual states of many linear molecules. Which case applies depends on the relative strength of the various couplings, or the relative energy of interaction between the angular momentum vectors. Hund distinguished between five different coupling cases, classified (a) through (e), where most observed or likely to be observed states of molecules can be approximated by cases (a) and (b) or intermediate between these two cases. CN is considered to conform closely to Hund's coupling case (b), which will be discussed in the next section. Detailed theoretical treatment of the topics of the following section can be found in the books of Herzberg (1950), Townes & Schawlow (1975) and Gordy & Cook (1984).

4.2 Hund's coupling case (b)

The appropriate vector diagram for Hund's coupling case (b) (and the special case of CN) is displayed in Fig. 4.1. In this case the electron spin is coupled more strongly to **N**=Λ+**O** than to the molecular axis. **L** is still strongly coupled to the molecular axis. Λ adds to **O** to form the total orbital angular momentum **N**. **N** and **S** add to **J**, about which they precess.

When $\Lambda = 0$ and $\mathrm{S} \neq 0$, as it is the case for CN, the electronic momentum is due to spin only and the spin moment becomes coupled to the axis of rotation **N**, now equivalent to **O** and perpendicular to the molecular axis, through a week magnetic field generated by the end-over-end rotation of the molecule. If the nuclear coupling is weaker than the spin-rotation interaction, the nuclear spin **I** adds to **N**+**S**=**J** to form the total angular momentum **F**.

4.2.1 Hamiltonian and molecular constants

The effective Hamiltonian of a molecule in a $^2\Sigma^+$ state, comprising spin-rotation interaction and centrifugal distortion $\mathcal{H}_{\mathrm{RFS}}$, magnetic nuclear interaction $\mathcal{H}_{\mathrm{MHF}}$ and nuclear quadrupole interaction $\mathcal{H}_{\mathrm{Q}}$ is given by Gordy & Cook (1984):

$$\begin{aligned}
\mathcal{H} &= \mathcal{H}_{\mathrm{RFS}} + \mathcal{H}_{\mathrm{MHF}} + \mathcal{H}_{\mathrm{Q}} \\
&= [\mathrm{B}_v - \mathrm{D}_v N(N+1)]\mathbf{N}^2 + \gamma_v\, \mathbf{S}\cdot\mathbf{N} \\
&\quad + \mathrm{b}_v\, \mathbf{I}\cdot\mathbf{S} + \mathrm{c}_v \mathrm{I}_z \mathrm{S}_z + \mathrm{C}_\mathrm{I}\ \mathbf{N}\cdot\mathbf{I} \\
&\quad + \frac{\mathrm{eQq}_v}{4}\, \mathrm{T}_0^{(2)}(\mathbf{I})
\end{aligned}$$

where B_v are the rotational, D_v the centrifugal distortion and γ_v the spin-rotation coupling constants. b_v, c_v and C_I designate the nuclear magnetic coupling constants. The index v refers to

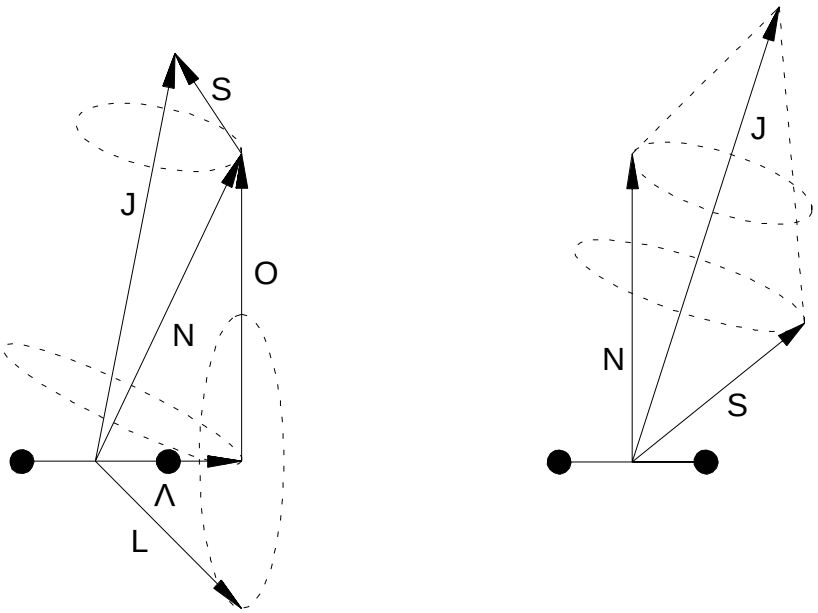

Fig. *4.1: Vector diagram for Hund's case (b) (left) and the special case of CN* $X^2\Sigma^+$ *(right). Note that hyperfine structure is not considered, i.e. the coupling* **N**+**S**+**I**=**F** *for CN.*

the dependence of the constants on the vibrational quantum number. Usually the quadrupole coupling is weak compared to magnetic interactions. Its contribution to the Hamiltonian is:

$$\frac{\mathrm{eQq}_v}{4}\,\mathrm{T}_0^{(2)}(\mathbf{I}) = \mathrm{eQq_v}\ \mathrm{f}\ (\mathrm{I},\mathrm{J},\mathrm{F})$$

where f (I,J,F) is the Casimir function, eQq_v the electric quadrupole constant and $\mathrm{T}_0^{(2)}(\mathrm{I})$ the molecule fixed zeroth component of the quadrupole moment tensor. The Casimir function is defined as:

$$\mathrm{f(I,J,F)} = \frac{\frac{3}{4}\,\mathrm{C(C+1)} - \mathrm{I(I+1)J(J+1)}}{2\mathrm{(2J+3)(2J-1)(2I-1)}}$$

where C$= \mathrm{F(F+1)} - \mathrm{I(I+1)} - \mathrm{J(J+1)}$. J takes on the values

$$\text{N+S, N+S–1, } \ldots, \mid \mathrm{N} - \mathrm{S} \mid,$$

which means that the rotational levels are split into (2S+1) fine structure levels. F takes on the values

$$\mathrm{J+I,\ J+I-1,}\ldots, \mid \mathrm{J-I} \mid.$$

In the case of CN, where $\mathrm{S} = 1/2$ and $\mathrm{I} = 1$, each rotational level $\mathrm{N} > 0$ is split into two fine structure (ρ-type doubling) and, for $\mathrm{J} \neq 1/2$, three hyperfine structure levels. The electric quadrupole interaction results in very small shifts of the hyperfine levels.

The mm and submm spectrum of CN in the first four vibrational states, comprising rotational transitions up to N=4→3 and including molecular constants, was first published by Skatrud et al. (1983). The CN ground state molecular constants from their work are listed in Table 4.1. The permanent electric dipole moment was determined to $\mu = 1.45$ Debye by Thomson & Dalby (1968) via optical Stark effect measurements.

B_0 [MHz]	D_0 [MHz]	γ_0 [MHz]	b_0 [MHz]	c_0 [MHz]	eQq_0 [MHz]	C_I [kHz]	μ [Debye]
56693.461(3)	0.19137(21)	217.499(5)	-33.987(16)	60.390(46)	-1.270(39)	5	1.45

Table *4.1: CN ground state molecular constants from Skatrud et al. (1983). Values in parentheses are* 1σ *deviations.*

4.2.2 Energy level diagram and relative intensities

The energy level diagram for the first four rotational levels of CN in its ground state is shown in Fig. 4.2. Straight arrows mark the hyperfine transitions which were observed within the scope of this work together with their relative intensities $s_{NJF\rightarrow N'J'F'}$ given in % of the intensity of the pure rotational transition. Following the notation of Gordy & Cook (1984), who give a detailed theoretical overview, the line strength of a transition $NJF \rightarrow N'J'F'$ is proportional to the sum of the squares of the dipole moment matrix elements over all directions in the space fixed system, all polarizations and magnetic quantum numbers and can be reduced to

$$S(NJF \rightarrow N'J'F') = |(NJF||\mu^{(1)}||N'J'F')|^2 \tag{4.1}$$

where $\mu^{(1)}$ stands for the reduced matrix element of the dipole moment tensor. The relative line strength of a single hyperfine line then is

$$s_{NJF\rightarrow N'J'F'} = \frac{S(NJF \rightarrow N'J'F')}{\sum_{FF'} S(NJF \rightarrow N'J'F')} \quad .$$

The selection rules resulting from (4.1) for the rotational transitions are

$$\begin{aligned} \Delta N &= \pm 1 \\ \Delta J &= 0, \pm 1 \\ \Delta F &= 0, \pm 1 \quad . \end{aligned}$$

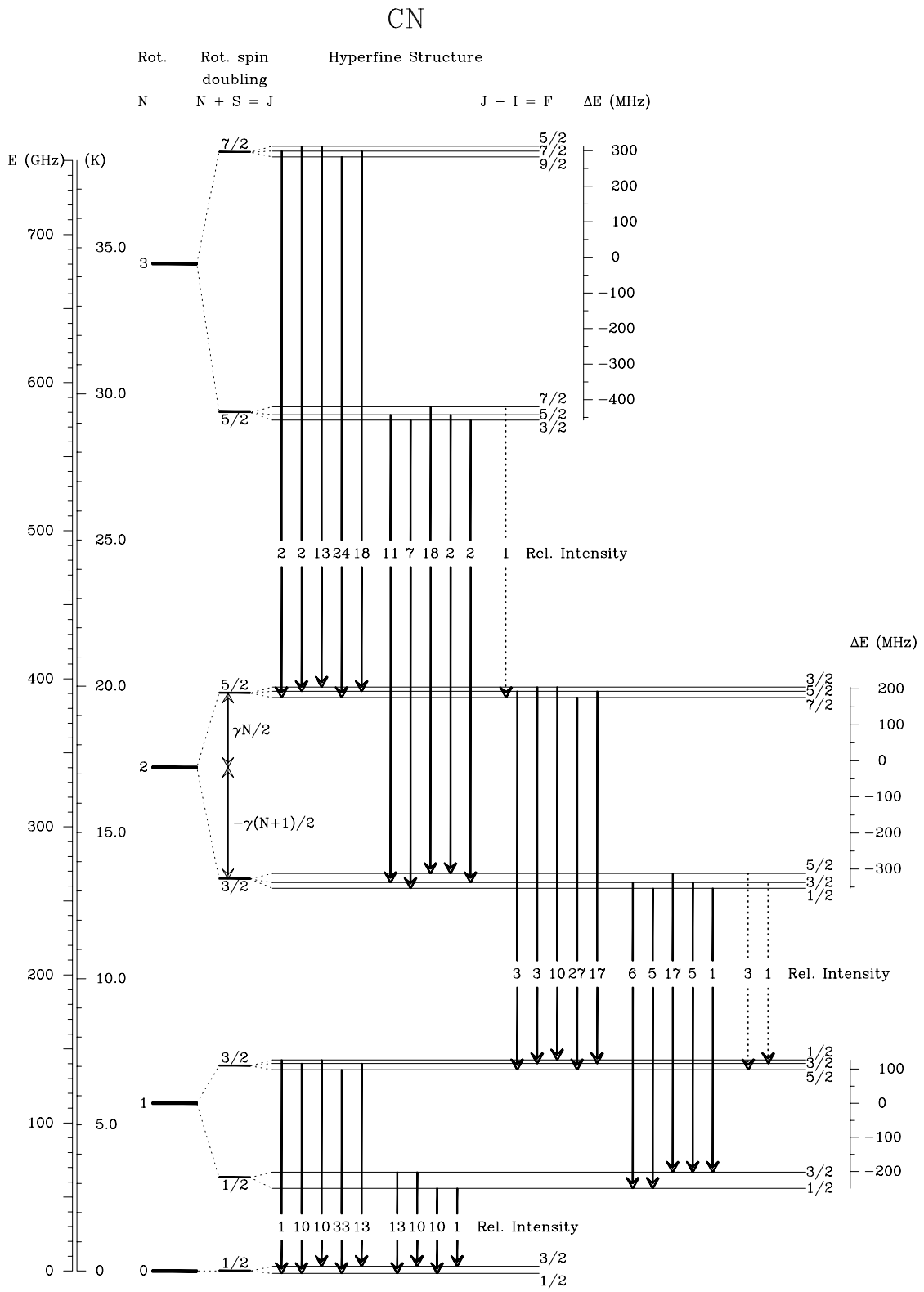

Fig. *4.2: Energy level diagram of the CN N=1→0 to N=3→2 rotational transitions. Relative intensities are given in percent of the total intensity of the rotational transition. Bold arrows mark the transitions observed in this work. The dashed arrows mark transitions in a spectral range not covered by our observations. Lines with relative intensities less than 1% were below the detection limit and have been neglected.*

The evaluation of the reduced matrix element depends on the coupling scheme and in the case of CN, where one has to consider rotation, fine and hyperfine structure, results in

$$\begin{aligned} \mathrm{S}_{\mathrm{NJF}\rightarrow\mathrm{N'J'F'}} &= \frac{(2\mathrm{F'}+1)(2\mathrm{F}+1)}{2\mathrm{I}+1} \left\{ \begin{array}{ccc} \mathrm{J'} & \mathrm{F'} & \mathrm{I} \\ \mathrm{F} & \mathrm{J} & 1 \end{array} \right\}^2 \\ &\times \frac{(2\mathrm{J'}+1)(2\mathrm{J}+1)}{2\mathrm{S}+1} \left\{ \begin{array}{ccc} \mathrm{N'} & \mathrm{J'} & \mathrm{S} \\ \mathrm{J} & \mathrm{N} & 1 \end{array} \right\}^2 \end{aligned} \tag{4.2}$$

where the symbol in braces is the $6j$ symbol. The normalization is such that within one rotational transition $\sum \mathrm{s}_{\mathrm{NJF}\rightarrow\mathrm{N'J'F'}} = 1$. Numbers for the relative intensities are given in the Appendix together with the transition frequencies.

The individual hyperfine transitions of each rotational transition displayed in the energy level diagram are descending in frequency from left to right so that they can easily be identified in the corresponding spectra presented in Fig. 4.3 to 4.5. Dashed arrows indicate transitions in a spectral range not covered by the backends.

4.2.3 Sample Spectra

Spectra of CN N=1→0 and N=2→1 are shown in Fig. 4.3 through 4.5. Spectra obtained at 9 single positions around the region of peak CN intensity in the northeastern part of the Orion Molecular Cloud 1 (OMC-1) have been averaged in order to enhance the signal to noise and to display the weaker hyperfine components. The corresponding complete data sets are presented and discussed in Chapter 7.

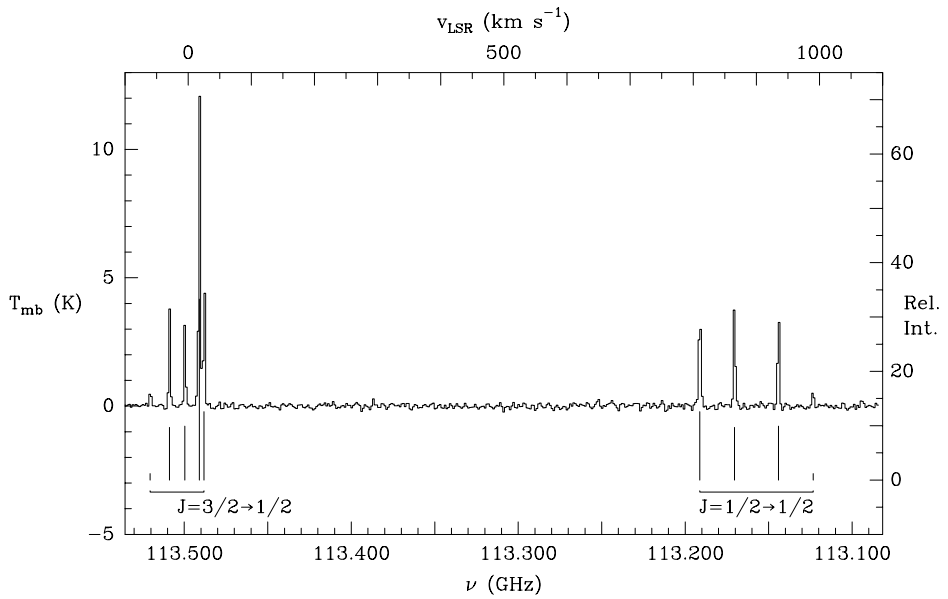

Fig. *4.3: CN N=1→0 spectrum obtained at the IRAM 30m telescope in OMC-1 with the 1 MHz resolution filterbank. The bars below the spectrum denote the positions and relative intensities in % (right axis) of the CN hyperfine lines in the optically thin case.*

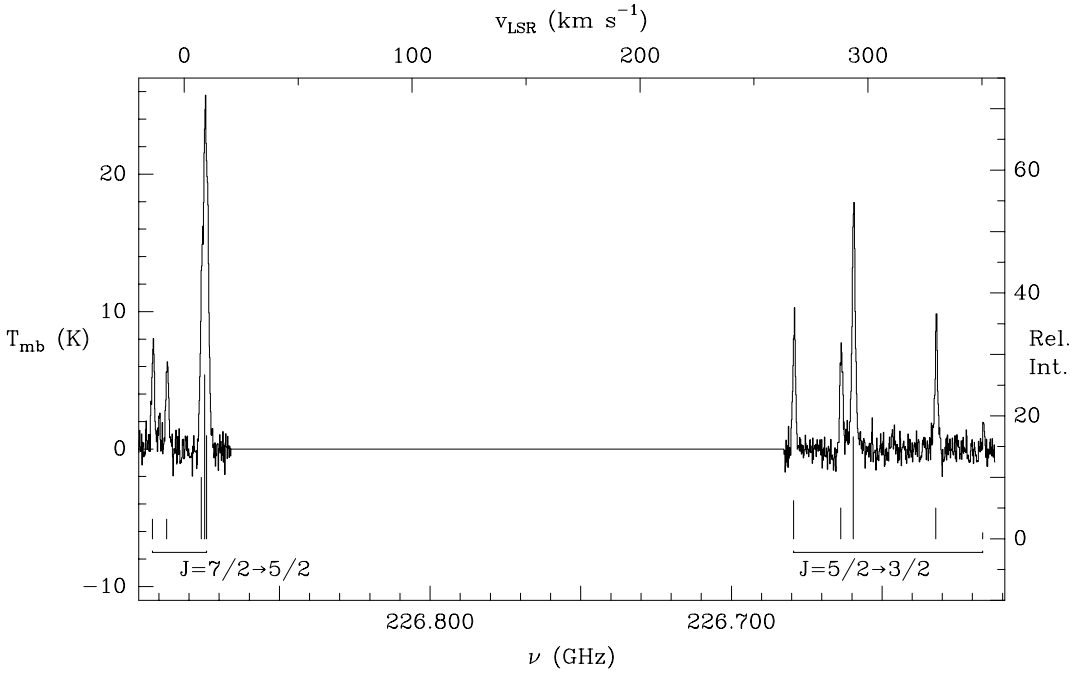

Fig. *4.4: CN N=2→1 spectrum obtained at the IRAM 30m telescope in OMC-1. The bars below the spectrum denote the positions and relative intensities in % (right axis) of the CN hyperfine lines in the optically thin case. Two parts of the IRAM autocorrelator have been merged.*

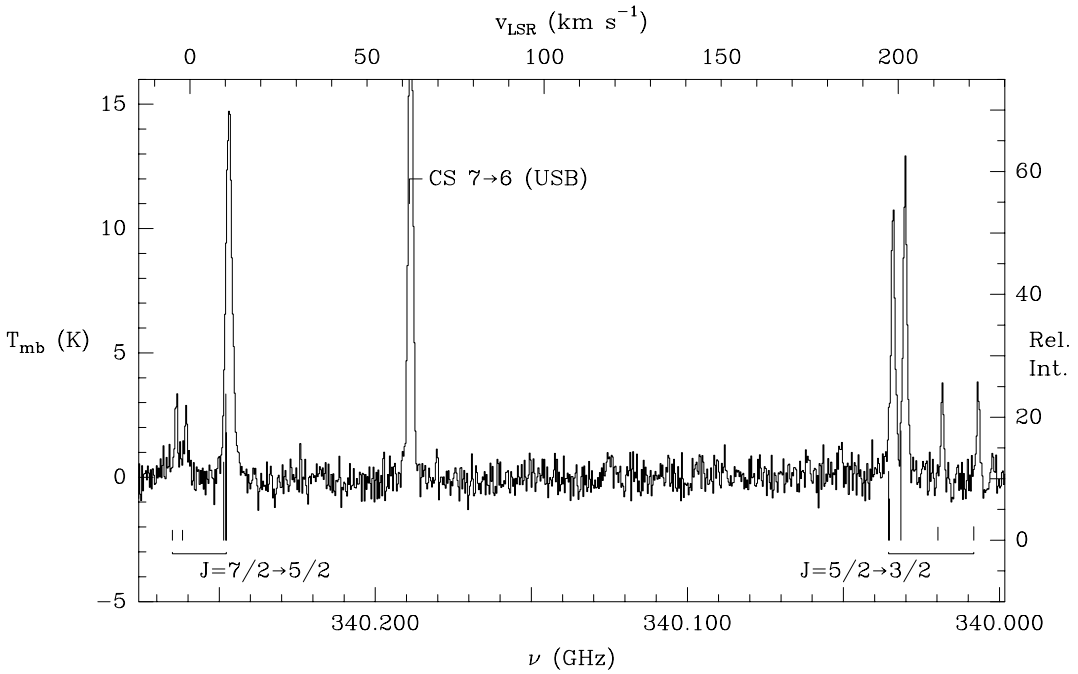

Fig. *4.5: CN N=3→2 spectrum together with the simultaneously observed CS J=7→6 transition from the upper sideband (USB) obtained at the JCMT 15m telescope in OMC-1. The bars below the spectrum denote the positions and relative intensities in % (right axis) of the CN hyperfine lines in the optically thin case.*

4.3 Einstein A coefficients and critical densities

The Einstein A coefficient for a pure rotational transition $\mathrm{N} \rightarrow \mathrm{N}'$ of a linear molecule at frequency ν is defined by the formula

$$\mathrm{A_{ul}} = \mathrm{A_{N\rightarrow N'}} = \frac{64\pi^4\nu^3}{3hc^3}|(\mathrm{N'}||\mu_{ij}||\mathrm{N})|^2 = \frac{64\pi^4\nu^3}{3hc^3}\frac{\mathrm{N}}{2\mathrm{N}+1}\mu^2 \tag{4.3}$$

and gives the rate of spontaneous emissions per second from the upper level N to the lower level N', where the factor $(\mathrm{N})/(2\mathrm{N}+1)$ results from the evaluation of the direction cosine matrix elements according to Gordy & Cook (1984) and μ denotes the electric dipole moment. The corresponding rate for collisions is represented by $\mathrm{C_{ul}}$. The critical density of a molecular transition is the density at which the timescales for spontaneous emission and collisional de-excitation are equal

$$\mathrm{n}_{crit} = \frac{\mathrm{A_{ul}}}{\gamma_{\mathrm{ul}}} = \mathrm{n}\frac{\mathrm{A_{ul}}}{\mathrm{C_{ul}}} \tag{4.4}$$

where $\gamma_{\mathrm{ul}} = \langle \sigma_{\mathrm{ul}}\, v(\mathrm{T})\rangle$ is the rate coefficient for collisional de-excitation which is comprised of the cross section for collision σ_{ul} and the relative velocity $v(\mathrm{T})$ between the molecules involved in the collision.

At densities well below the critical density, each collisional excitation leads to emission of a photon and the excitation conditions are dominated by the external radiation fields (at least the Cosmic Background radiation in the absence of other external radiation sources). At densities much higher than the critical density, collisions dominate. In both cases, the cloud is in local thermal equilibrium (LTE) and the levels are populated according to a Boltzmann distribution at the radiation temperature $\mathrm{T_{bg}}$ or the kinetic temperature T_{kin} respectively. The excitation then is called **thermal**.

Thermalization at the kinetic temperature can be maintained even at densities lower than the critical density if the optical depth of the line is high. In this non-LTE case, *trapping*, i.e. the absorption and reemission of a photon, leads to an effective lower value of the Einstein A coefficient, which in turn reduces the critical density. This effect is characterized by the escape probability β which will be briefly discussed in the following chapter.

At densities lower than the critical density, where trapping can not maintain thermalization, the collisional rates are low, resulting in radiative de-population of the upper levels. The population then corresponds to a Boltzmann distribution at a temperature $\mathrm{T}_{ex} < \mathrm{T}_{kin}$ and the excitation is called **subthermal**.

Since we are dealing with systems involving more than two energy levels, the collisional rate coefficient for the two level system represents a first order approximation and can be replaced by the sum over all collisional transitions out of the upper level. This will result in a lower value for the critical density than determined for the two level system. The critical densities listed in Table 4.2 are calculated for a two level system and three different kinetic temperatures. Since there are no collisional rate coefficients measured or calculated for CN, the values for CS, as

determined by Green & Chapman (1978), have been used.

Molecule	Transition	μ [Debye]	A_{ul} [s^{-1}]	n_{crit} [cm^{-3}]			E_{upper} [K]
				$T_{kin} = 10$K	40K	100K	
CN[a]	N=1→0	1.45	1.19×10^{-5}	1.0×10^{6}	7.5×10^{5}	7.5×10^{5}	5.4
	N=2→1		1.14×10^{-4}	3.9×10^{6}	2.9×10^{6}	2.9×10^{6}	16.0
	N=3→2		4.13×10^{-4}	9.0×10^{6}	9.2×10^{6}	9.6×10^{6}	32.6
CS[a]	J=3→2	1.96	6.07×10^{-5}	1.3×10^{6}	1.4×10^{6}	1.4×10^{6}	14.1
	J=5→4		2.98×10^{-4}	9.0×10^{6}	6.9×10^{6}	6.8×10^{6}	35.3
	J=7→6		8.39×10^{-4}	3.0×10^{7}	2.2×10^{7}	2.0×10^{7}	65.8
HCN[b]	J=1→0	2.96	2.40×10^{-5}	3.0×10^{6}	4.1×10^{6}	4.5×10^{6}	4.3
CO[c]	J=1→0	0.11	7.46×10^{-8}	3.2×10^{3}	2.3×10^{3}	1.5×10^{3}	5.5
	J=2→1		7.16×10^{-7}	2.6×10^{4}	1.5×10^{4}	8.2×10^{3}	16.6
	J=3→2		2.59×10^{-6}	1.0×10^{5}	4.0×10^{4}	2.6×10^{4}	33.2

Collisional Rate coefficients adopted from:

[a] Green & Chapman (1978)

[b] Green & Thaddeus (1974)

[c] Flower & Launey (1985)

Table *4.2: Dipole moments, Einstein A coefficients, critical densities for two level systems of CN and energies above the ground level in comparison to values for other molecules of astrophysical interest.*

4.4 The isotopomers ^{13}CN and C^{15}N

Like for the main isotopomer CN, each rotational level $\mathrm{N} > 0$ of the rarer species ^{13}CN and C^{15}N is split into a fine structure doublet due to the spin rotation interaction. Since the hyperfine structure is mainly caused by the magnetic interaction of electron and nuclear spin, differences between the isotopomers arise which are due to different nuclear spins.

4.4.1 ^{13}CN

For ^{13}CN, the nuclear spin $\mathrm{I}_1(^{13}\mathrm{C}) = 1/2$ leads to hyperfine doublets solely caused by the interaction of nuclear and electron spin. Equivalent to the situation for CN, each $^{13}\mathrm{C}$ hyperfine component $\mathrm{F}_1 \neq 0$ is split into three levels.

Due to the two nuclear spins of ^{13}CN, the energy levels of ^{13}CN are determined according to the coupling scheme

$$\mathrm{J} = \mathrm{N} + \mathrm{S}, \mathrm{F}_1 = \mathrm{J} + \mathrm{I}_1, \mathrm{F} = \mathrm{F}_1 + \mathrm{I}_2$$

where $\mathrm{I}_1 = \mathrm{I}(^{13}\mathrm{C}) = \frac{1}{2}$ and $\mathrm{I}_2 = \mathrm{I}(^{14}\mathrm{N}) = 1$. The selection rule $\Delta\mathrm{F} = 0, \pm 1$, valid for CN, has to be replaced by the selection rules $\Delta\mathrm{F}_1 = 0, \pm 1$ and $\Delta\mathrm{F} = 0, \pm 1$. The relative intensities of the hyperfine transitions are given by

$$\begin{aligned} S_{\mathrm{N\,JF} \rightarrow \mathrm{N'\,J'F'}} &= \frac{(2\mathrm{F'}+1)(2\mathrm{F}+1)}{2\mathrm{I}_2+1} \left\{ \begin{array}{ccc} \mathrm{F}_1' & \mathrm{F}' & \mathrm{I}_2 \\ \mathrm{F} & \mathrm{F}_1 & 1 \end{array} \right\}^2 \\ &\times \frac{(2\mathrm{F}_1'+1)(2\mathrm{F}_1+1)}{2\mathrm{I}_1+1} \left\{ \begin{array}{ccc} \mathrm{J}' & \mathrm{F}_1' & \mathrm{I}_1 \\ \mathrm{F}_1 & \mathrm{J} & 1 \end{array} \right\}^2 \\ &\times \frac{(2\mathrm{J}'+1)(2\mathrm{J}+1)}{2\mathrm{S}+1} \left\{ \begin{array}{ccc} \mathrm{N}' & \mathrm{J}' & \mathrm{S} \\ \mathrm{J} & \mathrm{N} & 1 \end{array} \right\}^2 . \end{aligned} \tag{4.5}$$

Bogey et al. (1984) published measurements of ^{13}CN in its ground state and in excited vibrational states up to $v = 9$, accompanied by a study of the isotopic dependence of the molecular constants. Shortly afterwards, the N=1→0 transition of ^{13}CN was detected for the first time in the interstellar medium in three Galactic sources (Gerin et al. 1984).

The energy level diagram for the first three rotational levels of ^{13}CN in its ground state is shown in Fig. 4.6. The individual hyperfine transitions are displayed descending in frequency from left to right so that they can easily be identified in the corresponding spectra presented in Fig. 4.7 and 4.8. Like for CN, spectra obtained at 9 single positions in the northeastern part of OMC-1 have been averaged in order to enhance the signal to noise of the ^{13}CN spectra.

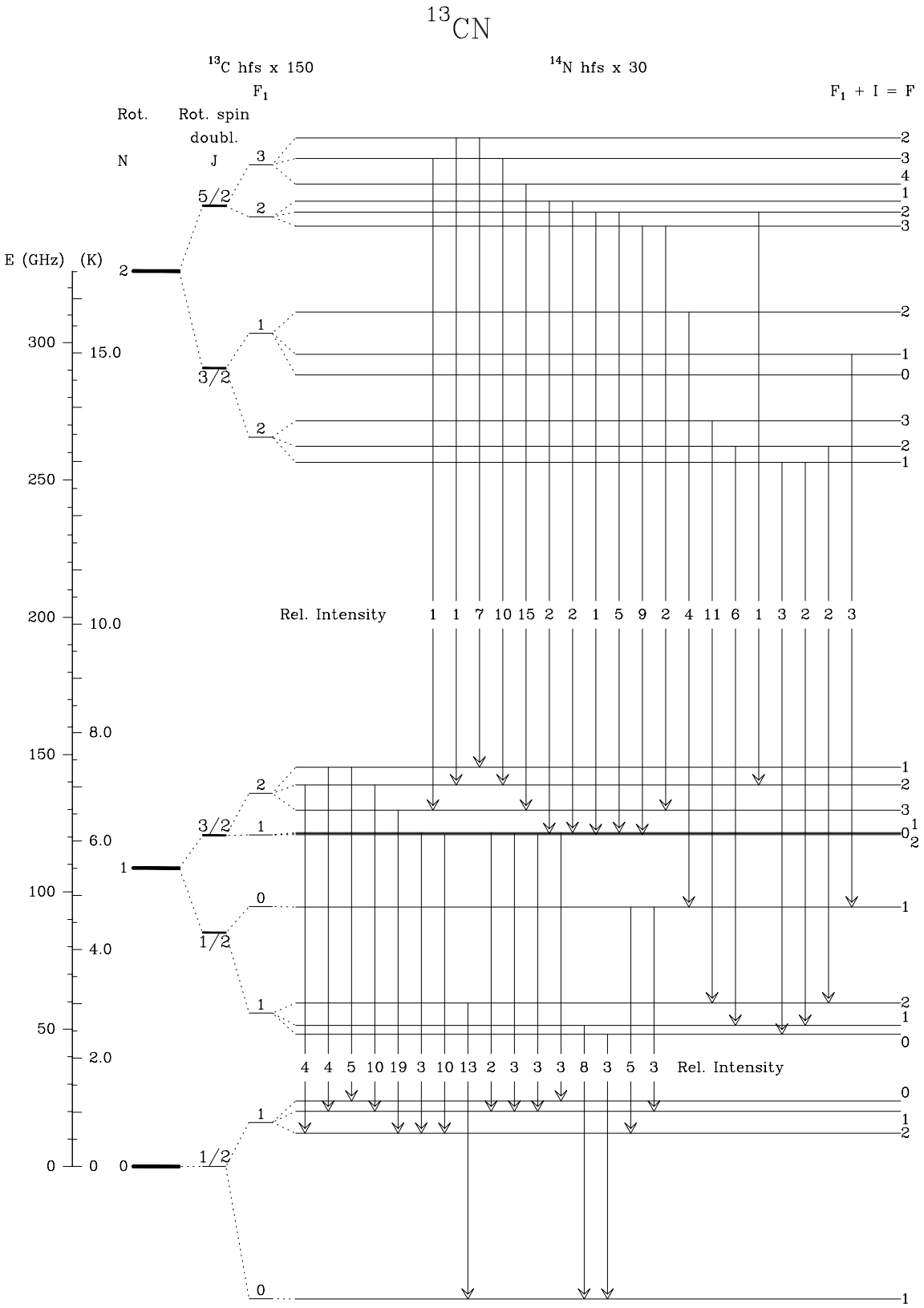

Fig. *4.6: Energy level diagram of the* ^{13}*CN N=1→0 and N=2→1 rotational transitions. The observed hyperfine components are indicated by arrows. Relative intensities are given in percent of the total intensity of the rotational transition.*

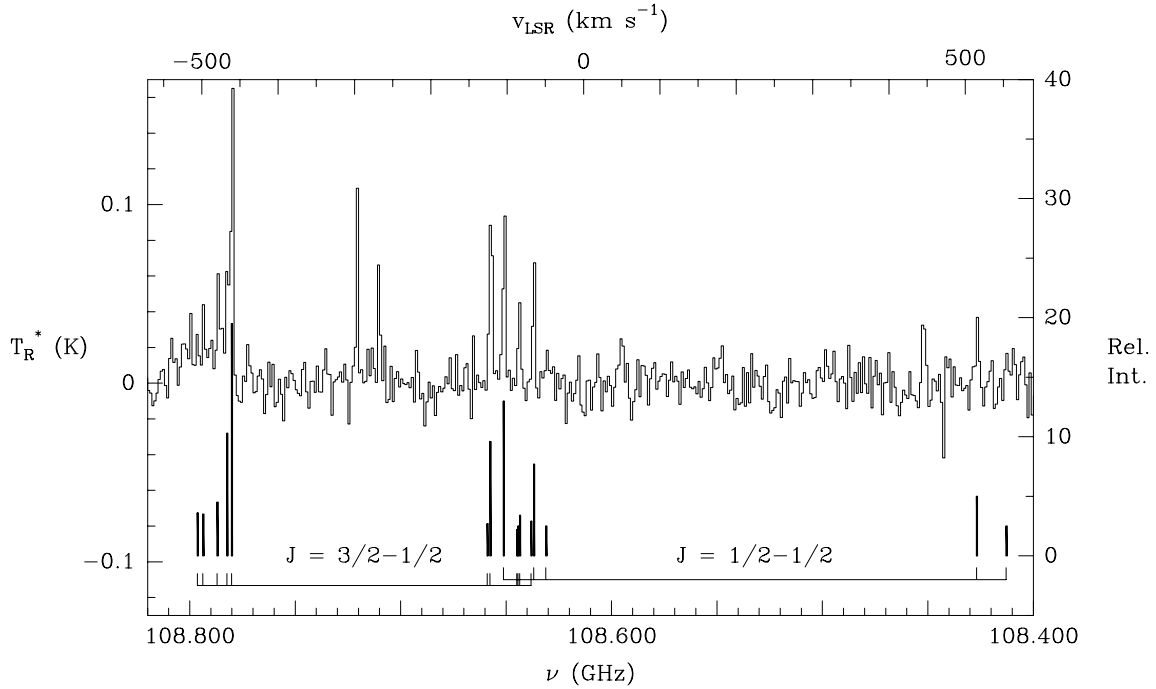

Fig. *4.7: ^{13}CN N=1→0 spectrum obtained at the IRAM 30m telescope in OMC-1 with the 1MHz resolution filterbank. The bars below the spectrum denote the positions and relative intensities in % (right axis) of the hyperfine lines in the optically thin case.*

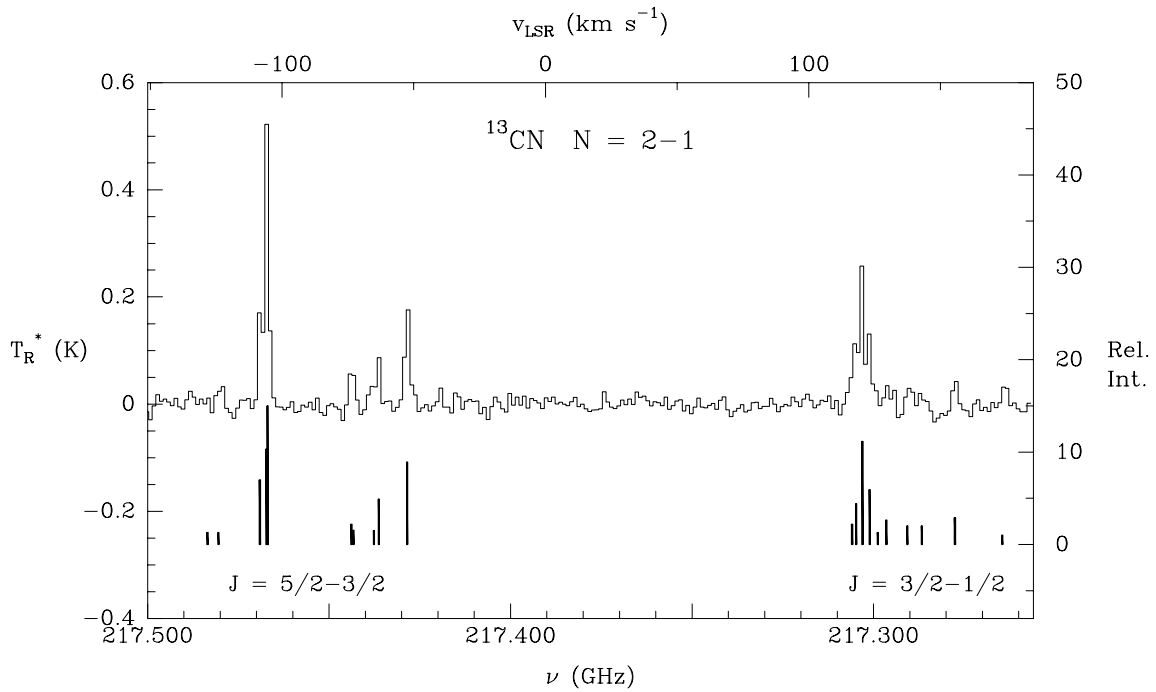

Fig. *4.8: The same as Fig 4.7 for ^{13}CN N=2→1.*

4.4.2 $C^{15}N$

As for ^{13}CN with $I(^{13}C) = 1/2$, the nuclear spin $I(^{15}N) = 1/2$ leads to hyperfine doublets for each fine structure level of $C^{15}N$. The selection rules are the same as for CN and the relative intensities of the $C^{15}N$ hyperfine lines are calculated according to equation (4.2). The energy level diagram for the first three rotational levels of $C^{15}N$ in its ground state is shown in Fig. 4.9.

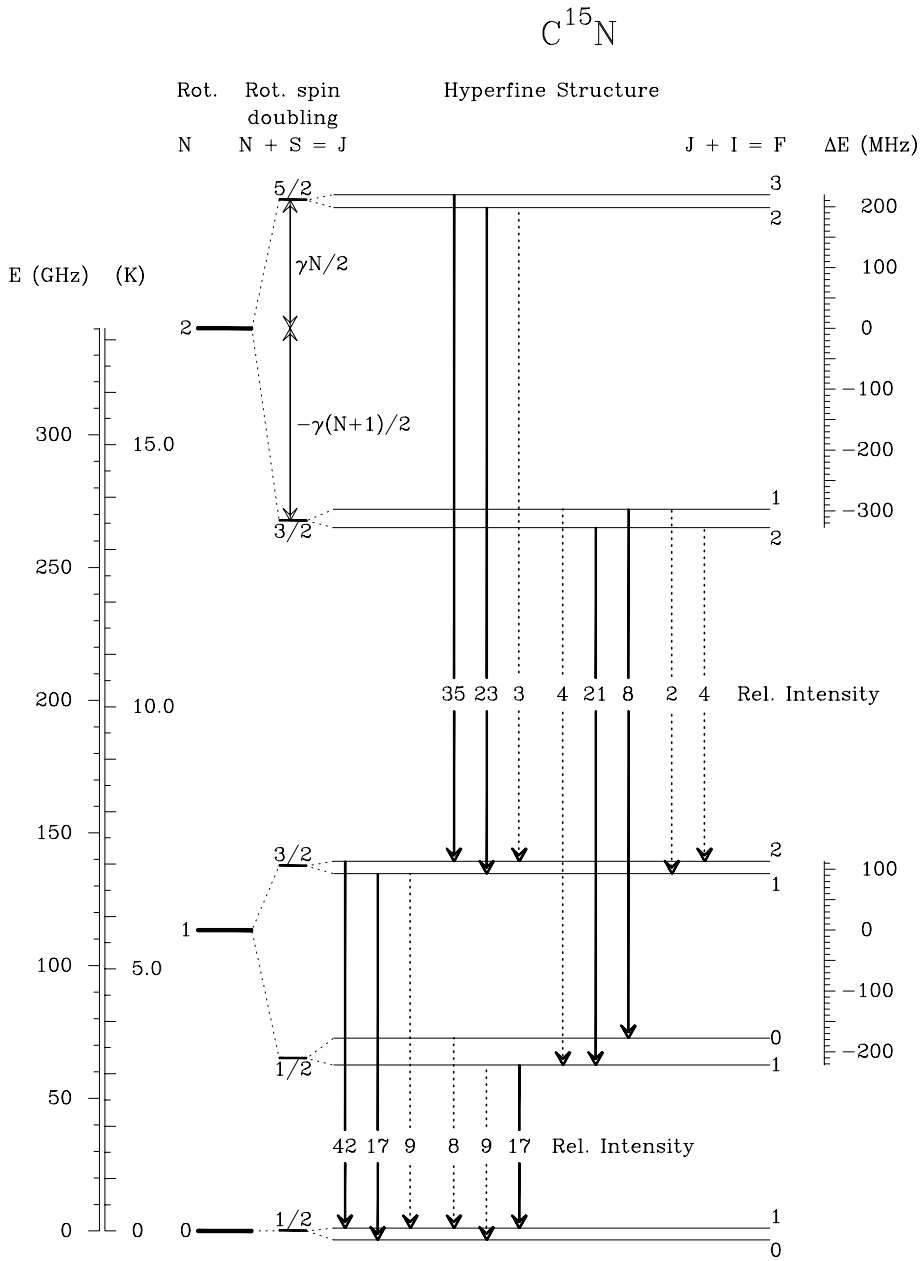

Fig. *4.9: Energy level diagram of the $C^{15}N$ N=1→0 and N=2→1 rotational transitions. The observed hyperfine components are indicated by bold arrows. The dashed arrows mark transitions below the detection limit or in a spectral range not covered by our observations. Relative intensities are given in percent of the total intensity of the rotational transition.*

Based on a study of the isotopic dependences of molecular rotational, spin doubling, and magnetic hyperfine parameters (for a detailed treatment of the theoretical aspect see Saleck 1995b), A.H. Saleck predicted the rotational spectrum of $C^{15}N$ up to N=3→2. Within the framework of the present thesis, the N=2→1 transitions were subsequently detected with the KOSMA 3m telescope towards Orion A for the first time by Saleck et al. (1993). Shortly afterwards we confirmed our previous first detection by observations of the hyperfine patterns of $C^{15}N$ N=1→0 and N=2→1 with the IRAM 30m telescope (Saleck, Simon, and Winnewisser 1994a) in the same source as well as in other Galactic sources. Spectra of $C^{15}N$ N=1→0 and N=2→1 obtained towards the region north-east of IRc2 in OMC-1 are shown in Chapter 7.

These new interstellar data provided the missing link in the available data set on the CN isotopomers for the derivation of isotopically invariant parameters and for a study of the validity of the Born-Oppenheimer approximation (for details see Saleck, Simon, and Winnewisser 1994a). The combination of astrophysical and laboratory data sets allowed, to a high level of confidence, the prediction of transition frequencies for CN and its various isotopomers into the submillimeter wave region. Frequencies up to N=8→7 at 890 GHz for CN, ^{13}CN, and $C^{15}N$ are listed in Appendix A.

4.4.3 Molecular constants for ^{13}CN and $C^{15}N$

Parameter		^{13}CN	$C^{15}N$
Rotation	B	54343.1412 (60)	54958.508 (20)
Centrifugal distortion	D	0.17666 (87)	0.18067 (25)
Spin-rotation	γ	208.501 (15)	210.857 (33)
Fermi contact	b_{F_C}	566.67 (12)	–
	b_{F_N}	-13.869 (16)	19.430 (18)
Spin-dipolar	t_C	56.764 (18)	–
	t_N	20.098 (22)	-28.212 (19)
Quadrupole	eQq	-1.316 (42)	–

Table *4.3: Ground state molecular constants of ^{13}CN and $C^{15}N$ in MHz from Bogey et al. (1984) and Saleck, Simon, and Winnewisser (1994a), respectively. Values in parentheses are 1σ deviations.*

Chapter 5. Radiative Transfer

5.1 Basic definitions

The general form of the equation of radiative transfer is:

$$\frac{d\mathrm{I}_\nu}{d\mathrm{s}} = \varepsilon_\nu - \kappa_\nu \mathrm{I}_\nu \quad , \tag{5.1}$$

where I_ν is the specific intensity and $\mathrm{I}_\nu d\Omega$ the portion of energy emitted per time, frequency and per area perpendicular to the line of sight and per solid angle $d\Omega$. The emissivity ε_ν for a transition from an upper level *u* to a lower level *l* is given by

$$\varepsilon_\nu = \frac{h\nu_{\mathrm{ul}}}{4\pi} \mathrm{n_u A_{ul}} \phi(\nu)$$

and the opacity κ_ν by

$$\kappa_\nu = \frac{h\nu_{\mathrm{ul}}}{\mathrm{c}} (\mathrm{n_l B_{lu}} - \mathrm{n_u B_{ul}}) \phi(\nu) \quad ,$$

where $\mathrm{A_{ul}}$, $\mathrm{B_{ul}}$ and $\mathrm{B_{lu}}$ are the Einstein coefficients of spontaneous and induced emission and absorption respectively, and $\mathrm{n_u}$ and $\mathrm{n_l}$ the number densities in the upper and the lower state. The profile function $\phi(\nu)$ defines the normalized probability for emission or absorption in the frequency interval $[\nu, \nu + d\nu]$.
Using the definition of the optical depth

$$\int \tau_\nu d\nu = \int\int \kappa_\nu d\mathrm{s} d\nu$$

and the source function $\mathrm{S}_\nu = \varepsilon_\nu / \kappa_\nu$, the equation of radiative transfer is

$$\frac{d\mathrm{I}_\nu}{d\tau_\nu} = \mathrm{S}_\nu - \mathrm{I}_\nu \quad . \tag{5.2}$$

Using the relations between the Einstein coefficients

$$\mathrm{g_l B_{lu}} = \mathrm{g_u B_{ul}} = \frac{\mathrm{c}^3}{8\pi h \nu_{\mathrm{ul}}^3} \mathrm{g_u A_{ul}} \quad ,$$

the source function S_ν can be written as

$$\mathrm{S}_\nu = \frac{2h\nu_{\mathrm{ul}}^3}{\mathrm{c}^2} \frac{1}{(\mathrm{n_l g_u / n_u g_l}) - 1} \quad .$$

For further considerations it is useful to define the excitation temperature $\mathrm{T_{ex}}$:

$$\frac{\mathrm{n_u}}{\mathrm{n_l}} = \frac{\mathrm{g_u}}{\mathrm{g_l}} \ \exp(-\frac{h\nu_{\mathrm{ul}}}{k\mathrm{T_{ex}}}) \ .$$

The excitation temperature is an equivalent Planck temperature that describes the population of states *l* and *u* through a thermal Boltzmann distribution (**L**ocal **T**hermodynamic **E**quilibrium, LTE). With this definition the source function becomes the Kirchhoff-Planck function $\mathrm{B}_\nu(\mathrm{T_{ex}})$

$$\mathrm{S}_\nu = \mathrm{B}_\nu(\mathrm{T_{ex}}) = \frac{2h\nu^3}{\mathrm{c}^2}\frac{1}{\exp(h\nu/(k\mathrm{T_{ex}})) - 1} \ .$$

As a convention in Radio Astronomy, the intensity is expressed in terms of a brightness temperature $\mathrm{T_b}$ by $\mathrm{I}_\nu = \mathrm{B}_\nu(\mathrm{T_b})$ which in the Rayleigh-Jeans limit ($h\nu \ll k\mathrm{T}$) takes the form

$$\mathrm{I}_\nu = \frac{2\nu^2 k}{\mathrm{c}^2}\mathrm{T_b} \ .$$

The Rayleigh-Jeans approximation is strictly valid only for $\lambda > 1$cm and $\mathrm{T} > 10$K. At submm wave lengths, $\mathrm{T_b}$ therefore has to be substituted by the radiation temperature $\mathrm{T_R}$, the Rayleigh-Jeans corrected brightness temperature

$$\mathrm{T_R}(\mathrm{T_b}, \nu) = \frac{h\nu}{k}\frac{1}{\exp(h\nu/(k\mathrm{T_b})) - 1} \simeq \mathrm{T_b} - \frac{h\nu}{2k} + \ldots$$

Equation (5.2), after formal integration and assuming a constant source function, yields

$$\mathrm{I}_\nu = \mathrm{S}_\nu(1 - \exp(-\tau_\nu)) + \mathrm{I}_{\nu,0}\exp(-\tau_\nu) \tag{5.3}$$

where $\mathrm{I}_{\nu,0}$ is the background intensity. Multiplying by a factor of $\mathrm{c}^2/2k\nu^2$ yields

$$\mathrm{J}_\nu(\mathrm{T_R}) = [\mathrm{J}_\nu(\mathrm{T_{ex}}) - \mathrm{J}_\nu(\mathrm{T_{bg}})]\,(1 - \exp(-\tau_\nu)) \tag{5.4}$$

where $\mathrm{J}_\nu(\mathrm{T}) = h\nu/k\,[\exp(h\nu/k\mathrm{T}) - 1]^{-1}$ is the normalized Planck intensity and $\mathrm{T_R}$ the radiation temperature of the source without background. The dominating contribution of the background emission is assumed to originate from the 2.74 K black body radiation of the Cosmic background.

If we take into account the coupling of the telescope beam to the source via the coupling efficiency η_c, the **detection equation** is expressed by

$$\mathrm{T}^*_\mathrm{R}(\nu) = \eta_\mathrm{c}\,[\mathrm{J}_\nu(\mathrm{T_{ex}}) - \mathrm{J}_\nu(\mathrm{T_{bg}})]\,(1 - \exp(-\tau_\nu)) \tag{5.5}$$

where T^*_R is the antenna temperature measured with the telescope and corrected for atmospheric and ohmic losses, rearward and forward spillover (for details see Kutner & Ulich 1981).

5.2 Derivation of column densities

In the presence of fine and hyperfine splitting, the optical depth as a function of frequency can be written as

$$\tau_\nu = \sum_{\mathrm{JF}} \tau_{\mathrm{NJF}} \phi(\nu - \nu_{\mathrm{NJF}})$$

where the optical depth τ_{NJF} in the line center of transition $\mathrm{NJF} \rightarrow \mathrm{N'J'F'}$ is given by

$$\begin{aligned} \tau_{\mathrm{NJF}} &= (\mathrm{n}_{\mathrm{N'J'F'}} \mathrm{B}_{\mathrm{N'J'F'} \rightarrow \mathrm{NJF}} - \mathrm{n}_{\mathrm{NJF}} \mathrm{B}_{\mathrm{NJF} \rightarrow \mathrm{N'J'F'}}) \frac{h\nu}{4\pi} \; \frac{1}{\Delta\nu_{\mathrm{D}}} \; \mathrm{L} \\ &= \frac{\mathrm{c}^2}{8\pi\nu^2} \; \mathcal{N}_{\mathrm{N'J'F'}} \; \frac{\mathrm{g}_{\mathrm{NJF}}}{\mathrm{g}_{\mathrm{N'J'F'}}} \; \mathrm{A}_{\mathrm{NJF} \rightarrow \mathrm{N'J'F'}} \; \frac{1}{\Delta\nu_{\mathrm{D}}} \left[1 - \exp\left(-\frac{h\nu_{\mathrm{NJF}}}{k\mathrm{T}_{\mathrm{ex}_{\mathrm{NJF}}}} \right) \right] \quad . \end{aligned} \tag{5.6}$$

$\mathrm{g}_{\mathrm{NJF}} = 2\mathrm{F} + 1$ and $\mathrm{g}_{\mathrm{N'J'F'}} = 2\mathrm{F'} + 1$ are the statistical weights of the upper and lower level of the transition $\mathrm{NJF} \rightarrow \mathrm{N'J'F'}$, and $\mathrm{T}_{\mathrm{ex}_{\mathrm{NJF}}}$ is the corresponding excitation temperature.
$\mathcal{N}_{\mathrm{N'J'F'}} = \mathrm{n}_{\mathrm{N'J'F'}} \cdot \mathrm{L}$ denotes the column density in the lower level along the path L in the molecular cloud, where $\mathrm{n}_{\mathrm{N'J'F'}}$ is the number density of molecules in the specific state $\mathrm{N'J'F'}$ and $\mathrm{A}_{\mathrm{NJF} \rightarrow \mathrm{N'J'F'}}$ the Einstein-A coefficient of the transition $\mathrm{NJF} \rightarrow \mathrm{N'J'F'}$.

$\phi(\nu)$ with $\phi(0) = 1$ is the Gaussian line profile, $\Delta\nu_{\mathrm{D}} = \int \phi(\nu) d\nu$ the equivalent width of line $\mathrm{NJF} \rightarrow \mathrm{N'J'F'}$. Assuming the line profile to be determined by thermal and local random motions (microturbulence), the profile function can be expressed by

$$\phi(\nu - \nu_{\mathrm{NJF}}) = \exp(-\pi \left(\frac{\nu - \nu_{\mathrm{NJF}}}{\Delta\nu_{\mathrm{D}}} \right)^2) \quad .$$

The equivalent width $\Delta\nu_{\mathrm{D}}$ and the FWHM $\Delta\mathrm{v}$ of the velocity distribution are related by

$$\Delta\nu_{\mathrm{D}} = \frac{1}{2} \sqrt{\frac{\pi}{\ln 2}} \; \frac{\nu_{\mathrm{NJF}}}{\mathrm{c}} \; \Delta\mathrm{v} \quad .$$

The source function at frequency ν is obtained by averaging the individual source functions of the involved transitions, weighted with the optical depth:

$$\mathrm{S}_\nu = \frac{\sum_{\mathrm{JF}} \tau_{\mathrm{NJF}} \; \phi(\nu - \nu_{\mathrm{NJF}}) \mathrm{S}_{\mathrm{NJF}}}{\sum_{\mathrm{JF}} \tau_{\mathrm{NJF}} \; \phi(\nu - \nu_{\mathrm{NJF}})}$$

with $\mathrm{S}_{\mathrm{NJF}} = 2k\nu^2/\mathrm{c}^2 \; \mathrm{J}_{\nu_{\mathrm{NJF}}}(\mathrm{T}_{\mathrm{ex}_{\mathrm{NJF}}})$.

Assuming equal excitation temperatures for all hyperfine transitions within the rotational transition, i.e. $\mathrm{T}_{\mathrm{ex}_{\mathrm{NJF}}} = \mathrm{T}_{\mathrm{ex}}$, and neglecting the small energy differences between the hyperfine levels within one rotational level, the hyperfine states are populated according to their statistical weights:

$$\mathrm{n_{N\,JF}} = \mathrm{g_{N\,JF}}\ \frac{\mathrm{n_N}}{\mathrm{g_N}}\ .$$

The $\mathrm{n_N}$ and $\mathrm{g_N}$ are the total populations and statistical weights of the rotational transition. The statistical weights, taking into account the projection of F on the axis of quantization $\mathrm{M_F}$, are defined as follows:

$$\mathrm{g_{N\,JF}} = \sum_{\mathrm{M_F=-F}}^{\mathrm{F}} \mathrm{g_{N\,JFM_F}} = \sum_{\mathrm{M_F=-F}}^{\mathrm{F}} 1 = 2\mathrm{F}+1$$

$$\mathrm{g_{N\,J}} = \sum_{\mathrm{F=|J-I|}}^{\mathrm{|J+I|}} \sum_{\mathrm{M_F=-F}}^{\mathrm{F}} \mathrm{g_{N\,JFM_F}} = (2\mathrm{I}+1)(2\mathrm{J}+1)$$

$$\mathrm{g_N} = \sum_{\mathrm{J=|N-S|}}^{\mathrm{|N+S|}} \sum_{\mathrm{F=|J-I|}}^{\mathrm{|J+I|}} \sum_{\mathrm{M_F=-F}}^{\mathrm{F}} \mathrm{g_{N\,JFM_F}} = (2\mathrm{I}+1)(2\mathrm{S}+1)(2\mathrm{N}+1)\ .$$

In the case of CN, where $\mathrm{I}=1$ and $\mathrm{S}=1/2$, $\mathrm{g_N}$ results in $6(2\mathrm{N}+1)$. The detection equation (5.5) in terms of the main beam brightness temperature now can be written as

$$\mathrm{T_{mb}}(\nu) = \eta_\mathrm{c}\left[\mathrm{J}_\nu(\mathrm{T_{ex}}) - \mathrm{J}_\nu(\mathrm{T_{bg}})\right]\left\{1-\exp\left(-\tau_{tot}\sum_{\mathrm{JF}}\mathrm{s_{N\,JF\rightarrow N'\,J'\,F'}}\,\phi(\nu-\nu_{\mathrm{N\,JF}})\right)\right\}\ . \qquad (5.7)$$

τ_{tot} stands for the total optical depth of the rotational transition in the absence of splitting and the $\mathrm{s_{N\,JF\rightarrow N'\,J'\,F'}}$ are the relative intensities of the hyperfine lines as given by (4.2).

The relation between the Einstein-A coefficients of each individual hyperfine transition and the rotational transition is obtained using the relative intensities and statistical weights

$$\mathrm{s_{N\,JF\rightarrow N'\,J'\,F'}} = \frac{\mathrm{g_{N\,JF}}\ \mathrm{A_{NJF\rightarrow N'J'F'}}}{\mathrm{g_N}\ \mathrm{A_{N\rightarrow N'}}}\ .$$

With this definition equation (5.6) results in

$$\tau_{tot} \;=\; \frac{\mathrm{c}^2}{8\pi\nu^2}\ \mathcal{N}_\mathrm{N}\ \mathrm{A_{N\rightarrow N'}}\ \frac{1}{\Delta\nu_\mathrm{D}}\left[\exp\frac{h\nu_{\mathrm{N\,JF}}}{k\mathrm{T_{ex_N}}}-1\right], \qquad (5.8)$$

where $\mathcal{N}_\mathrm{N}$ denotes the column density in the upper level of the rotational transition.

According to (5.7), the observed hyperfine spectrum depends on the total optical depth τ_{tot}, the line width $\Delta\mathrm{v}$, the Doppler velocity $\mathrm{v_{LSR}}$ of the source, and the so called amplitude factor

$\mathrm{A} = \eta_\mathrm{c}\,[\mathrm{J}_\nu(\mathrm{T_{ex}}) - \mathrm{J}_\nu(\mathrm{T_{bg}})]$. These parameters are derived by a least square fit to the observed spectrum which in the present work was realized with a method implemented in the Grenoble data reduction software CLASS. Input parameters are the number of hfs lines, the relative distances in velocity space with respect to the main component and the relative intensities of the lines. Fig. 5.1 shows two synthetic spectra calculated for different values of the total opacity in order to demonstrate the influence on the observed hyperfine pattern, together with a spectrum observed towards one position in the Orion Molecular Cloud 1 (OMC-1) and the corresponding fit. Note that two parts of the IRAM autocorrelator have been merged to one spectrum in order to display both fine structure transitions and to allow a simultaneous hyperfine fit to all observed components.

With the knowledge of τ_{tot} it is in principle possible to determine the excitation temperature and hence the upper state column density for the transition from the detection equation (5.5) and

$$\mathcal{N}_\mathrm{N} = \frac{8\pi\nu^3}{\mathrm{c}^3} \quad \frac{\tau_{tot}}{\mathrm{A_{N\rightarrow N'}}} \quad \frac{\frac{1}{2}\sqrt{\frac{\pi}{\ln 2}}\Delta\mathrm{v}}{\exp\frac{h\nu}{k\mathrm{T_{ex_N}}} - 1} \quad . \tag{5.9}$$

For optically thin emission, in fact only the product $\mathrm{J}_\nu(\mathrm{T_{ex}}) \times \tau_{tot}$ is well defined in the hyperfine fits and the excitation temperature can not be derived unambiguously in this case. However, integration of the detection equation in the optically thin limit, assuming $\mathrm{J}_\nu(\mathrm{T_{ex}}) \gg \mathrm{J}_\nu(\mathrm{T_{bg}})$, provides a formula for the upper state column density independent of $\mathrm{T_{ex}}$ and containing the total integrated line intensity of the rotational transition

$$\frac{\mathcal{N}_\mathrm{N}}{\mathrm{g_N}} = \frac{3k\mathrm{c}}{8\pi^3\mu^2\nu^2}\frac{\int \mathrm{T_{mb}}\,\mathrm{d}\nu}{\eta_\mathrm{c}\mathrm{S}} = \frac{3k}{8\pi^3\mu^2\nu}\frac{\int \mathrm{T_{mb}}\,\mathrm{dv}}{\eta_\mathrm{c}\mathrm{N}} \tag{5.10}$$

together with the intrinsic line strength S of the transition which, for a linear molecule without splitting, is given by the upper state rotational quantum number. The coupling efficiency η_c, which accounts for the convolution of the telescope beam with the intrinsic source structure, is generally difficult to determine due to the clumpy and filamentary nature of molecular clouds. If not given explicitly, its value is set to unity but since $\eta_\mathrm{c} \leq 1$, this will cause the line intensities, excitation temperatures and column densities derived to be lower limits.

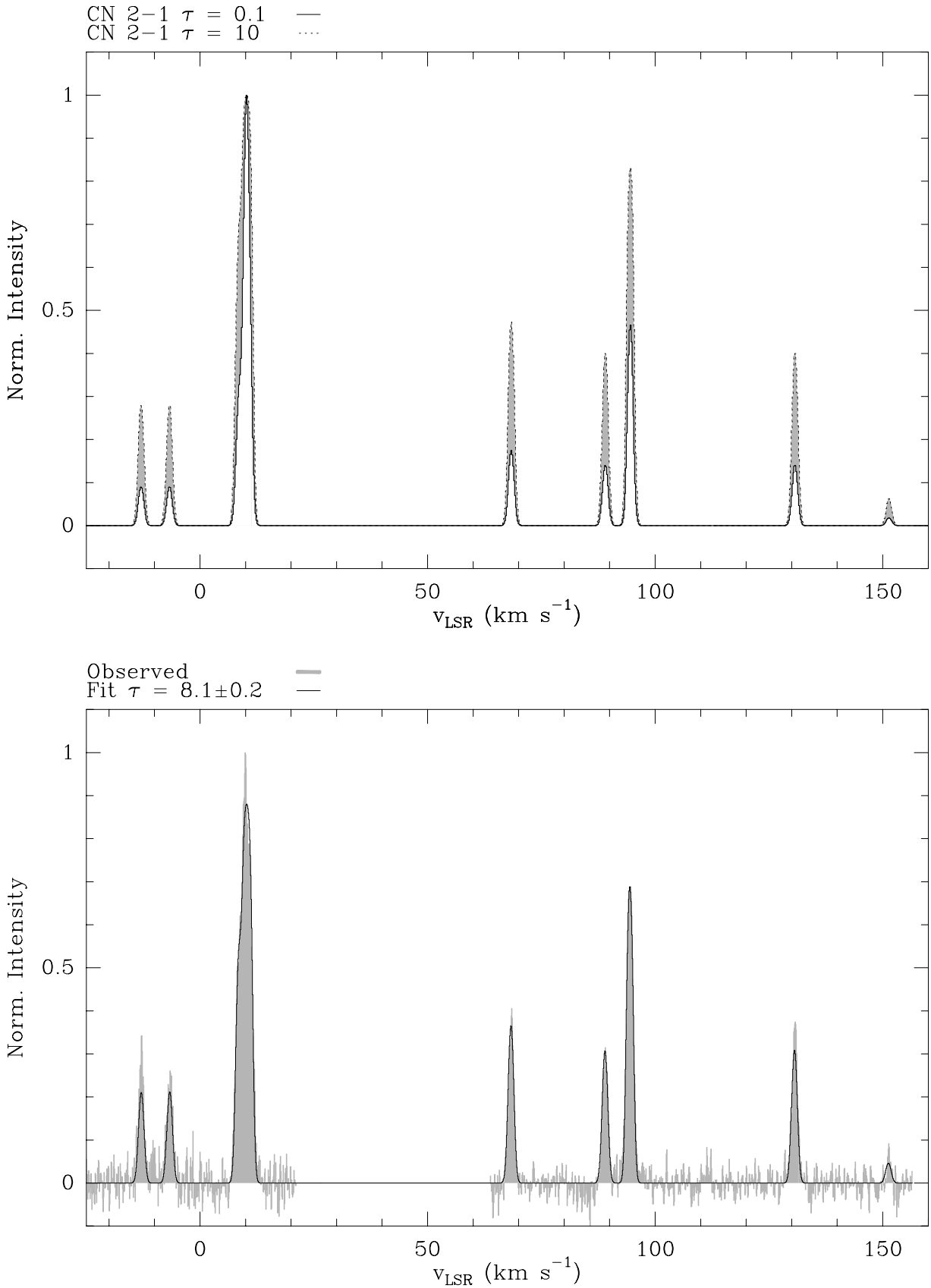

Fig. *5.1: Synthesized (upper) and observed CN N=2→1 spectra (lower panel) obtained with the IRAM 30m telescope in Orion OMC-1. The derived hyperfine fit is superposed on the spectrum.*

Provided that the level population can be described by a single excitation temperature, the so called rotational temperature T_{rot}, the total molecular column density is derived from the column density in a specific state via

$$\mathcal{N}_{tot} = \sum_{\mathrm{N}=0}^{\infty} \mathcal{N}_{\mathrm{N}} = \mathcal{N}_0 \mathcal{Z} = \mathcal{N}_0 \sum_{\mathrm{N}=0}^{\infty} \mathrm{g_N} \exp(-\frac{\mathrm{E}_{\mathrm{N}}^{rot}}{k\mathrm{T}_{rot}}) = \frac{\mathcal{N}_{\mathrm{N}} \mathcal{Z}(\mathrm{T}_{rot})}{\mathrm{g_N} \exp(-\mathrm{E}_{\mathrm{N}}^{rot}/(k\mathrm{T}_{rot}))} \tag{5.11}$$

with the partition function $\mathcal{Z}(\mathrm{T}_{rot})$ and the rotational energy of level N given by

$$\mathrm{E}_{\mathrm{N}}^{rot} = h\mathrm{BN}(\mathrm{N}+1) \ .$$

Rearranging (5.11) we can write

$$\frac{\mathcal{N}_{\mathrm{N}}}{\mathrm{g_N}} = \frac{\mathcal{N}_{tot}}{\mathcal{Z}(\mathrm{T}_{rot})} \exp(-\frac{\mathrm{E}_{\mathrm{N}}^{rot}}{k\mathrm{T}_{rot}}) \ . \tag{5.12}$$

The logarithm of the upper state column densities divided by the statistical weight and plotted versus the energy of the upper level then should yield a straight line in a so called Boltzmann plot or rotation diagram. T_{rot} is given by the slope of this line. The ordinate value at zero energy is proportional to the logarithm of the total molecular column density which is then calculated using the approximation of the partition function for a linear molecule

$$\mathcal{Z}(\mathrm{T}_{rot}) \sim \frac{k\mathrm{T}_{rot}}{h\mathrm{B}} \ .$$

This rotation diagram technique is commonly used (see e.g. Blake et al. 1987 for a variety of species in OMC-1), but it should be pointed out that density and temperature gradients in the clouds as well as non-LTE mechanisms like trapping in optically thick lines or subthermal excitation constrain the application of this simple, single temperature approach.

Since the optical depth of a rotational line increases with ν^3, trapping effects are likely to occur in the higher rotational transitions. Beam averaged upper state column densities determined from (5.10) are then underestimated which results in an underestimation of the rotational temperature from a Boltzmann plot and inaccurate values for the total molecular column density. As proposed by Stutzki et al. (1989), the upper state column densities have to be corrected up by an opacity correction factor defined by

$$\mathrm{G}(\tau) = \int \frac{[1-\exp(-\tau\phi(\mathrm{v}))]}{\tau} \frac{\mathrm{dv}}{\Delta\mathrm{v}} \tag{5.13}$$

with $\phi(\mathrm{v}) = \exp(-4\ln 2(\frac{\mathrm{v}-\mathrm{v}_0}{\Delta\mathrm{v}})^2)$. $\mathrm{G}(\tau)$ was numerically integrated over the appropriate velocity range. This factor is almost identical to the escape probability in the Large Velocity Gradient approximation introduced in the following section, with the exception that it properly accounts for contributions at velocities outside the line center for high opacities.

5.3 Escape Probability

Observations of several rotational transitions provide an additional independent possibility of determining the physical parameters of the observed gas by means of a radiative transfer analysis, the so called escape probability formalism. For reasons of simplicity, most models assume a homogeneous density distribution and constant temperature throughout the cloud. Since molecular clouds are known to have density and temperature gradients, the use of a single density, single temperature model is limited. As one example Castets et al. (1990) showed that the observed large scale line intensities of CO isotopomers in the Orion A clouds could not be accounted for in single component radiative transfer calculations. A more sophisticated approach to the problem are radiative transfer codes which explicitly model temperature and density gradients in the cloud and account for the radiative transfer in a clumpy medium (e.g. Gierens et al. 1992, Köster et al. 1994).

5.3.1 Theory

A useful simplification of the radiative transfer problem is the assumption of level populations which are independent of the position in the cloud. In this case, a formal solution to the equation of radiative transfer (5.1) can be calculated explicitly (see Stutzki & Winnewisser 1985).

The expression for the escape probability, which gives the normalized probability, averaged over frequency and direction, for a photon to leave the cloud without being absorbed, depends on the geometry considered and on the value of the optical depth. The most common geometries are the plane parallel and the spherical cloud. The escape probability in the plane parallel case is given by

$$\beta_\nu(\tau) = \frac{1-\exp(-3\tau)}{3\tau} \quad .$$

In the so called Sobolev or Large Velocity Gradient (LVG) approximation, the emitted radiation in a spherical homogeneous cloud can only be absorbed in a volume where the velocity shift, caused by a velocity gradient, is of the order of the line width. β_ν then is of the form (Mihalas 1978)

$$\beta_\nu(\tau) = \frac{1-\exp(-\tau)}{\tau} \quad .$$

In the present work, the escape probability formalism for a homogeneous spherical cloud described by Stutzki & Winnewisser (1985) was used. Extreme values for β_ν in the cloud center (r=0) and at the edge of the clump (r=R) are given by

$$\begin{aligned} \beta_\nu(\mathrm{r}=0) &= \exp(-\chi_\nu \mathrm{R}) = \exp(-\tau_\nu(\mathrm{R})) \\ \beta_\nu(\mathrm{r}=\mathrm{R}) &= \frac{1}{2}(1+\frac{1-\exp(-2\chi_\nu \mathrm{R})}{2\chi_\nu \mathrm{R}}) \quad . \end{aligned}$$

In the first case, the escape probability is given by the absorption coefficient χ_ν and the radius of the clump. At the cloud edge, β_ν for high optical depths is 1/2, since the photon may either escape into one half-space or will be trapped inside the cloud.

The values of β_ν for the different geometries agree to within a factor of 2.

5.3.2 Application to observations of different molecules

Necessary input parameters for the model are the Einstein-A-values and energies above the ground state, as well as the collisional rate coefficients of the transitions. Collisional rate coefficients of some of the most important interstellar species like CO, CS, HCN or CI are available in the literature obtained partly through laboratory measurements or ab initio calculations. Unfortunately, such results do not exist for the CN molecule. Therefore, the values for CS (Green & Chapman 1978) are *assumed* to be appropriate for CN. It should be noted that, in contrast to CS, CN has a nonzero spin and thus the interaction with ortho- and para-H_2 are likely to be different for both species. Even so, the typical rates have been estimated by Black & van Dishoeck (1991) not to be in error by more than factors of 2–3.

In those sources where we obtained several rotational transitions of CS and its isotopomers, the same escape probability analysis was done with the observed line intensities of this molecule.

The model computes line intensities, normalized integrated intensities, rotational temperatures, and optical depths in a user-defined data cube, spanned by the molecular column density, the H_2 density and the kinetic temperature. The physical parameters of the emitting gas, namely the column density of the observed molecule, the H_2 density and the kinetic temperature, are then evaluated from slices cut through the data cube, by finding regions where the observed line intensity or integrated intensity ratios and optical depths of the available rotational transitions fit in the *column density/density* plane for a certain kinetic temperature.

An essential advantage of this method is that the beam filling factor cancels out if intensity *ratios* of observations with similar angular resolution are considered. The inferred column densities are thus not affected by ambiguities due to substructures of the source not resolved by the beam. For this reason, the higher resolution data sets have been smoothed to the angular resolution at the lowest observed frequency whenever the method was applied.

Chapter 6. Datasets and data reduction

A detailed overview of the datasets acquired within the scope of the present thesis is given in the following Tables 6.1 to 6.8. Table 6.1 summarizes the observed main molecular transitions and some observational parameters which are related to the individual telescopes and backends used. Due to the availability of several receivers, covering three different spectral ranges at the IRAM 30m telescope, it was possible to observe other molecular species in parallel to CN and its isotopomers. The same holds for the IRAM HCN J=1$\rightarrow$0 observations.

The data have been acquired at the KOSMA 3m radio telescope on Gornergrat, Switzerland (Degiacomi et al. 1995), at the IRAM 30m telescope on Pico Veleta Spain (Baars et al. 1987), the IRAM Plateau de Bure Interferometer (PdBI, Guilloteau et al. 1992), the SEST 15m telescope (Booth et al. 1989), and at the JCMT 15m telescope on Mauna Kea, Hawaii (Annual report of the Royal Observatory, Edinburgh 1990). Table 6.1 does not contain all observed transitions in the spectral ranges covered, but focuses on those of particular interest for this work. The spectrometers used were mainly autocorrelator backends (*auto* in Table 6.1) at the JCMT and the IRAM 30m telescope, where the spectral resolution could be varied to have identical velocity resolutions for different molecular transitions, or Acousto Optical Spectrometers (AOS) at KOSMA and SEST. Note that only the highest spectral resolutions obtained for the individual species are displayed and that all IRAM spectra have been recorded in addition with a 1 MHz resolution filterbank at 512 MHz bandwidth simultaneously. Tables 6.2 through 6.8 display all observations in all sources involved in the study of CN, its isotopomers, and other molecular species as listed in Table 6.1. Transitions observed at the IRAM 30m telescope which appear more than once in the tables, have been recorded during different scheduled observing runs.

All KOSMA, JCMT, and the IRAM 3mm data are on a fully sampled grid. Due to the limited observing time, the grid spacing of some of the IRAM 2mm and 1.3 mm data corresponds to the 1.3 mm beam size (i.e. $12''$). The IRAM observations have been carried out in *single sideband* (SSB) mode. Since the KOSMA and JCMT data were observed in *double sideband* mode (DSB), the spectra had to be treated carefully with respect to line contributions from the different subbands. However, in the case of CN N=3$\rightarrow$2, observed with KOSMA and the JCMT, this turned out to be a great advantage, since it was possible to additionally observe CS J=7$\rightarrow$6 from the other sideband. System noise temperatures given in the tables are SSB for IRAM and DSB temperatures for KOSMA and JCMT observations.

All single dish observations have been obtained in a total power mode, where one reference position (OFF-position) free of emission was recorded before the scan on the source position (ON-position). The scan on the source consists either of a single position, a small map, typically 3×3 points, or the complete line of an on-the-fly (OTF) scan. The latter observing strategy has been used for data obtained with the JCMT only. The OFF-position is typically $10'$ or more offset from the map center and was checked for emission prior to the regular observations. No line emission was detected for the main isotopomers on the level of the noise temperature of the later observed source positions.

The integration times on the source were typically 20 to 30 seconds in order to guarantee for the stability of the complete system including atmospheric contributions. In the OTF mode used at

Molecule	Transition	Frequency (MHz)	Backend	$\Delta\nu$ (kHz)	Δv (km s^{-1})	F_{eff}	B_{eff}	η_{mb}	η_{fss}
CN	N=1→0	113490.99	IRAM auto	40	0.10	0.92	0.68		
	N=1→0	113490.99	SEST AOS	43	0.12				
	N=2→1	226874.75	IRAM auto	80	0.10	0.86	0.40		
			KOSMA AOS	165	0.22				0.70
	N=3→2	340247.90	KOSMA AOS	165	0.15				0.47
			JCMT auto	312	0.28			0.68	
^{13}CN	N=1→0	108780.20	IRAM auto	80	0.22	0.92	0.68		
	N=2→1	217467.04	IRAM auto	80	0.11	0.90	0.58		
C^{15}N	N=1→0	110024.53	IRAM auto	320	0.87	0.92	0.68		
	N=1→0	110024.53	SEST AOS	43	0.12			0.70	
	N=2→1	219934.84	IRAM auto	40	0.06	0.90	0.58		
			KOSMA AOS	165	0.23				0.70
CS	J=3→2	146969.05	IRAM 1MHz	1000	2.04	0.90	0.52		
	J=7→6	342882.95	KOSMA AOS	165	0.15				0.47
			JCMT auto	312	0.28			0.68	
C^{34}S	J=3→2	144617.15	IRAM auto	80	0.16	0.90	0.52		
	J=5→4	241016.18	IRAM auto	80	0.10	0.86	0.37		
CCH	N=1→0	87316.93	SEST AOS	43	0.15			0.75	
C^{13}CH	N=1→0	85229.39	SEST AOS	43	0.15			0.75	
	N=2→1	170490.61	IRAM auto	80	0.14	0.90	0.50		
^{13}CCH	N=2→1	168274.49	IRAM auto	80	0.14	0.90	0.50		
HCN	J=1→0	88631.85	IRAM auto	40	0.13	0.92	0.75		
H^{13}CN	J=3→2	259011.79	IRAM auto	80	0.10	0.68	0.37		
H^{15}NC	J=1→0	88865.69	IRAM auto	40	0.13	0.92	0.75		
CH_3CN	J=8→7	147174.59	IRAM 1MHz	1000	2.04	0.90	0.52		
CH_3CCH	J=10→9	170905.78	IRAM auto	80	0.14	0.90	0.52		

Table *6.1: Observational parameters related to the individual telescopes.*

the JCMT, spectra were dumped each 5 seconds, resulting in a spacing of $6''$ between individual map points. Considering the angular resolution of the JCMT of $14''$ at 340 GHz, this sampling avoids smearing effects caused by the telescopes' continuous move across the source. OFF-position integration times were evaluated according to how many ON-positions were considered for one OFF-position.

In all cases a chopper-wheel calibration was applied to the raw data, resulting in a T_A^* temperature

scale, following the notation of Kutner & Ulich (1981). The spectra were then transformed to a T_{mb} or $\mathrm{T}_{\mathrm{R}}^{*}$ scale, using the efficiencies given in Table 6.1 and the formulae

$$\mathrm{T}_{mb} = \frac{\mathrm{F}_{eff}}{\mathrm{B}_{eff}} \times \mathrm{T}_{\mathrm{A}}^{*}, \quad \mathrm{T}_{\mathrm{R}}^{*} = \frac{\mathrm{T}_{\mathrm{A}}^{*}}{\eta_{fss}}, \quad \mathrm{T}_{mb} = \frac{\mathrm{T}_{\mathrm{A}}^{*}}{\eta_{mb}}$$

for IRAM (see Downes 1989) for definitions of the efficiencies), KOSMA and JCMT data respectively. Under the assumption that the source is smaller than the error beam, $\mathrm{T}_{\mathrm{R}}^{*} = \mathrm{T}_{mb}$.

The data reduction and further processing, including the preparation of contour and greyscale plots of the mapped regions, has been done with the GILDAS software package. A first order baseline fit has been applied to all spectra in the first preliminary reduction step. Where necessary, a higher order baseline, typically 3^{rd} to 5^{th} order, was subtracted. Obvious bad channels, especially in the IRAM 1MHz filterbanks, have been removed. Some of the 30m spectra showed strong standing waves and needed a sinusoidal baseline fit. The period of the fitted sinus corresponds to a linear scale of $\sim$ 20 m, which is the distance from the receiver cabin to the subreflector.

During all observations the pointing was checked on a regular basis by either observing planets or, at the bigger telescopes with a higher sensitivity to weaker or point sources, quasars, masers or HII regions with spatially confined strong continuum emission. Generally, the pointing was found to be accurate to within $5''$ for the bigger telescopes and $\sim 15''$ for KOSMA. At the IRAM 30m telescope, the alignment of the receivers in the three simultaneously used spectral ranges was found to be of the order of $2''$.

For a proper use of the escape probability analysis, the spectral line maps of the different rotational transitions have been smoothed to the lowest observed angular resolution in order to avoid beam filling effects when estimating line ratios.

Due to the time and spatial limitations of this thesis, not all observations will be presented and analyzed in detail. This work will focus on the results obtained for the Orion A and B regions. Sample spectra and line maps of the other sources will be presented in the Appendix.

Orion A, OMC-1

Coordinates
$\alpha(1950.0) = \quad 05^h32^m46^s.6$
$\delta(1950.0) = -05^\circ24'22''$

Distance
460 pc

Molecule	Transition	Telescope/ Receiver	Beam size ($''$)	# Points	Grid	T_{sys} (K)/ τ_0
CN	N=1→0	IRAM 30m/3mm SIS	24$''$	155	12$''$	490/0.2
	N=2→1	IRAM 30m/1.3mm SIS	12$''$	155	12$''$	1020/0.4
	N=1→0	SEST 15m/3mm Schottky	48$''$	19	24$''$	550/0.1
	N=3→2	JCMT 15m/B3i SIS	14$''$	288	6$''$	920/0.1
	N=2→1	KOSMA 3m/1.3mm SIS	120$''$	86	60$''$	200/0.1
	N=3→2	KOSMA 3m/0.8mm SIS	80$''$	79	36$''$	675/0.5
^{13}CN	N=1→0	IRAM 30m/3mm SIS	24$''$	2	single	350/0.02
	N=2→1	IRAM 30m/1.3mm SIS	12$''$	2	single	1200/0.1
	N=1→0	IRAM 30m/3mm SIS	24$''$	114	12$''$	290/0.1
	N=2→1	IRAM 30m/1.3mm SIS	12$''$	114	12$''$	995/0.3
	N=1→0	SEST 15m/3mm Schottky	48$''$	18	24$''$	340/0.03
C^{15}N	N=1→0	IRAM 30m/3mm SIS	24$''$	3	single	400/0.13
	N=2→1	IRAM 30m/1.3mm SIS	12$''$	3	single	1040/0.21
	N=2→1	IRAM 30m/1.3mm SIS	12$''$	114	12$''$	1100/0.1
	N=1→0	SEST 15m/3mm Schottky	48$''$	8	single	390/0.07
	N=2→1	KOSMA 3m/1.3mm SIS	120$''$	1		300/0.18
CS	J=3→2	IRAM 30m/2mm SIS	16$''$	155	12$''$	440/0.2
	J=7→6	JCMT 15m/B3i SIS	14$''$	288	6$''$	920/0.1
	J=7→6	KOSMA 3m/0.8mm SIS	80$''$	79	36$''$	320/0.6
CH_3CN	J=8→7	IRAM 30m/2mm SIS	16$''$	155	12$''$	440/0.2
CH_3CCH	J=10→9	IRAM 30m/2mm SIS	16$''$	2	single	680/0.2
CCH	N=1→0	SEST 15m/3mm Shottky	60$''$	24	24$''$	1300
C^{13}CH	N=2→1	IRAM 30m/2mm SIS	60$''$	2	single	680/0.2
	N=1→0	SEST 15m/3mm Schottky	60$''$	1		350/0.1
^{13}CCH	N=2→1	IRAM 30m/2mm SIS	60$''$	2	single	930/0.3

Table *6.2: Observational parameters for OMC-1.*

Orion B

Coordinates: $\alpha(1950.0) = 05^h39^m13^s.0$, $\delta(1950.0) = -01^\circ57'08''$ — Distance: 415 pc

Molecule	Transition	Telescope/ Receiver	Beam size ($''$)	# Points	Grid	T_{sys} (K)/ τ_0
CN	N=1→0	IRAM 30m/3mm SIS	24″	93	12″	410/0.2
		IRAM PdB Interferometer	$4.''5 \times 3.''5$	1 field		
	N=2→1	IRAM 30m/1.3mm SIS	12″	93	12″	650/0.3
	N=1→0	IRAM 30m/3mm SIS	24″	151	6″	380/0.2
	N=2→1	IRAM 30m/1.3mm SIS	12″	151	6″	310/0.05
	N=1→0	SEST 15m/3mm Schottky	48″	187	24″	490/0.16
	N=3→2	JCMT 15m/B3i SIS	14″	269	6″	700/0.1
	N=3→2	KOSMA 3m/0.8mm SIS	80″	29	36″	1000/0.2
^{13}CN	N=1→0	IRAM 30m/3mm SIS	24″	1	single	420/0.15
	N=2→1	IRAM 30m/1.3mm SIS	12″	1	single	1700/0.4
	N=1→0	IRAM 30m/3mm SIS	24″	26	12″	200/0.1
	N=2→1	IRAM 30m/1.3mm SIS	12″	26	12″	1000/0.2
C^{15}N	N=1→0	IRAM 30m/3mm SIS	24″	1	single	300/0.1
	N=2→1	IRAM 30m/1.3mm SIS	12″	1	single	450/0.1
	N=2→1	IRAM 30m/1.3mm SIS	12″	26	12″	500/0.1
CS	J=3→2	IRAM 30m/2mm SIS	16″	93	12″	360/0.18
	J=7→6	JCMT 15m/B3i SIS	14″	269	6″	700/0.1
	J=7→6	KOSMA 3m/0.8mm SIS	80″	29	36″	1000/0.2
C^{34}S	J=3→2	IRAM 30m/2mm SIS	16″	151	6″	210/0.03
CH_3CN	J=8→7	IRAM 30m/2mm SIS	16″	93	12″	300/0.18

Table *6.3: Observational parameters for Orion B.*

Orion Bar

Coordinates: $\alpha(1950.0) = 05^h32^m52^s.7$, $\delta(1950.0) = -05^\circ27'00''$ — Distance: 460 pc

Molecule	Transition	Telescope/ Receiver	Beam size ($''$)	# Points	Grid	T_{sys} (K)/ τ_0
CN	N=3→2	JCMT 15m/B3i SIS	14$''$	269	6$''$	720/0.1
CS	J=7→6	JCMT 15m/B3i SIS	14$''$	269	6$''$	720/0.1

OMC-2

Coordinates: $\alpha(1950.0) = 05^h32^m59^s.0$, $\delta(1950.0) = -05^\circ11'54''$ — Distance: 460 pc

Molecule	Transition	Telescope/ Receiver	Beam size ($''$)	# Points	Grid	T_{sys} (K)/ τ_0
CN	N=1→0	SEST 15m/3mm Schottky	48$''$	84	48$''$	420/0.1

ρ Ophiuchus

Coordinates: $\alpha(1950.0) = 16^h23^m26^s.1$, $\delta(1950.0) = -24^\circ17'10''$ — Distance: 150 pc

Molecule	Transition	Telescope/ Receiver	Beam size ($''$)	# Points	Grid	T_{sys} (K)/ τ_0
CN	N=1→0	IRAM 30m/3mm SIS	24$''$	25	12$''$	440/0.2
	N=2→1	IRAM 30m/1.3mm SIS	12$''$	25	12$''$	380/0.1
$C^{34}S$	J=3→2	IRAM 30m/2mm SIS	16$''$	25	12$''$	240/0.05

Table *6.4: Observational parameters for the Orion Bar, OMC-2 and ρ Ophiuchus.*

S140

Coordinates: $\alpha(1950.0) = 22^h17^m42^s.0$, $\delta(1950.0) = 63°03'45''$ — Distance: 910 pc

Molecule	Transition	Telescope/ Receiver	Beam size ($''$)	# Points	Grid	T_{sys} (K)/ τ_0
CN	N=1→0	IRAM 30m/3mm SIS	24″	213	12″	500/0.2
	N=2→1	IRAM 30m/1.3mm SIS	12″	213	12″	700/0.1
	N=3→2	JCMT 15m/B3i SIS	14″	143	6″	1300/0.25
^{13}CN	N=1→0	IRAM 30m/3mm SIS	24″	1	single	300/0.1
	N=2→1	IRAM 30m/1.3mm SIS	12″	1	single	500/0.2
C^{15}N	N=2→1	IRAM 30m/1.3mm SIS	12″	1	single	450/0.15
CS	J=7→6	JCMT 15m/B3i SIS	14″	143	6″	1300/0.25
C^{34}S	J=3→2	IRAM 30m/2mm SIS	16″	213	12″	250/0.05
	J=5→4	IRAM 30m/1.3mm SIS	16″	89	12″	860/0.4
HCN	J=1→0	IRAM 30m/3mm SIS	16″	89	12″	250/0.1
H^{13}CN	J=3→2	IRAM 30m/1.3mm SIS	16″	89	12″	2400/0.5
H^{15}NC	J=1→0	IRAM 30m/3mm SIS	16″	89	12″	250/0.1

Table *6.5: Observational parameters for S140.*

S106						
Coordinates		Distance				
$\alpha(1950.0) = 20^h25^m33^s.8$		600 pc				
$\delta(1950.0) = 37°12'50''$						
Molecule	Transition	Telescope/ Receiver	Beam size ($''$)	# Points	Grid	T_{sys} (K)/ τ_0
CN	N=1→0	IRAM 30m/3mm SIS	24″	85	12″	370/0.2
	N=2→1	IRAM 30m/1.3mm SIS	12″	85	12″	330/0.1
	N=3→2	JCMT 15m/B3i SIS	14″	117	6″	1100/0.3
^{13}CN	N=1→0	IRAM 30m/3mm SIS	24″	25?	12″	210/0.1
	N=2→1	IRAM 30m/1.3mm SIS	12″	25?	12″	530/0.3
C^{15}N	N=1→0	IRAM 30m/3mm SIS	24″	25?	12″	270/0.1
CS	J=7→6	JCMT 15m/B3i SIS	14″	117	6″	1100/0.3
C^{34}S	J=3→2	IRAM 30m/2mm SIS	16″	85	6″	270/0.04
	J=5→4	IRAM 30m/1.3mm SIS	16″	46	6″	740/0.3
HCN	J=1→0	IRAM 30m/3mm SIS	16″	46	12″	240/0.1
H^{13}CN	J=3→2	IRAM 30m/1.3mm SIS	16″	46	12″	2000/0.4
H^{15}NC	J=1→0	IRAM 30m/3mm SIS	16″	46	12″	240/0.1

Table *6.6: Observational parameters for S106.*

S255

Coordinates: $\alpha(1950.0) = 06^h09^m58^s.4$, $\delta(1950.0) = 18°00'13''$
Distance: 2.5 kpc

Molecule	Transition	Telescope/ Receiver	Beam size ($''$)	# Points	Grid	T_{sys} (K)/ τ_0
CN	N=1→0	IRAM 30m/3mm SIS	$24''$	153	$12''$	410/0.2
	N=2→1	IRAM 30m/1.3mm SIS	$12''$	153	$12''$	380/0.1
	N=3→2	JCMT 15m/B3i SIS	$14''$	135	$6''$	950/0.1
^{13}CN	N=1→0	IRAM 30m/3mm SIS	$24''$	6?	$12''$	230/0.1
	N=2→1	IRAM 30m/1.3mm SIS	$12''$	6?	$12''$	550/0.2
C^{15}N	N=2→1	IRAM 30m/1.3mm SIS	$12''$	6?	$12''$	420/0.2
CS	J=7→6	JCMT 15m/B3i SIS	$14''$	135	$6''$	950/0.1
C^{34}S	J=3→2	IRAM 30m/2mm SIS	$16''$	153	$6''$	230/0.05
	J=5→4	IRAM 30m/1.3mm SIS	$16''$	27	$6''$	430/0.2
HCN	J=1→0	IRAM 30m/3mm SIS	$16''$	27	$12''$	210/0.1
H^{13}CN	J=3→2	IRAM 30m/1.3mm SIS	$16''$	27	$12''$	1200/0.2
H^{15}NC	J=1→0	IRAM 30m/3mm SIS	$16''$	27	$12''$	210/0.1

W49

Coordinates: $\alpha(1950.0) = 19^h32^m07^s.0$, $\delta(1950.0) = 09°01'20''.0$
Distance: 13.8 kpc

Molecule	Transition	Telescope/ Receiver	Beam size ($''$)	# Points	Grid	T_{sys} (K)/ τ_0
CN	N=1→0	IRAM 30m/3mm SIS	$24''$	100	$12''$	500/0.2
	N=2→1	IRAM 30m/1.3mm SIS	$12''$	100	$12''$	880/0.2
C^{34}S	J=3→2	IRAM 30m/2mm SIS	$16''$	100	$6''$	300/0.1

Table *6.7: Observational parameters for S255 and W49.*

W51

Coordinates: $\alpha(1950.0) = 19^h21^m27^s.0$, $\delta(1950.0) = 14°24'40''$ — Distance: 7.5 kpc

Molecule	Transition	Telescope/ Receiver	Beam size ($''$)	# Points	Grid	T_{sys} (K)/ τ_0
CN	N=1→0	IRAM 30m/3mm SIS	24$''$	186	12$''$	460/0.2
	N=2→1	IRAM 30m/1.3mm SIS	12$''$	186	12$''$	820/0.2
	N=3→2	KOSMA 3m/0.8mm SIS	80$''$	35	36$''$	300/0.4
CS	J=7→6	KOSMA 3m/0.8mm SIS	80$''$	35	36$''$	300/0.4
$C^{34}S$	J=3→2	IRAM 30m/2mm SIS	16$''$	186	6$''$	260/0.1

IRC+10216

Coordinates: $\alpha(1950.0) = 09^h45^m14^s.8$, $\delta(1950.0) = 13°30'40''$ — Distance: 100 pc

Molecule	Transition	Telescope/ Receiver	Beam size ($''$)	# Points	Grid	T_{sys} (K)/ τ_0
^{13}CN	N=1→0	IRAM 30m/3mm SIS	24$''$	49	6$''$	210/0.1
	N=2→1	IRAM 30m/1.3mm SIS	12$''$	49	6$''$	460/0.3
$C^{15}N$	N=2→1	IRAM 30m/1.3mm SIS	12$''$	49	6$''$	330/0.2
$C^{34}S$	J=5→4	IRAM 30m/1.3mm SIS	16$''$	49	6$''$	730/0.4
HCN	J=1→0	IRAM 30m/3mm SIS	16$''$	49	6$''$	260/0.1
$H^{13}CN$	J=3→2	IRAM 30m/1.3mm SIS	16$''$	49	6$''$	1900/0.4
$H^{15}NC$	J=1→0	IRAM 30m/3mm SIS	16$''$	49	6$''$	260/0.1

Table *6.8: Observational parameters for W51 and IRC+10216.*

Chapter 7. Results for Orion A

7.1 The molecular clouds in Orion

Located in the constellation of Orion at a distance of roughly 450 pc from the sun, the molecular clouds associated with the Orion A and B HII regions, each containing gas masses of $\sim 10^5 \mathrm{M}_\odot$, together with the Monoceros R2 cloud build up the Giant Molecular Cloud (GMC) complex closest to the Earth. The complete spatial extent of the molecular clouds is outlined in Fig. 7.1 which shows a comparison of the lowest level of CO J=1$\rightarrow$0 emission observed by Maddalena et al. (1986) with an IRAS (**I**nfra**R**ed **A**stronomical **S**atellite) image. Since the clouds are located $\sim 100 - 150$ pc below the Galactic plane, no contamination by back- or foreground material is to be expected for the observed emission. In this ensemble of clumps and filaments, covering nearly $30 \times 30 \ \mathrm{deg}^2$ in the sky, the Orion Molecular Cloud-1 (OMC-1), located behind the great Orion nebula, constitutes the nearest (480 ± 80 pc, Genzel et al. 1981) region with ongoing low and high mass star formation, which makes it particularly interesting for observations at all accessible wavelengths. Some of the to date achieved observational results will be briefly summarized in this section. A more detailed review is given in Genzel & Stutzki (1989).

Prominent features in the optical spectral range are the bright HII regions in Orion A and B together with the associated stellar clusters. The large scale infrared emission at wavelengths $12 - 120 \mu$m obtained with IRAS shows a striking correspondence with the CO emission (see Fig. 7.1), giving evidence for the mixing of gas and dust. The extended infrared emission indicates dust of temperature ~ 50 K while the large scale kinetic gas temperatures are in the range $10 - 50$ K.

7.2 The Orion A clouds

Detailed mapping of the Orion A clouds in the ^{13}CO J=1$\rightarrow$0 transition by Bally et al. (1987, Fig. 7.2) reveals that the Orion A molecular ridge is comprised of a $\int$-shaped filament in the north, centered on the Orion nebula, and a Λ-shaped one (L1641) adjacent to it in the south. The whole subcomplex extends over ~ 35 pc in nearly north-south orientation, parallel to the Galactic plane. Typical parameters for molecular emission from this region, whose northernmost part in the $\int$-filament is commonly referred to as the Orion **extended ridge**, are Local Standard of Rest (LSR) velocities around 9 km s^{-1}, with a velocity gradient from south to north (4 to 12 km s^{-1}), line widths of $1 - 4$ km s^{-1} and H_2 densities of $10^3 - 10^5$cm^{-3}.

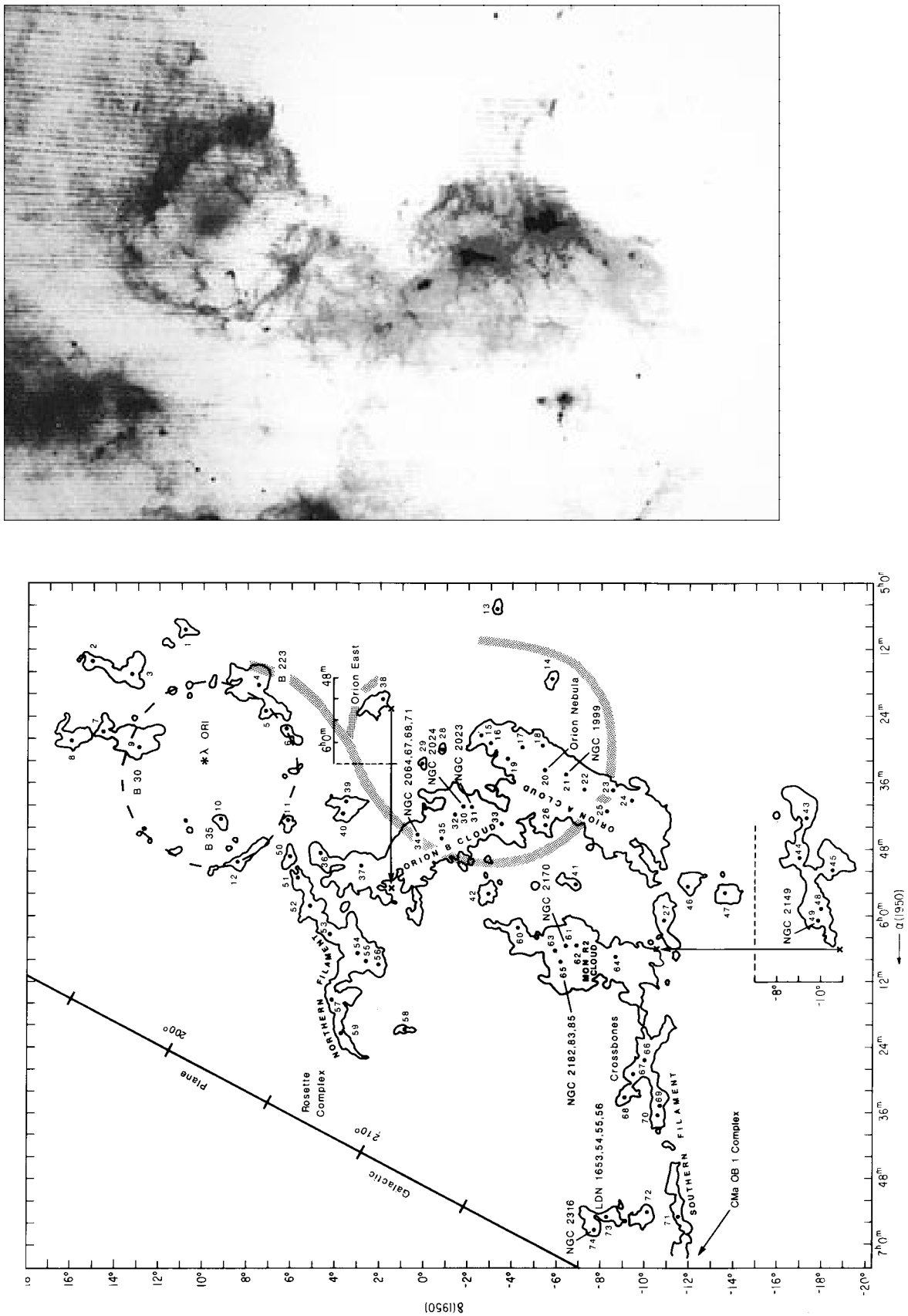

Fig. *7.1: The molecular clouds in Orion as traced by the CO J=1→0 transition (Maddalena et al. 1986) and an IRAS infrared composite image of the same region.*

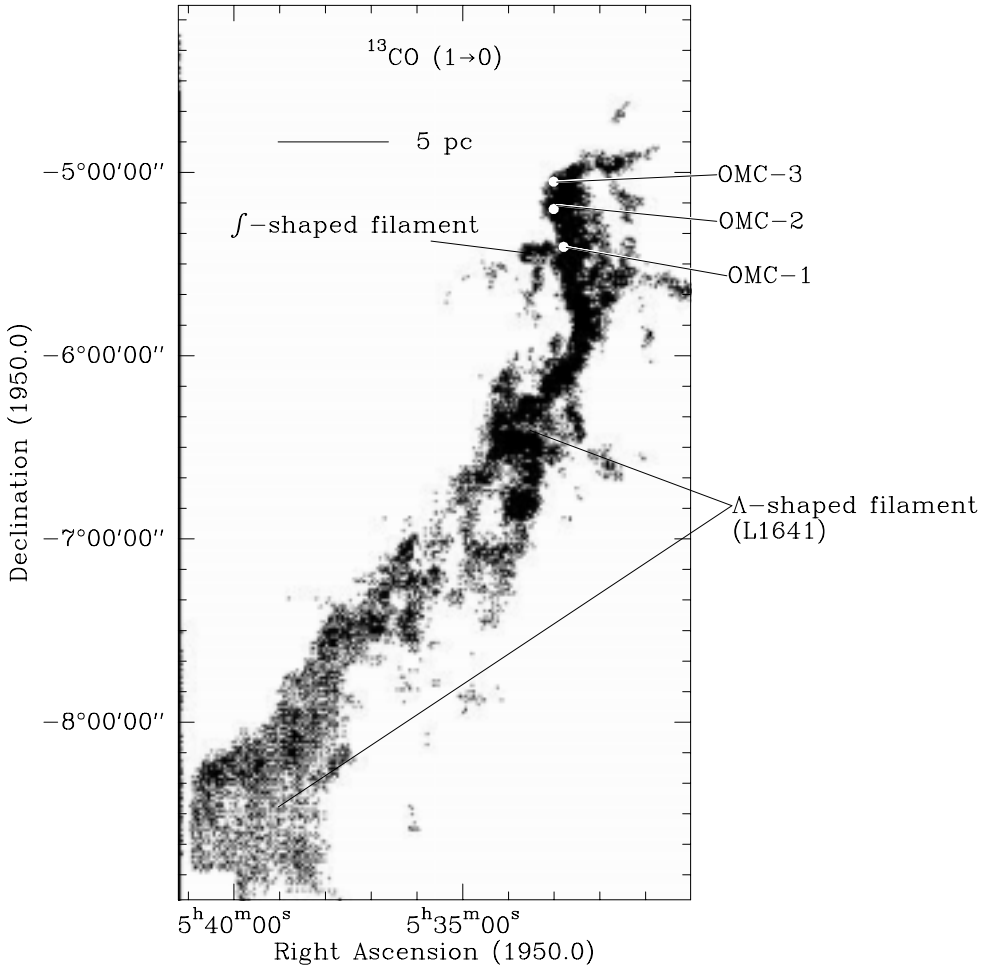

Fig. *7.2: ^{13}CO J=1→0 emission in the Orion A clouds adopted from Bally et al. (1987).*

Observations of the higher density tracers NH_3 (e.g. Cesaroni & Wilson 1994) and CS (e.g. Tatematsu et al. 1993) reveal the $\int$-shaped filament to contain a chain of condensations of density $\sim 10^6 \mathrm{cm}^{-3}$, stretching from the edge of L1641 in the south to OMC-1 in the center and OMC-2 and 3 in the north. The dense clumps either contain embedded stars detectable in the near infrared (NIR), far infrared peaks, water masers and molecular outflows, all signs of recent and ongoing star formation, or they are cold protostellar condensations and hence candidates for collapsing cloud cores and future star formation.

The following sections will focus on the best studied region, the HII region M42 and the associated molecular cloud OMC-1, since a major part of the results of the present work have been obtained here. Because of its proximity and brightness at all wavelengths, it is an ideal object to study the interstellar medium and the processes involved in star formation. The first protostar candidates and most interstellar molecules have been discovered here.

7.3 M42 and OMC-1

An optical image of the central part of the $\int$-shaped filament obtained with the Hubble Space Telescope (HST) is displayed in Fig. 7.3. Most prominent in this image of the HII region M42 are the stars of the Orion Id OB association, whose brightest four members form the **Trapezium** ($\theta^1\mathrm{A} - \mathrm{D}$), the **dark** dust **bay**, and the sharp ionization front of the **Orion Bar**.

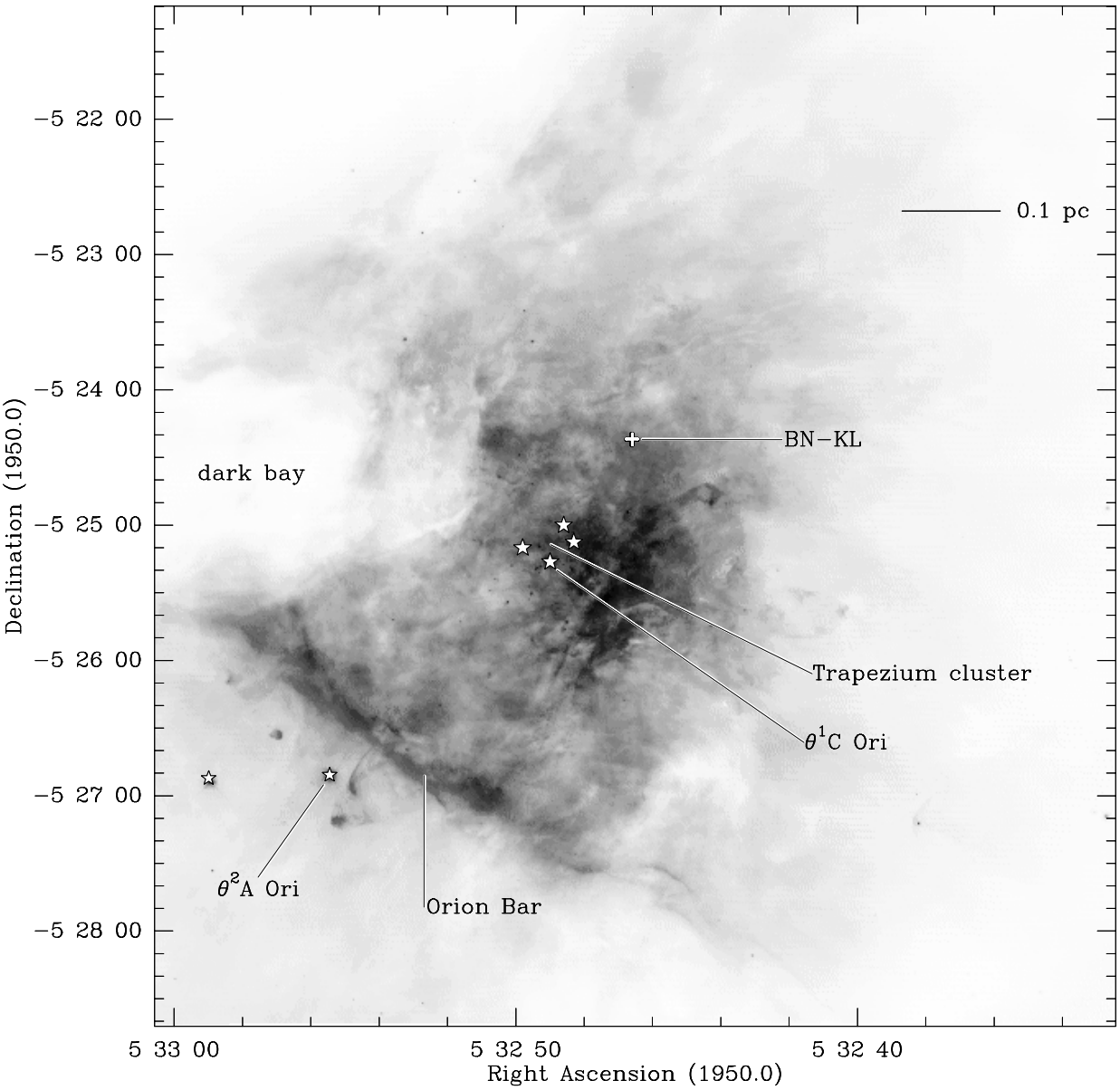

Fig. *7.3: Optical negative of the central part of the M42 HII region obtained with the Hubble Space Telescope (C.R. O'Dell & S.K. Wong, Rice University, STScI Press Release PRC95-45a) and finding chart for selected objects.*

According to the 'blister' model, first suggested by Zuckermann (1973), the stellar cluster eroded a cavity in the parental molecular cloud OMC-1, which is located behind the cavity walls seen in the light of recombination lines in the optical. The ultra violet (UV) radiation is not only responsible for the heating, photodissociation and photoionization of the gas, it also influences the chemistry at the interface from the HII region to the molecular cloud. Since the UV photons, depending on the degree of clumpiness, may penetrate deep into the molecular cloud, they create photon dominated regions (PDRs) at its surface and at the surfaces of embedded clumps. Extended emission of PDR tracers like ionized carbon [CII] and neutral oxygen [OI] (Herrmann et al. 1997) suggests that the cavity walls are associated with an extended face-on PDR. The Orion Bar is believed to be the edge-on part of this PDR cavity and will be discussed in more detail in a following section.

Theoretical models about how stars are formed suggest that dust disks around young stars constitute the origin for planets in a solar system. The great number of cusp- or disk-like objects recently found in the HST images of the M42 HII region (O'Dell et al. 1993) are high density neutral cores ionized from the outside by θ^1C Ori, some having counterparts in the infrared. These objects are thus very suspicious of being protoplanetary disks of size of some 100 AU, so called *proplyds*, surrounding pre-main-sequence stars. However, the massive influence of UV radiation and the motion of the proplyds through the gas will cause some of them to evaporate with time. Nevertheless, the observations of such a great number of proplyds suggest that they are a common concomitant phenomenon in star forming regions.

K-band ($\lambda = 2.2\mu$m) infrared images of the center of M42 at high angular resolution, reveal more than 700 near-infrared stars embedded in extended, nebulous infrared emission (Genzel & Stutzki 1989) and give evidence for the high star formation efficiency in this region. The most prominent objects are the members of the infrared cluster IRc1 through 9, concentrated within a radius of $30''$ in the BN-KL region, named after the Kleinmann-Low infrared nebulosity (Kleinmann & Low 1967) and the brightest object north of KL at 2.2μm, the Becklin-Neugebauer source (identical with IRc1, Becklin & Neugebauer 1967). A close-up 11.7μm image, suitable as finding chart for this region, is shown in Fig. 7.4. The image was obtained with the Cornell University SpectroCam–10 infrared camera at the 200 inch Hale telescope of the Palomar Observatory.

The molecular clumps within 0.1 pc of BN-KL are characterized by H_2 densities and column densities of 10^5cm^{-3} and 10^{23}cm^{-2} respectively and a kinetic temperature of $T_{kin} = 70$ K. Molecular emission from this so called **quiescent ridge**, which is associated with the extended ridge, is centered on $v_{\rm LSR} = 9$ km s^{-1} with line widths of $3 - 4$ km s^{-1}.

7.3.1 The BN-KL region

Due to a lack of angular resolution, BN and IRc2 were for a long time believed to dominate the energetics of the KL nebula as single sources. Recent sub-arcsecond near infrared images of the cluster by Dougados et al. (1993) partially resolve the BN object and show no evidence of any asymmetry for this source, whereas IRc2 splits up into four subsources. The associated compact radio continuum source I (Churchwell et al. 1987) most likely is the dominant energy source for the region which drives the prominent bipolar outflow of Orion KL, but additional embedded

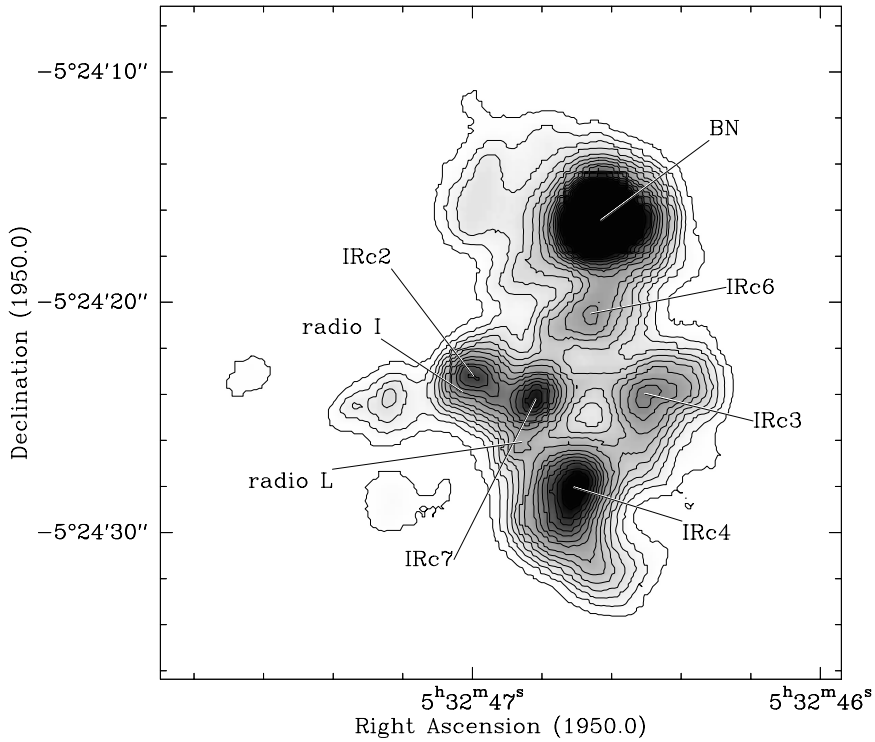

Fig. *7.4: Infrared image of Orion BN-KL at* 11.7μ*m obtained with the SpectroCam–10 infrared camera (Cornell University).*

lower luminosity objects are not excluded (Blake et al. 1996).

Since the gas in the immediate environment of BN-KL is significantly influenced by dynamic processes (shocks, high velocity outflows, internal heating by self luminous objects), molecular emission lines here exhibit complex profiles as a combination of emission from the additional different kinematic components discussed below.

- The **compact ridge** is a quiescent condensation of size 0.03 pc in the south-west of the KL nebula where oxygen-rich chemical species are overabundant compared to the extended ridge. Typical line widths are $3-5$ km s^{-1} at $v_{\rm LSR} = 7-8$ km s^{-1} and $\mathrm{T}_{kin} = 100-150$ K.

- Observations of NH_3 and HC_3N (Genzel et al. 1982, and Mundy et al. 1988), as well as the 3mm continuum (Masson & Mundy 1988) show a dense, opaque gas and dust ridge wrapped around the southern edge of IRc2. Emission from this **hot core** is characteristic of $v_{\rm LSR} = 3-5$ km s^{-1} and line widths of $5-10$ km s^{-1}. The H_2 density and column density is estimated to be in the range $1-3\times10^7$ cm^{-3} and at least 10^{24} cm^{-2} respectively.

- Streaming away from within a few arcseconds of IRc2, low and high velocity outflowing gas is detectable in the spectra of certain molecular species, mainly CO and SO, up to a distance of 0.1 pc from the center. The low velocity component, the ‘expanding doughnut’ (Plambeck et al. 1982), has a width of 35 km s^{-1} while the high velocity or **plateau** emission line wings (of e.g. CO) extend to values as high as 250 km s^{-1}. Both kinematic

components are centered on $v_{\rm LSR} = 8$ km s^{-1}. At locations where the high velocity flow hits the boundaries of the surrounding molecular cloud, H_2O masers and emission from vibrationally excited H_2 (Beck & Beckwith 1983) indicate the presence of shocked gas at kinetic temperatures of up to 3000 K.

For a more detailed discussion of the BN-KL region and its complex kinematics and chemistry see e.g. the review of Genzel & Stutzki (1989) and the line survey of Blake et al. (1987).

7.4 The first detection of interstellar $C^{15}N$

7.4.1 KOSMA results

With the availability of a 1.3 mm SIS receiver in 1993, previous observations of the CN N=2→1 transition in OMC-1, obtained at the KOSMA 3m telescope with a Schottky receiver (Simon 1992), could be extended to 86 position on a fully sampled (i.e. $60''$) grid on a very short timescale. Fig. 7.5 displays a spectrum obtained with this receiver in the region of peak radical emission in OMC-1, $2'$ north-west of BN-KL. The fine and hyperfine structure is partly resolved, as can be seen from the bars above the spectrum.

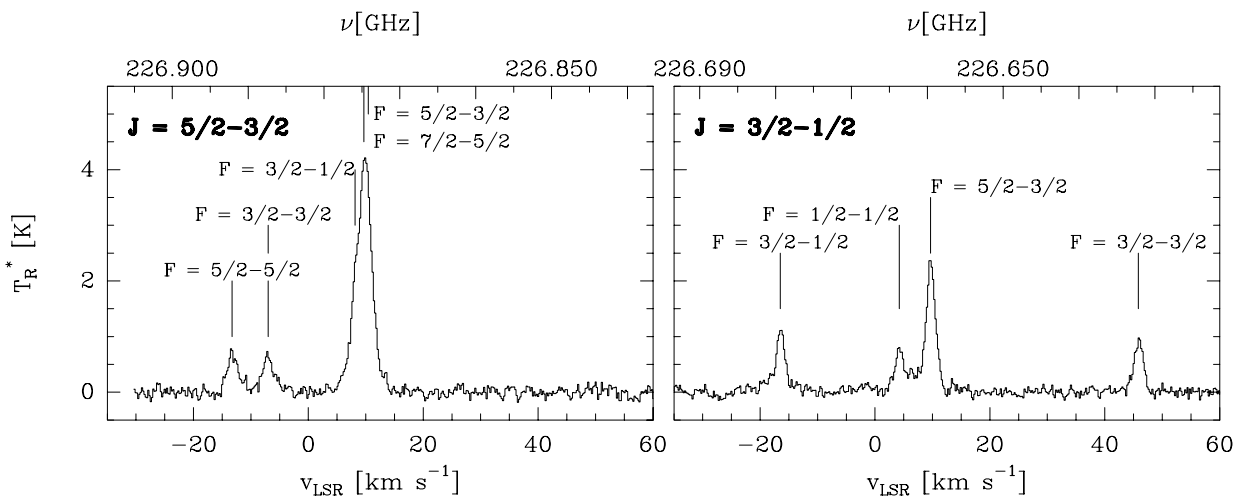

Fig. *7.5: Hyperfine patterns of the two strongest fine structure transitions of CN N=2→1 observed at the position of peak CN emission in the KOSMA map ($1'$ east and $2'$ north of BN-KL).*

The distribution of the intensity of the blend of the three strongest components (as seen in the left panel) integrated over the range $v_{\rm LSR} = 9 - 12$ km s^{-1} is shown in Fig. 7.6.

The CN emission basically traces the north south oriented extended ridge but clearly does not peak towards BN-KL. Strong emission is found $2'$ north-east of BN-KL and towards the Orion Bar.

Based on a study of the isotopic dependences of molecular rotational, spin-doubling and magnetic hyperfine parameters, the rotational spectrum of $C^{15}N$ was predicted up to N=3→2. The strongest components of the N=2→1 transition at 229.9 GHz have subsequently been searched for and detected in OMC-1 using the KOSMA 3m telescope (Saleck et al. 1993). The measurements were carried out during two nights in January 1993 with the KOSMA SIS mixer receiver

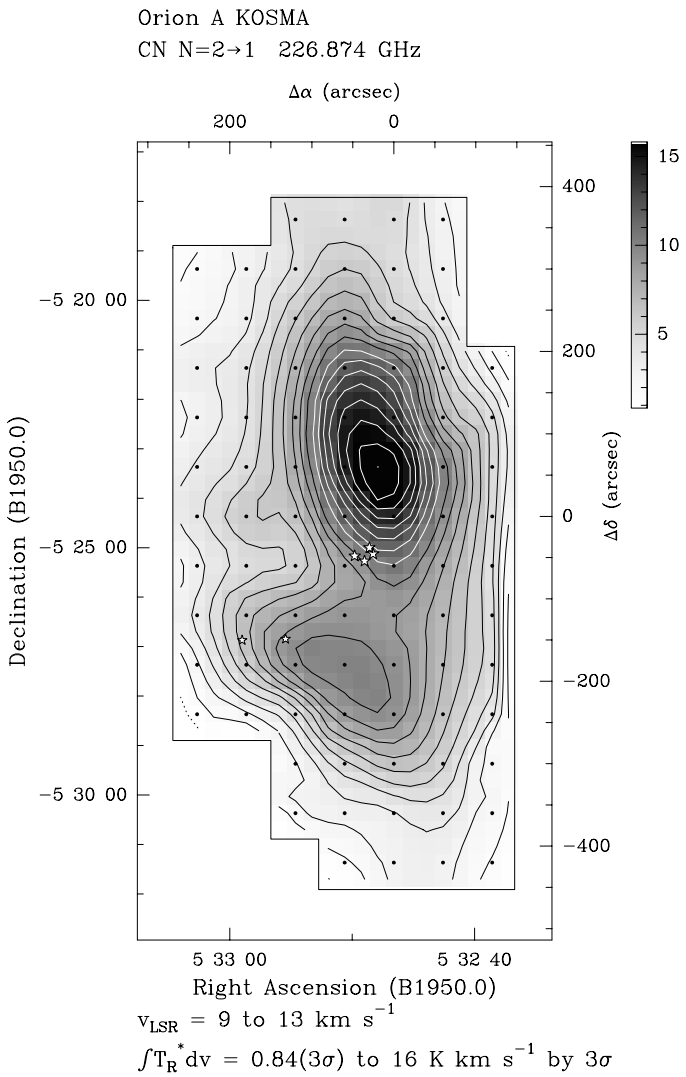

Fig. *7.6: Integrated intensity distribution of CN N=2→1 obtained with the KOSMA 3m telescope. BN-KL is located at zero offset.*

and the resulting spectrum is shown in Fig. 7.7 together with a theoretically calculated pattern.

Since the receiver was operated in double-sideband mode, the LSR velocity scale was shifted by $+10$km s^{-1} in the second night, resulting in a total difference of the lower sideband emission features of 20km s^{-1} in the two nights. Thus, lower and upper sideband emission could be unambiguously distinguished. We selected a position $1'$ east and $2'$ north of the BN-KL region to search for C^{15}N. There are several reasons for choosing this position rather than BN-KL itself. From Fig. 7.6 it is obvious that the strongest CN N=2$\rightarrow$1 emission in OMC-1 arises from this selected region and not towards BN-KL. Previous studies of CN and other molecules reveal the reactive molecular species, including CN, to suffer from significant depletion in the vicinity of BN-KL (Turner & Thaddeus 1977; Blake et al. 1987). Accordingly, the KOSMA spectrum towards BN-KL shows no significant line broadening due to emission from the hot core or plateau sources as it is observed in the transitions of more stable molecules such as CO, HCN or HC_3N. The CN lines are slightly broadened ($\Delta v = 4$km s^{-1}), indicating emission only from the warmer part of the extended ridge. This explains the lack of a C^{15}N emission feature in the frequency

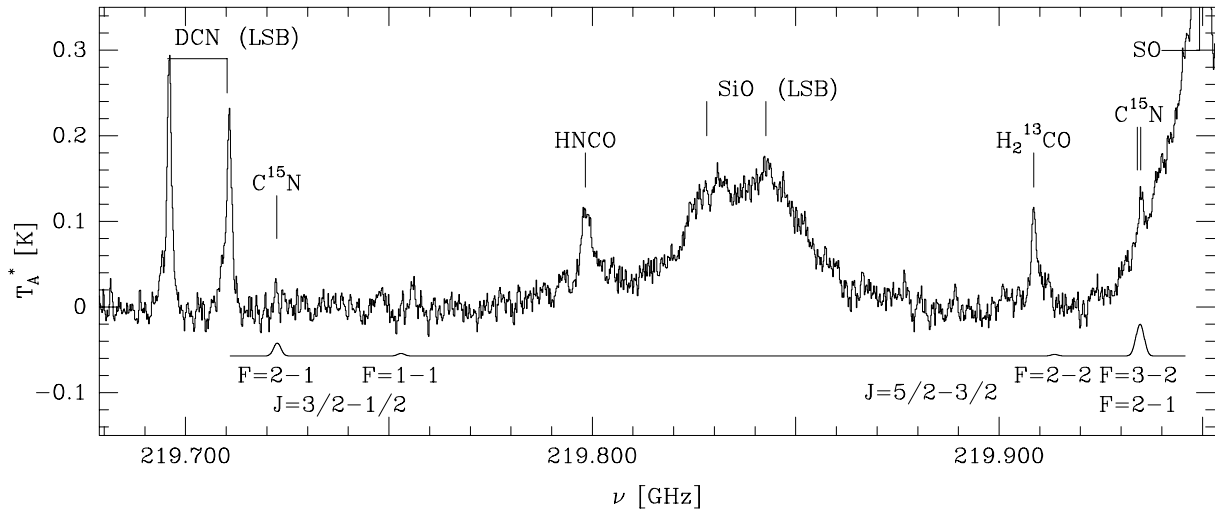

Fig. *7.7: Complete spectral scan toward the position $1'$ east and $2'$ north of BN-KL. The emission features arising from the two strongest components of the $C^{15}N$ N=2→1 transition are present on the wing of the SO line at 219.9 GHz. The expected $C^{15}N$ frequencies are indicated by the theoretically calculated spectrum for $v_{\rm LSR} = 9.7$ km s^{-1} and $\Delta v = 2.0$ km s^{-1}.*

survey of BN-KL performed by Blake et al. (1987) within their observational uncertainties.

On the other hand, the smaller line widths observed at the position selected for the search for $C^{15}N$ prevents the expected faint lines from being blurred by broad emission from abundant stable molecules as it is the case toward BN-KL. A fit of the hyperfine pattern of CN N=2→1 in Fig. 7.5 yields a LSR velocity of 9.7 km s^{-1} and a line width of 2.0 km s^{-1}, assumed to hold also for $C^{15}N$. A two-component Gaussian fit with the above derived parameters has been applied to the strongest $C^{15}N$ feature (Fig. 7.8).

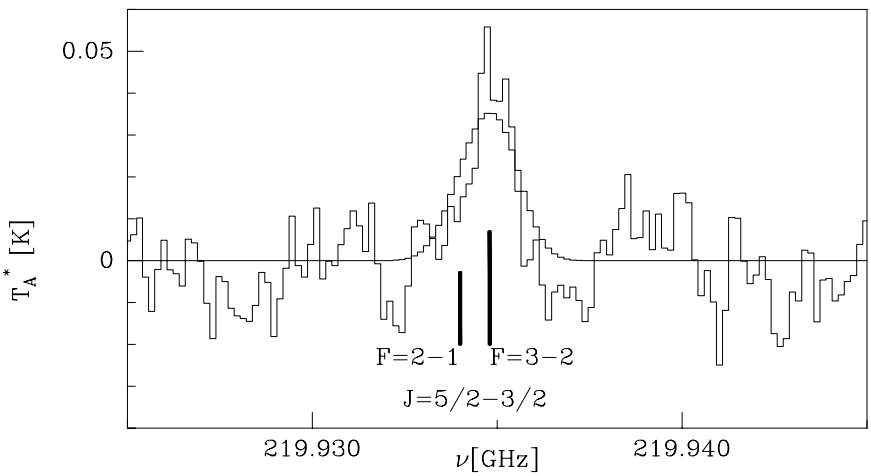

Fig. *7.8: Two-component Gaussian fit superposed on a part of the spectrum presented in Fig. 7.7. A third-order baseline fit has been applied to remove contributions from the SO line wing.*

The relative intensities of the hyperfine lines of CN suggest that only the weaker components show optically thin emission, while the stronger ones appear slightly saturated. The optically

thin lines, i.e. those with $< 7\%$ of the rotational transition's total intensity, are used together with the fitted, presumably optically thin, $C^{15}N$ transitions to derive an isotopic ratio $[C^{14}N]/[C^{15}N]$ of 290 ± 40. This result is in good agreement with the solar system value of 272 ± 6 (IUPAC 1988) and those determined from observations of $H^{13}CN$ and $HC^{15}N$: Wannier (1980) calculates 340 for Orion A and Wannier, Linke & Penzias (1981) estimate 300 for giant molecular clouds in the outer Galaxy at approximately the same galactocentric radius as that of the solar system.

7.4.2 Confirmation with the IRAM 30m telescope

The detection of $C^{15}N$ N=2→1 with the KOSMA 3m telescope is confirmed by follow-up observations of the strongest components of the rotational transitions N=1→0 and N=2→1 with the IRAM 30m telescope in OMC-1 (Saleck, Simon, and Winnewisser 1994a). The $C^{15}N$ N=1→0 spectrum was observed in one part of the autocorrelator configured with a bandwidth of 350 MHz and a resolution of 320 kHz. The second part of the autocorrelator, with a bandwidth of 20 MHz and 40 kHz resolution, was shifted to the two strongest spin-doubling components of the $C^{15}N$ N=2→1 transition at 219.935 GHz. In order to observe the strongest lines of the second, weaker spin-doubling component, which had been below the detection limit in the original detection of $C^{15}N$ (Saleck et al. 1993), a 1 MHz resolution and 512 MHz bandwidth filterbank was used. The resulting spectra are displayed in Fig. 7.9 and 7.10.

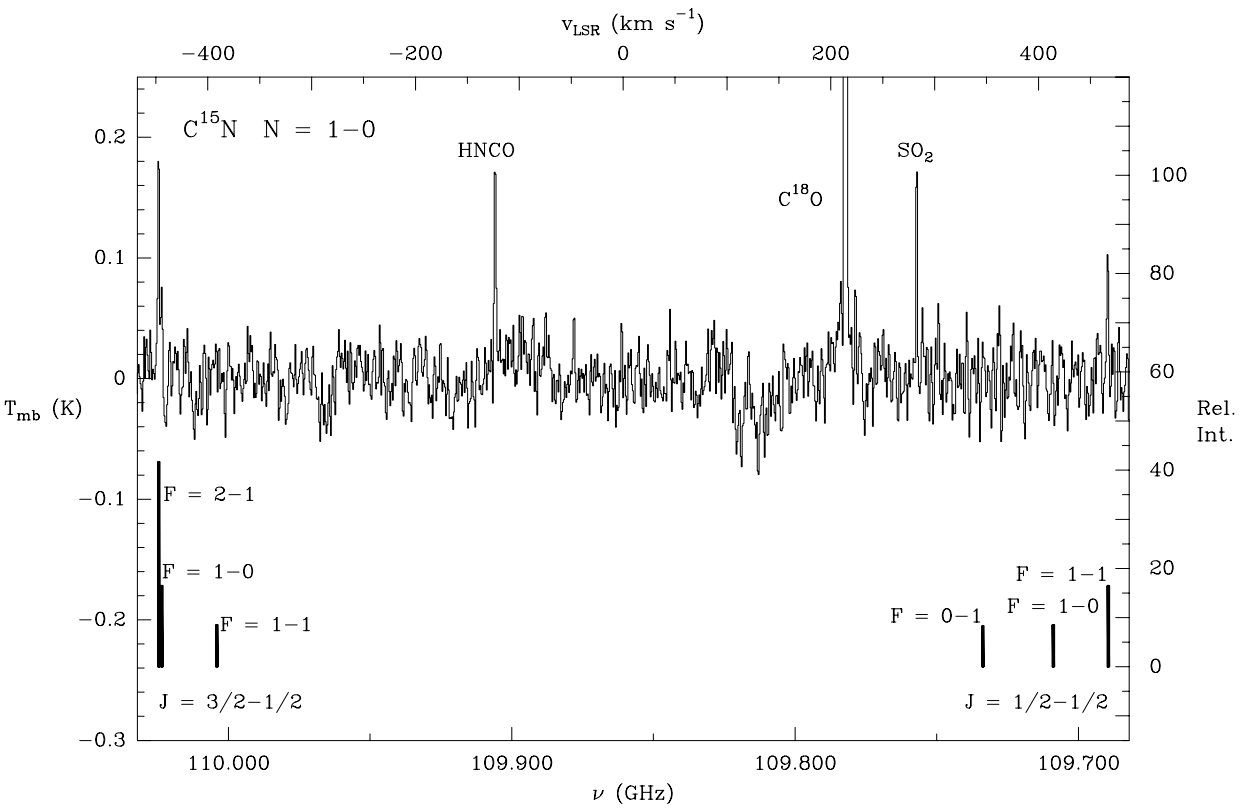

Fig. *7.9: Spectrum of $C^{15}N$ N=1→0 toward the position (24″,72″) relative to BN-KL in Orion A. Relative intensities of the hyperfine pattern are indicated corresponding to optically thin emission. The transitions are labeled by the appropriate quantum numbers.*

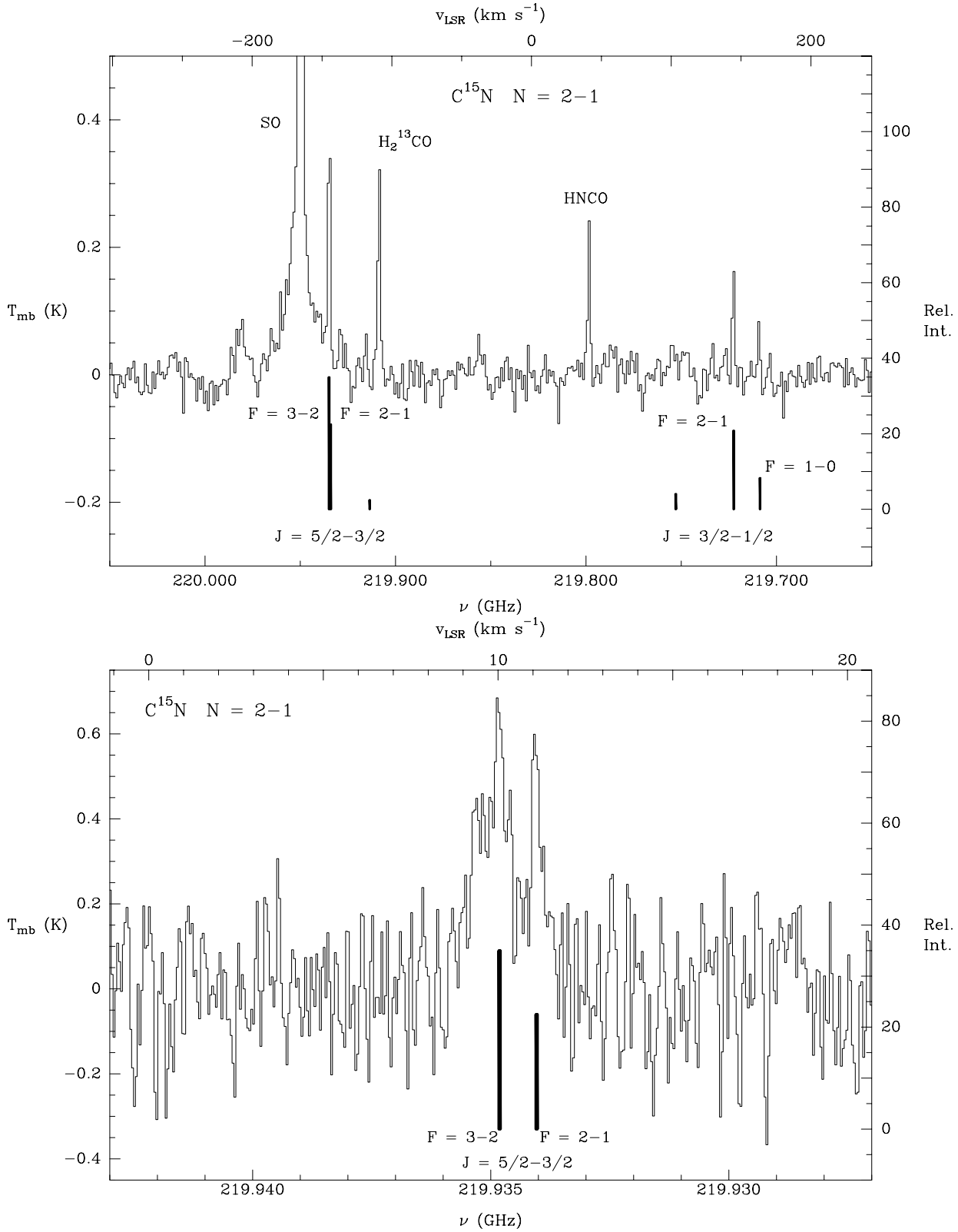

Fig. *7.10: Same as Fig. 7.9 for $C^{15}N$ N=2→1. The spectrum in the top panel was recorded with a 1MHz resolution filterbank. The bottom panel shows the strongest fine structure transition recorded with the autocorrelator at 40kHz resolution.*

The position $(24'', 72'')$ relative to IRc–2 was selected because the CN lines exhibit the highest intensities and small line widths (~ 1.5 km s^{-1}) there.

An appropriate source position was selected by using small maps performed in CN N=1→0 and N=2→1 prior to the C^{15}N observations. These maps were used as a pathfinder for the peak CN intensity and are presented in the next section.

Since previous analyses of CN were based on the isotopomers CN and ^{13}CN only, these new interstellar data provide the missing link in the presently available data set on the CN isotopomers for the derivation of isotopically invariant parameters and for a study of the validity of the Born-Oppenheimer approximation, as already performed for other diatomic molecules such as O_2 (Tiemann 1982), CO (Dale et al. 1979), and NO (Saleck et al. 1991). Furthermore, the CN rotational spectrum is predicted up to 1 THz with a high level of confidence (see the Appendix). For more details on the spectroscopic analysis see the original paper (Saleck, Simon, and Winnewisser 1994a).

7.4.3 Detection of interstellar ^{13}CCH and $C^{13}CH$

Parts of the long time integrations scheduled for CN isotopomers at the IRAM 30m telescope at 1.3 and 3mm, have been used for a simultaneous search for the ^{13}C substituted forms of the ethynyl radical (C_2H). The observations have been carried out with the 2mm SIS receiver which was available in parallel. The unambiguous detection of the ^{13}CCH and $C^{13}CH$ isotopomers of C_2H towards the Orion A ridge is reported by Saleck et al. (1994b) with the identification of the N=2→1 transitions. These measurements confirm an earlier tentative detection of four hyperfine components of $C^{13}CH$ with the KOSMA 3m telescope. Although uncertainties in the calibration of the line intensities are not completely settled, the observations suggest that $C^{13}CH$ might be the more abundant of the two ^{13}C isotopomers. This tentative finding pertains towards the region where the emission of molecular radicals peaks, i.e. north-east of the Kleinmann-Low nebula. Furthermore, the N=1→0 transition of $C^{13}CH$ has been detected in the same region with the SEST 15 m telescope. In combination with laboratory N=$4 \leftarrow 3$ and N=$5 \leftarrow 4$ data, improved ground state rotational constants for both species are derived.

7.5 Submillimeter KOSMA CN and CS observations

In January 1995, the central region of OMC-1 was observed in the CN N=3→2 and CS J=7→6 transitions simultaneously in both sidebands of the KOSMA 0.8 mm SIS receiver (see Fig. 7.11 for a sample spectrum). The distributions of the integrated intensity are displayed in Fig. 7.12. Like CN N=2→1, the N=3→2 transition traces the radical ridge north-east of IRc2 and the Orion Bar. Additionally, due to the higher angular resolution at 340 GHz, a clump $\sim 100''$ south of IRc2, which corresponds to S6 in the nomenclature of ammonia peaks given by Batrla et al. (1983), shows up in the CS data. In contrast to CN, CS clearly peaks towards IRc2 and S6 and shows broad line wings, indicating emission from the plateau source. This assures accurate pointing for both maps to within $10''$. Note that offsets are given with respect to a position in the center of the BN-KL complex ($\alpha(1950.0) = 5^h32^m46^s.6$, $\delta(1950.0) = -5°24'22''$) and that IRc2 itself is indicated by a cross. The high quality of the data, as can also be seen from the observational parameters listed in Table 6.2, proves the excellent weather conditions of the Gornergrat location, especially in winter.

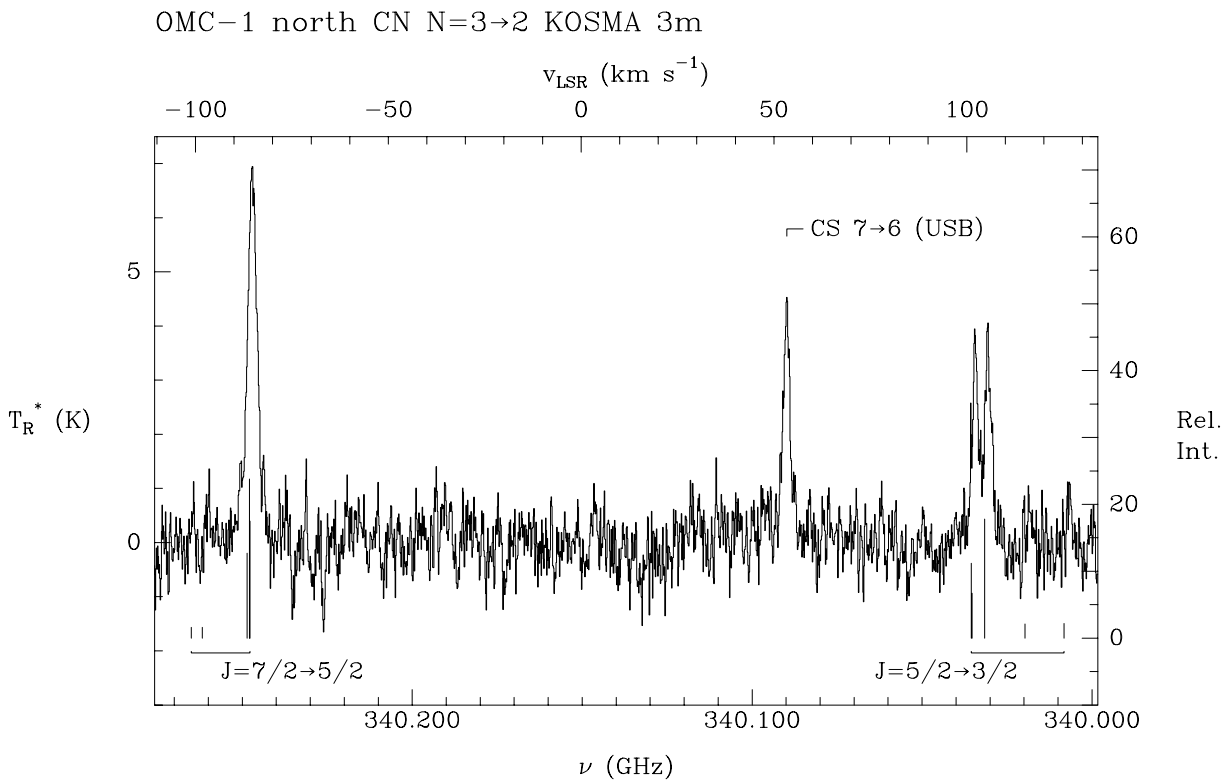

Fig. *7.11: KOSMA CN N=3→2 and CS J=7→6 spectrum obtained in OMC-1.*

All further analysis concerning OMC-1 and the Orion Bar region, including the application of the escape probability formalism to the observed lines, will be done with the IRAM and JCMT data since they provide higher angular resolutions and a greater number of observed rotational transitions of CN and CS.

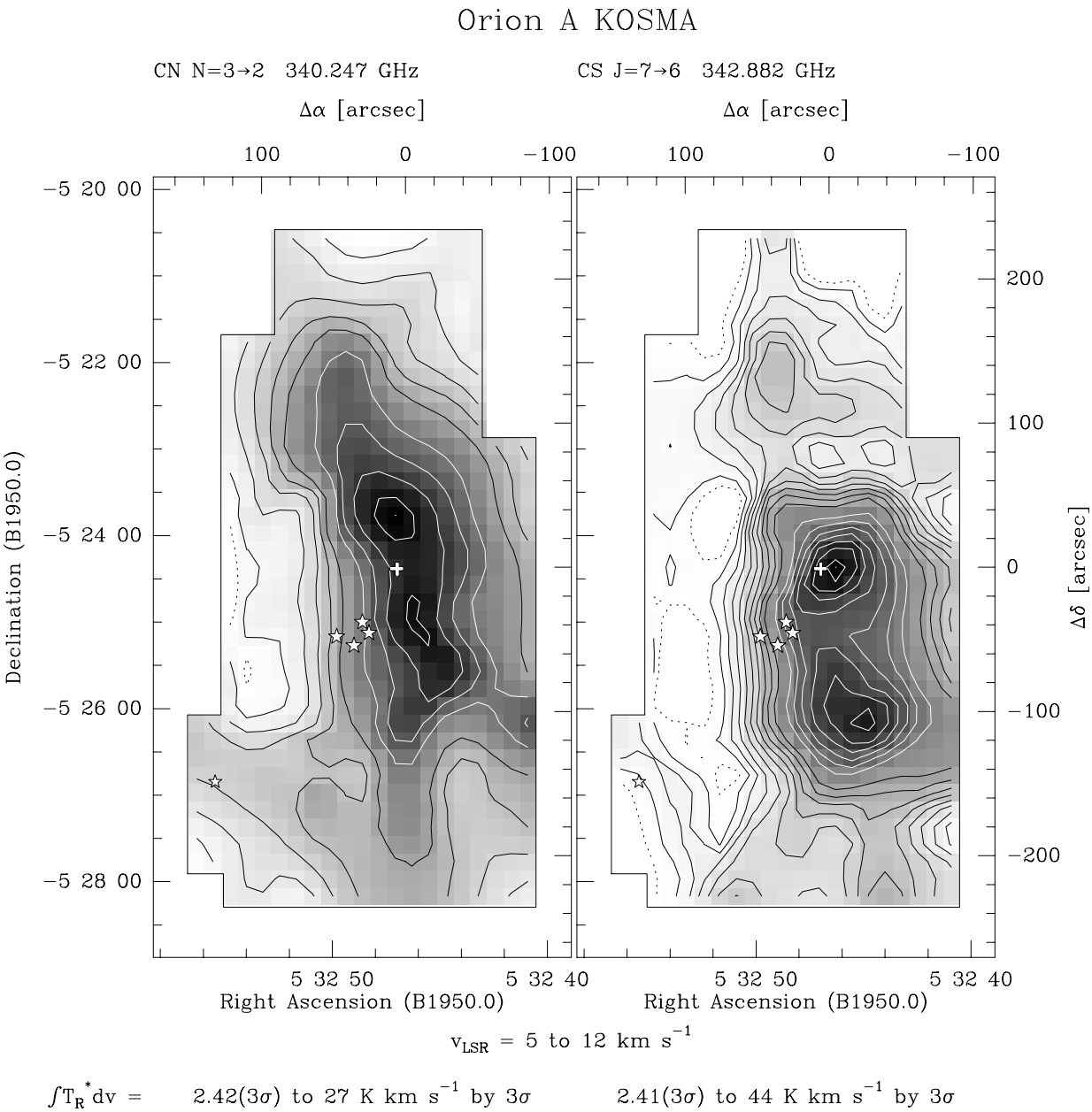

Fig. *7.12: Comparison of the intensity of the CN N=3→2 and CS J=7→6 transitions integrated over* $v_{\rm LSR} = 5 - 12$ *km s*$^{-1}$ *in OMC-1 as measured with the KOSMA 3m telescope. The Trapezium is indicated and the cross marks the position of IRc2. The angular resolution of the maps, which are on a fully sampled grid, is 80″.*

7.6 High angular resolution IRAM and JCMT data

7.6.1 Morphology

In order to display the morphological appearance of the core of OMC-1 in different molecular tracers and to estimate the pointing accuracy in the individual datasets, a selection of interstellar molecular species, whose transitions lay adjacent to the CN and CS transitions and were observed in parallel, is shown in Fig. 7.13. The transition frequencies of those species which are not included in the observations section (see Table 6.1) are given in Table 7.1.

Molecule	Transition			Frequency (MHz)
$HCOOCH_3$	$20_{2,19}$	$\rightarrow$	$19_{2,18}$	226713.04
^{34}SO	9_8	$\rightarrow$	8_7	339857.28
CH_3OH	2_2	$\rightarrow$	3_1 A+	340141.22

Table *7.1: Observational parameters related to molecular species shown in Fig. 7.13 and not listed in Table 6.1.*

The corresponding intensity distributions for the three lowest rotational transitions of CN are shown as channel maps of the strongest hyperfine component of each transition in Fig. 7.14 to 7.16. The velocity range has been selected in order to cover emission relevant for the Bar, S6 and the northern part of the ridge according to the north-south velocity gradient. The filled triangles mark the positions of the mm dust continuum peaks (FIR1 through 4 from north to south, FIR2 corresponds to IRc2, FIR4 to S6) as introduced by Mezger et al. (1989).

The extended CN, CS and partly CH_3CN emission follows the north-south elongated extended molecular ridge and traces several embedded condensations, whereas ^{34}SO, CH_3OH and $HCOOCH_3$ are spatially confined to the immediate vicinity of IRc2. According to results of former observations of Orion IRc2 (see e.g. Blake et al. 1987), the SO abundance is strongly enhanced in the plateau source and hence SO emission is expected to peak towards IRc2. The ^{34}SO emission observed with the JCMT clearly shows this behavior, indicating that the pointing is very accurate. This finding is further supported by the observed distribution of CH_3OH which, as an oxygen rich species, is produced in the compact ridge south of and wrapped around IRc2, which is visible as a trend in the contour plots. The CS J=3$\rightarrow$2 and J=7$\rightarrow$6 emission maxima are shifted by $\sim 5''$ in Right Ascension with respect to each other, as are the peaks of the compact ridge tracers CH_3OH and $HCOOCH_3$. The overall pointing uncertainties among the different datasets are thus estimated to be less than $5''$.

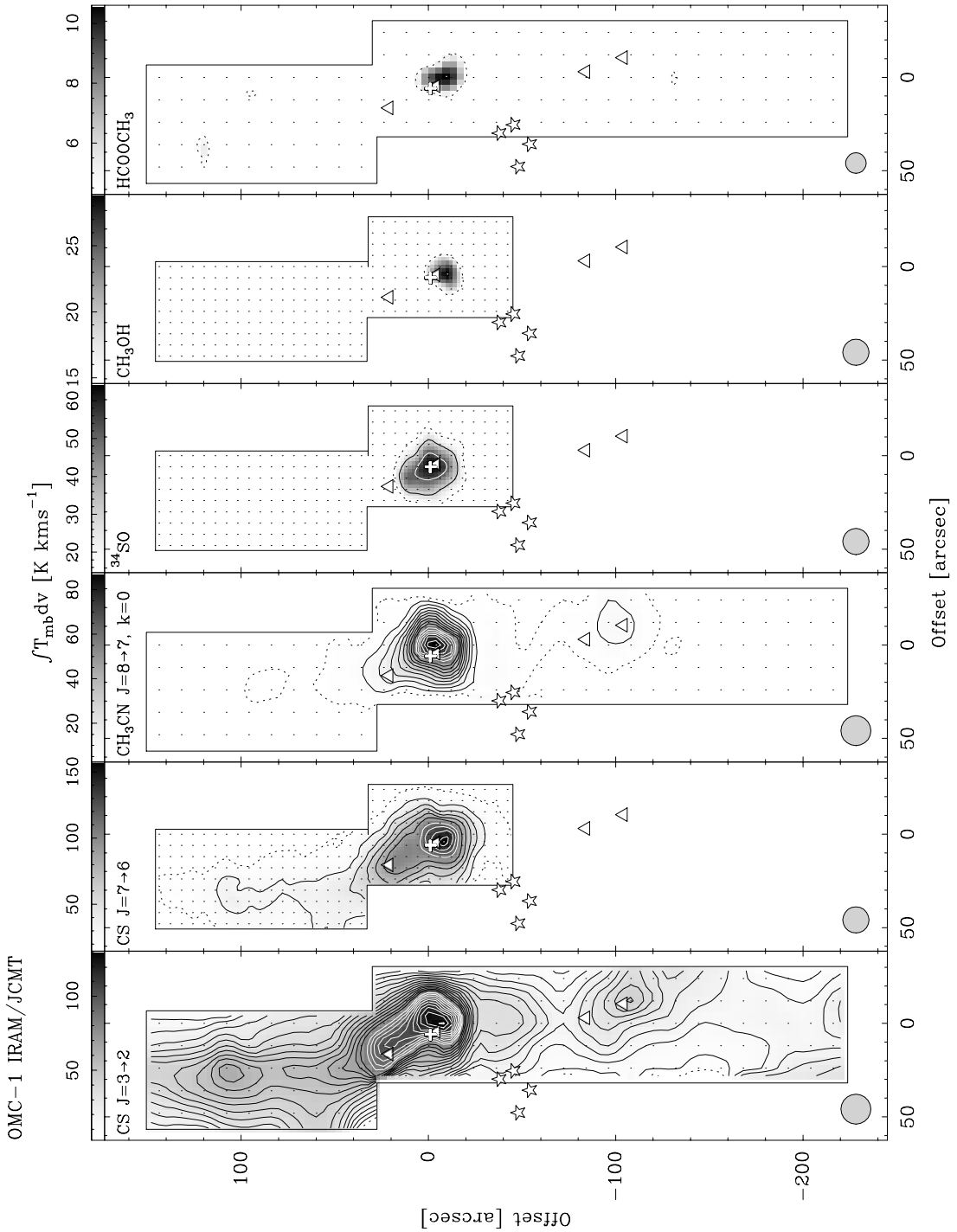

Fig. *7.13: Comparison of CS and CH_3CN to emission of the molecular species listed in Table 7.1. The stars mark the Trapezium, the white cross the position of IRc2, and the triangles the positions of peak continuum maxima as determined by Mezger et al. (1989). Offsets are relative to* $(\alpha = 5^h32^m55^s.4$, $\delta = -5°26'50''.7)$*, a position in the center of the BN-KL complex. Contour levels start with* 3σ *(lowest, dashed contour) and increase to the maximum in steps of either* 6σ *(for CS J=3→2 and CH_3CN) or* 3σ *in the other cases. The integrated intensity greyscale range is given with the wedge on top of each panel. The beam size is given in the lower left corner for each transition.*

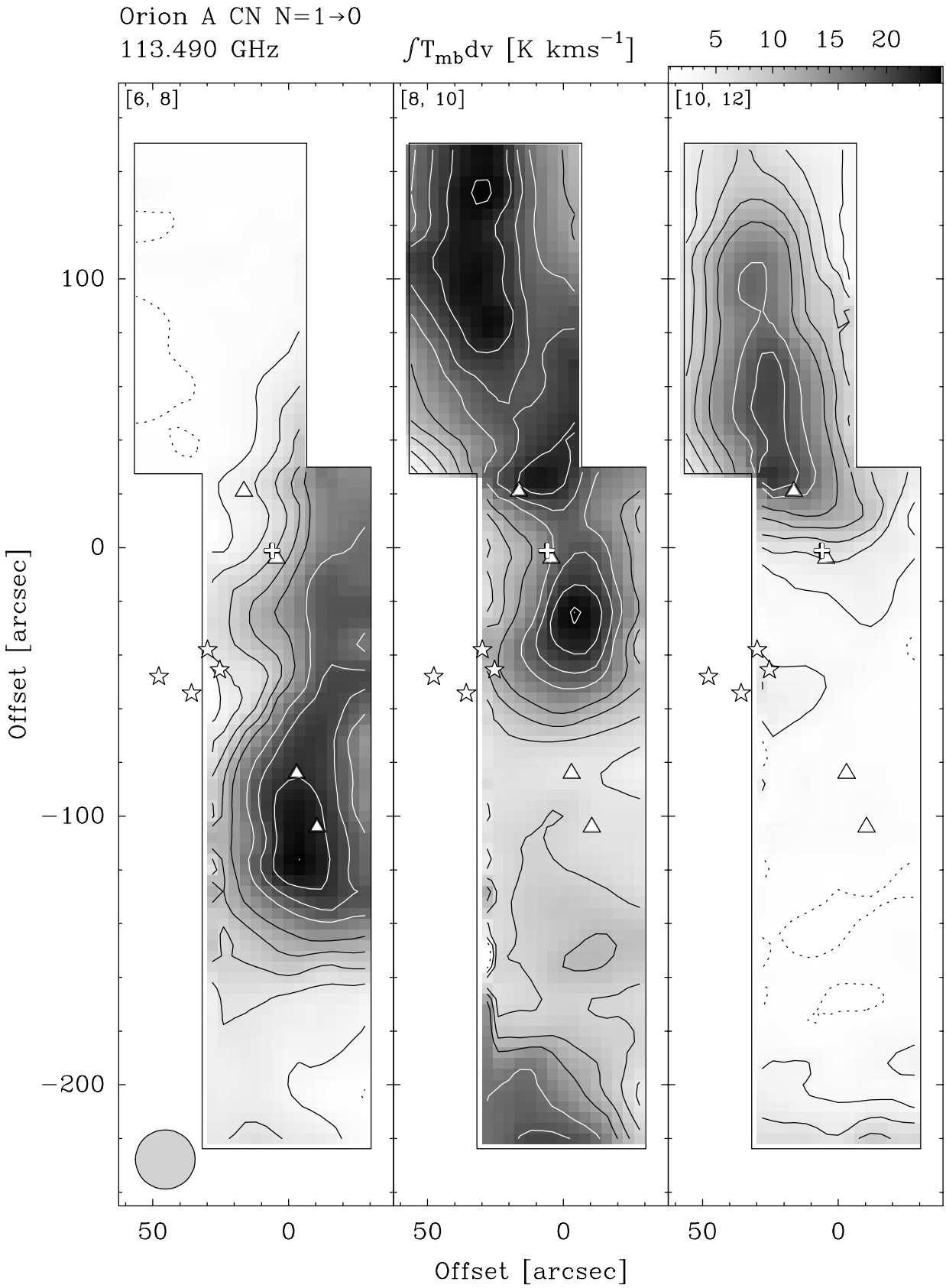

Fig. *7.14: Channel maps of CN N=1→0 in OMC-1 observed with the IRAM 30m telescope. The velocity interval in km s^{-1} is given in the top left corner of each panel. Contour levels increase in steps of* $3\sigma = 0.95$ *K km s^{-1} to the maximum value given on top of the last panel. The beam size is indicated in the first panel. Offsets are relative to BN-KL.*

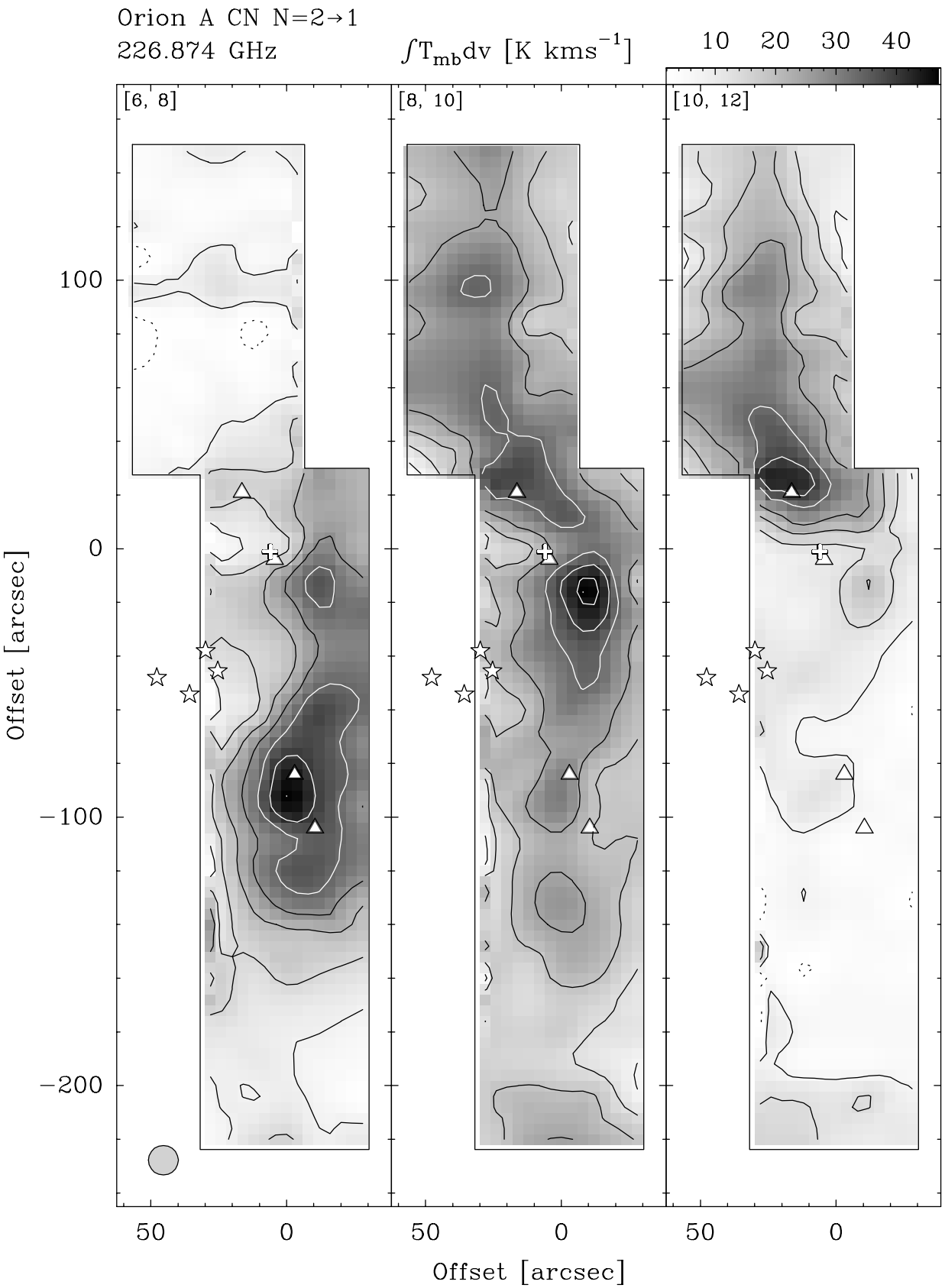

Fig. *7.15: The same as Fig. 7.14 for CN N=2→1. Contour levels are* $3\sigma = 1.94(1.94)$ *K km s*$^{-1}$ *to the maximum.*

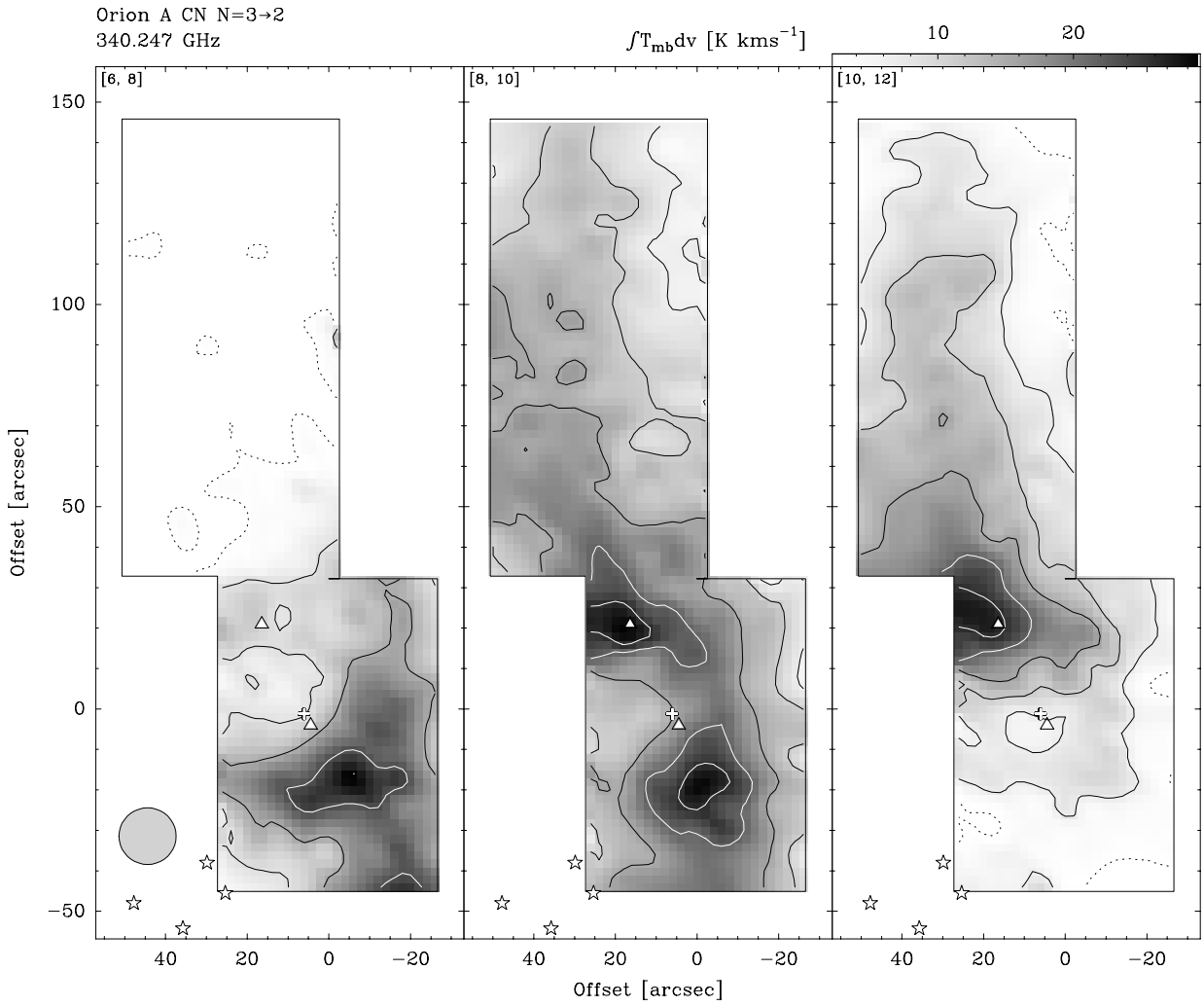

Fig. *7.16: The same as Fig. 7.14 for the CN N=3→2 data obtained at the JCMT. Contour levels are* $3\sigma = 3.78(2.52)$ *K km s*$^{-1}$ *to the maximum.*

Generally, the CN emission is most pronounced in the north-eastern part of the cloud and south of IRc2, where the differences between the distributions of the three rotational transitions reflect the different excitation conditions. While CN N=1→0 traces the dense but cooler ridge to the north, enhanced N=2→1 and, even more suspicious, N=3→2 emission is distributed closer to the warmer part of the cloud in the direction toward IRc2. Remarkable is the lack of CN emission towards IRc2 itself, where the density should be sufficiently high to thermalize the CN transitions. In fact, endothermic chemical reactions in this hot and shock influenced environment lead to the depletion of CN in favor of more stable molecules, especially HCN, which shows a pronounced peak at this position (Schilke et al. 1992).

Enhanced CN N=1→0 emission from the northern part of the ridge was already reported by Turner & Gammon (1974). In this henceforth so called **radical ridge**, $3'$ north of IRc2, molecules like HCO^+ and N_2H^+ have their emission peaks. Nevertheless, a *lack* of enhanced CN N=2→1 emission in the ridge was reported by Greaves & White (1992), which they attributed to the derived low excitation temperatures. This topic will be discussed in detail in a following section.

The clump S6 $\sim 100''$ south of IRc2 is traced by CN N=1$\rightarrow$0 and N=2$\rightarrow$1in the lower velocity channels, and by CS and CH_3CN, revealing itself as a warmer condensation in the extended ridge. This source is believed to contain an embedded newly born star (see e.g. the intesidiscovery of a highly collimated outflow by Schmid-Burgk 1990). Batrla et al. (1983), from their NH_3 observations, derived a kinetic temperature of 75–100 K and a molecular hydrogen density of 6×10^7 cm^{-3}, and Mezger et al. (1989) determined a dust temperature of ~ 65 K at their mm continuum peaks FIR3 and 4, associated with S6. In the northern molecular ridge, away from IRc2, the temperatures are of the order of 15–30 K according to the results obtained from ammonia observations by Batrla et al.

With the exception of IRc2/FIR2, where CN is chemically depleted, CN emission correlates well with the mm dust continuum emission peaks FIR 1, 3 and 4 observed by Mezger et al. (1989). Since the dust temperatures derived for the clumps embedded in the extended ridge are of the order of $T_{dust} \sim 65 - 100$ K and agree fairly well with the temperatures derived from ammonia observations (Batrla et al. 1983), the conclusion is suggested that CN and mm continuum emission should generally correlate well in the warm and dense, but anticorrelate in dense and hot or shock influenced environments.

7.6.2 Results from the hyperfine fits

Before fitting the observed CN spectra as described in Chapter 5, the CN N=2$\rightarrow$1 and N=3$\rightarrow$2 data have been smoothed to the angular resolution of the N=1$\rightarrow$0 observations (i.e. $24''$) in order to avoid beam filling effects due to different beam sizes. This results in an improved signal to noise ratio for the smoothed data at the individual positions (note that the grid spacing for the CN N=3$\rightarrow$2 observations was modified from $6''$ to $12''$) and is inevitable if one compares later derived physical parameters position by position. Values for the source LSR velocity, the CN line width and the optical depth distribution obtained from the hyperfine fitting procedure are shown in Fig. 7.17 to 7.18.

The well known velocity gradient (increasing v_{LSR} from south to north) of the Orion ridge is visible in Fig. 7.17 for all of the three rotational transitions. Its origin is still a topic under discussion in terms of rotation of a cloud (e.g. Kutner et al. 1981) or the superposition of two clouds with distinct radial velocities (e.g. Ho & Barrett 1978). The N=1$\rightarrow$0 and N=2$\rightarrow$1 transitions in the southernmost part of the maps show an LSR velocity increase towards this region of the ridge, which can be partly attributed to the connection of the extended ridge to the Orion Bar since LSR velocities of the Bar are centered on ~ 11.0 km s^{-1}. A detailed analysis of high resolution CN and CS observations in the Orion Bar region is presented in one of the next sections.

No prominent CN N=1$\rightarrow$0 line wings are visible in Fig. 7.17, probably due to the low optical depth of the transition (see the Fig. 7.18). The clump S6 is again visible in the N=2$\rightarrow$1 transition with a moderate line broadening. In the north-eastern part of the extended ridge, the CN lines show remarkably small line widths of only 1.5–2 km s^{-1} in all three transitions, indicating the quiescent character of this region. Most striking in Fig. 7.17 is the enhanced line width of the CN N=3$\rightarrow$2 lines east and west of IRc2 although the opacities here are low. The bipolar morphological appearance of the line wing distribution is suggestive of being influenced by a

complex interplay between chemical depletion in the center close to IRc2 and excitation effects in the ambient material, where the high velocity outflow, which divides the quiescent ridge, hits the surrounding gas east and west of IRc2. Such a geometrical picture and the orientation of the outflow have been extracted from high resolution molecular line observations at the origin of the flows, in the vicinity of IRc2 (see e.g. Masson & Mundy 1988 and Wynn-Williams et al. 1984). The latter authors propose a clumpy cavity produced by the stellar wind(s) of the embedded source(s) near IRc2. Similar to the distribution of the warm and dense gas tracing HC_3N (Rodríguez-Franco et al. 1992), the CN emission (see Fig. 7.14 to 7.16) surrounds the *expanding doughnut* reported by Plambeck et al. (1982) and traces the interface between quiescent gas and the hot cavity wall.

In this context, it is remarkable that the distribution of the warm and dense gas tracing CN N=3$\rightarrow$2 emission (see the plots of the integrated intensity and the optical depth in Fig. 7.16 and 7.18) is almost exactly perpendicular (i.e. north and south oriented) to the distribution of broad CN lines. A possible explanation is that the CN radical is still depleted in the warmer gas influenced by the flow, but the remaining CN shows up with enhanced line widths and intensities exclusively in a transition requiring higher excitation (the N=3 level is 32 K above the ground state). In fact, CN N=3$\rightarrow$2 spectra in the vicinity of IRc2 along the east-west axis of the flow (Fig. 7.19) show that a small fraction of CN is found in the outflow. The same holds for the N=2$\rightarrow$1 spectrum, which is not shown here, and was already reported for N=2$\rightarrow$1 independently by Greaves & White (1992). The larger optical depth, and hence column density, of CN N=2$\rightarrow$1 and N=3$\rightarrow$2 is found in the adjacent, more quiescent but still warm and dense gas of the ridge, where depletion is diminished.

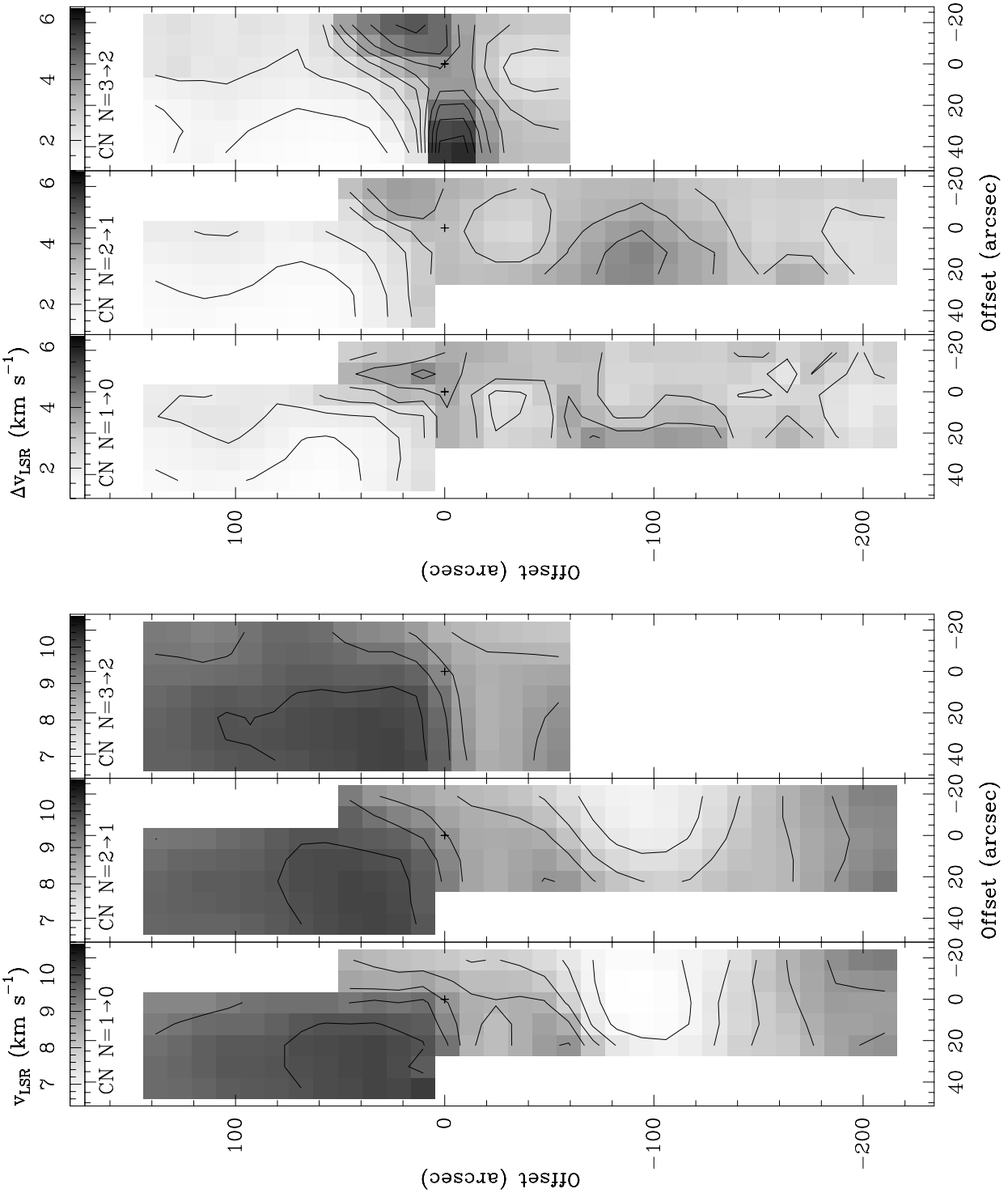

Fig. *7.17: Results from the CN hyperfine fits to the smoothed datasets from the IRAM 30m (CN N=1→0 and N=2→1) and the JCMT (CN N=3→2): LSR velocities (bottom panels) and line width (top panels) in the OMC-1 ridge. Contour levels are 6.4(0.5)9.4 km s^{-1} and 1.0(0.5)6.0 km s^{-1} respectively. The position of IRc2 is indicated by a cross.*

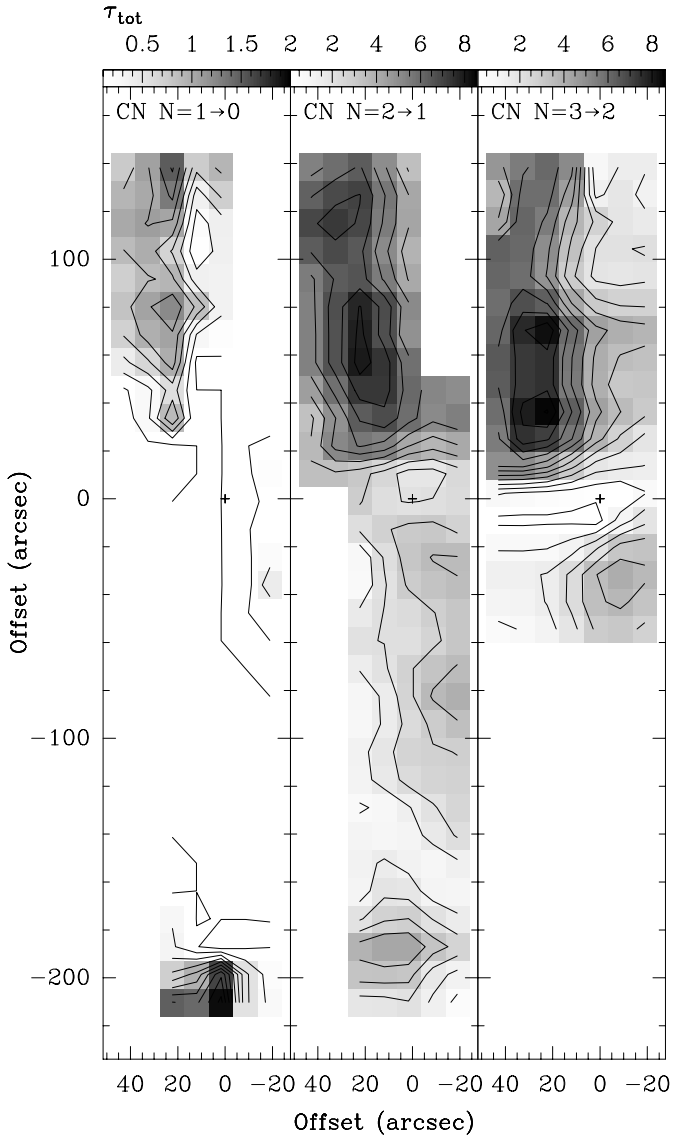

Fig. *7.18: Distribution of the total optical depth of each observed rotational transition from the hyperfine fits. Contour levels are 0.1(0.2)2.0 for CN N=1→0 and 0.1(0.7)8.5 for CN N=2→1 and N=3→2.*

Excitation and non-LTE effects

Almost everywhere in the observed part of OMC-1, the CN N=1→0 opacities are low. Excitation temperatures for this transition, as argued in Chapter 5, are thus only determined with great ambiguities. At those positions where significant optical depths are observed for the N=2→1 and N=3→2 transitions, beam averaged excitation temperatures from (5.5) are typically in the range $10 - 30$ K with a trend to lower values in the northern- (the *radical ridge*) and southernmost parts of the ridge. This finding also emerges from the plot of the peak antenna temperatures presented in Fig. 7.20, which in fact constitute lower limits to the excitation temperature at the individual cloud positions.

Greaves & White (1992), from their CN N=2→1 observations, derive excitation temperatures of the order of 10 K by averaging spectra from areas $\sim 1' \times 1'$ along the north-south axis of the ridge. The plot of the peak temperatures of the main hyperfine components (Fig. 7.20) reveals that the

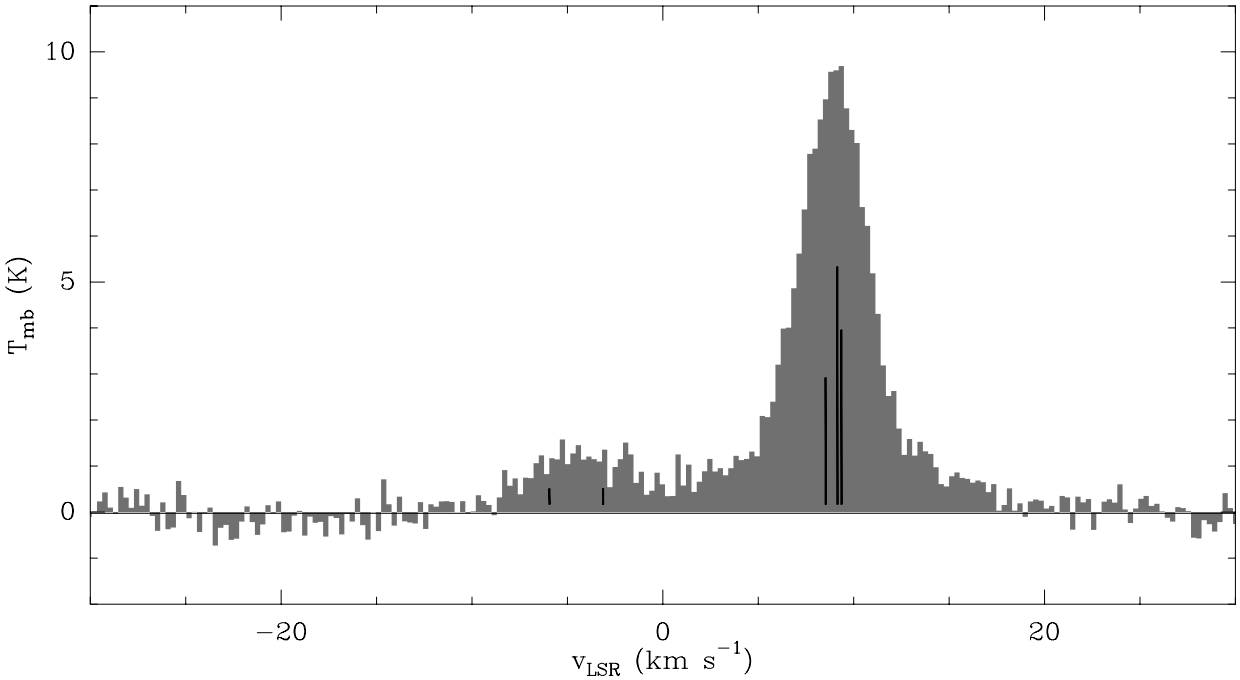

Fig. *7.19: CN N=3→2 scan from the IRc2 region. Positions and relative intensities in the optically thin case are plotted as bars below the spectrum. Emission of CN in the outflow is visible as faint pedestal.*

ridge is quite narrow and well defined. At high angular resolution the emission clearly shows no evidence for very low excitation temperatures of CN at the center of the north-south extended ridge. Due to the error beam of the IRAM 30m telescope, which contributes significantly at frequencies higher than 200 GHz and for extended sources (Garcia-Burillo et al. 1993, Schneider et al. 1997), the CN N=2→1 temperatures may be overestimated but, since CN emission is well confined, the resulting effect should be small. This means that the low excitation temperatures derived by Greaves & White have to be attributed to their smoothing procedure.

CN N=1→0 shows somewhat lower peak antenna temperatures than N=2→1 due to the low optical depths of this transition: the optically thin CN N=1→0 emission emerges from the more shielded and hence colder molecular material, whereas the optically thick N=2→1 transition traces the outer and warmer parts of the externally heated cloud. Since the kinetic temperature and density are expected to be of the order of $20-40$ K and 10^4-10^6 cm^{-3} (which is close to the critical densities of the lower CN transitions) in the quiescent ridge, subthermal excitation of CN N=2→1 and N=3→2, in spite of the high optical depths of these transitions, is not excluded. Toward the warmer and higher density condensations, where the excitation temperatures at least for the optically thick N=2→1 transition should be close to the kinetic temperature, this possibility should be borne in mind and is strongly suggested by the lower peak antenna temperatures of the N=3→2 transition. At the lower excitation temperatures in the northernmost part of the cloud, most of the emission is expected to arise from the lowest rotational transition and this explains the pronounced CN N=1→0 emission from the **radical ridge** originally reported by Turner & Gammon (1974).

Greaves & White also report unexpectedly high intensities of some weaker N=2→1 hyperfine lines and antenna temperatures for the $J = 5/2$ fine structure group which are enhanced by a

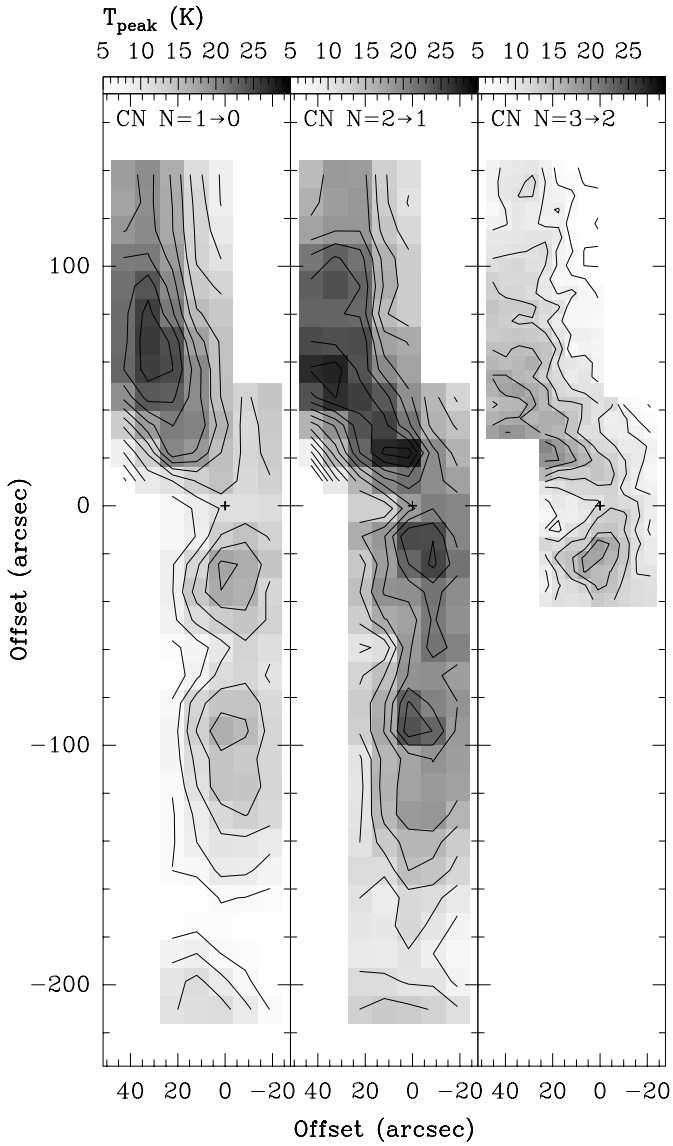

Fig. *7.20: Peak temperatures of the main hyperfine component of each observed rotational transition. Contour levels are 5(2)30 K.*

factor of 1.6 with respect to $J = 3/2$. They attribute this finding to non-LTE effects affecting the N=2→1 *fine* structure levels. Within the observational uncertainties, such a behavior is not supported by the data presented in this thesis. At least within both observed *fine* structure transitions the line intensities are well compatible with the fitted opacities.

Previous observations by Crutcher et al. (1984) toward TMC-1 and ρ Ophiuchus suggested deviations from LTE for *hyperfine* line intensities in the CN N=1→0 and N=2→1 rotational transitions. Such effects may be mimicked by self-absorption toward cold foreground envelopes and are definitely occurring in ρ Ophiuchus A, a source well known to show self-absorption in molecular lines. Fig. B.14 in the Appendix displays a small map of this region obtained at the IRAM 30m telescope and shows clear evidence for unusual line intensities caused by self-absorption. As mentioned by Crutcher et al., the same phenomenon may also occur toward TMC-1.

High signal to noise spectra from OMC-1 north, obtained within the scope of this work, reveal that selective collisional pumping between *hyperfine* levels may indeed play a significant role and thus renders the knowledge of collision rates between individual hyperfine levels important. A suspicious example for this is shown in Fig. 7.21 where the two weakest hfs components of the $\mathrm{J} = 5/2 \rightarrow 3/2$ fine structure, which have similar relative intensities, indicate a deviation from LTE. Spectra from this region do not show any signs of self-absorption effects. Considering the noise level of the spectrum, the deviation from the LTE case is (41 ± 5)%.

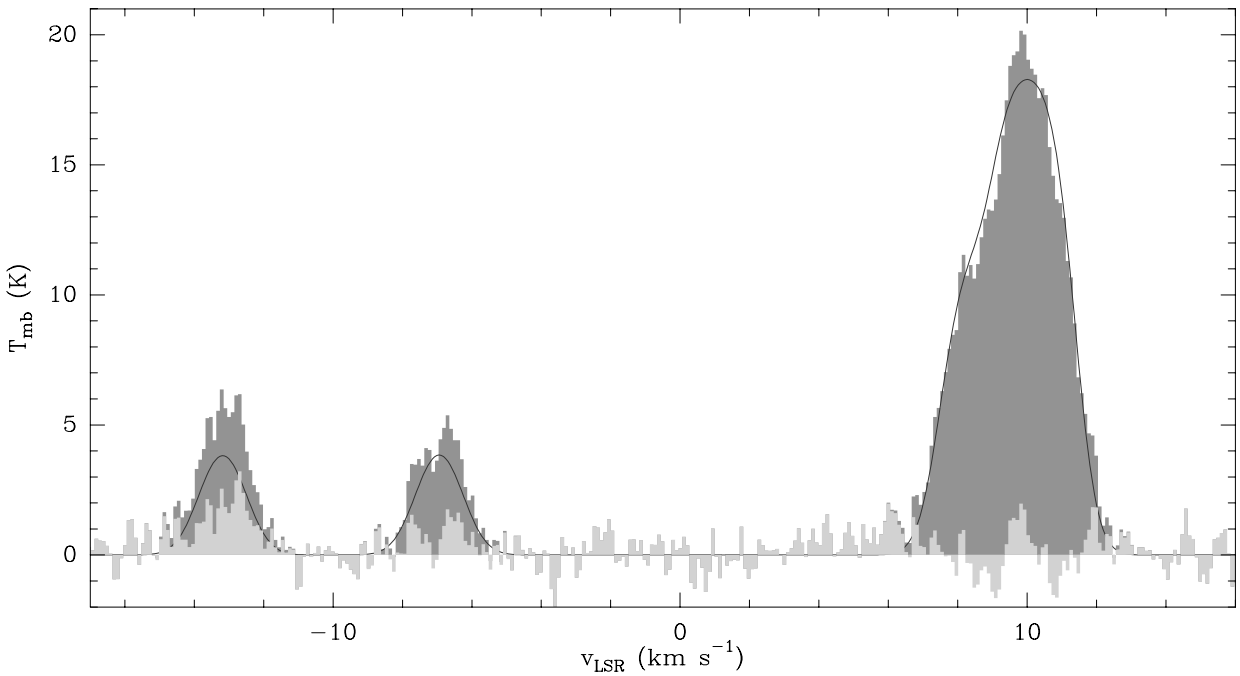

Fig. *7.21: High signal to noise spectrum of CN N=2→1* $\mathrm{J} = 5/2 \rightarrow 3/2$ *from the northern part of OMC-1. The two weakest hfs components have almost equal relative intensities (3.17 and 3.19% of the total intensity) and show a clear deviation from the expected line intensities. The light grey histogram displays the residuals of the fit.*

7.6.3 Physical parameters

With the knowledge of the optical depths from the hyperfine fits to the spectra, it is now possible to derive opacity corrected upper state column densities from the integrated line intensities as described in Chapter 5. Only map positions where all three transitions have been observed are used in the following analysis. If the rotational levels are populated according to a single rotational temperature, total molecular column densities are derived in a straight forward way from the corresponding rotation diagram. One typical example of such a rotation diagram for one position north of IRc2 is displayed in Fig. 7.22. Filled squares correspond to the upper state column densities derived from the optically thin approach (5.10), while open squares with typical error bars represent the same values corrected for the fitted opacity. Without this correction, a larger amount of CN is suspected at lower temperatures and wrong estimates for the total CN column density result, depending on the product $\mathcal{N}_0 \times \mathcal{Z}(\mathrm{T}_{rot})$.

The straight line shows the result of a linear fit to the three opacity corrected data points. The

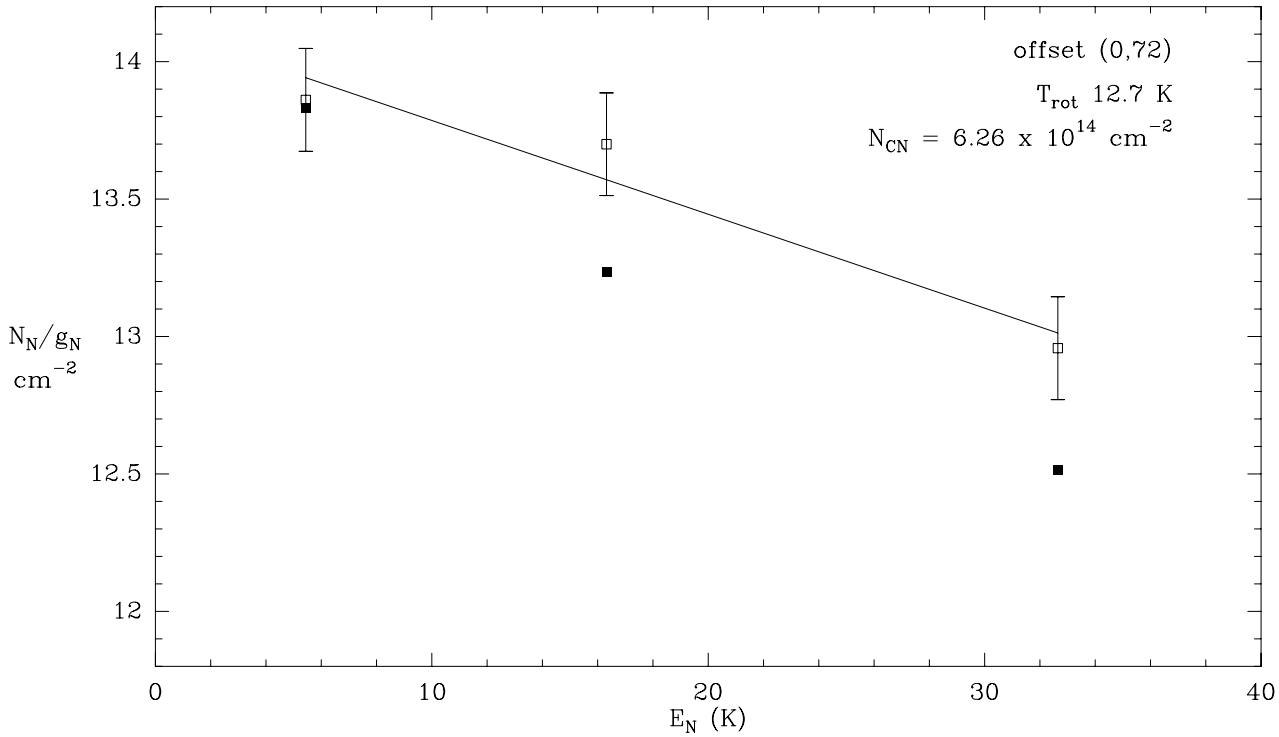

Fig. *7.22: Sample rotation diagram for CN N=1→0, N=2→1 and N=3→2 at offset (0″,72″) from IRc2 in OMC-1. Upper state column densities derived from the optically thin approximation (filled squares) and the opacity correction (open squares) are shown. The straight line correspond to the fit result for the three components.*

deviation of the data points from this line strongly suggests that at least the N=3→2 transition is subthermally excited which is expected due to the high critical density of this transition. This finding was already implied by the weakness of the CN N=3→2 line temperatures obvious in Fig. 7.20. As already mentioned earlier, the N_2 data point may be overestimated due to pick up in the IRAM 30m error beam, but the resulting column densities will not be overestimated by more than a factor of 2 which in turn, see Fig. 7.22, would have no significant influence on the slope of the fitted line. Note that a similar column density distribution results for almost every position in the cloud, a finding which initially motivated the later following analysis with the single density, single temperature escape probability model.

Fig. 7.23 displays the total CN column density distribution derived together with the fit results for the rotational temperature. These results further support the findings discussed in the previous section, namely that the CN column density is highest in the vicinity north and south of IRc2 and lowest in the vicinity of the dense and hot environment. Enhanced rotational temperatures can be found toward the column density maximum, but it should be noted that the *rotational* temperatures have to be considered as lower limits to the *excitation* temperatures, due to the subthermal excitation of the N=3→2 transition. Thus, the peak antenna temperatures of the optically thick lines are fairly well estimates of the true excitation temperatures.

Total CN column densities for the whole region considered in the analysis are in the range $3 - 16 \times 10^{14}$ cm^{-2} and, with regard to our higher angular resolution, compare well to the values derived by Turner & Gammon (1974) of $\sim 2 - 5 \times 10^{14}$ cm^{-2} with a 65″ beam from N=1→0

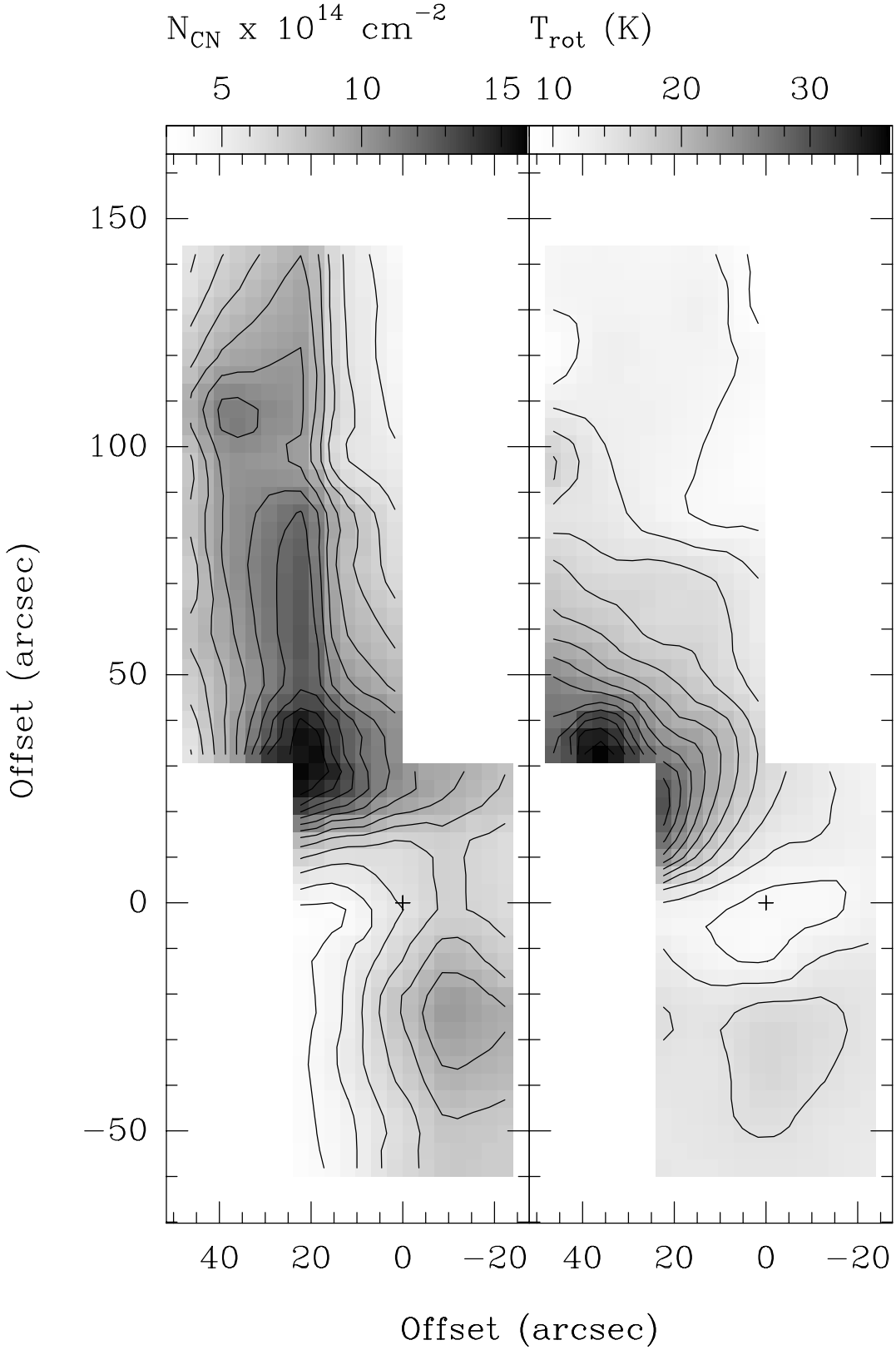

Fig. *7.23: Distribution of the total CN column density as derived from the rotation diagrams (levels are* $2(0.5)7 \times 10^{14}$ *cm*$^{-2}$*) and lower limits to the rotational temperatures (levels are* $8(1)30$ *K).*

observations only. Toward IRc2, Blake et al. (1987) determine a CN column density of 1×10^{15} cm^{-2} from their N=1→0 observation and an assumed rotational temperature of 60 K in contrast to 6.2×10^{14} cm^{-2} from this work. This apparent discrepancy can be explained with the high rotational temperature used by Blake et al. (the lower limit from our analysis toward IRc2 is 20 K). If only our $\mathcal{N}_1$ data point in conjunction with a rotational temperature of 60 K is used, the resulting total CN column density is 1.4×10^{15} cm^{-2}, in fairly well agreement with the value reported by Blake et al. Adopting their H_2 column density (3×10^{23} cm^{-2}), we derive a CN abundance toward IRc2 of 2.1×10^{-9} which is slightly lower than 3.3×10^{-9} determined by Blake et al. but should be more reliable since the present analysis incorporates information on the population of energetically higher states and less assumptions. Table 7.2 summarizes the CN abundance along the north-south axis of the extended ridge derived from the total CN column densities and H_2 column densities reported by Schilke et al. (1992) from their HCN observations and $C^{18}O$ data of Wilson et al. (1986). The Table also contains their estimates of the kinetic temperature and H_2 volume density.

Position offset	T_{kin} K	$n(H_2)$ $\times 10^5$ cm^{-3}	$N(H_2)$ $\times 10^{22}$ cm^{-2}	N_{CN} $\times 10^{14}$ cm^{-2}	X(CN) $\times 10^{-9}$
(24″,96″)	35	3	8	10.1	12.6
(24″,84″)	41	21	14	11.8	8.4
(24″,60″)	45	9	18	12.4	6.9
(24″,50″)	50	7	31	12.1	3.9
(24″,24″)	48	7	22	14.0	6.4
BN-KL	70	9	36	6.2	2.1
(-12″,-24″)	41	27	17	9.8	5.8
FIR3[a]	38	5	5	14	28.0
FIR4[a]	40	27	22	12	5.5

[a] values obtained from a Boltzmann plot with N=1→0 and N=2→1 only

Table *7.2: CN abundances X(CN) along the extended ridge from the H_2 column densities reported by Schilke et al. (1992). Their derived H_2 densities and kinetic temperatures are cited for reasons of completeness.*

Escape probability analysis

At those positions from Table 7.2 where the complete set of three CN rotational transitions is available, a comparison of parameters derived above for CN with the results of the escape probability formalism was performed. A typical example, showing slices of the modeled data cube at four kinetic temperatures for the position (24″,24″) relative to IRc2, is shown in Fig. 7.24. The plot contains curves representing two integrated intensity ratios and two optical depths as observed (black contours), as well as grey contours representing 50% deviation from the observed values. The model yields fairly well defined ranges of parameters in the H_2 density and CN column density plane. Assuming kinetic temperatures of 20 – 40 K for the northern OMC-1

ridge, gas densities of 10^5 cm^{-3} and, considering typical line widths of 2 – 3 km s^{-1} from the hyperfine fits, CN molecular column densities of some 10^{14} cm^{-2} result for the region. Generally, the CN column densities presented in Table 7.2 are confirmed within factors of 2 and at most 5. However, at each position the values derived from the escape probability model are lower, which might be attributed to the fact that, since there are no collisional rate coefficients available for CN, the model was calculated with CS rates and hyperfine splitting was not considered. This means that the integrated intensity ratios from the observations used as input were determined from the sum of the integrated intensities of all hyperfine components. It should be noted that the H_2 volume densities compatible with the observed integrated line intensity ratios and optical depths are lower than the values given in Table 7.2 (adopted from Schilke et al. 1992 derived from $C^{18}O$ data of Wilson et al. (1986) on the basis of line intensities of higher density tracing HCN). Different absolute quantities than theirs are also conceivable, e.g. Batrla et al. (1983) use H_2 densities of a few 10^4 cm^{-3} and lower kinetic temperatures in their ammonia analysis. On the other hand, the difference in the gas densities might simply reflect that CN emission originates in colder gas of lower density.

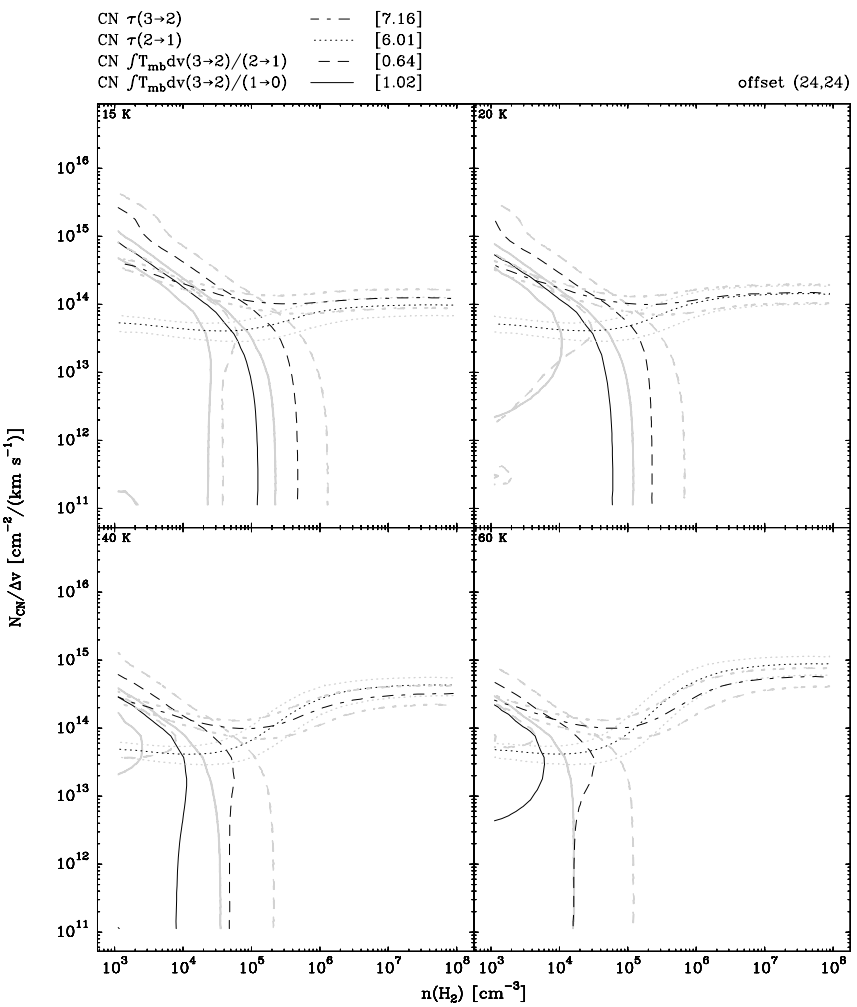

Fig. *7.24: Results of the escape probability calculations for observational parameters toward the position (24″,24″) relative to IRc2.*

7.6.4 ^{13}CN and isotopic fractionation

Isotopic molecular abundances in conjunction with isotopic carbon chemistry play an important role in the interpretation of Galactic chemical evolution and the physical conditions in the interstellar medium. However, column density ratios of carbon bearing main and rarer isotopomers do not necessarily reflect the true carbon isotope ratios since photodissociation and isotopic chemistry may significantly alter the molecular abundances. Optical techniques using line absorption spectra of CH^+ and CN (e.g. Kaiser et al. 1991, and references therein) toward nearby diffuse and translucent clouds with bright background sources, as well as radio observations of formaldehyde (e.g. Henkel et al. 1982) and CO (e.g. Langer & Penzias 1990) toward distant and more opaque interstellar clouds have been used to investigate the isotopic carbon ratio. The latter authors find a systematic gradient in the ratio across the Galaxy with values between 30 and 70 with increasing distance from the Galactic Center.

For CO and its isotopomers, as the most easily observable molecular species at radio wavelengths, the effects of isotope selective photodissociation and fractionation are fairly well understood theoretically and confirmed by observations in a variety of sources (see van Dishoeck & Black 1991 and Langer & Penzias 1993 for detailed theoretical treatment and observations). Unfortunately, detailed theoretical considerations for CN are not available and it is not known whether CN is dissociated by continuum or line absorption, as it is the case for CO.

While in the well shielded cores of dark dense clouds essentially all of the gaseous carbon is believed to be in CO, and the isotopomers then reflect the true carbon isotope abundance, UV rich environments provide the conditions to significantly alter the isotopomeric abundances:

- Self-shielding of the main isotopomers against dissociation by absorption of radiation in discrete lines or bands (as is the case for CO) in conjunction with isotopic frequency shifts result in the preferential destruction of the less self-shielding (i.e. rarer) species.
- Exchange reactions incorporating ionized carbon isotopes lead to a chemical enhancement of the rarer species.

The isotopic exchange reaction for CN is very similar to that for CO (Kaiser et al. 1991)

$$^{13}\mathrm{C}^+ + ^{12}\mathrm{CN} \quad \rightleftharpoons \quad ^{13}\mathrm{CN} + ^{12}\mathrm{C}^+ + \Delta\mathrm{E} \tag{7.1}$$

with the ground state energy difference $\Delta\mathrm{E} = 34$ K. The reverse reaction is reduced by the factor $\exp(-\Delta\mathrm{E}/(k\mathrm{T}))$ and the more massive isotopomer is the energetically preferred state. Thus fractionation in favor of ^{13}CN may occur, provided C^+ is available and temperatures are low enough to drive the reaction.

In particular, the competing effects of self-shielding and chemical fractionation can affect the abundances at the edges of clouds and near embedded sources or, if a significant degree of clumpiness is present, throughout an even larger part of the cloud in favor of either the main or the rarer species depending on physical conditions. Moreover, the variability of CO abundances

can impact the isotopic abundances of other carbon molecules since isotopic enhancement of one CO species (e.g. ^{12}CO) results in the reverse enhancement of the exchange ion (e.g. $^{13}C^{+}$).

Observations of ^{13}CN at radio wavelengths have been reported first by Bogey et al. (1984) from the laboratory and by Gerin et al. (1984) from three Galactic sources including OMC-1. Since CN emission in a variety of sources proved to be extended and relatively strong, a large scale survey in the two lowest rotational transitions of the rarer ^{13}CN isotopomer, in order to study possible fractionation effects for CN, constituted a promising project. High spectral resolution scans of the two observed rotational transitions from long time integrations in the frame of this study are shown in Fig. 7.25.

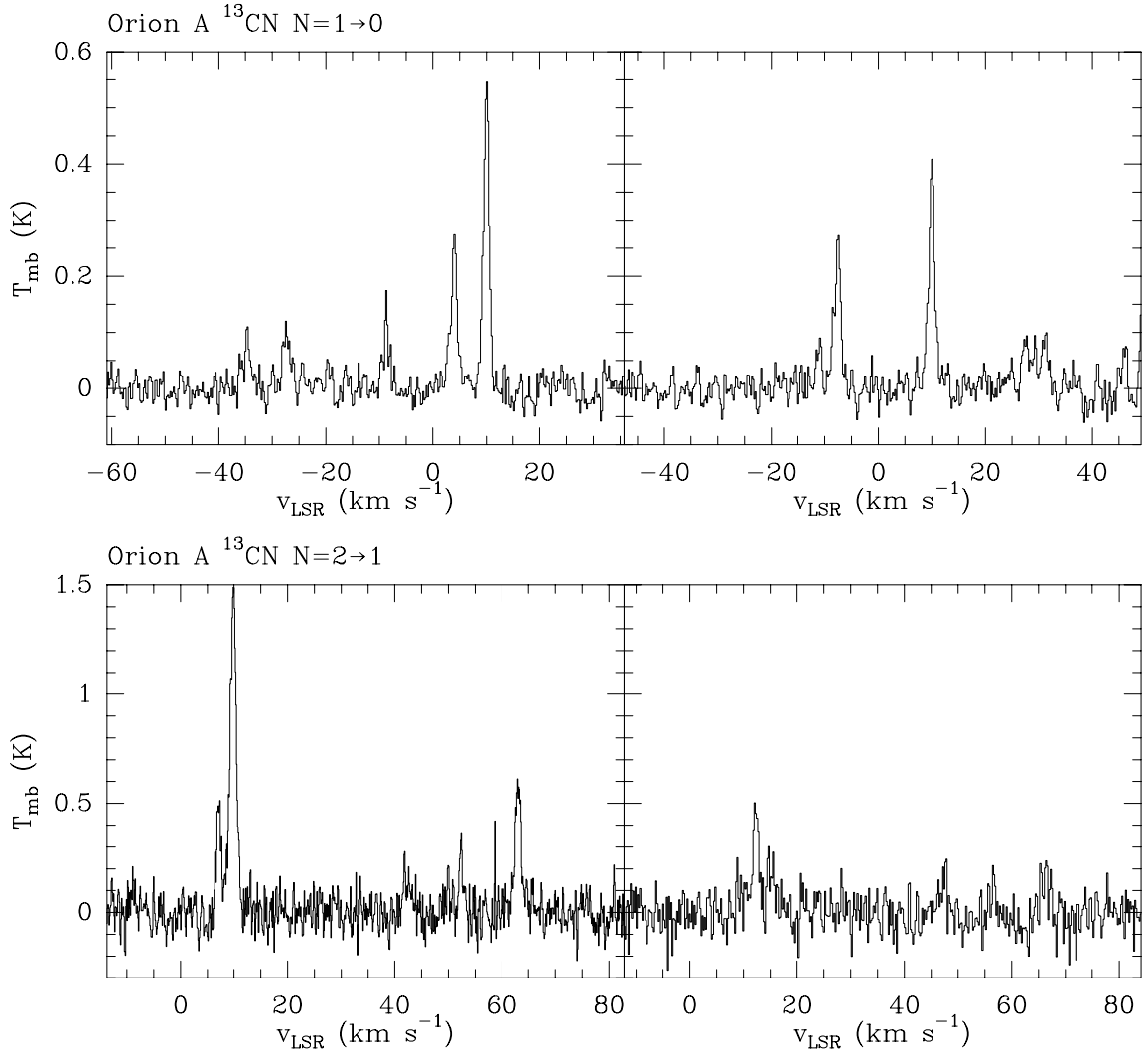

Fig. *7.25:* ^{13}*CN N=1→0 and N=2→1 observations obtained during a long time single position integration at the IRAM 30m telescope in the northern part of OMC-1 at offset* $(24'', 72'')$*.*

The first ever observed ^{13}CN maps, obtained at the IRAM 30m telescope, are presented in Fig. 7.26 in comparison to emission from the main isotopomer. The intensity of the strongest group of hyperfine lines, centered near 10 km s^{-1} in the spectra, has been integrated to derive these maps. The spectra, in particular those with high signal to noise and those from the vicinity of BN-KL, have been carefully checked for emission of other species. There is an unidentified

weak line at ~ 30 km s^{-1} in the strongest fine structure group of ^{13}CN N=1→0, which shows up only in the region around BN-KL, but no other contaminations above the noise level are obvious. The individual spectra of the maps have a lower signal to noise ratio than the spectra shown in Fig. 7.25. Note that ^{13}CN N=3→2 is not observable with ground based telescopes since the frequencies of the hyperfine lines are almost identical with that of the strong water line at 325.153 GHz.

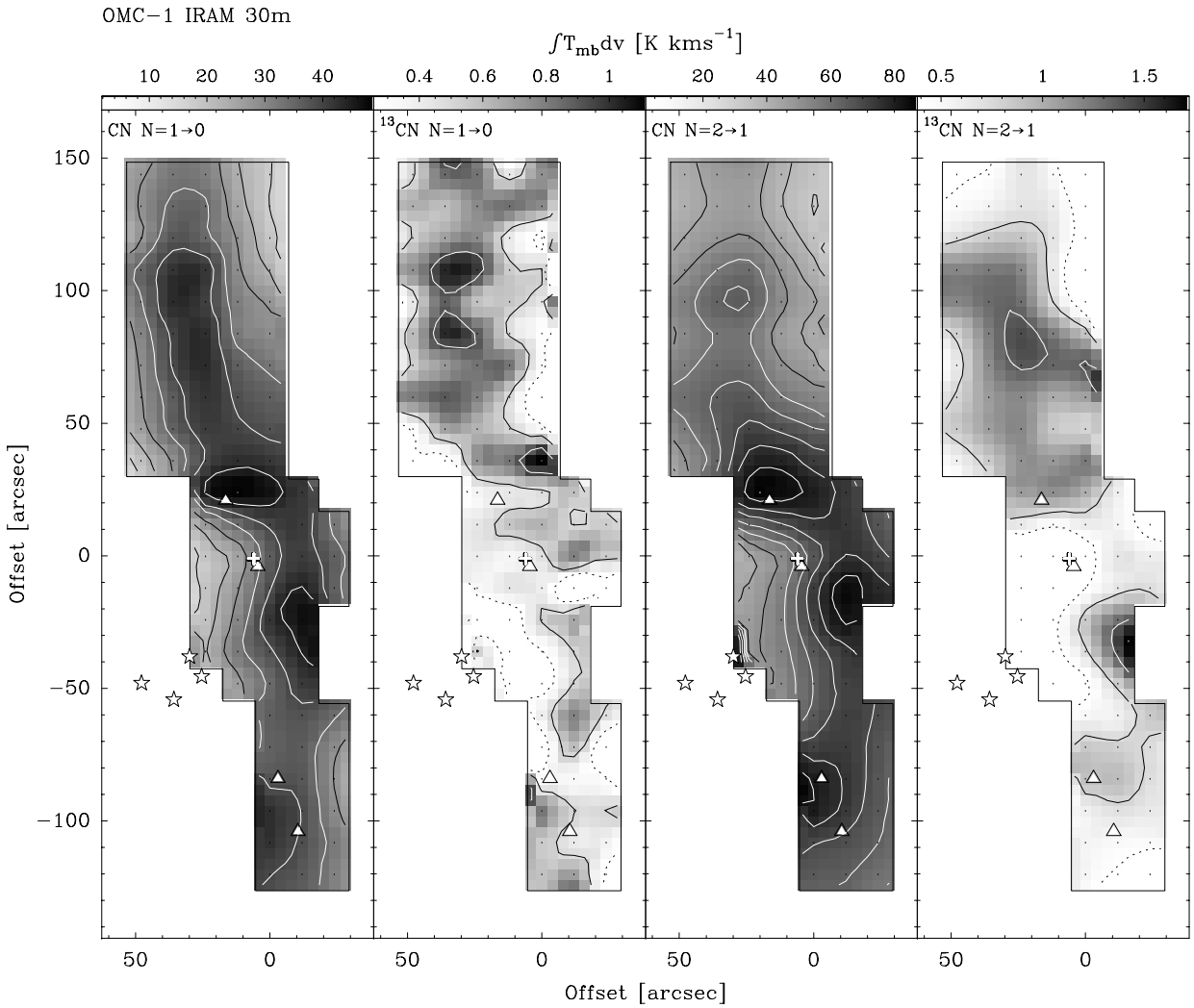

Fig. *7.26: A comparison of CN and ^{13}CN N=1→0 and N=2→1 emission in OMC-1. The 3σ level is indicated by the dashed contours.*

Although much weaker, the ^{13}CN emission traces the same basic morphology as CN, including the lack of emission toward IRc2. In order to enhance the signal to noise ratio of the faint ^{13}CN observations, spectra along the north-south axis of the ridge were smoothed to a strip of $24''$spacing. For these positions, upper state column densities from the integrated line intensities of ^{13}CN in the optically thin case (this is well justified for this rare isotopomer) and opacity corrected CN column densities were used to derive the isotopomeric ratios along the strip. The results including 1σ deviations are shown in Table 7.3. Only at one position the combined noise level of the N=2→1 observations permits the determination of the ratio for this transition.

Declination offset	$[^{12}CN]/[^{13}CN]$ (1σ) N=1→0	$[^{12}CN]/[^{13}CN]$ (1σ) N=2→1
108″	37(5)	
72″	36(3)	70(40)
36″	40(4)	
0″	43(7)	
–36″	65(18)	
–72″	62(18)	
–108″	41(8)	

Table *7.3: CN column density ratios along the north-south axis of the extended ridge.*

Previous determinations of the carbon isotopic ratio in the Orion A region range between roughly 25 and 80. Langer & Penzias (1990) derive a value of 67 ± 3 in the northern part of the ridge (at offset (30″,150″) from BN-KL) and 79 ± 7 toward BN-KL from their observations of CO isotopomers. The high ratio for CO and the low ratio for CN toward IRc2 indicates that the main CO isotopomer is enhanced due to self-shielding effects and in turn, as discussed above, the rare ^{13}CN species is enhanced due to chemical fractionation in the colder but still UV influenced region in the northern part of the molecular cloud. This in fact means that the gas must be clumpy in order to allow the UV photons to penetrate deep into the cloud. The high abundance of carbon ions over the whole region is obvious from the extended C^+ emission observed by Herrmann et al. (1997). The higher ratio of CN to ^{13}CN in the southern part of the ridge may be explained by a higher gas temperature which suppresses the fractionation reaction.

7.7 Conclusions

Emission of the CN radical basically follows the well known north-south oriented Orion extended ridge but is reduced in the hot and dense core around IRc2 due to chemical depletion. With this exception, CN emission correlates well with the mm dust continuum emission from the warm and dense condensations in the ridge. Enhanced emission of CN N=2→1 and N=3→2 is found north and south of IRc2 where the peaks in total column densities are located. Enhanced CN N=1→0 emission from the northern quiescent ridge is explained by the low excitation temperatures in this region. The CN N=2→1 and N=3→2 transitions are likely to be subthermally excited toward the warmer condensations in spite of the high optical depths found in this part of the cloud since the densities are below the critical densities. The CN abundances derived are slightly lower than the value previously reported by Blake et al. (1987) toward IRc2, due to the lower excitation temperatures. Adopting H_2 column densities derived by Schilke et al. (1992), significant variation in the CN abundance along the axis of the ridge with a minimum toward BN-KL and increasing values to the north is observed. Large scale ^{13}CN observations reveal that chemical fractionation in the region north of IRc2 enhances the ^{13}CN abundance. This finding strongly suggests the influence of UV photons on the chemistry on very large scales and supports a clumpy and filamentary scenario for the molecular clouds.

7.8 Chemical stratification in the Orion Bar region: CN and CS submillimeter observations

In this section, we present fully sampled spectral line maps of the Orion Bar region observed simultaneously in the CN N=3→2 and CS J=7→6 rotational transitions with the JCMT at an angular resolution of $14''$. We find that the CN emission specifically traces an intermediate cloud layer located between the peaks of vibrationally excited H_2 and HCO^+ emission located closer to the ionization front, and CS emission originating closer to the cloud core. By comparing the observed spatial displacement of CN and CS emission with PDR models we infer a density of $\sim 2\times10^5$cm^{-3} for these cloud layers. This value is in agreement with the results of an escape probability radiative transfer analysis of our CN and CS line observations. We conclude that the observed distribution of H_2/CN/CS is consistent with chemical stratification in an edge-on PDR in which high density gas ($\sim 2\times10^5$cm^{-3}) is distributed homogeneously.

7.8.1 Introduction

Photon-dominated regions (PDRs) are found in a variety of Galactic and extragalactic sources with significant variation in the incident far ultraviolet (FUV) flux and the gas density. They show bright emission in their most important UV excited and cooling lines (in sequence according to the distance from the edge of the molecular cloud), namely fluorescent vibrational molecular hydrogen (H_2^*) lines, the atomic fine structure transitions of [CII] at 158μm and [OI] at 63μm, and in mm/submm emission lines of [CI], CO and other molecular species.

The Orion Bar region is widely considered as a prototype of an edge-on PDR associated with a dense molecular cloud. It is exposed to a high flux of FUV photons from the Trapezium cluster, a group of young OB stars, which is located at a projected distance of 0.25 pc from the ionization front (IF), outlined by radio continuum emission (Yusef-Zadeh 1990) ($\chi\sim 4\times10^4$ in units of the standard interstellar radiation field (Draine 1978) at the edge of the IF (see e.g. Tielens & Hollenbach 1985b and van der Werf et al. 1995 (vdW96)).

Recent model calculations (Sternberg & Dalgarno 1995 (SD95), Jansen et al. 1996) predict that homogeneous (i.e. constant density) PDRs consist of several distinct chemical zones each governed by specific sets of chemical reactions and decreasing photodissociation and photoionization rates. For example, in the model presented by SD95, HCO^+ and CN molecules are abundant in zones closer to the PDR surface where the UV radiation field is only partly attenuated, whereas CS and HCN become abundant at larger (and more shielded) cloud depths closer to the cloud core.

Due to its proximity ($\sim$460 pc), the Orion Bar is a unique region to study the morphology and chemical composition of a dense PDR and to resolve a possible stratified emission distribution. Consequently, many interstellar species and transitions have been observed at a great variety of frequencies towards this source (see e.g. Tauber et al. 1994, 1995, Störzer et al. 1995, vdW96, Hogerheijde et al. 1995, White & Sandell 1995, and references therein). Many efforts have been made to derive a consistent interpretation of the observations using theoretical models which consider either homogeneous gas distributions or a combined clump-interclump morphology

(e.g. Tielens & Hollenbach 1985a, Köster et al. 1994, Sternberg & Dalgarno 1989, 1995, Hogerheijde et al. 1995, Tauber et al. 1994, 1995, vdW96). In the latter case, the attenuation of the FUV radiation is provided by the interclump material (with a density of typically 5×10^4 cm^{-3}) and emission from high density tracers arises from small embedded high density ($> 10^6$ cm^{-3}) clumps. Hogerheijde et al. (1995) attribute the observed molecular column density enhancement towards the Bar to a change from face-on to edge-on and back to face-on geometry.

The CN radical with its dipole moment of 1.45 Debye (comparable to 1.96 Debye for CS) serves as a probe for high density molecular material. Assuming CS collisional rate coefficients (Green & Chapman 1978) to be appropriate for CN, the critical density of the N=3→2 transition is $\sim9\times10^6$ cm^{-3} ($\sim3\times10^7$ cm^{-3} for CS J=7→6). The rotational transitions of CN exhibit simultaneously observable fine and hyperfine structure (hfs) which allows direct determination of the optical depth from the relative line intensities. Column densities in the energy levels connected to the observed transitions are thus determined without assuming isotopic abundances and without possible ambiguities due to high optical depth.

In this section we present maps of the CN and CS integrated intensities and discuss their spatial distribution perpendicular to the IF. We use the observed spatial displacement of the CN and CS emission maxima together with PDR models and assume an edge-on geometry to infer the density of the emitting gas. Molecular abundances from the model in conjunction with results of a (single-component) escape-probability analysis are used to derive the line-of-sight thickness of the edge-on PDR.

7.8.2 Observations

The CN and CS submillimeter observations were obtained at the James Clerk Maxwell Telescope (JCMT) on Mauna Kea, Hawaii, during one shift in February 1995. The hfs pattern of CN N=3→2 (340247.90 MHz for the strongest hfs component) was observed simultaneously with the CS J=7→6 transition (342882.95 MHz) from the other sideband, using the B3i SIS receiver. This procedure guarantees identical pointing between the two line maps. Fig. 7.27 shows a spectrum recorded in the region of peak CN intensity. Typical system noise temperatures were 720 K, including an average atmospheric zenith opacity of 0.1. The angular resolution of the telescope at 340 GHz is $14''$. Spectra at the individual map positions were obtained in an 'on the fly' fast mapping technique, scanning the source in Right Ascension at constant Declination. The resulting grid spacing was $6''$ and the integration time on each source position 10s, resulting in an r.m.s. noise temperature of 0.9 K in a 0.28 km s^{-1} velocity bin. Pointing was checked regularly and found to be better than $2''$.

The spectra were calibrated for atmospheric attenuation with a standard chopper wheel method. We used the 500 MHz wide standard configuration of the autocorrelator, providing a channel spacing of 313 kHz. A sideband ratio of unity was assumed. The line intensities are given on a $\mathrm{T_{mb}}$ scale (using a value of $\eta_{mb} = 0.68$ at 340 GHz, as determined from observations of Jupiter and Mars).

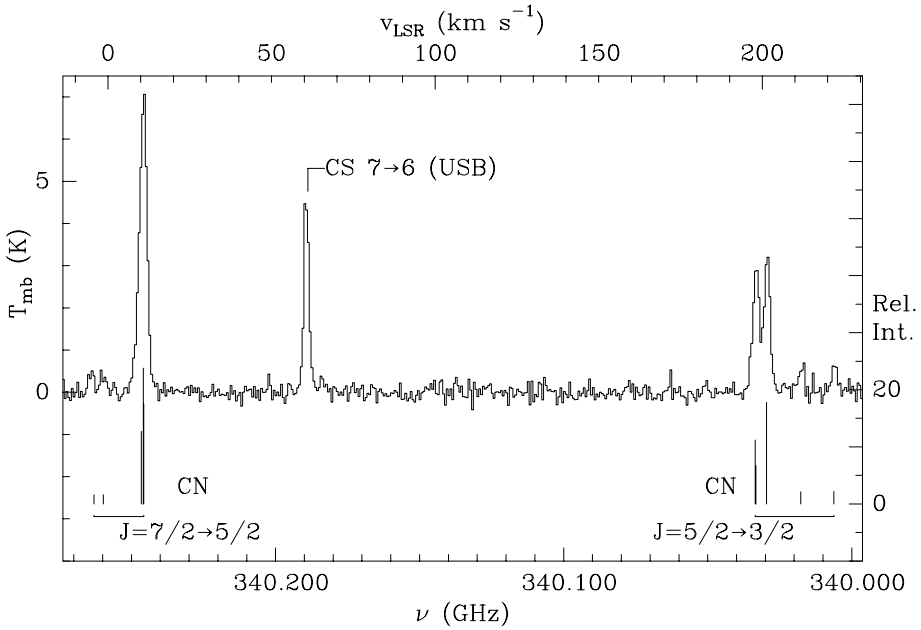

Fig. *7.27: CN N=3→2 with the fine and hyperfine structure resolved, and CS J=7→6 in the region of peak CN intensity. The vertical bars denote the positions and low opacity intensities of the CN hfs lines.*

7.8.3 Chemical Stratification

Fig. 7.28 shows the observed CN and CS intensity distribution towards the Orion Bar integrated over the relevant velocity range 9.5 to 12.5 km s^{-1}and a comparison of CN N=3→2 to H_2^* 2.12μm S(1) v=1→0 (vdW96) emission. The H_2^* emitting region, which marks the transition zone from atomic to molecular hydrogen, lies closest to the exciting stars, the Trapezium, located in the north-west. CS emission is produced in two prominent clumps at the north-east and south-west boundaries of the Bar (vdW96), and in a dense ridge between the clumps. However, the CN emission originates closer to the IF, and is more prominent near the UV illuminated edges of the clumps and ridge seen in CS emission. The observations thus reveal a stratified distribution of molecular emission along the direction towards the star cluster.

The CN emission in the ridge is much more pronounced than in the adjacent clumps, probably indicating the significant influence of FUV radiation at this location as opposed to the clumps at the boundaries of the Bar. Fig. 7.29a displays the intensity profile perpendicular to the IF, derived by averaging data from the boxed region shown in Fig. 7.28. From this cut we infer the intensity peaks of CN and CS to be located at distances of 0.045 and 0.067 pc ($20''$ and $30''$) respectively from the IF, whereas enhanced emission from H_2^*, HCO^+ and CO^+, as derived from similar cuts in vdW96 and Störzer et al. (1995), occurs at 0.033 pc ($\sim 15''$). The distribution of the optical depth of the CN N=3→2 transition along the cut, as derived from the hfs line intensities, is shown as a third curve in Fig. 7.29a. It closely follows the CN intensity distribution and shows that the CN intensity maximum coincides with the location of peak CN column density.

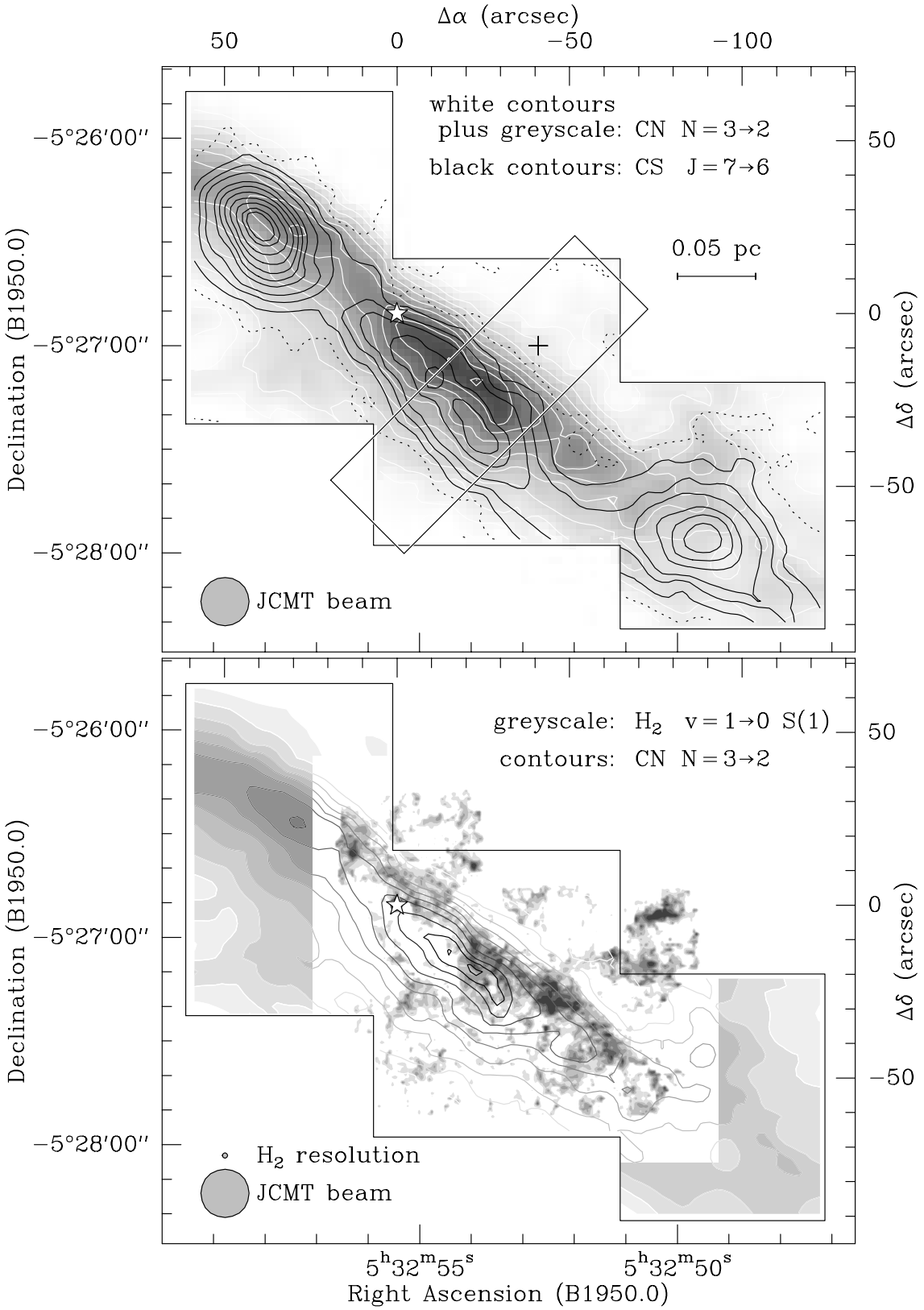

Fig. *7.28: CN N=3→2, CS J=7→6 (mapped area outlined by a polygon) and H_2^* v=1→0 S(1) (vdW96) emission towards the Orion Bar. Offsets are relative to θ^2A Ori ($\alpha = 5^h32^m55^s.4$, $\delta = -5°26'50''.7$). CN and CS intensities are integrated over 9.5 to 12.5 km s^{-1}, relevant for emission from the Orion Bar. Contours range from 2.4 K km s^{-1} (3σ, dashed) to 24.3 K km s^{-1} and 28.1 K km s^{-1} for CN and CS respectively in steps of 3σ. Greyscales in the H_2^* image range from 0.25 to 3.5×10^{-4} erg s^{-1} cm^{-2} sr^{-1}. The boxed area indicates the region where spectra have been averaged to create the cut presented in Fig. 7.29 with the cross at the position of the IF.*

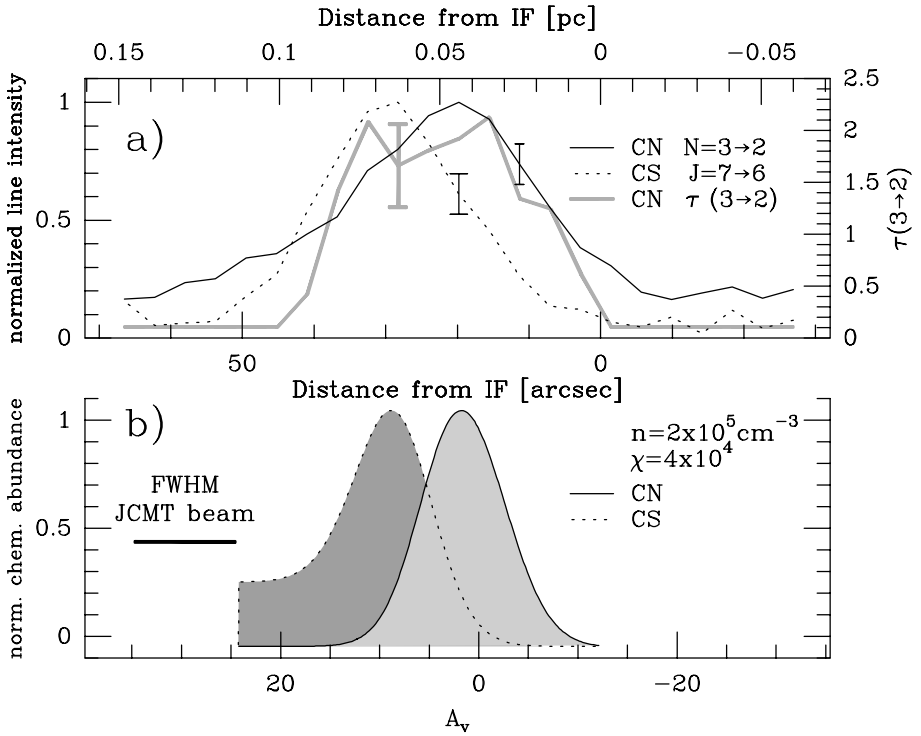

Fig. *7.29: a) CN N=3→2 and CS J=7→6 emission profile and CN N=3→2 optical depth (right axis) along the cut marked in Fig. 7.28. Typical* 1σ *error bars are indicated.*
b) Normalized abundances from the modified SD95 model with the given parameters and convolved with the JCMT $14''$ *beam.*

The observed CN and CS transitions have similar critical densities but, due to the higher energy above ground level of the CS J=7 rotational level (66 K compared to 33 K for the N=3 level of CN), CS J=7→6 should trace a warmer part of the cloud, i.e. *closer* to the IF than CN N=3→2, contrary to what is observed. This suggests that the positionally displaced CN and CS emission peaks reflect actual abundance variations of chemical origin. Indeed, in the SD95 model the CN abundance is largest near the inner edge of the CII zone at a cloud depth corresponding to a visual extinction A_v=2 (where the CS abundance is very small) and the CS abundance is largest at the inner edge of the SI zone at A_v=8.

For the model calculations presented below, we employed the SD95 model. We adopted gas-phase oxygen and carbon abundances of 6×10^{-4} and 3×10^{-4} respectively, and a sulfur abundance of 2×10^{-7} appropriate for the Orion Bar region (Jansen et al. 1996). We used the UMIST chemical rate-coefficients listed by Millar et al. (1997) and the photo rates listed by SD95. We then calculated PDR models for a range in hydrogen density and the intensity of the FUV radiation field. The results show that for a fixed χ the separation between the CN and CS peaks remains fixed and close to $\Delta\mathrm{A}_v$=6 for hydrogen gas densities between 10^4 and 10^7 cm^{-3}. Similar behavior is apparent in the chemical model results for the Orion Bar presented by Jansen et al. (1996). Varying the FUV intensity (at fixed density) shifts the locations of the CN and CS density peaks relative to the cloud surface, but the separation between them again remains close to $\Delta\mathrm{A}_v$=6. In the following, we adopt a value of $\chi = 4\times10^4$ at the edge of the IF. Using the canonical value of $\langle \mathrm{N(H)} + 2\mathrm{N(H_2)} \rangle = 1.9\times10^{21}$ cm^{-2} per magnitude of visual extinction

(Bohlin et al., 1978) and a distance of 460 pc, the calculated shift between the peaks is translated to a linear scale in the cloud and, together with the observed displacement, constrains the density of a homogeneous edge-on PDR to 1–4$\times 10^5$cm^{-3}.

The absolute chemical abundances resulting from the models have to be treated with caution since the use of different chemical and photo rates may, for certain species like CN, result in differences as large as an order of magnitude. However, the quantities from the modified SD95 model presented here agree with the values reported by Jansen et al. (1996) to within a factor of 4 for CN and 2 for CS. The model abundances of CN and CS (normalized to their peak values) calculated for χ=4×10^4 and $n_{\rm H_2}$=2×10^5cm^{-3} and convolved with the 14″ JCMT beam are shown in Fig. 7.29b. The extent of the lower excitation CN emission beyond the boundaries of the Bar, as seen in the cut, might be attributed to emission from the back surface of the cavity walls seen face-on, and supports the global geometrical picture of the PDR changing from face-on to edge-on and back to face-on, as proposed by Hogerheijde et al. (1995).

The arguments up to here are based on the relative displacement between the CN and CS emission peaks only. Shifting the chemical model results in position to coincide with the observed peaks, we see that, provided the absolute pointing in our observations is accurate, the location of the IF does not coincide with the zero point of the $\rm A_v$ scale in the chemical model (Fig. 7.29). This suggests that the FUV attenuation within the first $\sim 2\rm A_v$ of the cloud may be provided by lower density material, where an average PDR model density of $\sim 3\times 10^4$cm^{-3} is appropriate to account for the offset between the distance and the $\rm A_v$ scale. vdW96 analyzed CS line ratios and confirmed with a completely different method that there is a density enhancement at the CS layer. The densities agree very well with the values we derived. A lower density regime is expected at the interface, since the density should increase gradually from the cavity around the Trapezium, devoid of molecules, to the molecular cloud. Emission of specific high density tracers in this region is interpreted to originate from high density clumps with low volume filling factors embedded in the lower density material providing the UV attenuation. Such a picture is readily supported by the high degree of fragmentation in the $\rm H_2^*$ image between the IF and the CN emission peak.

7.8.4 Excitation Analysis

We used a single component escape probability code (Stutzki & Winnewisser 1985) together with our CN N=3→2 and CS J=7→6 data, the CN N=1→0, N=2→1 and CS J=5→4 observations reported by Fuente et al. (1996) and vdW96, as well as the CN optical depths from the hyperfine fits, to determine the hydrogen gas density and CN and CS column density in the emitting region. For the unknown CN collisional rate coefficients we adopted the CS rates from Green & Chapman (1978). We considered kinetic temperatures of 40–100 K to be appropriate for the Bar material. From the intensity ratios of the rotational transitions and the CN optical depths, we infer hydrogen densities of 1–4$\times 10^5$cm^{-3} for the CN and the CS peak. Moreover, the absolute line intensities of CN N=3→2 and CS J=7→6 imply beam filling factors of unity. Values for the CN and CS column density 20″ (and 30″) from the IF are determined to be 1×10^{14} (2×10^{14}) and 5×10^{13} (5×10^{14}) cm^{-2} respectively.

The absolute values of the molecular abundances from the SD95 model, convolved with the

JCMT beam, take values of 6×10^{-10} and 1×10^{-9} for CN and CS respectively at the CN maximum and 2×10^{-10} and 4×10^{-10} at the CS peak. Together with the molecular column densities from the escape probability analysis, this results in molecular hydrogen column densities of $1-2\times10^{23}$ cm^{-2}. At a homogeneous density of 2×10^{5} cm^{-3}, the line of sight thickness of the edge-on PDR is determined to 0.16–0.27 pc (or 70″–120″), which compares well with independent results obtained by Werner et al. (1976, 0.12 pc) and Jansen et al. (1996, 0.6 pc). Assuming a width of the PDR of 0.07 pc (or 30″which corresponds to the width at half maximum in the cut), this results in an aspect ratio of 2–4.

7.8.5 Conclusions

The observed stratified distribution and the enhancement of certain chemical species towards the edge of the Orion Bar can adequately be modelled within the framework of an edge-on PDR with a homogeneous density distribution at 1–4$\times10^{5}$cm^{-3}. Results from an escape probability radiative transfer analysis of various CN and CS lines suggest densities in the same range and beam filling factors of unity, further supporting the homogeneous nature of the edge-on part of the Orion Bar PDR in the derived density regime.

Our observations and modelling give clear evidence for homogeneous high density gas at the edge-on part of the Orion Bar PDR. These results do not exclude the presence of embedded higher density clumps, as suggested by observations of specific high density tracers or CO^{+} (Störzer et al. 1995), but, due to their low volume filling factor, these clumps do not affect the chemistry and the thickness of the PDR.

The derived density is thus substantially higher than that proposed by Hogerheijde et al. (1995), who infer values of 1–4$\times10^{4}$cm^{-3} for the homogeneous gas. Additional extended emission beyond the boundaries of the Bar agrees with their global scenario of a PDR changing from face-on to edge-on and back to face-on.

7.9 Other PDRs in OMC-1

Apart from the Orion Bar, other less prominent PDRs are found in the radio continuum image of Yusef-Zadeh (1990) which either surround the ionizing Trapezium cluster and appear relatively sharp bounded, or are obvious by more diffuse and extended face-on emission from the back surface of the cavity wall over the whole region. Fig. 7.30 shows an overlay of the 20cm continuum with the CN N=3→2 emission. Similar to the case of the Orion Bar discussed in the previous section, CN emission is again found to be enhanced close to an ionization front in the PDR environment north of IRc2. The overlay with CS J=7→6 in the left panel of Fig. 7.31 reveals the well known pronounced peak of CS emission toward IRc2. However, a stratified distribution of CN and CS emission with respect to the ionizing star θ^1C Ori, like it is observed in the Orion Bar, is not evident for this region, either due to the immediate vicinity and strong influence of IRc2 or projection effects.

Observations of [OI] and [CII] fine structure lines in OMC-1/2 (Herrmann et al. 1997) reveal a more prominent PDR at these wavelengths associated with the clump S6, originally found in the ammonia survey by Batrla et al. (1983). Since the emission peaks of the atomic fine structure maps are found to be shifted toward the ionizing star, the emission is interpreted as originating from PDRs at the surface of the condensation. CN N=1→0 and N=2→1 emission from S6 appears to be shifted in the same sense and in a similar manner, as observed in the Orion Bar region for CN N=3→2. This finding is supported by the distribution of the simultaneously observed CS J=3→2 emission shown in the overlay to CN N=2→1 presented in the right panel of Fig. 7.31. CS has its emission maximum at the position FIR4, well separated from the CN peak located close to FIR3. Note that the combination of these transitions has been chosen since there are no CN N=3→2 and CS J=7→6 observations available for this source.

A *Third Bar* (in addition to the extended ridge and the Orion Bar) associated with ionized material and traced by molecular emission lines including CN N=2→1 has recently been reported by Greaves & Church (1992). It is located east of the northern PDR in a region not covered by our observations. This filament connects the northern PDR, as traced by our CN observations, and the north-eastern tip of the Orion Bar in north-west to south-east direction, forming the third side of a triangle enclosing the Trapezium cluster.

Our high angular resolution observations thus reveal that the stratified distribution of certain molecular species, in particular of CN and CS, in PDR regions appears to be a common phenomenon which is predicted and fairly well explained by chemical models.

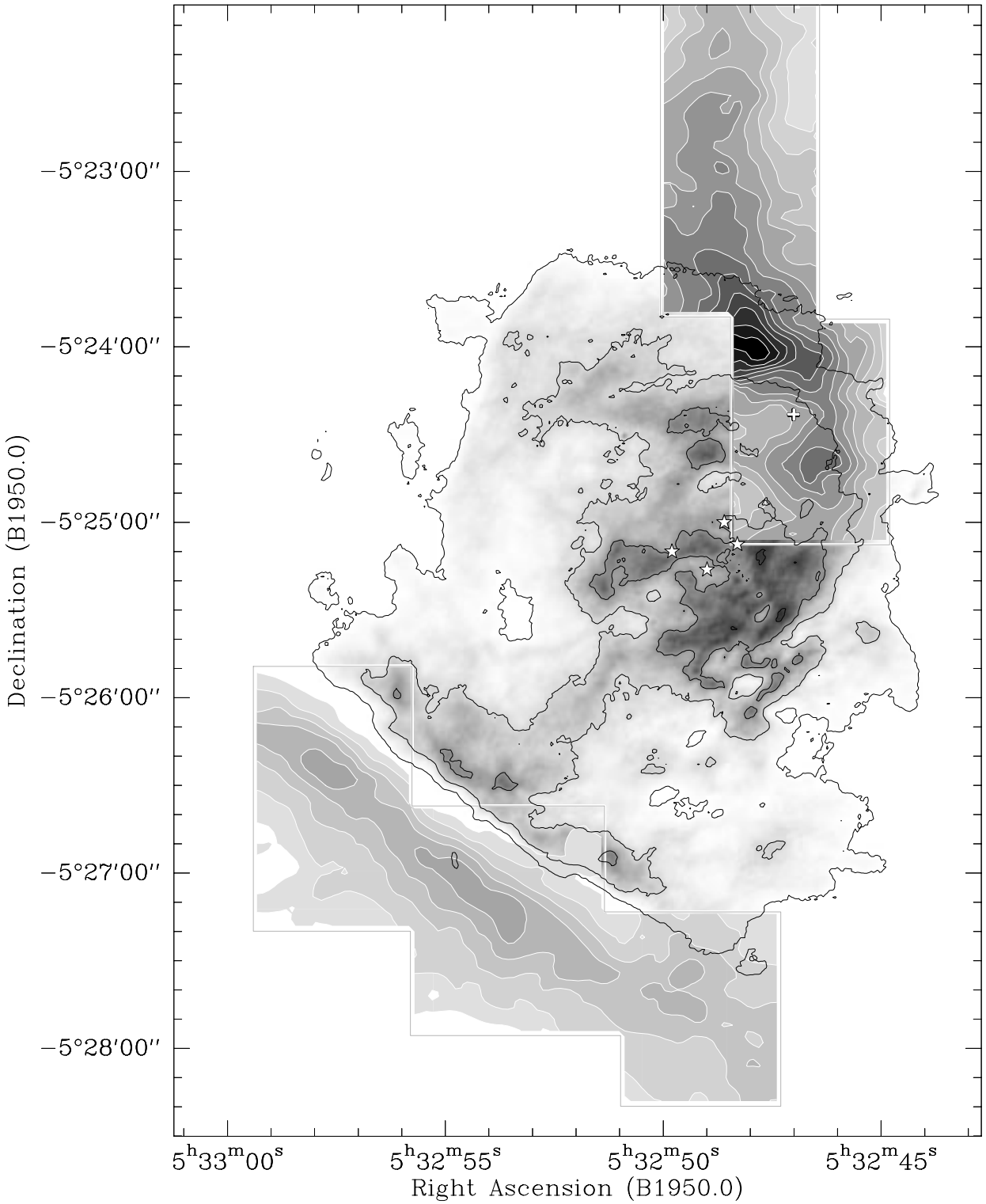

Fig. *7.30: Overlay of 20 cm radio continuum emission (grey scale and black contours, Yusef-Zadeh 1990) and the CN N=3→2 intensity integrated from 8 to 12 km* s^{-1} *(grey scale and white contours) from the Orion Bar and the northern extended ridge.*

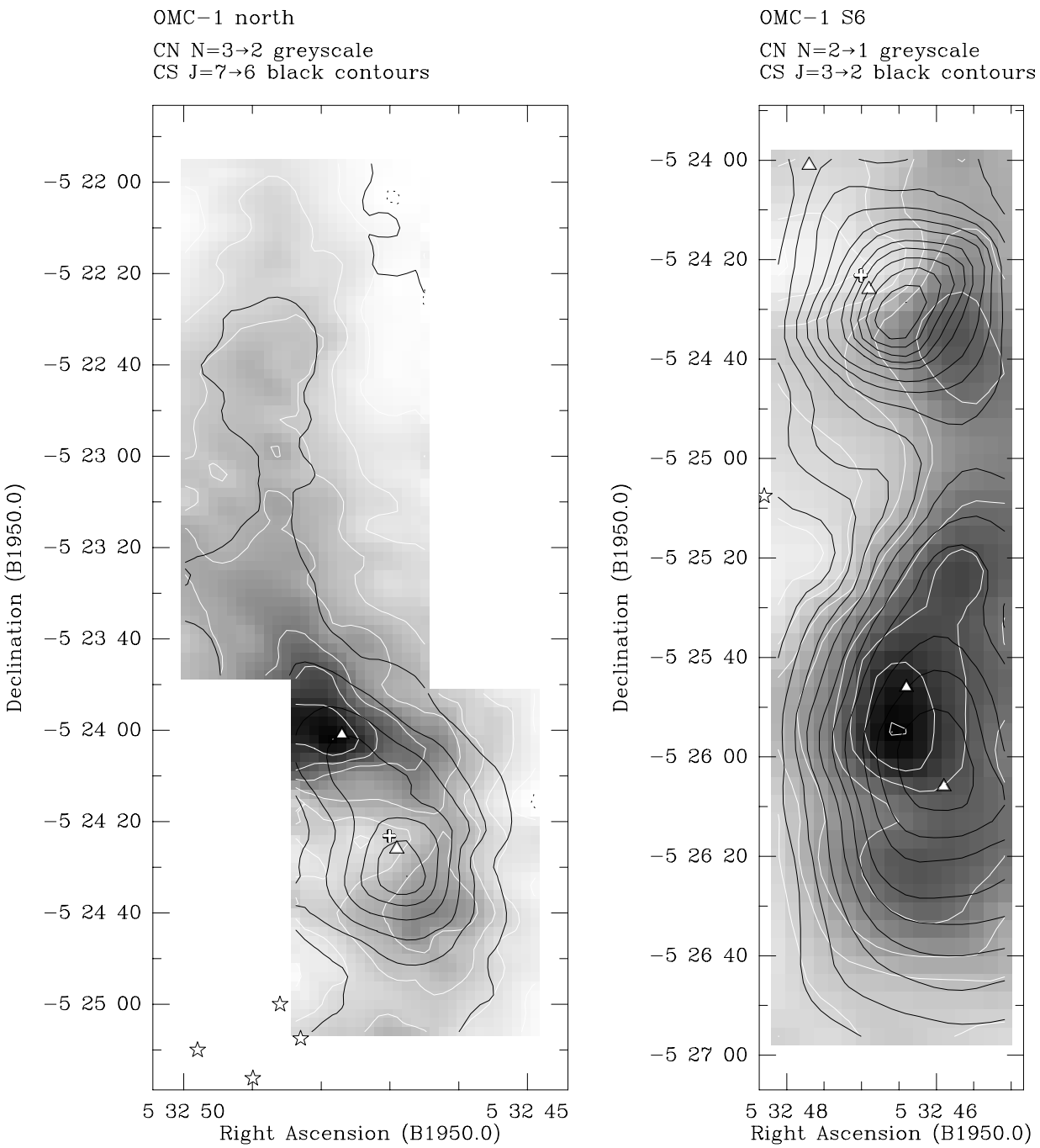

Fig. *7.31:* **Left panel:** *CN N=3→2 intensity integrated from 8 to 12 km s^{-1} (grey scale and white contours, levels are 6.2(6.2)55.8 K km s^{-1}) and the corresponding CS J=7→6 emission (levels 6.2(24.5)152.0 K km s^{-1}) from the the northern extended ridge. Symbols are the same as in previous sections.*
Right panel: *CN N=2→1 intensity integrated from 6 to 8 km s^{-1} (grey scale and white contours, levels are 2.1(4.2)39.9 K km s^{-1}) and the corresponding CS J=3→2 emission (levels 1.5(6.0)85.5 K km s^{-1}) from the southern clump S6.*

Chapter 8. Results for Orion B

8.1 The Orion B clouds

Along with the Orion A clouds discussed in the previous section, the Orion B molecular clouds (another commonly used designation is L1630), associated with the bright HII region NGC 2024, are the most prominent features in the CO and infrared images shown in Fig. 7.1. The distance of the whole large scale complex has been estimated by Anthony-Twarog (1982) to 390 – 415 pc by means of a study of the distances to B stars in the Orion association.

The L1630 cloud was included in several large scale surveys of CO isotopomers in the Orion region (see e.g. Maddalena et al. 1986 and Fig. 7.1, Bally et al. 1987). Lada et al. (1991) performed a large scale survey for dense cloud cores in the CS J=2→1 transition. The distribution of the CS J=2→1 integrated intensity from their observations is shown in Fig. 8.1.

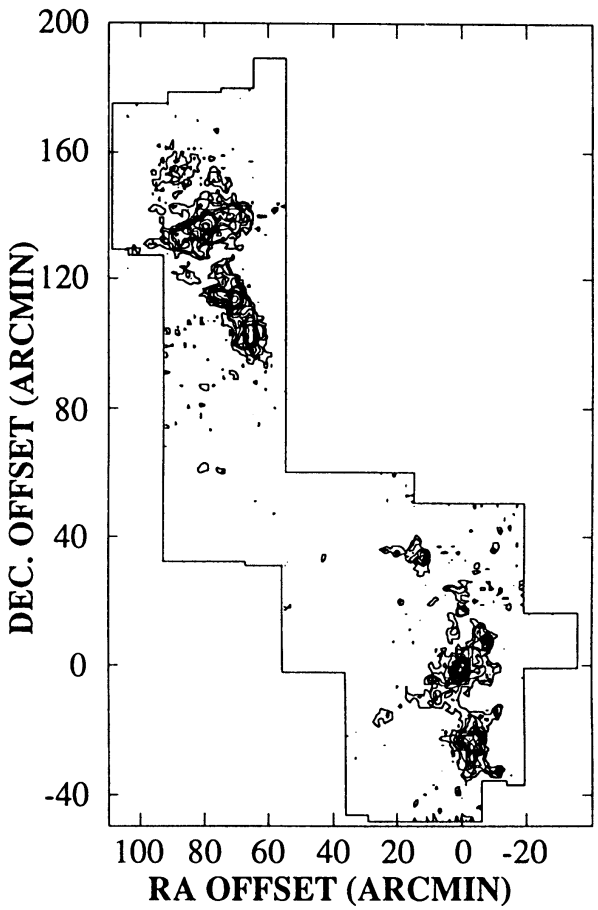

Fig. *8.1: Distribution of the integrated intensity of the CS J=2→1 transition in L1630 from Lada et al. (1991). Offsets are relative to the center of the NGC 2024 HII region (see Fig. 8.2 for an optical image of this region).*

The extended cloud, as seen in the large scale CO surveys, splits into two distinct highly fragmented regions of dense cores. The south-western part of the two clump ensembles constitutes the NGC 2023/2024 complex (see Fig. 8.2 for an optical image). Lada et al. identify 42 dense

clumps and derive a mass of 3000 $M_\odot$ contained within the cores compared to the value of 8×10^4 $M_\odot$ derived for the whole region from CO observations (Maddalena et al. 1986). Since the CS survey only covers $\sim 20\%$ of the region observed in CO, it is estimated that roughly 20% of the molecular material in L1630 is comprised in dense clumps.

A digitized negative of an optical image (taken by David Malin at the UK Schmidt Telescope of the Anglo Australien Observatory) of the south-western part of the L1630 cloud is presented in Fig. 8.2. It shows the prominent HII region NGC 2024 adjacent to the southernmost belt star of the Orion constellation (Alnitak), the reflection nebula NGC 2023 and the famous Horsehead nebula (IC434 or B33). The dense molecular cloud behind the visible HII region and the obscuring dust lane in NGC 2024 constitutes one of the five most massive clumps found in the CS survey of Lada et al. and will be the main topic of the next paragraphs.

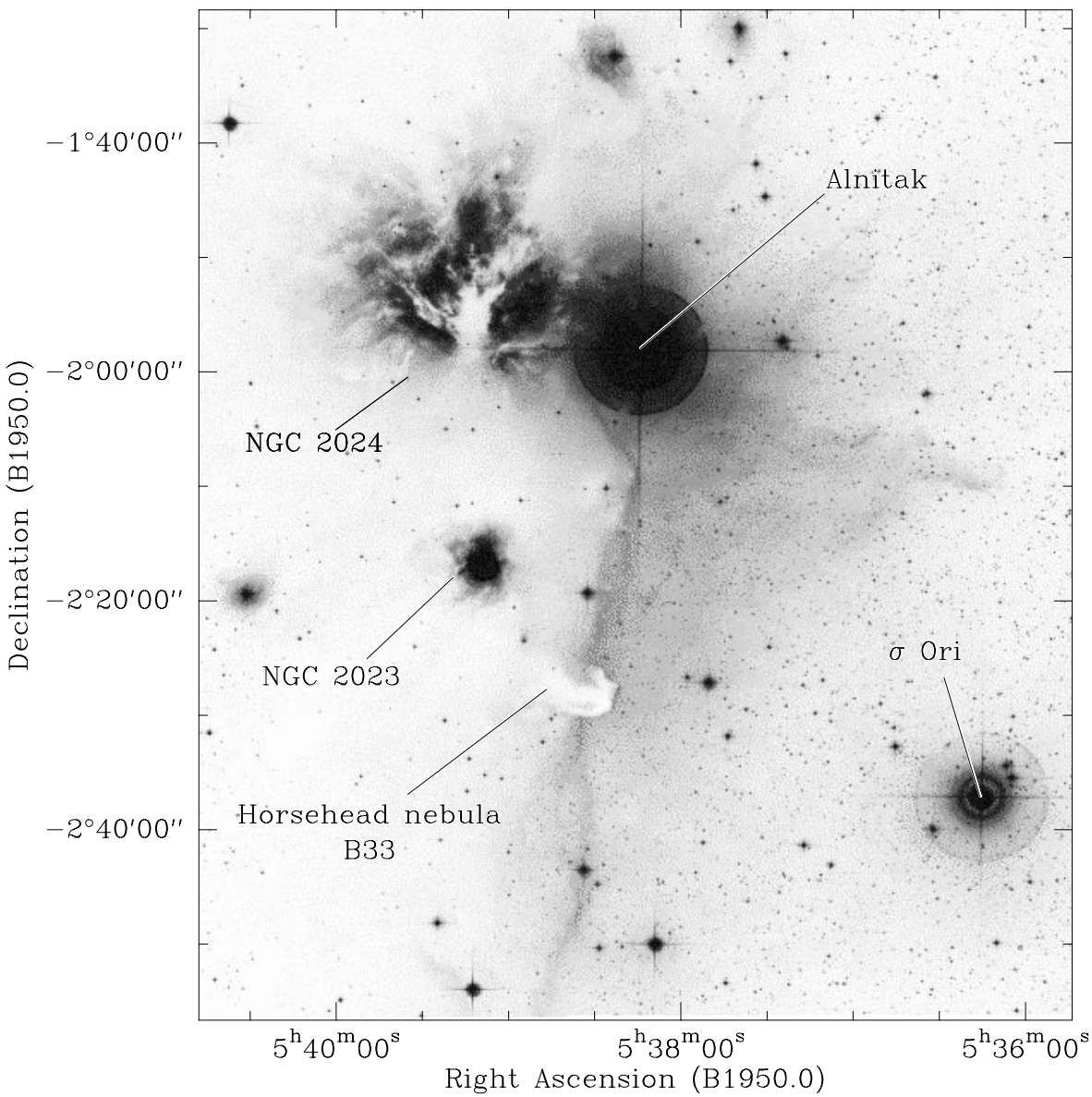

Fig. *8.2: Optical image of the NGC 2023/2024 region. Note the dark dust lane in front of the bright HII region NGC 2024.*

8.2 The NGC 2024 star forming region

In this section we will present single-dish observations of the three lowest rotational transitions of the CN radical and the J=3→2 and J=7→6 transitions of CS toward NGC 2024. These data are complemented by high angular resolution ($\sim 4''$) interferometer observations of CN N=1→0 and 2.7mm continuum emission toward two selected cores.

8.2.1 Introduction

The NGC 2024 HII region/molecular cloud complex, located at a distance of 415 pc (Anthony-Twarog 1982), has become one of the best studied star forming regions in our Galaxy. Continuum and line observations at various wavelengths and successively increasing angular resolution contributed to the development of a consistent, detailed model for the region.

The prominent obscuring dust lane, which is oriented almost in north-south direction in front of the optically visible nebula, is associated with a molecular cloud of moderate density (8×10^4 cm^{-3}). This conclusion is based on observations of H_2CO and OH absorption lines against the background HII region (Crutcher et al. 1986, Barnes et al. 1989), as well as on optically thin molecular line emission (e.g. low-J $C^{18}O$ transitions observed by Richer et al. 1989, Graf et al. 1993) which all appear at the same LSR velocities around ~ 9.5 km s^{-1}.

Behind the dust lane, radio continuum observations reveal two emission maxima (the northern and southern continuum peak, NCP and SCP) of ionized hot gas in the HII region embedded in an east-west oriented extended continuum (e.g. Crutcher et al. 1986 (see Fig.8.3 for an overlay with the submm dust continuum which is introduced later), Barnes et al. 1989, and Gaume et al. 1992). Due to the high extinction in the foreground dust lane ($A_v \sim 30^m$, Crutcher et al.

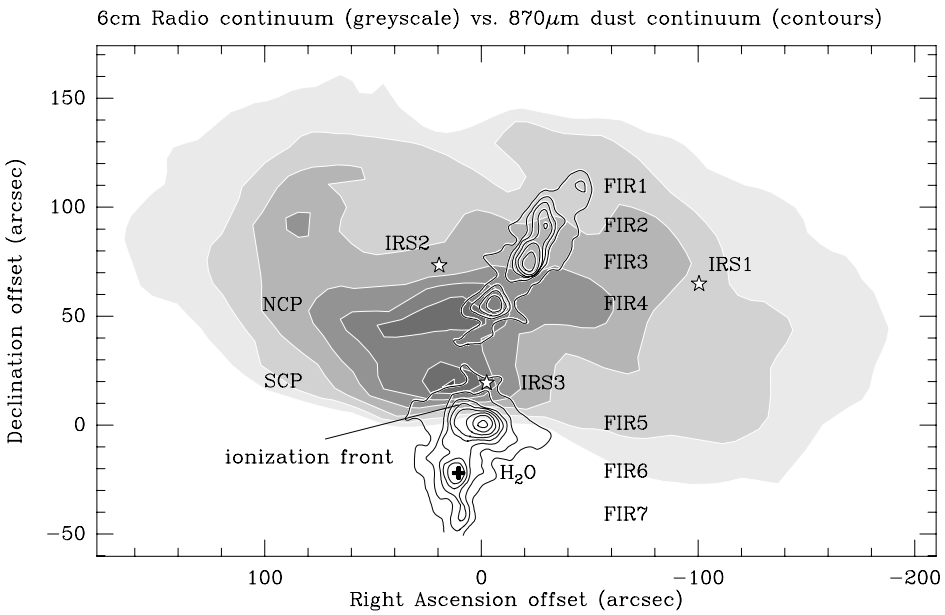

Fig. *8.3: 6cm radio continuum (Crutcher et al. 1986, 12″ resolution) and 870μm dust continuum (Mezger et al. 1992, 8″ resolution). This image is intended to serve as finding chart for objects addressed in the text. Offsets are relative to the strongest dust continuum peak FIR5.*

1986), the ionizing source has not yet been identified unambiguously. Thorough inspection of the numerous NIR point sources (Barnes et al. 1989) associated with the region of strongest radio continuum emission showed that each one of them alone could not account for the photon flux required to ionize the region. Considering the large number of near infrared sources, evident in the infrared image displayed in the lower panel of Fig. 8.4, it is thus concluded that the region is ionized by an ensemble of members of the embedded stellar cluster.

The bulk of the molecular material and the colder dust, as traced by molecular line and (sub)mm continuum emission, is located behind this blister HII region, in a cloud with density $\mathrm{n} > 10^5$ cm^{-3} and an LSR velocity around 11 km s^{-1}. It is thus kinematically distinct, at higher red shifts, from the foreground gas. The expanding ionized bubble of the HII region naturally accounts for the observed velocity structure of the optically thin, low density tracing molecular lines (see e.g. the double peaked C^{18}O lines observed by Richer et al. 1992 and Graf et al. 1993), since foreground gas should be blue shifted and background material red shifted with respect to the center of expansion.

Comprised within the extended molecular cloud is a dense ($\mathrm{n} > 10^6$ cm^{-3}) ridge of gas and dust covering roughly 0.3×0.5 pc^2 which, in contrast to the distribution of hot ionized gas, is oriented in north-south direction, coinciding by chance with the foreground dust lane. The large scale distribution of this dense ridge gas, as traced by the CN N=1$\rightarrow$0 transition obtained at the SEST 15m telescope, is shown in the upper panel of Fig. 8.4 on top of the appropriate part of the Palomar Observatory sky survey.

The NCP is most probably associated with the protrusion of the northern part of this dense molecular ridge into the HII region, while the SCP lies close to the sharp edge of an edge-on ionization front (prominent in the various radio continuum images) at the boundary to the southern part of the dense molecular ridge. Here, the background molecular cloud wraps around the ionized cavity and connects to the lower density foreground cloud. As a consequence, emission lines especially south of the interface are comprised of contributions from a variety of velocity components along the line of sight.

Associated with the dense molecular ridge is the most collimated large scale molecular outflow known which was first reported by Sanders & Willner (1985) in their CO J=1$\rightarrow$0 and J=2$\rightarrow$1 observations. A prominent extended red lobe pointing southward and a fainter, spatially more confined blue lobe to the north, are centered close to the ionization front. Richer et al. (1989), on the basis of their high resolution CO J=2$\rightarrow$1 observations, disputed the bipolar nature of the outflow since they found no signs of blue shifted emission in their spectra. The discovery by Subrahmanyan (1992) of a spectacular radio continuum jet aligned with the molecular outflow, together with the geometrical picture outlined above, might explain the faintness or lack of blue shifted CO: the molecular emission becomes undetectable as the northern lobe breaks through the cavity wall of the HII region towards the observer, now showing up as ionized, less collimated radio continuum jet, while the red lobe propagates southward into the molecular cloud, away from the HII region.

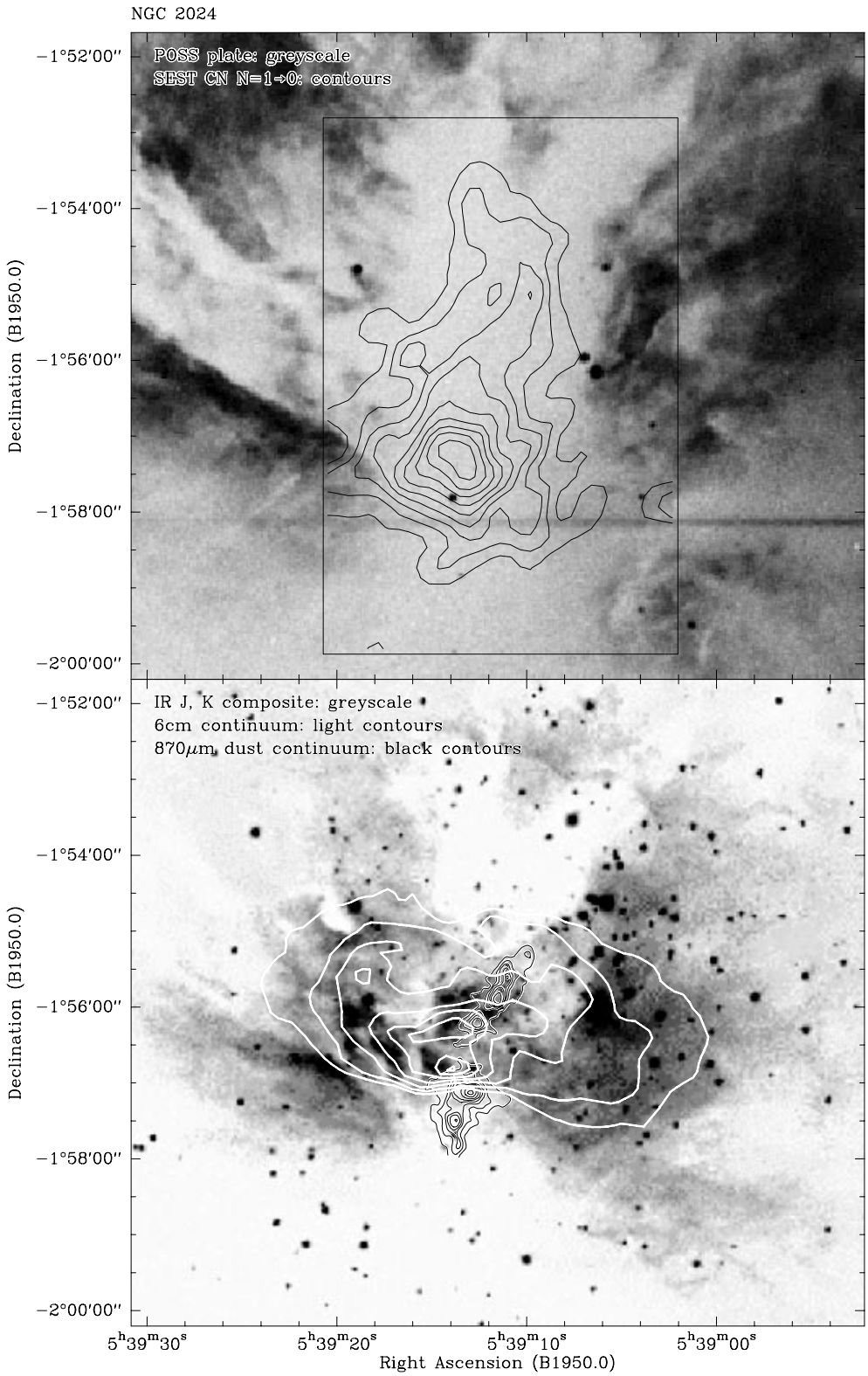

Fig. *8.4:* **Top:** *A fully sampled (48″ beam) CN N=1→0 map obtained at the SEST 15m telescope (contours) with a negative optical image of the NGC 2024 region adopted from the Palomar Digital Sky Survey (DSS). CN emission traces the dense molecular cloud located behind the dust lane and the bright HII region.* **Bottom:** *Negative greyscales of a J, K infrared composite image of NGC 2024 (obtained with the twin-channel UCLA camera on the Lick 3m telescope) with light contours of the 6cm radio continuum (Crutcher et al. 1986) and black contours of the 870μm dust continuum adopted from Mezger et al. (1992, see the text for details).*

Embedded in the dense ridge are seven compact condensations which evince the highest contrast in far infrared continuum maps at 1300 and 870 μm (Mezger et al. 1988, 1992). Their interpretation of the condensations (labeled FIR1 through 7) as being cold and very dense isothermal protostars, with molecules possibly frozen out onto dust grains, marked the beginning of a controversial discussion on the true nature of these objects. Observations of high density tracers such as CS and HCN toward the compact condensations indicate large amounts of dense and warm gas. On the other hand, the densities from the line observations fall short by a factor of 10 or more compared to the values derived by Mezger et al. and the gas temperatures are higher than their proposed dust temperatures. We will return to this discussion in more detail in a later paragraph.

It should be noted that, besides the existence of the young NIR cluster, the region shows a variety of other signs related to recent and ongoing star formation like young, compact outflows and water maser activity.

In order to study in detail the morphological relation of dust and gas in the immediate vicinity of the compact sources, we started a multiline study of the CN radical and simultaneously observable high density tracing CS transitions toward FIR1–7 with the highest possible angular resolution and sensitivity feasible at single-dish telescopes. In addition, we used the Plateau de Bure Interferometer to take advantage of the possibility to simultaneously observe CN molecular line emission and mm dust continuum at very high angular resolution.

8.3 Observations

8.3.1 Single-dish IRAM 30m and JCMT data

The source reference position of the single-dish data is at $(\alpha(1950.0) = 5^h39^m13^s.0$, $\delta(1950.0) = -1^\circ57'08'')$, which corresponds to the position of FIR5 (Mezger et al. (1992). The blank sky position is located at offset $-600''$ in Right Ascension from the center.

The fine and hyperfine structure of the N=1→0 and N=2→1 rotational transitions of CN and the CS and $C^{34}S$ J=3→2 transitions have been mapped using the IRAM 30 m telescope during two observing runs in September 1993 and January 1994.

Spectra were obtained simultaneously using the IRAM 3mm, 2mm and 230 G1 SIS–receivers at center frequencies of 113.340 and 226.775 GHz for CN, 144.617 and 147.072 GHz for CS respectively. Typical system noise temperatures were 500 K, 350 K and 740 K with the 3mm, the 2mm and 230 G1 receivers respectively. Angular resolutions of the telescope are $24''$ and $12''$ for CN N=1→0 and N=2→1, and $18''$ for the CS frequencies. The 1993 maps have been performed in position switching mode on a $12''$ grid and are fully sampled in the N=1→0 transition, while the 1994 observations consist of 5×5 maps centered on the FIR peaks 1 to 6 on a $6''$ grid (i.e. fully sampled in the CN N=2→1 transition). The spectra, which were calibrated using the standard IRAM chopper wheel method, have been recorded with the 500 MHz wide filterbanks and at higher spectral resolutions between 40 and 80 kHz, with parts of the autocorrelator shifted to the appropriate groups of hyperfine lines.

The CN and CS submillimeter observations were obtained at the JCMT in March 1995 in the

same manner as the Orion Bar data. This procedure guarantees accurate relative pointing between the two line maps. Typical system noise temperatures were 1000 K. The angular resolution of the telescope at 340 GHz is 14″. Spectra at the individual map positions were obtained in an 'on the fly' fast mapping technique with a resulting grid spacing of 6″ (fully sampled). We used the 500 MHz wide standard configuration of the autocorrelator, providing a channel spacing of 313 kHz. A sideband ratio of unity was assumed when scaling the line intensities to T_{mb} temperatures. The integration time on each source position of 10s resulted in an r.m.s. noise temperature of 0.9 K in a 0.28 km s^{-1} velocity bin. The spectra were calibrated for atmospheric attenuation with a standard chopper wheel method.

At both telescopes the pointing and alignment was checked regularly and found to be better than 2″ between the individual IRAM receivers and generally accurate to within 5″.

8.3.2 Plateau de Bure Interferometer observations

The interferometric CN N=1→0 and λ = 2.7mm continuum observations have been carried out with the IRAM Plateau de Bure Interferometer (PdBI) in March and April 1994. At that time, the array consisted of four individual 15m antennas. The phase reference center is at (α(1950.0) = $5^h39^m13^s.0$, δ(1950.0) = $-1°57'19''.0$), which is located halfway between the positions of FIR5 and FIR6 (Mezger et al. 1992). We used the so called C and D configuration which resulted in projected uv radii from 17 to 175m. The center tuning frequency was chosen in order to cover the eight strongest CN N=1→0 hyperfine components in the upper sideband and the ^{13}CO J=1→0 transition in the lower sideband. It should be noted that, due to the extended emission of ^{13}CO, the north-south orientation and low Declination of the source, which results in a synthesized *dirty* beam with an orientation parallel to the emission, serious deconvolution problems are to be expected. These restrictions are not that severe for the CN lines since their emission is supposed to be spatially more confined. The dirty beam pattern and the uv-coverage are shown in Fig.8.5.

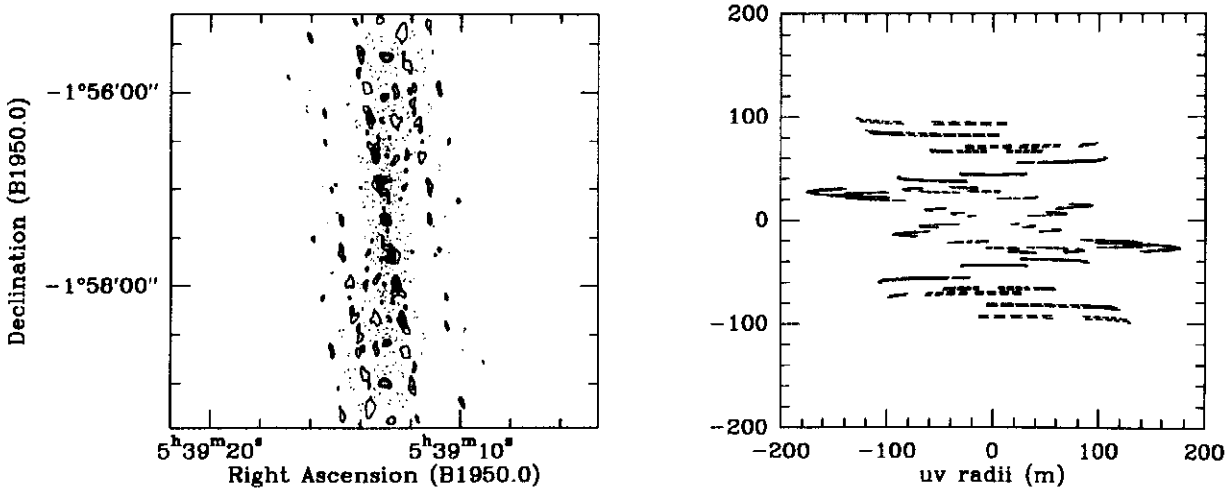

Fig. *8.5: Synthesized dirty beam (left) and uv-coverage for the PdBI observations.*

Typical double sideband receiver temperatures were 60–100 K. Individual parts of the autocorrelator with band widths of 20 MHz were shifted to the CN hfs components and the ^{13}CO line. The

channel separation of 80 kHz corresponds to a velocity resolution of 0.2 km s^{-1} at the observed frequency. An additional 150 MHz wide window was used to record the continuum emission from the observed region in the lower sideband at 111.8 GHz. The visibility data were calibrated using observations of the quasars 0458–020 and 3C84 for passband, phase and amplitude calibration. Zero spacing information obtained from the IRAM 30m observations and the interferometer data were merged to a final visibility set. For this purpose, the single-dish data were weighted according to the inverse square of their rms noise and the resulting visibilities were adjusted to fit the corresponding values of the short interferometer uv spacings. The calibrated visibilities were gridded and Fourier transformed using natural weighting and no uv taper to $256 \times 256 \times 1''$ pixels, sufficient to include the significant side lobes of the resulting dirty beam. Cleaning of the individual spectral channels and the continuum was performed with the Clark algorithm (implemented in the Grenoble GILDAS package) in the inner quarter to the rms noise level of the maps (6 mJy $beam^{-1}$ for continuum and 80 mJy $beam^{-1}$ for the line observations). Due to the low continuum fluxes at $\lambda = 3$ mm, the subtraction of the continuum from the spectral line channels proved to have no influence on the maps. The synthesized clean beam sizes are $4.''7 \times 3.''2$ at position angle (PA) 18° and $4.''9 \times 3.''6$ at PA 16° for the continuum and CN N=1$\rightarrow$0 respectively. A correction was applied to the final maps in order to account for the primary beam attenuation of the interferometer which results in an increasing noise level toward the edge of the maps.

8.4 Morphology and kinematics

The discovery of the seven compact condensations from the mm and submm continuum observations of Mezger et al. (1988, 1992), and the interpretation of them as very cold and dense isothermal protostars, initiated a controversial discussion concerning the true nature of the sources. Mezger et al., on the basis of a fit to the spectral energy distribution of the continuum emission, derive hydrogen densities and column densities of n $\sim 10^8 - 10^9$ cm^{-3} and N $\sim 10^{25}$ cm^{-2} respectively, and dust temperatures of the order of 20 K. In contrast, molecular line observations of various species imply lower densities ($n(H_2) \sim 10^6 - 10^7$ cm^{-3} and $N(H_2)$ of the order of 10^{23} cm^{-2}) and gas temperatures of 30 K or higher. This discrepancy, and the lack of contrast in molecular line maps compared to the continuum emission reported from a variety of observations (e.g. Mezger et al. 1992 and Mauersberger et al. 1992), led to the conclusion of these authors that molecules are frozen out onto dust grains in the vicinity of the cold and compact condensations. One consequence of this freeze-out scenario is that molecular line observations are particularly unsuitable to trace the dense cores and thus fail to yield accurate physical parameters toward them.

In the following, the relation of gas and dust, as seen in the CN and CS transitions observed within the scope of this thesis, and in high angular resolution dust continuum observations, will be investigated. In order to examine the morphology of the dense molecular ridge in NGC 2024, as traced by the CN and CS channel maps, it is first inevitable to study the observed spectra with respect to emission which *arises* and is *absorbed* along the line of sight and thus to determine the appropriate velocity range for *emission* from the condensations embedded in the background cloud.

8.4.1 Complex line-shapes toward FIR5/6

The geometrical picture presented in the Introduction implies that, especially toward the region close to the interface around FIR5 and 6, where the dense background cloud wraps around the HII cavity and connects to the lower density foreground cloud, the line-shapes are expected to show self-absorption features depending on the gas temperatures and optical depths of the transitions in the different cloud components along the line of sight. In order to demonstrate the variation in the CN line-shapes across the region around FIR5, spectra of CN N=1→0 and N=2→1 are stamped on a 5×5 grid in Fig. 8.6. The strongest hyperfine component of the N=1→0 and N=2→1 rotational transitions, in the case of CN N=2→1 this is a blend of the three strongest hyperfine lines labeled 3 through 5 in the middle panel of Fig. B.2, is shown since they will have the highest opacity and thus will be most influenced by self-absorption. In addition, one weaker, and hence more optically thin, line is shown for comparison. Offsets are give in arcsec relative to the center position between FIR5 and 6, FIR5 is located at the center of the field.

As can be seen from the spectra, the total velocity range relevant for emission from NGC 2024 is 8 – 14 km s^{-1}. The main hyperfine lines of both rotational transitions are clearly self-absorbed on the low velocity wing centered on 9 – 10 km s^{-1} across the whole region. A second absorption feature is visible particularly in the main hyperfine component of CN N=1→0 at ∼12 km s^{-1} and has a counterpart in ^{13}CO J=3→2 lines (Graf et al. 1993, individual spectra have been provided by private communication).

The weaker CN N=1→0 line shows the same basic appearance as the main line including faint signatures of self-absorption at the appropriate velocities. It should be noted that the contrast in relative line intensity for the N=1→0 lines is not very pronounced (33 to 13% of the total intensity of the rotational transition in the optically thin limit) which leads to significant optical depths, and hence self-absorption, even for the weaker components. This contrast is much stronger for the N=2→1 transitions where the blended lines comprise ∼54% of the total intensity of the optically thin rotational transition compared to only 3% in the weaker component. The self-absorption feature in the main N=1→0 line at ∼11.8 km s^{-1} is hardly discernible in the N=2→1 pattern but seems to appear in emission for the N=2→1 low relative intensity satellite (whose center velocity is clearly shifted from that of the main N=1→0 line), which is expected for this optically thin hyperfine component.

A compilation of CN and CS (this work) together with CO spectra (Graf et al. 1993) obtained toward the strongest dust continuum source FIR5 is presented in Fig. 8.7. The CN lines shown in this figure have been chosen with respect to the results from Fig. 8.6. Instead of the blend of the three strongest hyperfine lines of CN N=2→1, which are severely self-absorbed, the strongest not blended lines of CN N=2→1 and N=3→2 are displayed.

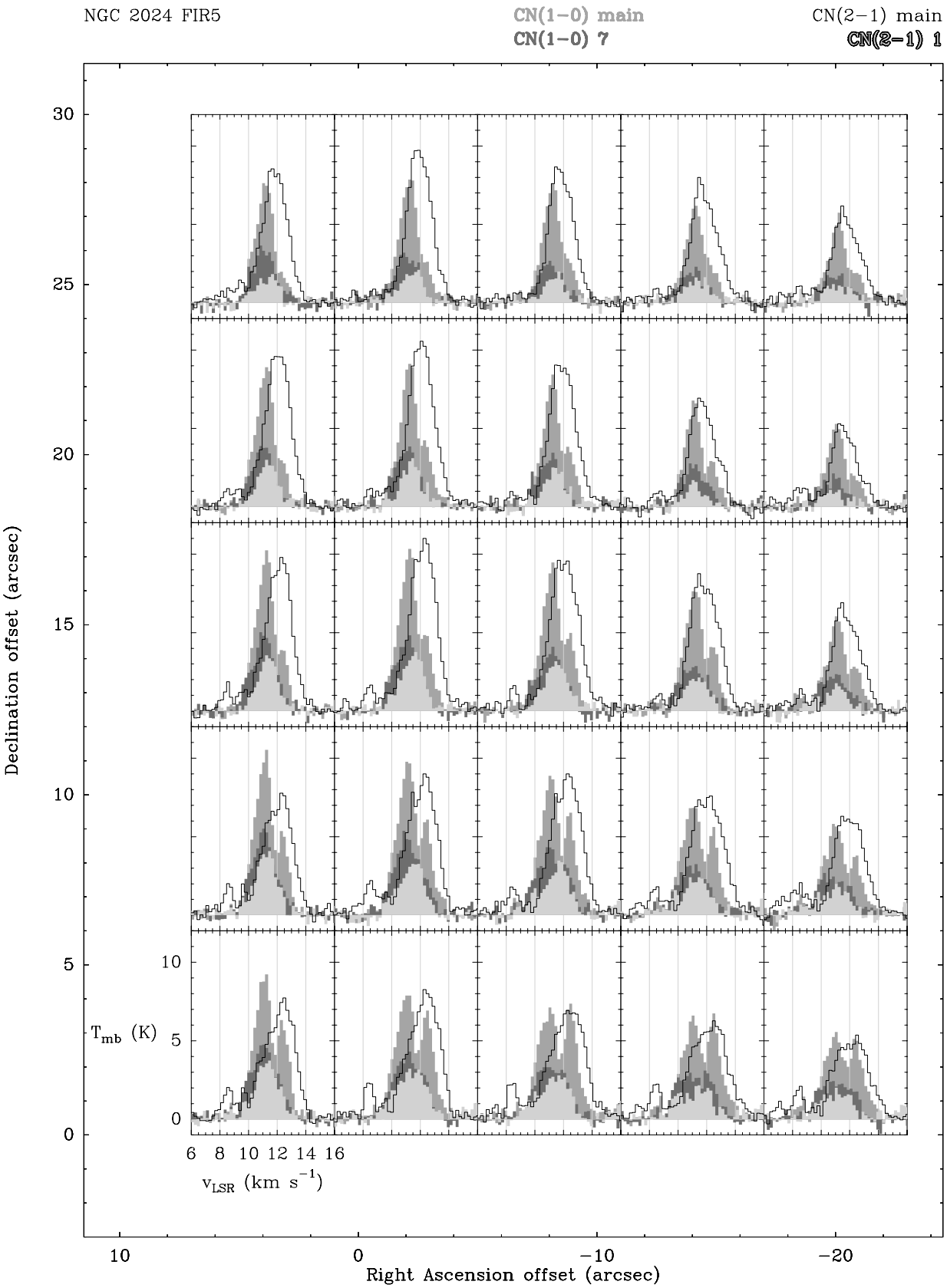

Fig. *8.6: Spectra of CN in the region around FIR5, which is located in the center, labeled according to the notation introduced in Fig. B.2.*

Grey filled spectra: *CN N=1→0 main and weaker hyperfine component (no. 4 and 7 in Fig. B.2, dark and medium grey) and N=2→1 weak satellite line (no. 1 in Fig. B.2, light grey).*

Black line: *N=2→1 blend of the three strongest components (no. 4,5,6 in Fig. B.2).*

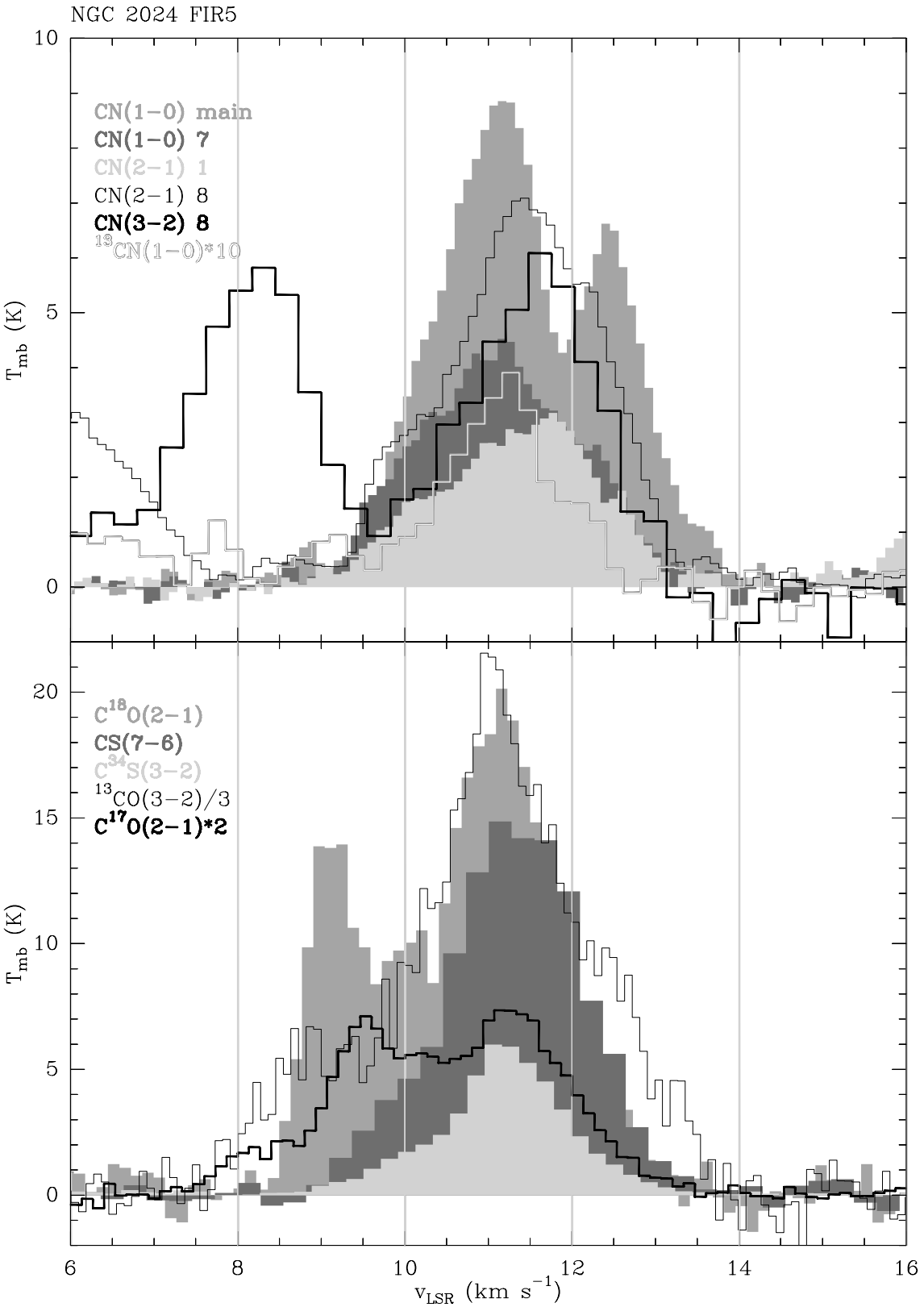

Fig. *8.7: Spectra of CN (top panel) in comparison with emission from other species toward FIR5 (bottom panel). The upper panel contains, labeled from top to bottom, the N=1→0 main hyperfine line and a weaker component (no. 4 and 7 in Fig. B.2), a weaker and the strongest not blended N=2→1 hyperfine line (no. 1 and 8 in Fig. B.2), the strongest not blended N=3→2 hyperfine line (no. 8 in Fig. B.2), and the main* ^{13}*CN N=1→0 line. The CO spectra in the bottom panel are adopted from Graf et al. (1993) and the CS data are from this thesis.*

The $C^{17}O$ and $C^{18}O$ lines exhibit two distinct peaks at 9 and 11 km s^{-1} corresponding mainly to fore- and background emission without self-absorption (see Graf et al. 1993) and additional low level emission between the peaks. The slight shift in the low velocity $C^{18}O$ component compared to the rarer $C^{17}O$ even implies a moderate opacity for this transition (Graf et al. derive a $C^{18}O$ optical depth of 1.0 for the foreground material toward FIR5) and thus the possibility of self-absorption even for the rare $C^{18}O$ species. ^{13}CO J=3$\rightarrow$2 emission shows a pronounced peak at 11 km s^{-1} and weak self-absorption at 9.5 and 12 km s^{-1}. The line is rather bright ($T_{\rm mb}$ $\sim$60 K) since mid- and low-J CO observations trace a transition zone from the warm surface of the HII cavity wall into the colder molecular cloud with successively lower rotational transitions and the J=3$\rightarrow$2 emission is produced in the warm gas closer to the ionization front. Optically thick ^{12}CO lines suffer from deep absorption (Graf et al. 1993, these spectra are not shown here) over a wide range in velocity ($\sim$9 – 12 km s^{-1}). This absorption causes an artificial red shifted emission feature (the peak occurs at $\sim$13 km s^{-1}) and implies that at least part of the foreground material has to be very cold. A similar absorption effect is apparent for the blend of the three strongest hyperfine components of the CN N=2$\rightarrow$1 transition over the whole region (see Fig.8.6). The asymmetric line-shapes of the CN hyperfine transitions between 9.5 and 11 km s^{-1} reveal that apparently not all of the strong self-absorption is caused by a well defined component at 9 km s^{-1} and it is thus concluded that part of the absorption originates from homogeneous optically thick foreground gas at velocities between 9 and 11 km s^{-1}.

In contrast to CO, where the density in the foreground material of the order of 10^5 cm^{-3} is sufficient to thermalize the lower-J level populations, the deep absorption in the main CN and in lower-J CS (see e.g. Schulz et al. 1991) lines implies subthermal excitation and high optical depths for these species in the foreground gas. This conclusion holds for all CN transitions discussed in this section and at least for CS transitions with upper states J$\leq$5. Like for CO, emission associated with the dense background cloud and the embedded condensations for CN and CS peaks between 11 and 11.5 km s^{-1}.

Besides the deep absorption at 9 km s^{-1}, the main hyperfine component of CN N=1$\rightarrow$0 in Fig. 8.7 shows the second prominent absorption feature on the high velocity wing at 11.9 km s^{-1} as already identified in Fig. 8.6. An emission line at 12.5 km s^{-1} can be ruled out from the optically thin CO emission and in particular from the ^{13}CN spectrum. This absorption component is also visible in the strongest not blended CN N=2$\rightarrow$1 line and appears to be seen in emission in the optically thin N=2$\rightarrow$1 line. Fig. 8.6 reveals that this absorption is strongest south of FIR5. At Declination offsets south of $\sim -20''$ from FIR5, this distinct self-absorption feature is shifted to lower velocities across the main emission line at 11 km s^{-1} and mimics a peak at 12 km s^{-1}.

Emission toward the northern sources FIR1 – 4 does not show the degree of complexity in the line-shapes detected toward the southern condensations. At FIR4, the H_2CO absorption (Crutcher et al. 1986) gets weaker and its velocity is shifted to higher values which results in less severe self-absorption and a blending with the background emission component. At Declination offsets north of FIR3, the self-absorption in the molecular lines of CN and lower-J CS (e.g. Schulz et al. 1991) increases along with again stronger H_2CO absorption lines centered on 9.6 – 9.9 km s^{-1}. However, all stronger hyperfine components of CN, in particular the main

N=2→1 lines, show evidence for self-absorption everywhere along the molecular ridge.

To summarize, the complex line-shapes in NGC 2024, especially toward the southern sources FIR5 and 6, make it particularly difficult to disentangle the various contributions along the line of sight:

- In the vicinity of FIR5 and 6, the dense background molecular cloud wraps around the HII region and connects to the lower density, lower temperature foreground cloud.
- The source has an overall north-south velocity gradient.
- Colder foreground material along the line of sight causes self-absorption in the background emission for a velocity range between 9 and 12 km s^{-1}. Although the absorption features at 9 and 12 km s^{-1} are well defined and likely to be caused by distinct clumps, some of the absorption seems to originate from more or less homogeneously distributed gas.
- CO lines at energetically higher rotational transitions trace gas at increasing temperature closer to the ionization front, i.e. shifted toward the 6cm continuum peaks.
- Emission from the dense condensations is expected for velocities centered between 11 and 11.5 km s^{-1} for the southern part and, due to the velocity gradient, between 10 and 11 km s^{-1} in the northern part of the cloud.

8.4.2 Single-dish channel maps and large scale morphology

With the exception of CS J=3→2, where only spectra with a 1 MHz (or 2 km s^{-1}) resolution filter bank were obtained and consequently, instead of channel maps, the total integrated line intensity is shown (Fig. 8.8), the high spectral resolutions provided by the different autocorrelator units resulted in velocity resolutions of the order 0.2 km s^{-1} or better for all other observations (see Table 6.1 for details). Figures 8.9 to 8.14 depict selected channel maps of the CN data, which were chosen on the basis of the conclusions drawn in the previous section on the complex line-shapes, and the CS observations available in parallel. Each Figure is labeled with the corresponding transition frequency and contains a comparison to the 870μm dust continuum contours adopted from Mezger et al. (1992) in the top left panel. The dust continuum positions are represented by triangles. In addition, a map of the transitions peak antenna temperature is included in the second panel.

For the CN N=1→0 rotational transition, where no blending of hyperfine lines occurs, the strongest and one weaker hyperfine component (no. 3 in Fig. B.2) were selected. For CN N=2→1, the strongest not blended component (no. 8), instead of the blend of the three strongest lines, which show severe self-absorption especially toward the southern sources, is displayed. Similar to N=2→1, the strongest observable feature of the CN N=3→2 transition is a blend of the three strongest individual hyperfine lines but the distances in velocity space in this case are much smaller and there seems to occur only weak self-absorption on the low velocity wing due to the higher critical density of the transition. Therefore, and because of the higher signal to noise ratio of the stronger components, channel maps of this composite line are shown.

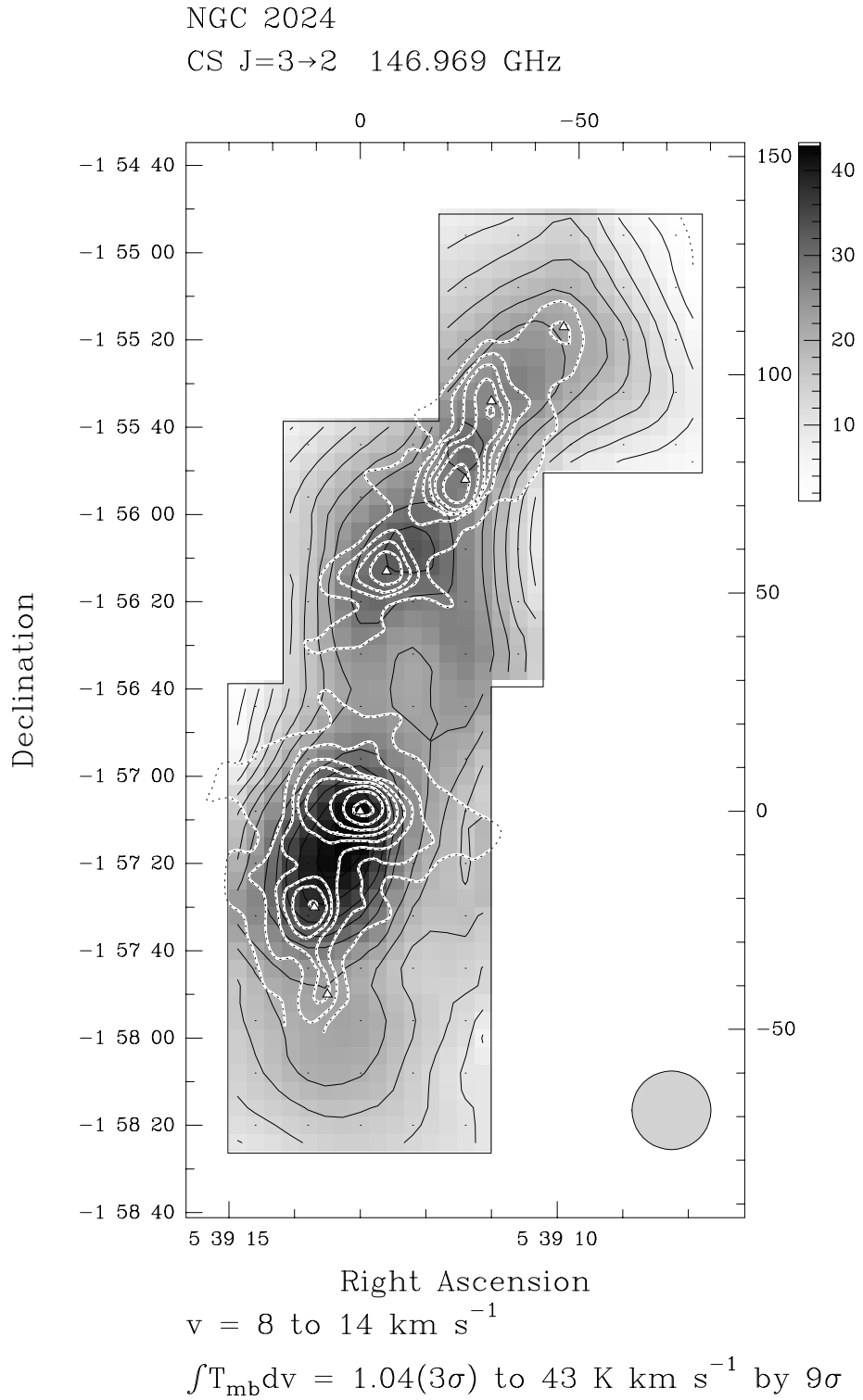

Fig. *8.8: Intensity of CS J=3→2 integrated from 8 to 14 km s^{-1} in NGC 2024 observed with the IRAM 30m telescope (greyscales). A circle corresponding to the beam size is drawn in the lower right corner. The overlay with dashed contours corresponds to the 870μm dust continuum emission as observed by Mezger et al. (1992). Offsets are given in arcsec relative to FIR5.*

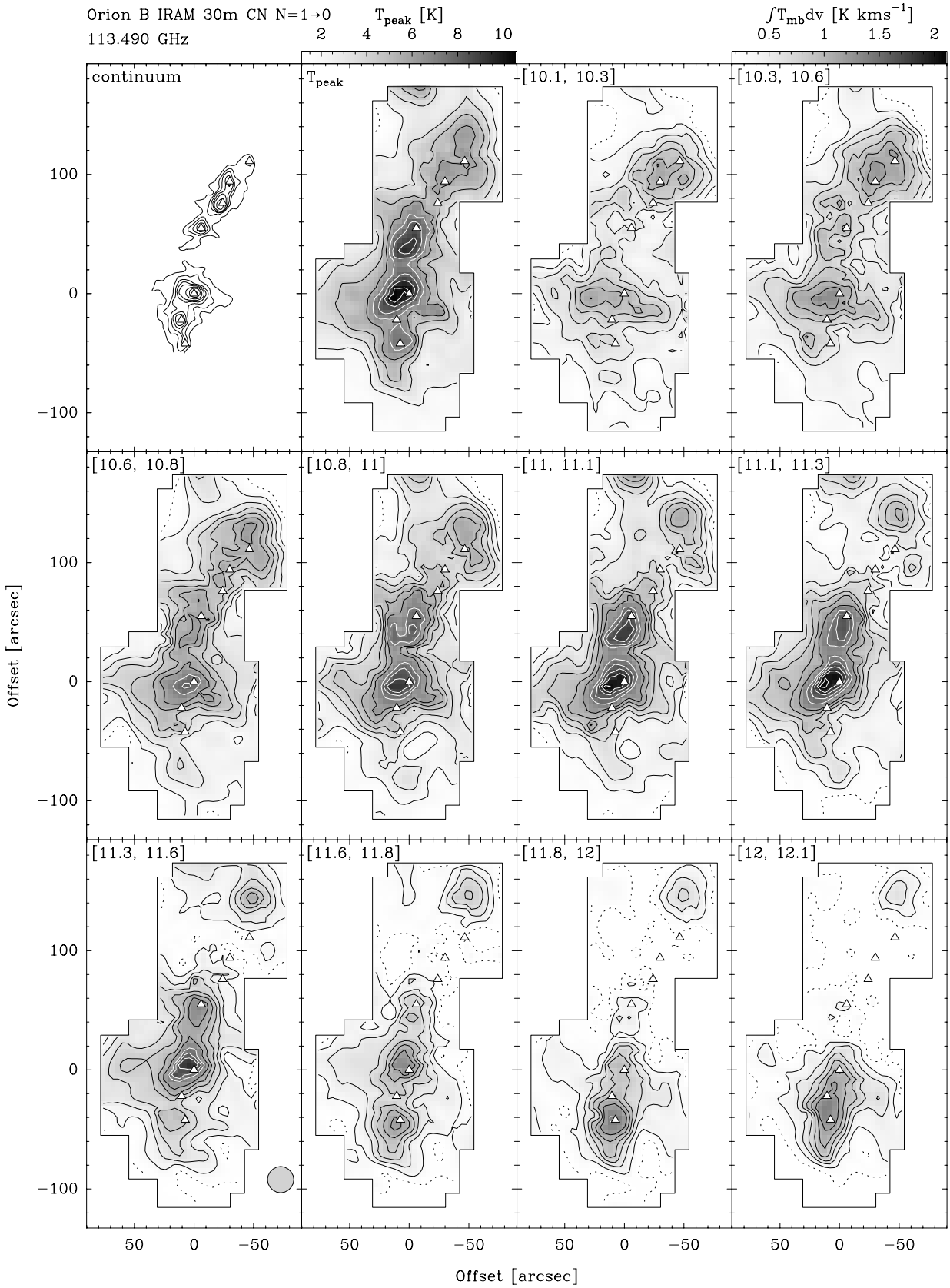

Fig. *8.9: Dust continuum emission at 870μm (Mezger et al. 1992) in comparison to peak temperatures and channel maps of the CN N=1→0* **main hyperfine line** *in NGC 2024 observed with the IRAM 30m telescope. The velocity interval is given in the top left corner of each panel. Contour levels are 3σ = 0.15(0.15)2.10 K km s^{-1}. A circle corresponding to the beam size is drawn in the lower left panel.*

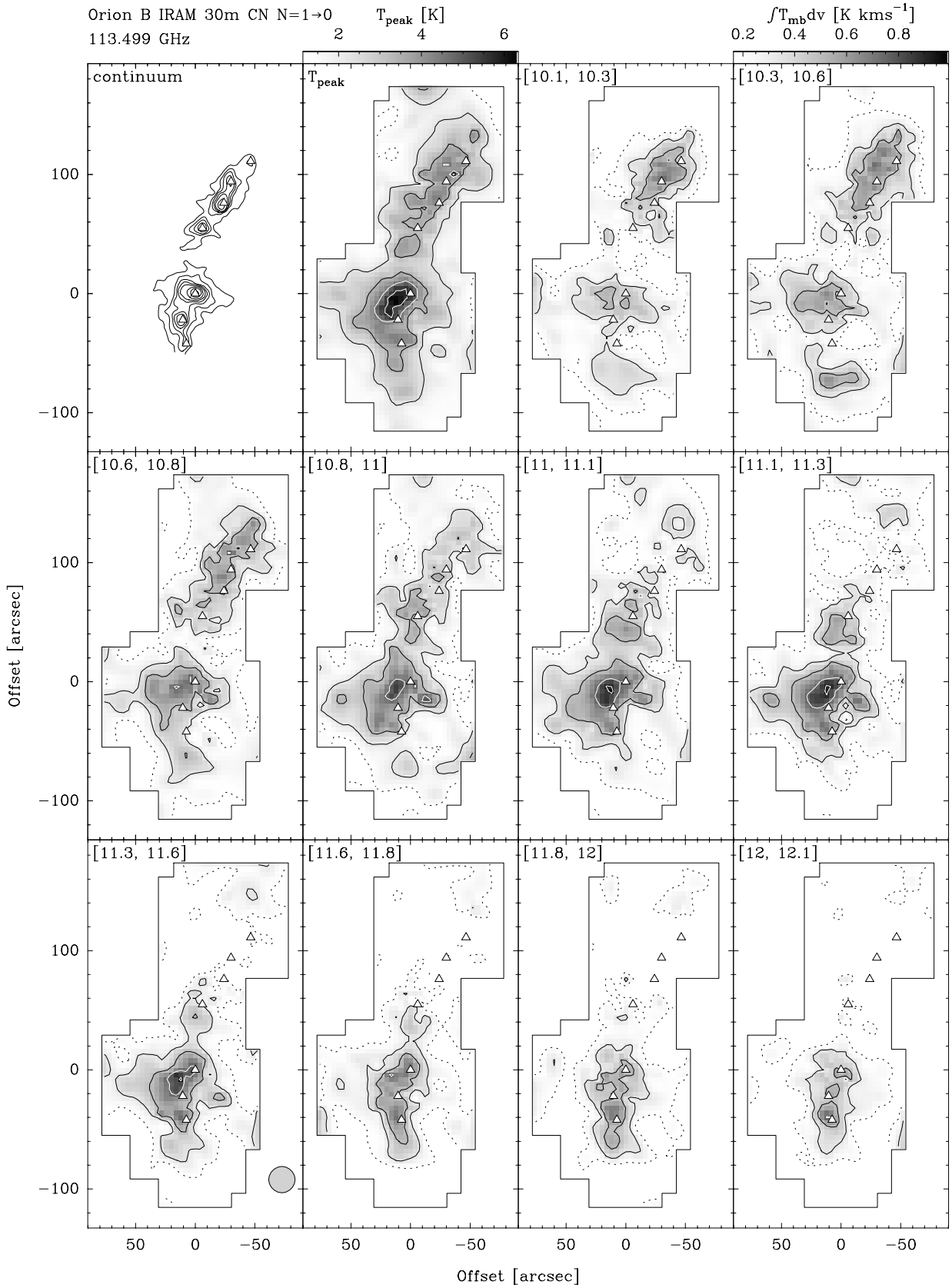

Fig. *8.10: Channel maps of CN N=1→0* **component no. 3** *in NGC 2024 observed with the IRAM 30m telescope. Contour levels are 3σ = 0.15(0.15)0.90 K km s^{-1}. A circle corresponding to the beam size is drawn in the lower left panel.*

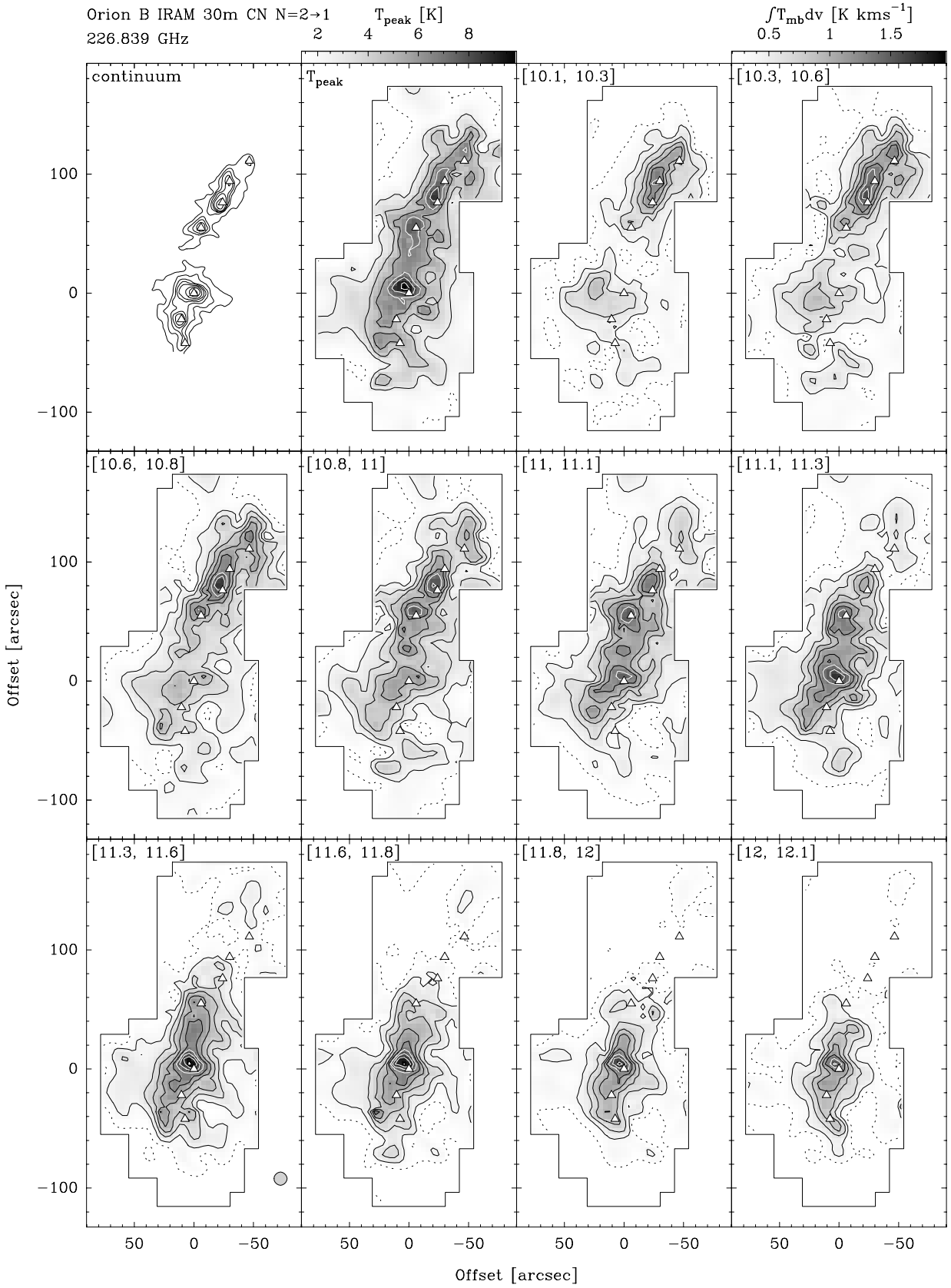

Fig. *8.11: The same as Fig. 8.9 for* **component no. 8** *of CN N=2→1. Contour levels are* 3σ = *0.19(0.19)1.90 K km s*$^{-1}$*. A circle corresponding to the beam size is drawn in the lower left panel.*

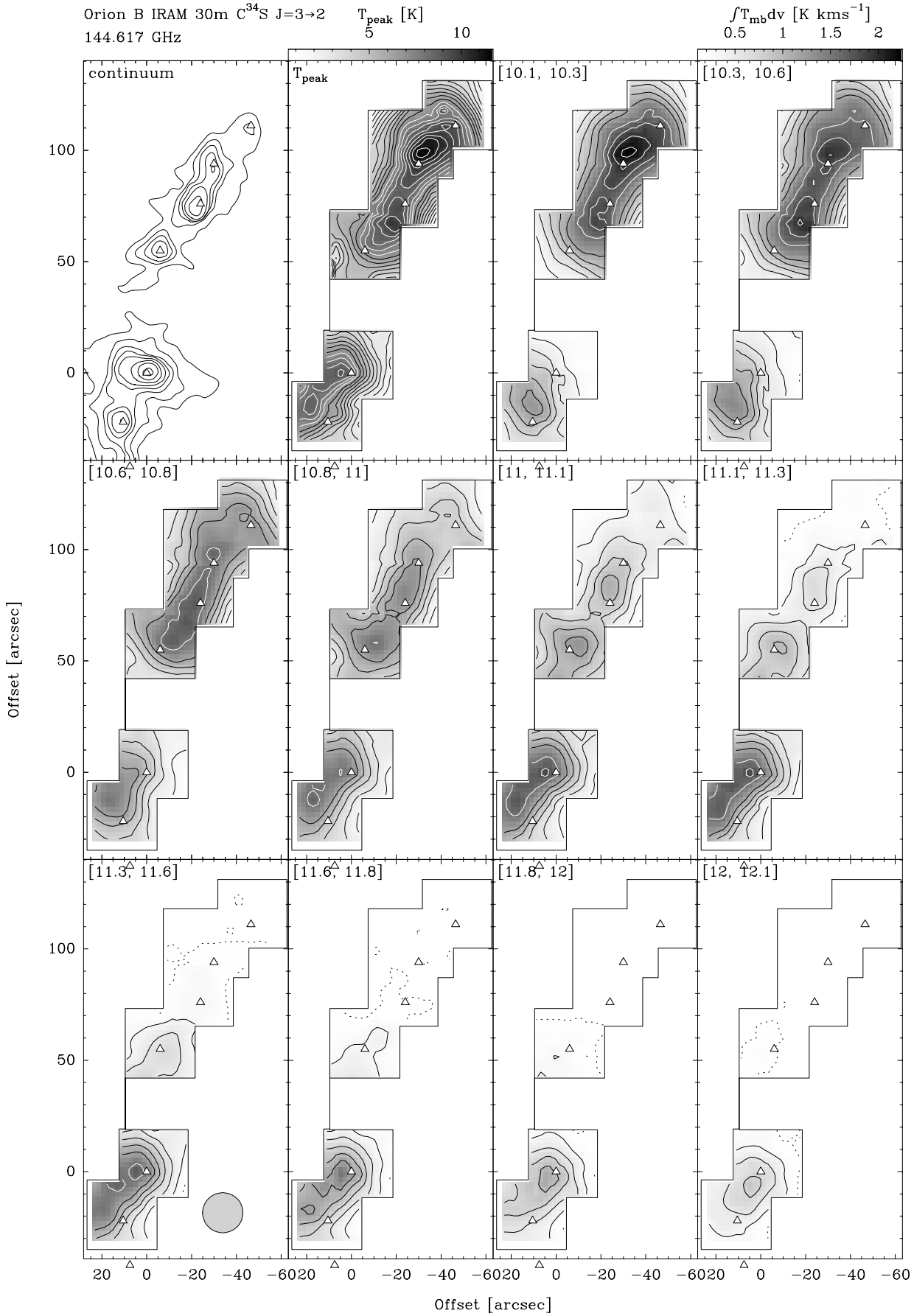

Fig. *8.12: The same as Fig. 8.9 for $C^{34}S$ J=3→2. Contour levels are 3σ = 0.11(0.22)2.09 K km s^{-1}. A circle corresponding to the beam size is drawn in the lower left panel. Note that the observed grid is different since this data set exclusively contains the 5×5 maps centered on FIR1–6 which were recorded during the January 1994 observing run.*

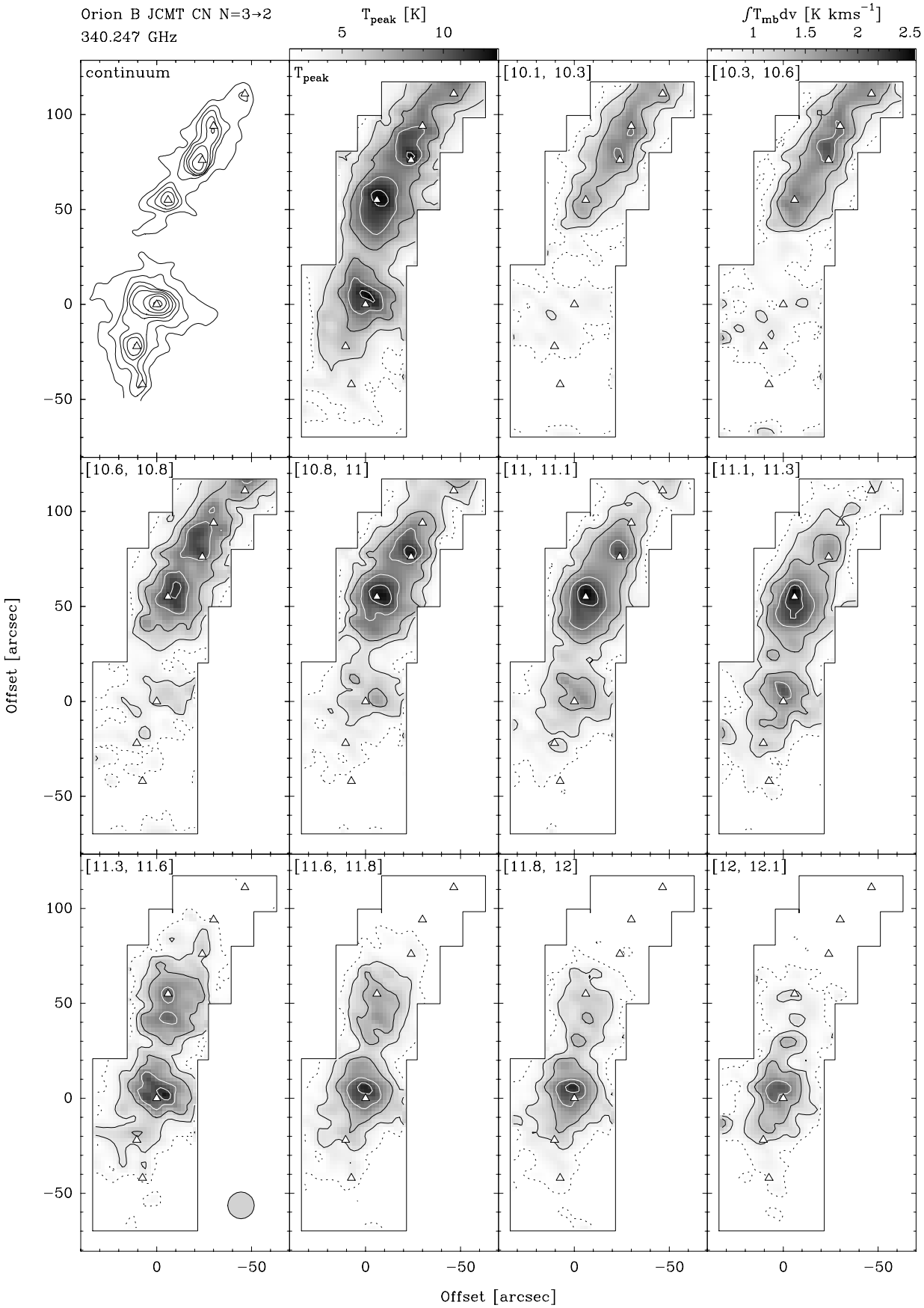

Fig. *8.13: Channel maps of CN N=3→2 in NGC 2024 observed with the JCMT. As in Fig. 8.9 the velocity interval is given in the top left corner of each panel. Contour levels are* 3σ *= 0.56(0.37)2.41 K km s*$^{-1}$*. A circle corresponding to the beam size is drawn in the lower left panel.*

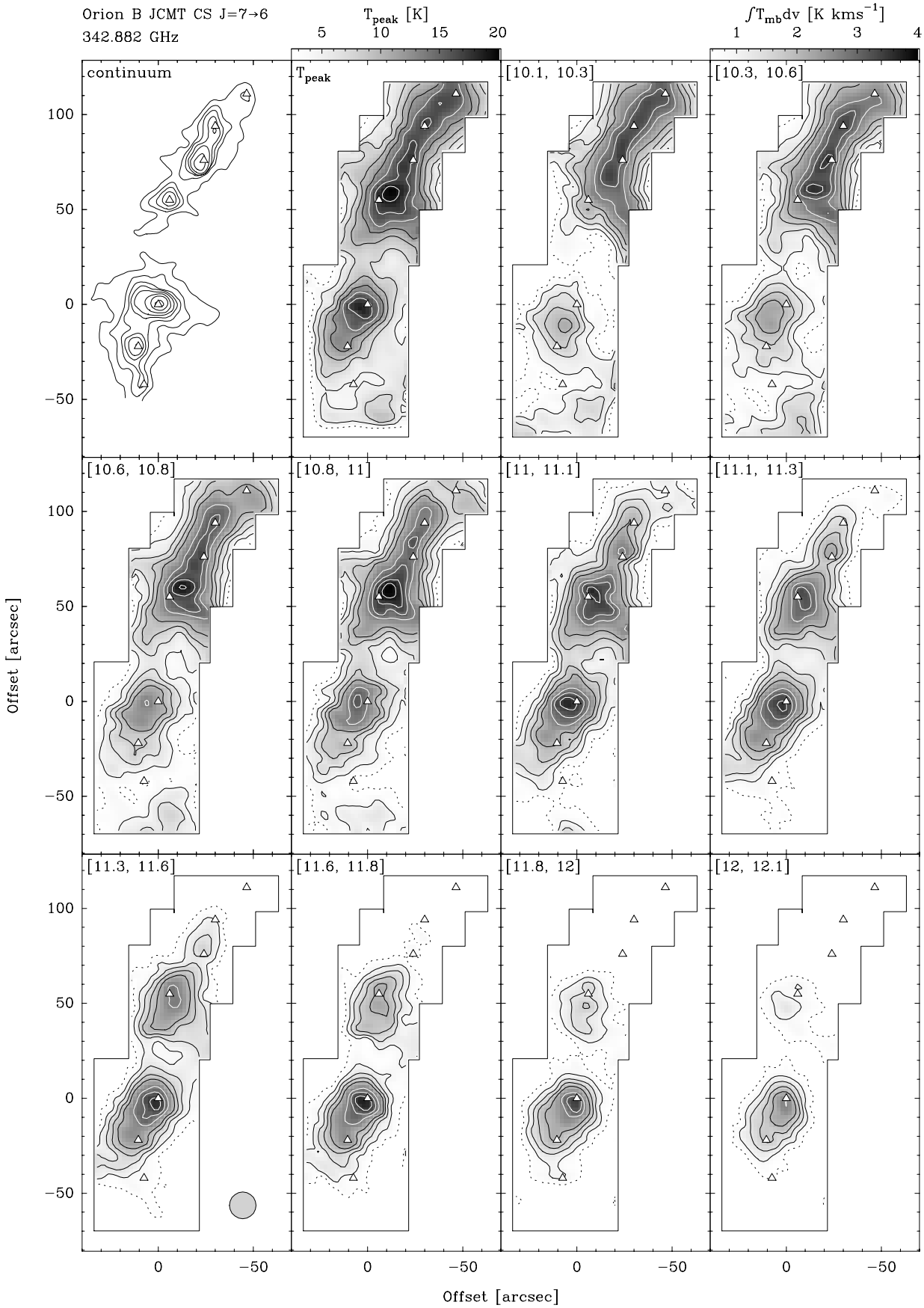

Fig. *8.14: The same as Fig. 8.13 for CS J=7→6. Contour levels are* 3σ *= 0.56(0.37)3.89 K km s*$^{-1}$*. A circle corresponding to the beam size is drawn in the lower left panel.*

All transitions fairly well trace the north-south oriented dense molecular ridge, several clumps embedded along the main axis, and follow the same basic morphology as the submm dust continuum. A velocity gradient of –0.7 km s^{-1} $arcmin^{-1}$ from south to north is visible and the ridge breaks up into two subclouds separated by the ionization front and SCP as already obvious in the overlay of radio and dust continuum emission in Fig. 8.4. On smaller angular scales, morphological differences in the emission distribution between the individual tracers or even within different transitions of the same species occur. The reasons for this, apart from pointing uncertainties and differing angular resolutions, may be either different opacities, self-absorption and excitation effects, or variations in the molecular abundances.

Channel maps of the CN N=1→0 main hyperfine line and the velocity integrated intensity map of CS J=3→2 are similar in the sense that they fairly well trace the ridge but are only marginally well correlated with the dust continuum peaks toward the northern condensations and peak between FIR5 and 6 in the southern part of the region. This finding is partly explained by the lower angular resolution and the fact that the lines are affected by self-absorption. In addition, considering the complex morphology and velocity structure of the source, it is by no means surprising that maps of the *total integrated* line intensity of various optically thick molecular transitions, including our CS J=3→2 observations, show a lack of contrast and correspondence compared to optically thin mm dust continuum emission, as it was already reported by e.g. Mezger et al. (1992) and Mauersberger et al. (1992). A detailed morphological correspondence with material traced by the dust measurements can only be expected for high spatial *and* spectral resolution data of optically thin molecular emission. Indeed, the weaker hyperfine satellite of CN N=1→0 and the rarer isotopomer $C^{34}S$ (see Fig. 8.10 and 8.12) reveal a better agreement of line emission and continuum peaks in the channel maps at least for the northern sources and a trend for the molecular emission to peak close to and east of FIR5 in the south. The correlation between gas and dust is even better in the CN N=2→1 channel maps, which furthermore show an increased contrast due to the higher angular resolution.

The most striking correspondence of molecular line and dust continuum emission is evident in the channel maps for the higher density and higher temperature tracing CN N=3→2 and CS J=7→6 transitions. Even more pronounced than in the other transitions discussed above, the FIR peaks have their molecular counterparts in the velocity channels relevant for emission from the dense background cloud (11 – 11.5 km s^{-1}), as identified in the previous sections and determined by the overall velocity gradient.

To date, there have been two CS J=7→6 maps reported in the literature. Moore et al. (1989a) obtained a nearly fully sampled map at the JCMT, covering the region from FIR 2 to 6. Their integrated intensity distribution resembles closely to our equivalent shown in Fig. 7.29, but due to the improved receiver performance since their observations, the data obtained for the present thesis provide a factor of 2 higher sensitivity. The region around FIR5 and 6 has been mapped in the same transition at the IRAM 30m telescope by Schulz et al. (1991). Our and their results show the same basic morphology but disagree with respect to the location and intensity of the peak emission. Their integrated intensity map shows a pronounced peak close to FIR6 and a weaker maximum barely associated with FIR5, while in our observations the situation is just

opposite. We believe that this discrepancy has to be attributed to the beam pattern of the 30m telescope. At this high frequency, the main beam efficiency is 20% and pick-up from an extended error-beam is significant which has to be corrected for (Greve et al. 1997).

Careful inspection of the CN N=3→2 and CS J=7→6 maps at the locations close to the ionization front (i.e. on the clump surfaces in the northern part of FIR5, where the IF is seen almost edge-on, and south-east of FIR4) reveals a difference in the emission distribution of both molecules with the CN peaks located closer to the 6cm continuum peaks. Since both transitions have been observed in two different sidebands of the same receiver, pointing uncertainties are excluded. Similar to the situation in the Orion Bar region, this stratification is of chemical origin and produced in the transition zone from a UV photon dominated environment to a dense molecular clump. In order to investigate this finding in more detail, a comparison of the integrated intensity maps of CN N=3→2 and CS J=7→6 with the 6cm continuum (Crutcher et al. 1986) is given in Fig. 8.15 overlaid on the appropriate part of the near infrared image introduced in Fig. 8.4.

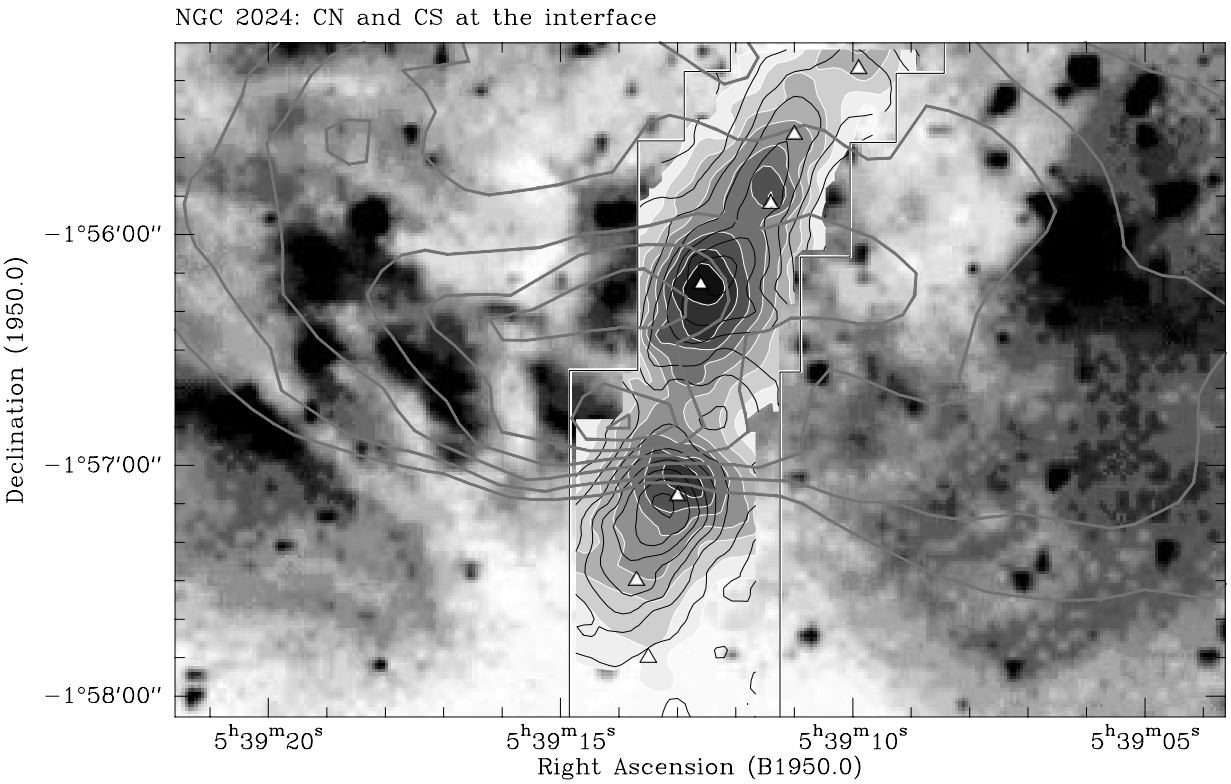

Fig. *8.15: Overlay of 6cm radio continuum (white dashed contours, Crutcher et al. 1986), CS J=7→6 (black contours), CN N=3→2 emission (grey filled contours) on a part cut out from the infrared image introduced in Fig. 8.4. The dust continuum peaks FIR1 – 7 are indicated by triangles, other point sources by stars (prominent optically visible or infrared objects, see Fig. 8.3) and the H_2O maser by a cross.*

CN N=3→2 clearly peaks at the IF marked by the sharp edge in the 6cm emission at FIR5 and the NCP south-east of FIR4. From the cut along the north-south axis through the condensations presented in Fig. 8.16, the above drawn conclusion is further supported. Provided the pointing between the JCMT data and the dust continuum is accurate, FIR5 even appears to be sandwiched between the CN and CS emission peaks.

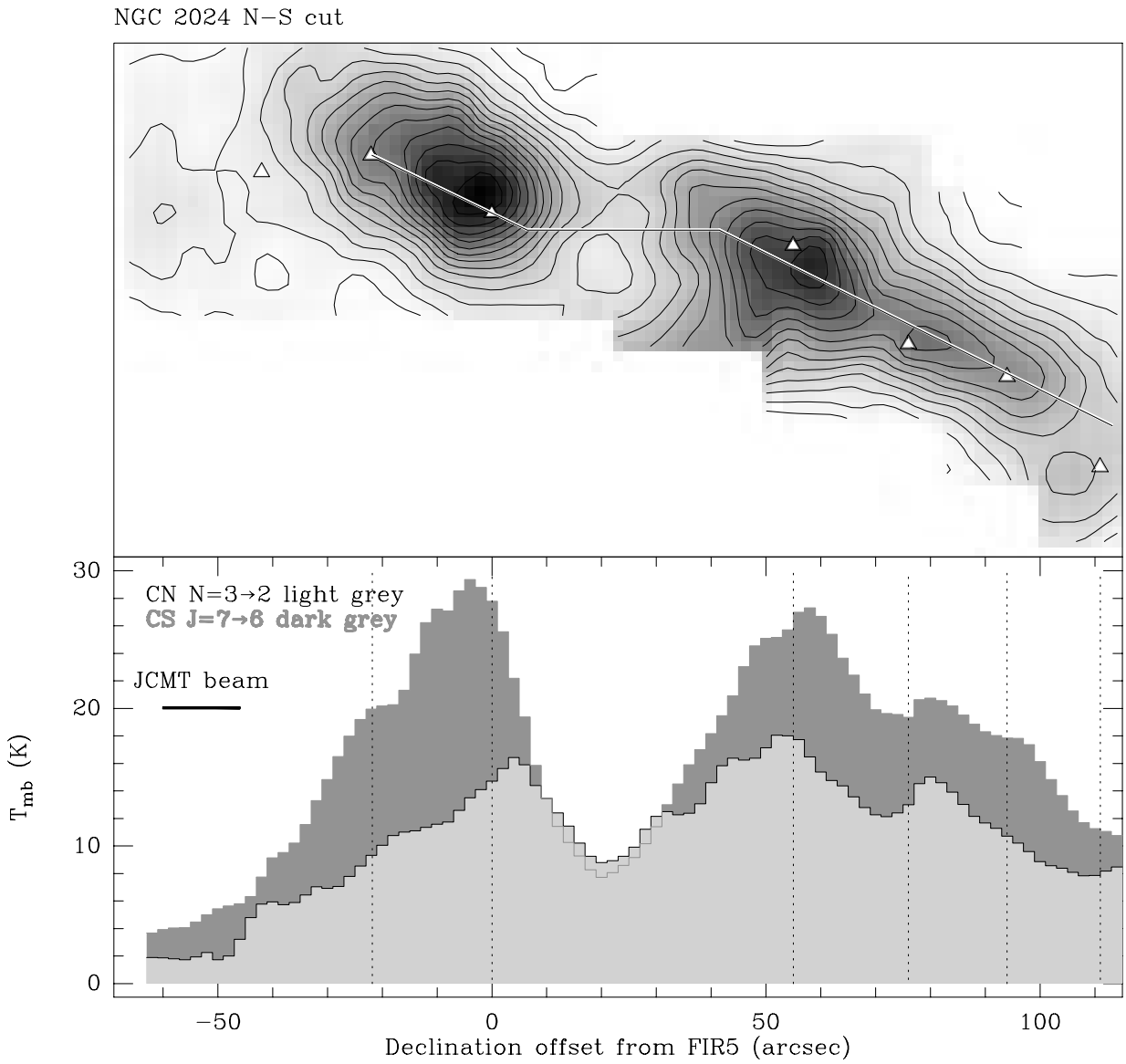

Fig. *8.16: A cut of CN N=3→2 (light grey) and CS J=7→6 (dark grey histogram) along the north-south axis through the FIR peaks (the direction of the cut is indicated in the top panel which shows the total integrated intensity map of CS J=7→6).*

8.4.3 Hyperfine fits to the spectra

In order to derive proper physical parameters from the CN observations toward the dense condensations, the individual hyperfine patterns have to be fitted with consideration of the conclusions derived in the previous sections concerning the different contributions from back- and foreground material along the line of sight. For this purpose, a least square fitting procedure was developed which explicitly considers four distinct velocity components. The first component accounts for the emission from the dense warm background cloud centered on 11 – 11.5 km $s^{-1}$and with line widths of the order of 2 km s^{-1}. The following three correspond to the absorption features at 12 km s^{-1} (a distinct component assumed to have small line width of the order of 1 km s^{-1} or less), $\sim$10 km s^{-1} (accounting for the homogeneously distributed cold foreground gas mentioned in

the previous section, thus having larger line width of the order of 2 km s^{-1}) and 9 km s^{-1} (an additional distinct component associated with the dark dust lane closest to the observer, again with smaller line width as above).

Starting from this closest foreground cloud, the complete formula as given in Eq. 5.3 was used:

$$\mathrm{I}_\nu = \mathrm{S}_{\nu,1}(1 - \exp(-\tau_{\nu,1})) + \mathrm{I}_{\mathrm{bg},1} \exp(-\tau_{\nu,1}) \ .$$

The second term on the right hand side, which describes the background contribution, contains the remaining two absorptions and the emission from the dense background ridge.

$$\mathrm{I}_{\mathrm{bg},1} = \mathrm{S}_{\nu,2}(1 - \exp(-\tau_{\nu,2})) + \mathrm{I}_{\mathrm{bg},2} \exp(-\tau_{\nu,2}) \ .$$

The right hand side now accounts for the second absorption component in the line of sight and its corresponding composed background. The second expression is split again into two parts in the same manner as before and so forth until the dense background component is reached, whose background in turn is the Cosmic Background radiation. The complete hyperfine pattern of the CN rotational transition is fitted simultaneously for the amplitude factor, the total optical depth, the LSR velocity, and the line width as described in detail in Section 5.2 for each of the 4 assumed velocity components. This results in 16 free parameters for each of the three observed rotational transitions. Spectra at the positions FIR1 – 6 have been smoothed to the angular resolution of the CN N=1$\rightarrow$0 observations, i.e. $22''$, prior to the fitting procedure. Regarding the large number of free parameters, the initial guesses have to be chosen carefully. Reasonable first guesses are obtained from the conclusions already drawn in conjunction with results from other observations, e.g. appropriate LSR velocities and line widths for the individual components. In addition, it was carefully checked that emission and absorption features were unambiguously identified in the fits to all of the three rotational transitions with respect to LSR velocity and line width at each position in the cloud.

The resulting fit parameters for the emission component from the background were used to derive CN column densities in the same manner as described in Section 7.6.3 for the Orion A region and molecular abundances by adopting the H_2 column densities given in Table 8.1 which summarizes the results.

Although the nature of the sources might be more complex as to be properly described by the simple assumption of four distinct components along the line of sight, this method surely is a better approach to derive physical parameters toward the condensations than to apply a one component fit only. As one example, the fit results for CN N=1$\rightarrow$0 and N=2$\rightarrow$1 toward FIR5 are displayed in Fig. 8.17.

The fit results are reasonable in the sense that the foreground components are identified with low amplitudes, high optical depths (of the order of 3 – 8), and small line widths ($<$1 km s^{-1} for the distinct components) characteristic for cold absorbing material while the background contributes emission from warmer gas with larger line width ($\sim$2 km s^{-1}) and moderate optical depth. Moreover, the velocity gradient in the background cloud is well reproduced. Toward FIR5,

Position	v_{LSR} km s^{-1}	N(H_2)[a] $\times 10^{23}$ cm^{-2}	N_{CN} $\times 10^{14}$ cm^{-2}	X(CN) $\times 10^{-9}$
FIR1	10.5	4	1.6	0.4
FIR2	10.3	4	3.6	0.9
FIR3	10.6	7	1.4	0.2
FIR4	10.8	4	3.1	0.8
FIR5	11.2	6	6.1	1.0
FIR5[b]		2	6.1	3.1
FIR6	11.2	6	7.1	1.2

[a] Values adopted from Schulz et al. (1991) from their CS results assuming [CS]/[H_2] $\sim 2.5\ 10^{-9}$

[b] N(H_2) adopted from Graf et al. (1993) calculated explicitly for the background component

Table *8.1: LSR velocities and total CN column densities derived from the fit results for the background emission component and CN abundances X(CN) along the NGC 2024 ridge determined from the adopted H_2 column densities.*

our LSR velocity results for the strong fore- and background of 9.2 and 11.2 km s^{-1} respectively are almost identical to the values determined by Graf et al. (1993) from a simultaneous two component fit to their CO data.

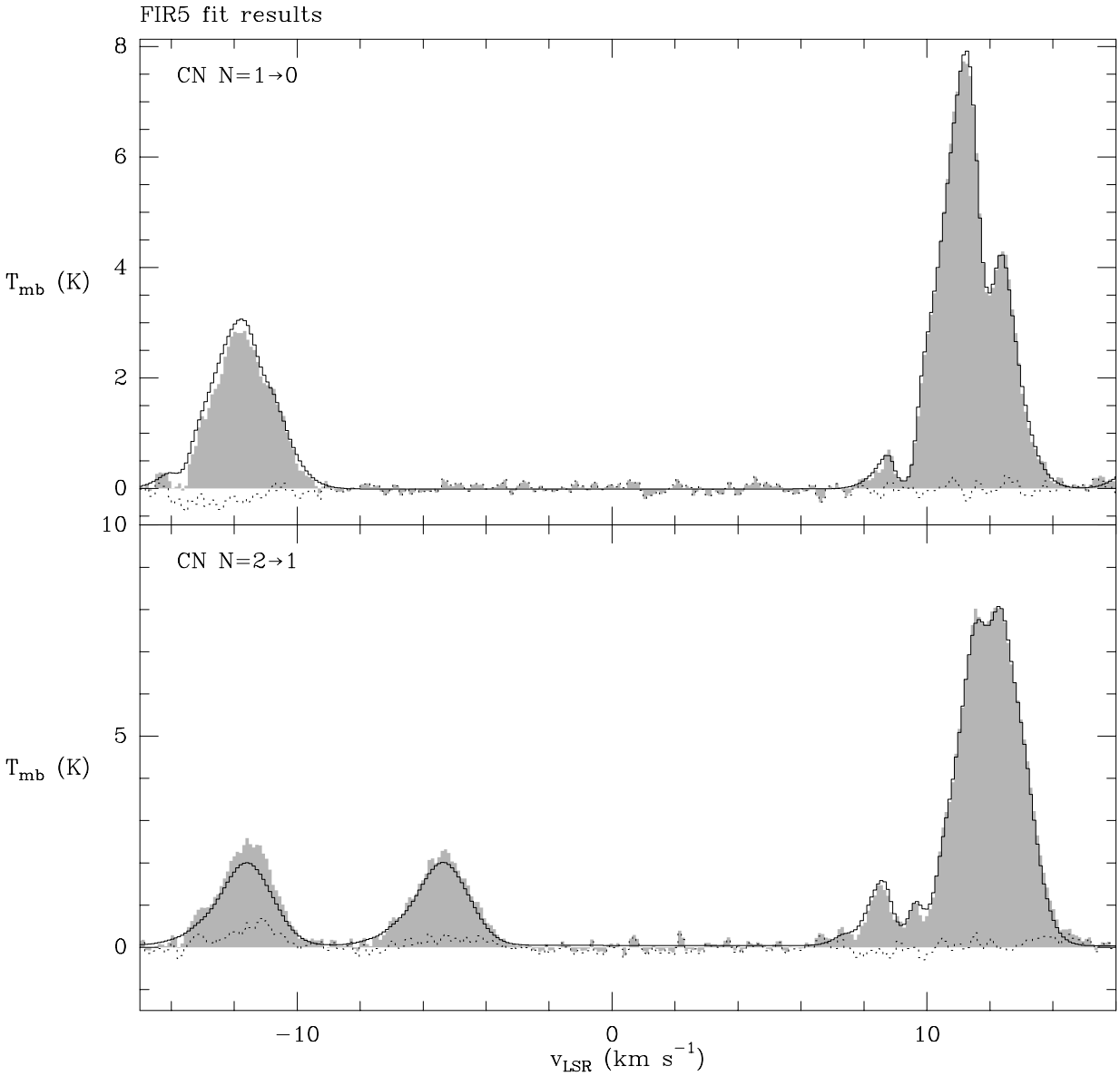

Fig. *8.17: Fit results for CN N=1→0 and N=2→1 toward FIR5 (solid lines on the observed grey filled spectra, residuals are indicated by the dashed lines). The main lines and adjacent weaker satellites are shown for comparison. Parameters for CN from the fits toward FIR1 – 6 are listed in Table 8.1.*

8.4.4 Plateau de Bure Interferometer results

The λ = 2.7mm dust continuum emission, as observed in parallel to the CN observations with the Plateau de Bure Interferometer, is shown in Fig. 8.18 together with the single-dish continuum results adopted from Mezger et al. (1992).

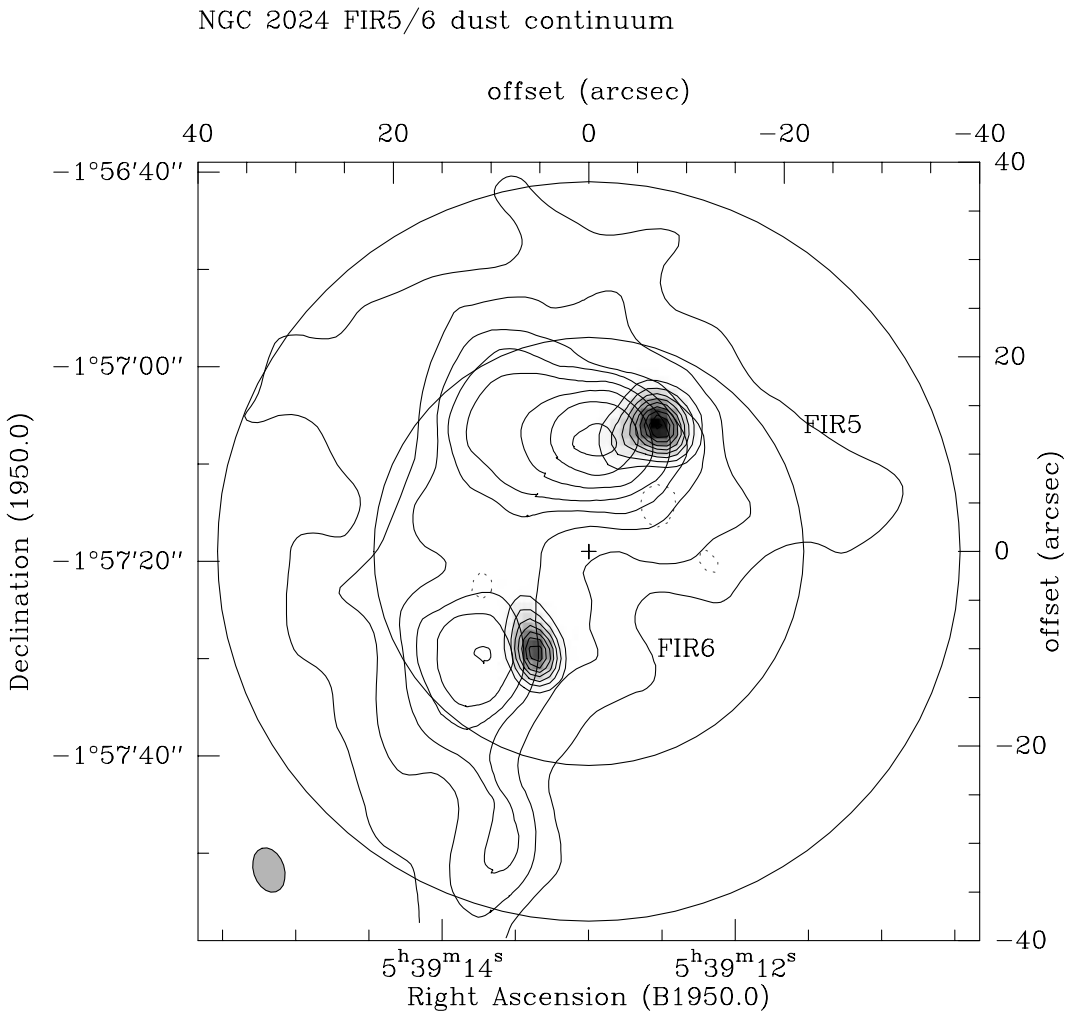

Fig. *8.18: Dust continuum emission at λ = 2.7mm from FIR5 and 6 (greyscales). Contour levels are 18(18)180 mJy beam^{-1}. The circles correspond to the half power (inner) and first null (outer) contour of the single-dish interferometer beam. The clean beam is drawn in the lower left corner and the phase reference center is indicated by a cross. Overlaid are contours of the λ = 870μm dust continuum (8″ resolution) adopted from Mezger et al. (1992).*

The interferometer data show two distinct peaks, FIR5 and 6, while extended dust emission, due to the lack of short spacings, is resolved out. A pointing offset of $\sim$6″ between the two maps is evident. FIR5 is extended east-west, perpendicular to the orientation of the beam, which is a clear indication that the source consists of at least two components. Wiesemeyer et al. (1996), with their slightly higher angular resolution of 3.″8 $\times$ 1.″6, partly resolve the eastern subsource. The appearance of FIR6 is that of a true point source since it reflects the size and orientation of the elliptical clean beam. Parameters of the continuum observations are listed in Table 8.2.

	Coordinates	S_ν (mJy)	T_b (K)
FIR5	$\alpha(1950.0) = 05^h39^m12^s.52$ $\delta(1950.0) = -01^\circ57'06''.0$	300	1.20
FIR6	$\alpha(1950.0) = 05^h39^m13^s.36$ $\delta(1950.0) = -01^\circ57'29''.5$	175	0.96

Table *8.2: Derived source coordinates, flux densities S_ν and beam averaged brightness temperatures T_b for the λ = 2.7mm continuum emission from FIR5 and 6.*

The uncertainty in the determination of the flux densities, resulting from the combined errors in the absolute calibration and the cleaning procedure, are estimated to be of the order of 20%.

A comparison of our dust continuum peak positions with those determined from other interferometric observations by Wilson et al. (1995), Chandler & Carlstrom (1996) and Wiesemeyer et al. (1996) reveals that all positions agree to within $4''$ with a trend of the values reported by the above mentioned authors to peak *between* our positions and those derived by Mezger et al. (1992). The overall pointing uncertainties between the individual datasets can thus be estimated to at most $6''$. Our listed flux densities at 111.8 GHz agree fairly well with the quantities determined by Chandler & Carlstrom at the slightly higher frequency of 112.4 GHz, namely 268 mJy and 175 mJy for FIR5 and 6 respectively.

Cleaned spectral channel maps of the strongest hyperfine line and one weaker satellite (no. 3 in Fig. B.2) are shown in Fig. 8.19 and 8.20 together with the simultaneously observed 2.7 mm dust continuum. Note that due to the correction for the primary beam attenuation, the noise in the spectral line maps increases toward the edge of the observed field.

Since the longer baselines contribute somewhat higher noise and in order to check if the emission found by the cleaning procedure in the high angular resolution data is real, we reduced the data set without the single-dish visibilities and by applying a uv taper of 30m. The resulting channel maps, although smoother due to the larger synthesized clean beam, basically show the same appearance with a slightly enhanced signal to noise ratio. This means that the emission features identified in the untapered higher angular resolution data are reliable. A comparison of the fluxes obtained with the single-dish telescope and the array alone shows that the interferometer detects $\sim$30% of the total CN flux, which reflects that CN emission is extended.

The interferometer channel maps confirm the strong CN N=1$\rightarrow$0 peak south-east of FIR5 already visible in the single-dish results, but reveal additional small scale structure spatially and kinematically. At the high resolution obtained with the interferometer, the CN clump breaks up into several subclumps in velocity space which trace almost the same features in the main and the satellite line. Slight differences occur at $\sim$12 km s^{-1} where self-absorption for the main line is strongest, and at the velocity of peak emission from the dense clumps between 11 and 11.4 km s^{-1}, where the more optically thin line almost perfectly traces the FIR5 clump.

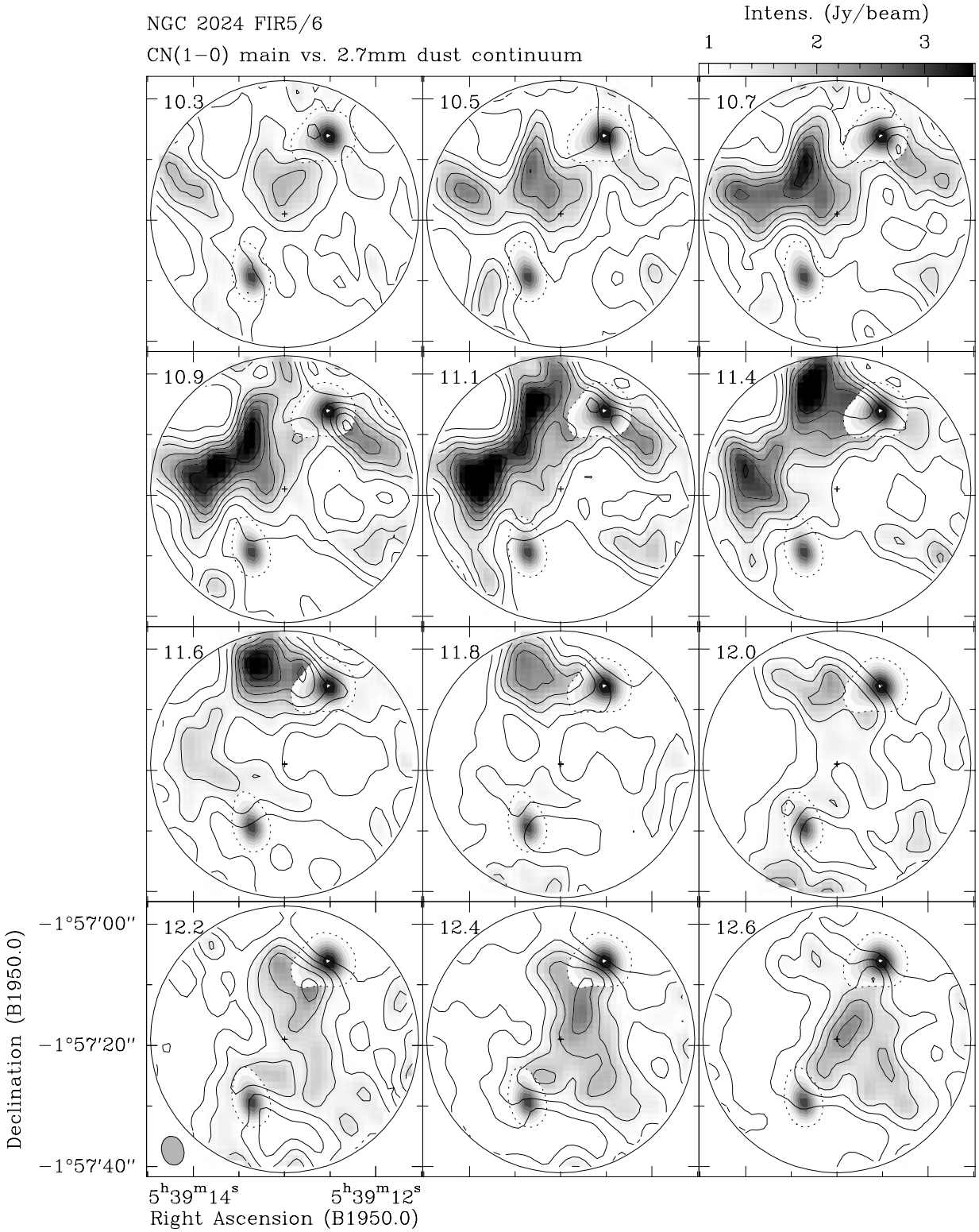

Fig. *8.19: Interferometer velocity channel maps of the main component of CN N=1→0 in a greyscale plus contour representation. Contour levels are 0.90(0.45)3.15 Jy beam*$^{-1}$ *(the beam size is indicated in the lower left panel). For comparison, the corresponding 2.7mm dust continuum emission, as grey filled contours with a dashed 3*σ *contour, is given in each panel.*

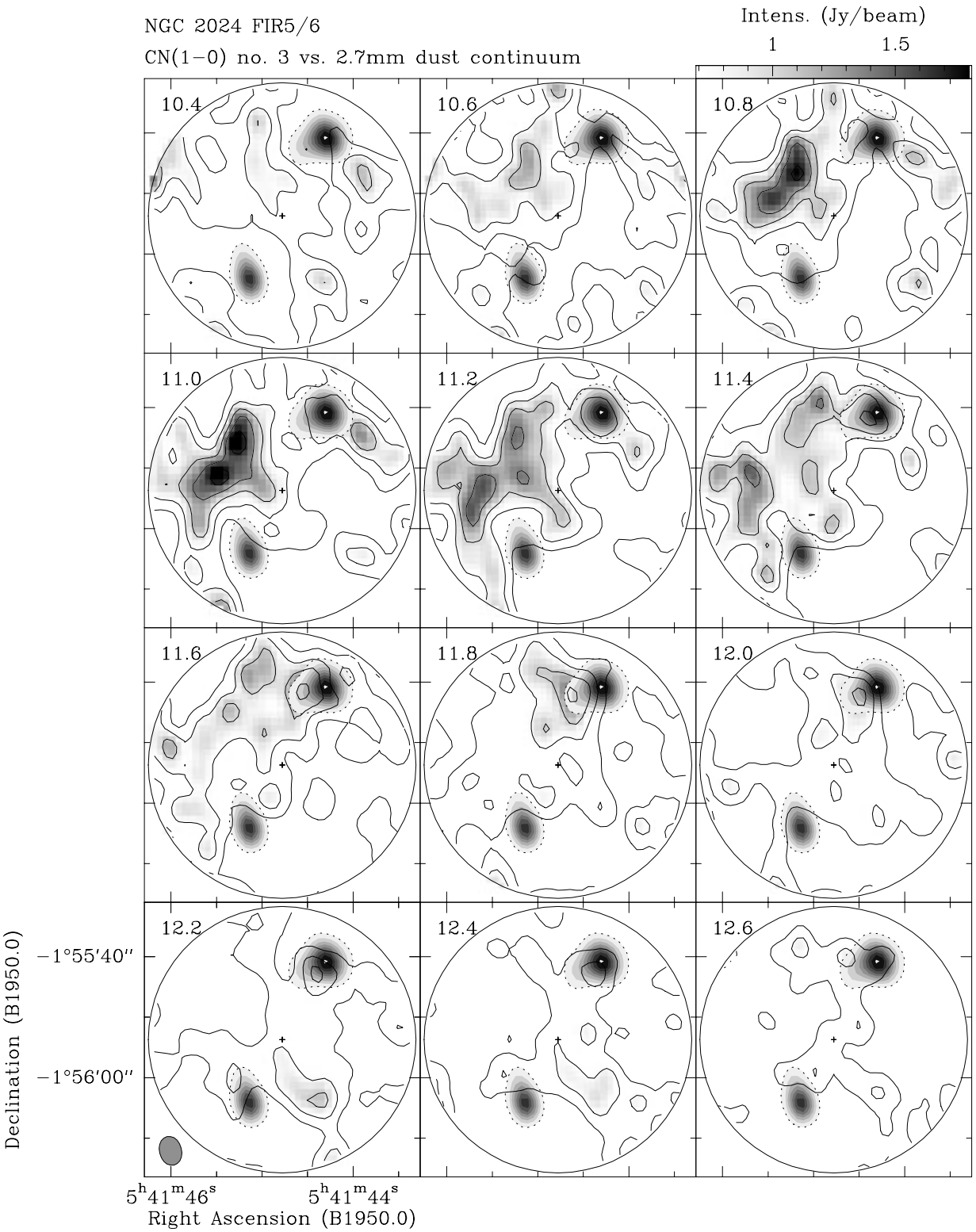

Fig. *8.20: The same as Fig. 8.19 for the weaker hyperfine component no. 3 in Fig. B.2.*

Moreover, CN N=1→0 emission between 10.3 to 12 km s^{-1} swaps from west to east across FIR5 which probably indicates rotation of molecular material with FIR5 at the center. This finding is further supported by the series of position velocity cuts at constant Declination through FIR5 presented in Fig. 8.21.

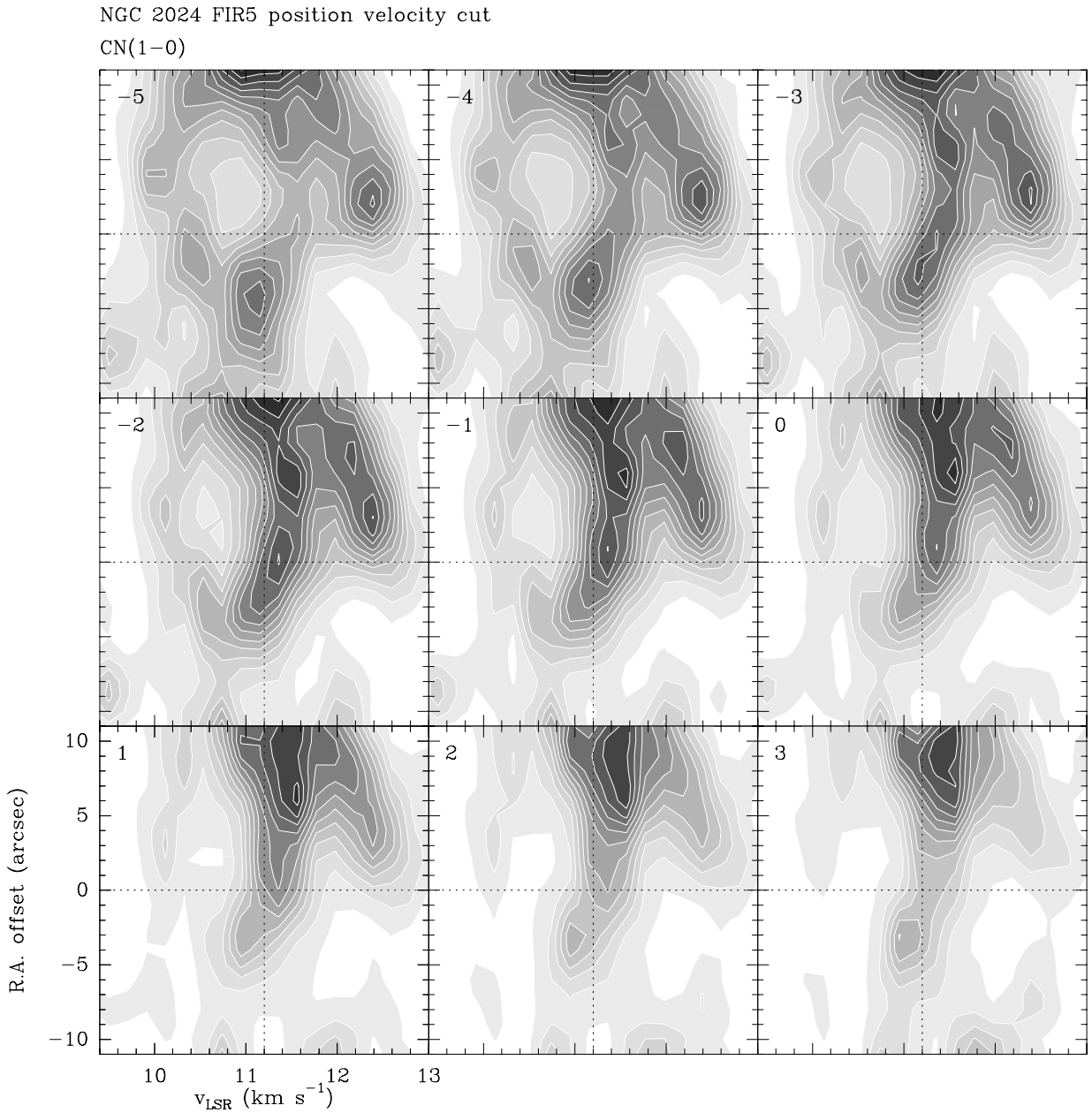

Fig. *8.21: Position velocity cuts at constant Declination through FIR5 for a CN N=1→0 satellite line. Right Ascension (left axes) and Declination (indicated as numbers in the top left corner of each panel) offsets are given in arcsec relative to the peak position of FIR5. The Right Ascension zero offset and the expected center velocity for emission are indicated by the dashed lines.*

The plot ranges of the individual panels have been selected in order to emphasize the part of the molecular emission corresponding to FIR5 in the sense that emission from the dense condensations is expected to be centered on 11.2 km s^{-1} and zero Right Ascension and Declination offsets with respect to the dust continuum peak position. These values are indicated by the dashed lines. The emission is dominated by the prominent CN clump seen in the channel maps east of FIR5 which is visible in the position velocity slices at extreme positive Right Ascension offsets. Emission associated with FIR5 is visible starting at negative Right Ascension offsets and lower velocities in the first panel moving toward positive offsets and higher velocities with increasing Declination offsets.

A fairly well defined velocity structure is seen north of FIR5 which suggests that similar to the situation for CN N=3$\rightarrow$2 discussed in the previous section, CN emission is pronounced close to the IF.

Spectra extracted at individual positions of the maps (Fig. 8.22 and 8.23) reveal a high degree of variation in the line-shapes with position, mainly due to self-absorption in the colder foreground gas. A comparison of the main and one satellite CN line over the whole field in Fig. 8.22 and 8.23 in addition confirms the conclusion drawn in the previous section that, due to the low contrast in relative intensity between the CN N=1$\rightarrow$0 hyperfine lines, even the weaker lines show signatures of self-absorption. The channel maps also show that there is in fact a high level of CN emission at velocities typical for the dense background cloud toward FIR5 and 6 and in particular in the more optically thin satellite line toward FIR5.

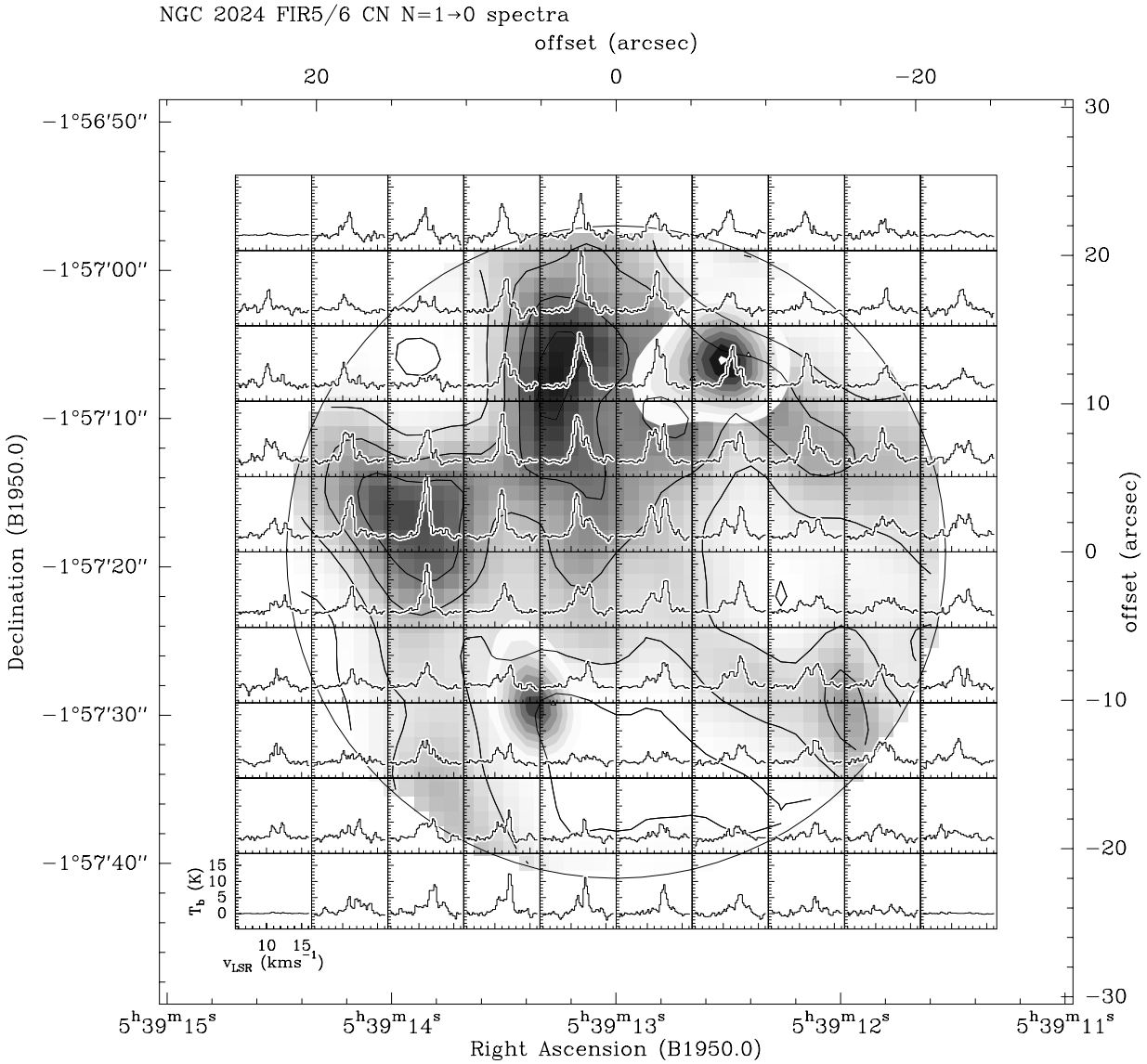

Fig. *8.22: Plateau de Bure Interferometer spectra of the CN N=1→0 main hyperfine line on top of the integrated intensity map (greyscales and black contours, see also Fig. 8.19) and the 2.7mm dust continuum emission (grey filled contours). The circle corresponds to the half power contour of the interferometer single-dish beam. Offsets are relative to the phase reference center.*

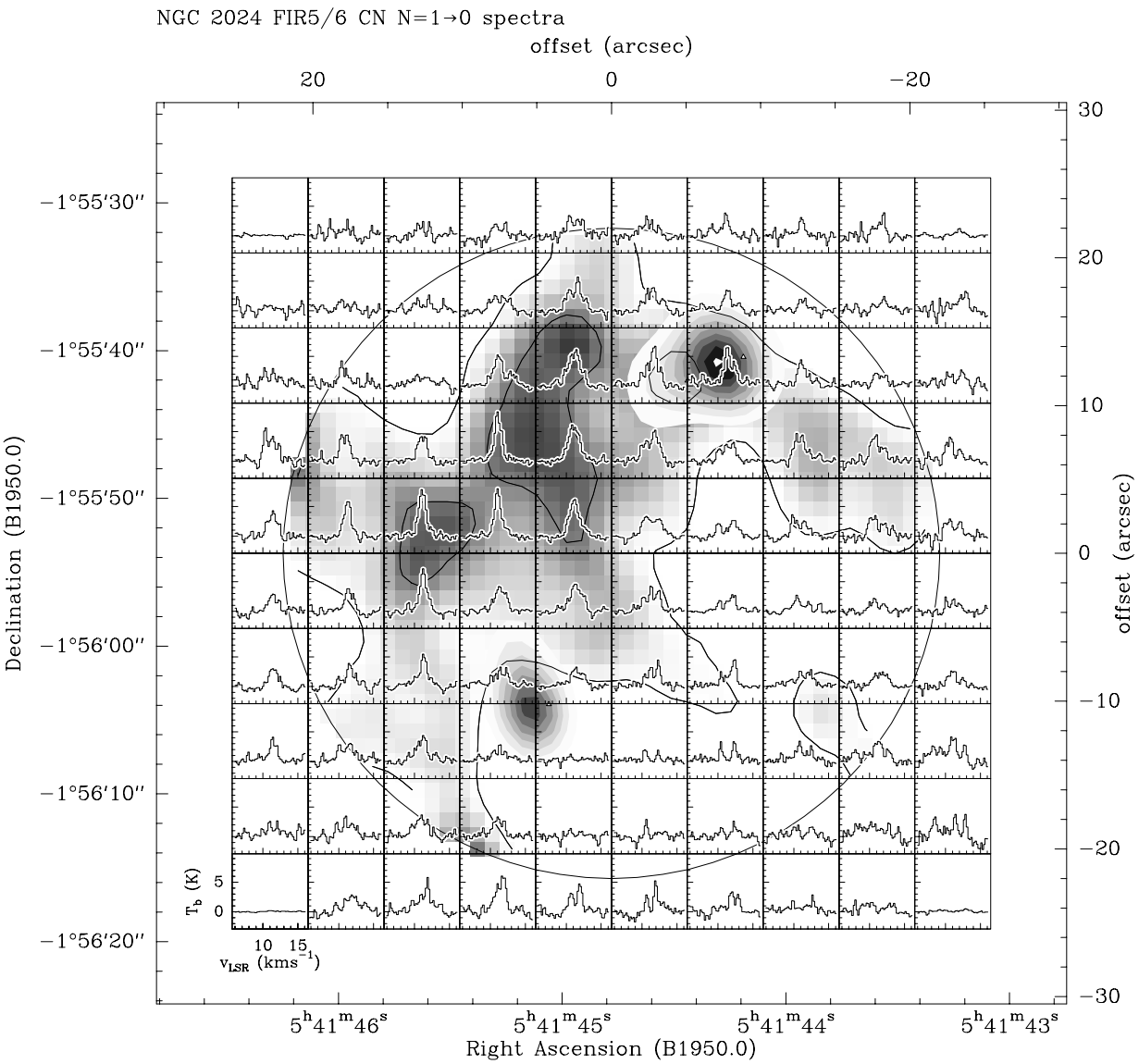

Fig. *8.23: The same as Fig. 8.22 for component no. 3 of the CN N=1→0 transition.*

8.5 Discussion

The close morphological correlation of molecular line and mm/submm dust continuum emission along the dense ridge, down to the smallest scales accessible with the interferometer, implies that both trace essentially the same material. However, results for the physical parameters summarized below, i.e. volume and column densities as well as kinetic temperatures derived from the different methods of analysis and under certain assumptions, show significant discrepancies.

Results from a number of isotopomeric molecular line studies in CS (Mundy et al. 1986, Snell et al. 1984, Moore et al. 1989a, Schulz et al. 1991, Chandler et al. 1992), HCO^+ (Lis et al. 1991, Richer et al. 1989) and NH_3 (Schulz et al. 1991, Ho et al. 1993) correspondingly imply gas temperatures of 30 – 50 K and H_2 densities and column densities of the order of $10^6 - 10^7$ cm^{-3} and 10^{23} cm^{-2} for the molecular material. Escape probability calculations with the CS data obtained in this thesis confirm the results from the multiline study of Schulz et al. (1991). Since their study already incorporated CS J=7→6, J=3→2 and additional CS lines not contained in our survey, we do not present the corresponding multiline results in detail.

According to the results from mid-J CO (Graf et al. 1993), H_2O (Mangum et al. 1997) observations, and the analysis of CS and dust continuum data observed by Chandler & Carlstrom (1996), even temperatures of 100 K or more are not excluded towards the dense condensations. However, part of the high temperature molecular gas may be located close to the HII region/molecular cloud interface in the line of sight, but the dense condensations have to be relatively close by, as concluded by Graf et al. (1993) from the comparison of low- to mid-J CO lines.

A similar conclusion is implied by our high temperature and high density tracing CN N=3→2 and CS J=7→6 observations (the N=3 and J=7 levels of CN and CS are 33 and 66 K above the ground state respectively and the critical densities of both transitions are of the order of 10^7 cm^{-3}). In particular for these two transitions, each of the far infrared peaks has its molecular counterpart in the velocity channel corresponding to emission from the dense background cloud. A simple by chance coincidence is excluded regarding the good correlation of warm and dense gas with the dust continuum toward all of the condensations along the ridge. Even a stratified distribution of CN N=3→2 and CS J=7→6 emission toward FIR4 and 5 associated with the NCP and SCP is visible in Fig. 8.15 and the cut in Fig. 8.16. Similar to the situation in the Orion Bar region, this effect can not be explained by a variation of the excitation conditions, since in this case CS J=7→6 emission should show a peak closer to the warmer part of the interface, but reflects abundance variations of chemical origin in a UV photon dominated environment. The dense condensations thus have to be very close to the interface and it is likely that they are externally heated. This finding in addition explains the differences in emission between the three rotational transitions of CN in the vicinity of the southern interface region. The N=1→0 observations predominantly trace the bulk of colder and less dense gas while, as one moves to higher frequencies, the peak intensity shifts and is dominated by emission originating in warmer and denser gas closer to the interface region. Besides optical depth effects, a similar argument holds for the observed differences in emission of CS J=7→6 compared to lower-J rotational transitions of this molecule.

The trend for CN to peak closer to the ionization front north of FIR5 than CS is also suggested

by a comparison of our high angular resolution CN N=1→0 and dust continuum observations obtained at the Plateau de Bure Interferometer and the interferometric CS observations by Wiesemeyer et al. (1996, $C^{34}S$ J=2→1) and Chandler & Carlstrom (1996, CS J=2→1). The optically thick CS J=2→1 emission peaks between and east of FIR5 and 6 in a similar manner as seen in the channel maps of the main CN N=1→0 line (Fig. 8.9 for single-dish and Fig. 8.19 for interferometer data). The emission of the weaker, more optically thin component of CN (Fig. 8.20) and of $C^{34}S$ J=2→1 from Wiesemeyer et al., peaks closer to the most prominent clump FIR5 and correspond fairly well to each other in the higher velocity channel maps (>12 km s^{-1}). For velocities between 11 and 12 km s^{-1}, CN emission is well correlated with the dust continuum and peaks slightly north of the $C^{34}S$ emission in the direction toward the ionization front.

At the very high densities ($\sim 10^7$ cm^{-3}) derived from *both* molecular line and dust continuum observations toward the FIR condensations, gas and dust are expected to be thermally coupled. At least part of the dust thus should reflect the high temperatures obtained from the molecular line observations. It is important to mention in this context that the decomposition of the spectral energy distribution of the dust emission is not unique, as has been pointed out and shown by a number of authors. A serious constraint in the procedure to derive spectral fits to the continuum fluxes is the unknown dependence of the dust opacity index on the frequency ($\tau_\nu \propto \nu^\beta$) in the mm to submm wave length range. Mezger et al. (1988, 1992) use a value of $\beta = 2$ which corresponds to the theoretical limit for small grains, whereas values of $\beta < 2$ are conceivable depending on the grain properties. Wiesemeyer et al. (1996) determine values of $1.0 - 1.4$ from a continuum radiative transfer model and dust temperatures of the order of 20 K but also note the possibility of higher dust temperatures as being appropriate because of a lack in high resolution short wavelength observations of the continuum spectrum. Direct evidence for variations in β recently was reported from continuum observations at 450 and 800μm obtained by Visser et al. (1996).

As a matter of fact, the three component spectral fits of Mezger et al. (1988, 1992), which result in the very low dust temperatures for the FIR cores, require a warm dust component (~ 45 K) in order to adequately account for the high fluxes at short wavelengths between 40 and 160μm. Moreover, the observed mm and submm continuum spectrum is even well reproduced without invoking the presence of very cold dust. Schulz et al. (1991) reanalyzed the dust emission from NGC 2024 in terms of a two component model with $\beta = 2$, resulting in higher dust temperatures between 35 and 50 K for both components. Moore et al. (1989a) showed that the observed flux densities are well fitted with only one warm dust component at $T_{dust} = 47$ K if one assumes a dust opacity index $\beta = 1.6$.

One possible scenario compatible with the above findings is that of a dense, externally heated clump, where the molecules and the warm dust trace the UV heated surface layers and the cold dust in the core is too deeply embedded to be significantly heated from outside. Under the assumption that no embedded stellar core has formed yet, molecules would experience significant depletion due to freeze-out onto dust grains at the high densities and low temperatures postulated for these conditions. The relative abundances resulting for CN by adopting H_2 column densities from the literature are only slightly lower than the values determined for the OMC-1 ridge

(see Table 7.2), and agree fairly well with the chemical model results for the Orion Bar region obtained in Section 7.8. Moreover, the values determined for the total CN column density, in particular toward the southern condensations FIR5 and 6 (see Table 8.1), agree fairly well with those obtained for the warm and dense OMC-1. Regarding the uncertainties in the adopted H_2 column densities, our CN observations do *not* indicate any depletion effects for this species. Graf et al. (1993), from the low intensities of low-J isotopomeric CO lines toward FIR5, exclude the presence of large amounts of very cold and dense gas. They also do not find any signature of an extended layer of molecular material tracing intermediate temperatures in a potential transition zone from the warm, externally heated clump surface ($\sim$50 K) to the cold cloud core ($<$20 K). Together with the above shown lack of depletion for CN, the picture of externally heated but inside heavily depleted clumps seems less convincing.

The apparent density dilemma between molecular line and dust continuum results is solved if one assumes centrally heated cores rather than cold isothermal condensations since in this case the densities and column densities derived from the continuum observations are lowered substantially and the dust temperature increases, leading to a much better agreement between the parameters derived from molecular line and dust emission observations. An additional attractive feature of centrally heated cores is the fact that the lack in contrast between molecular line and continuum maps can be explained with the different sensitivities of the two observational techniques to temperature and column density. As first pointed out by Goldsmith (1988) and Richer (1990), optically thin molecular line emission measures $\mathrm{N_{mol}}/\mathrm{T_{gas}}$ whereas optically thin dust emission measures $\mathrm{N}_{dust} \times \mathrm{T}_{dust}$. Mm and submm dust continuum emission consequently should peak toward embedded heating sources while molecular line emission is expected to have a more flattened distribution, as it is observed.

However, the most compelling independent evidence that at least some of the clumps contain evolved central objects comes from observations of unusual activity towards them. The center of the extended CO outflow discovered by Sanders & Willner (1985) is close to and likely associated with FIR5, although the exact location of the driving source is difficult to identify due to the lack of prominent blue shifted emission. The dynamical timescale for the FIR5 outflow is of the order $\mathrm{t}_{dyn} \sim 10^4$ yr (Richer et al. 1992). Compact outflows on a much shorter dynamical timescale have been detected toward FIR4 ($\mathrm{t}_{dyn} \sim 10^3$ yr, Chandler & Carlstrom 1996) and FIR6 ($\mathrm{t}_{dyn} \sim 400$ yr, Richer et al. 1990). While the outflow of FIR6 is bipolar and associated with an H_2O maser (Genzel & Downes 1982), FIR4 only shows a red lobe, but an adjacent infrared reflection nebulosity counterpart (Moore & Yamashita 1995) and a NIR point source (Moore & Chandler 1989b) at the center between them.

The observed short timescales of the outflows together with the fact that the dust masses in the envelopes of FIR5 and FIR6 are much larger than the masses of any possible, yet undetected, circumstellar disk (Chandler & Carlstrom 1996 and Wiesemeyer et al. 1996), suggest that all objects are very young and lend support to an evolutionary sequence in star formation for the region. As proposed by Chandler & Carlstrom (1996), this sequence has been triggered by the interaction between the expanding HII region and the molecular cloud. Following their conclusions, FIR4 and FIR5, which are associated with the NCP and SCP, are thus older, FIR6 is a

younger active object and the remaining FIR sources are all less luminous and in an earlier stage of their evolution.

8.6 Conclusions

High angular *and* spectral resolution observations of CN rotational transitions reveal a good correlation of molecular and dust continuum emission, in particular for the more optically thin hyperfine lines and for the higher density and temperature tracing transitions.

The striking correlation of dense and warm gas, as found in simultaneous observations of CN N=3→2 and CS J=7→6 transitions, and the dust continuum, provide important new evidence that the compact condensations, originally found in the mm and submm continuum, are likely to be warm and externally heated cores with additional embedded heating sources in some, if not all of them.

Our CN column densities and relative abundances show no signatures for significant molecular depletion in the cores.

The close relation of warm, dense, UV influenced gas and the compact sources supports a scenario in which sequential star formation has been triggered by the expanding HII region.

Similar to the results obtained for the Orion Bar region, the CN and CS observations show a UV influenced stratified distribution of both molecules at the ionization front associated with the dust continuum peak FIR5.

Chapter 9. Future prospects

Observations of the CN radical proved to be an important tool in probing the interstellar medium from mm to submm wave lengths. Especially in conjunction with molecules like HCN (as proposed by e.g. Fuente et al. 1996) and CS from this work, the differences in the emission distributions yield important information on the excitation and chemistry in the observed cloud layers. The refinement of chemical models already provided substantial new understanding of some high resolution observational features like the stratified distribution of CN and CS in photon dominated regions, which, as indicated by some results from this thesis, seems to be a common phenomenon in interstellar space. Along with the development of clumpy chemical models, interesting new results for the above mentioned species are to be expected. In this context, observations of higher excited rotational transitions deep into the submm wave length range will help to settle the excitation conditions for CN in particular at the warm and dense surface layers of UV irradiated clumps.

For some sources, e.g. S140 and S106, there already exist complete data sets for the lowest three CN rotational transitions (maps are introduced in the Appendix) which are employed together with available [CII] and [OI] fine structure observations (Schneider 1995) for a detailed analysis of regions with different morphology and incident UV field than found in Orion A. Corresponding publication are in preparation.

With the improved receiver sensitivity at hand it is now possible to observe even the rarer isotopomer ^{13}CN over a wide range of sources and thus to use chemical fractionation effects as a probe of the UV field in the clouds.

Unlike most other molecular tracers, CN emission follows the mm and submm dust continuum fairly well in a variety of sources. The reasons for this may be manifold and depend on the overall properties of the sources. Much confusion stems from the ambiguities related to the determination of the dust temperature from the spectral energy distribution. High resolution observations at shorter wave lengths with ISO or SOFIA will help to settle the turn-over of the dust spectrum and thus will yield more reliable fits and decompositions into contributions from dust at the various temperatures.

Chapter 10. The development of a new continuum backend for KOSMA

The continuum backend (COBAC) detects the intermediate frequency (IF) signal corresponding to the total incoming power within the bandpass of the receiver without analyzing it spectroscopically. It is used at the KOSMA 3m radio telescope for a variety of essential tasks briefly summarized below.

- Strong, well confined continuum sources, in the case of KOSMA these are the brighter planets, are observed to determine the positioning and to monitor the pointing accuracy of the telescope by means of cross scans centered on the object.
- Observations of planets and the moon yield important information on the antenna pattern and the angular extent and efficiency of the main beam, as well as of the side-lobes, and possible error-beams.
- COBAC counts from absorbers at ambient (hot) and liquid nitrogen (cold load) temperature are used in continuum mode to calibrate the temperature scale of the receiver.
- Continuous skydip scans record the atmospheric noise as a function of elevation and thus allow to infer the atmospheric transmission (opacity) at the observed frequency and the forward efficiency (η_l).
- The appropriate focus position of the subreflector is determined either by scans across the edge of the moon or by continuously moving the subreflector while pointing on a strong source (e.g. Jupiter). This procedure is in principle possible for three main axes.
- Measurements of the main dish surface accuracy are performed by means of a phase retrieval method (often referred to as *Holography*) with a transmitter as emission source.

10.1 Motivation for a new COBAC

With the former COBAC (Krotz-Vogel 1984), the IF signal from the receiver was transformed into a voltage using a diode detector, it was amplified and then converted into a proportional frequency by a voltage controlled oscillator (VCO). The resulting frequency was counted and further processed by the main computer which at that time was a PDP11/53. It was a single channel backend with a limited dynamic range, and fixed signal/reference (S/R) cycle lengths and dead times. Data transfer was performed via a parallel interface.

Several basic changes at the KOSMA observatory resulted in the necessity for a new design of the COBAC, primarily the replacement of the PDP by a μVAX supporting only communication via Ethernet with DECnet protocol. An improved primary mirror for the telescope, with a surface accuracy of the individual segments of the order of 10μm rms, imposed an additional requirement to the dynamic range for the holographic method and the adjustment of the panels.

The spectral line receiver development changed from a single toward a dual frequency design, resulting in the need for at least one additional COBAC input channel. It was also planned to have an additional channel available for the holographic measurements, with a refined observational procedure incorporating two receivers.

For reasons of more flexibility, the new COBAC should allow the use of variable lengths of the S/R cycles and variable dead times in order to properly handle observations with choppers (e.g. wobbling secondary or beam switch mirror). The COBAC should be fully operational in a stand-alone mode without the central computer.

10.2 Concept and realization

Under consideration of the above listed requirements, a new hard- and software concept was developed within the framework of the present and one other thesis (Schneider 1995).

10.2.1 Hardware

The new COBAC consists of three individual units: two detectors and a PC for data acquisition. The first device contains a detector diode of extremely well linearity which is responsible for the conversion of the total IF power to a proportional voltage. This voltage is amplified by a low noise amplifier (60dB gain). The second backend is a single channel acousto-optical spectrometer with a photo-multiplier as the central detecting unit and was developed in parallel at the institute by Feckler (1993) and Siebertz (1995). The resulting signal is amplified and pre-integrated by an RC-device.

The data acquisition is performed with an analog to digital converter (A/DC) plug-in on a standard carrier module. In addition, the carrier contains a 12 bit digital to analog converter (D/AC) which allows the connection of a chart recorder. The carrier itself is installed on a standard 80386 PC.

The output voltages from the detectors are adjusted to match the appropriate input range of the A/DC ($\pm$5V). Considering the requirements concerning the dynamic range for the holographic measurements ($\sim$40dB), a 16 bit resolution A/DC was chosen, providing a dynamic range of 48dB. The module has a maximum of four differential input channels or one single ended coaxial input. Data acquisition is initiated by an external 200 Hz (5ms) pacer which triggers the read-out of the A/DC and constitutes the minimum S- and R-cycle time as well as the minimum dead time for operation. S/R cycle lengths and dead times are chosen in units of this minimum time. The pacer signal is provided by an external distribution box (KOSMA 1994) which uses the output of an atomic clock as frequency standard or, in the stand-alone mode, by an internal 1 MHz quartz clock. With one pacer signal all connected input channels are read out sequentially (the conversion and settling time of the A/DC is 16μs) and an output signal on the D/AC for the chart recorder is generated by the software. Most of the components in use and listed below are standard hardware and, with the exception of the AOC, completely new hardware developments were kept to a minimum.

Detector: Hewlett Packard HP8471D Schottky diode, max. input power is 100mW
Characteristics: voltage = –4.863 V + 10.402 mV/μW $\times$ P_{out}

Amplifier: ITHACO/HMS 566 Low Noise Amplifier, 40/60dB gain
Carrier: Burr-Brown PCI 20001C–2A for three plug-in modules
A/DC: Burr-Brown PCI 20341M–1 16bit, 4 differential input channels
D/AC: Burr-Brown PCI 20003M–2 12bit, 2 output channels

10.2.2 Software

The data transfer and communication with the central computer, as well as the stand-alone user interface, is provided by software modules written in C which are also used as modified applications on other PCs of the observatory. Programming of the data acquisition in this software environment and the timing, particularly in conjunction with astronomical and holographic measurements, where the synchronization with the telescope and the central computer is essential, was one of the main tasks in the realization of the new COBAC.

Due to the 200 Hz pacer signal, the A/DC is continuously converting the input signals even without starting a regular measurement which is particularly useful when using a chart recorder. The actual converted voltage is accessed by a read-out from a fixed register address which is composed of the carriers base address in the PC memory and an offset corresponding to the slot where the module is plugged in. An external *data valid* signal, either coming from the central computer as soon as the telescope is in position, or from a keyboard input in stand-alone mode, starts the acquisition of *valid* data. The number of channels of the actual scan and the length of each channel in units of 5ms, as well as dead times, are variable and handled by software counters on the basis of 5ms. The individual 5ms values within each channel are averaged.

In the so called *switch power* observing mode, which is used in conjunction with a wobbling secondary, a beam switch mirror, or for frequency switching, it is necessary to unambiguously discern the signal from the reference cycle. For this purpose, the external S/R signal, which is generated by the distribution box and used to trigger the chopper, is used as additional input on the carrier to make the subdivision of the measured counts into S and R. This distinction is redundant in *total power* mode since in this case there is no difference between signal and reference phase.

Since all signals relevant for the timing are connected to the carrier, their status is known to the software at any time and simply extracted from the bit sequence at the appropriate base address. The timing is sketched in the timing diagram displayed in Fig. 10.1. Each 5ms pacer signal triggers the successive conversion of all connected channels, at most 4 as indicated in the example. The read-outs are only valid if the corresponding data valid signal is present. Variable dead times at the beginning of each S and R cycle are considered. They are longer for the Holography mode due to the settling time constant in the AOC. The S and R data for each channel are written to corresponding signal and reference arrays in the PC memory and, once the scan is finished, are transfered to the main computer or may be saved on files on the hard disk in stand-alone mode.

The new COBAC was implemented into the system on Gornergrat in 1994 and is fully operational since then. By the time this thesis was finished, measurements of the surface accuracy of the new improved telescope dish and its adjustment were still in progress and so far an improvement to a

value of $\sim 30\mu$m was achieved.

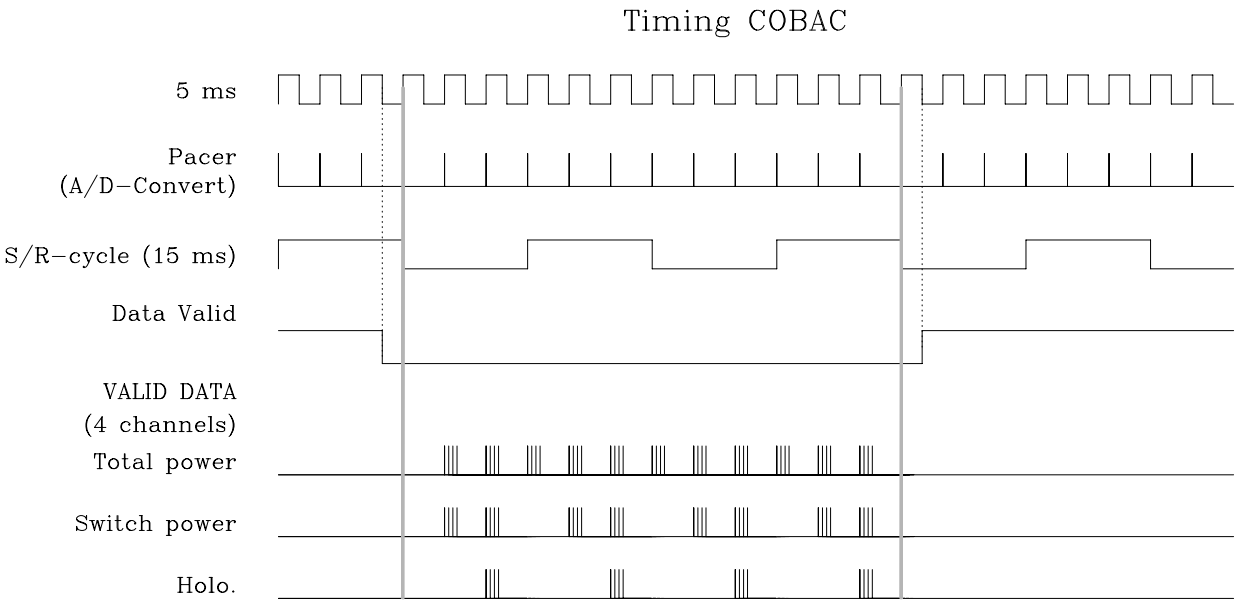

Fig. *10.1: Timing diagram of the new COBAC for representative total power, switch power and holographic measurements.*

References

Adams, W.S., 1941, ApJ 93, 11

Anthony-Twarog, B.J., 1982, AJ, 87, 1213

Baars, J.W.M., Hooghoudt, B.G., Mezger, P.G., de Jonge, M.J., 1987, A&A, 175, 319

Bally, J., Langer, W.D., Stark, A.A., Wilson, R.W., 1987, ApJ, 312, L45

Barnes, P.J., Crutcher, R.M., Bieging, J.H., Storey, J.W.V., Willner, S.P., 1989, ApJ, 342, 883

Barnes, P.J., Crutcher, R.M., 1990, ApJ, 351, 176

Batrla, W., Wilson, T.L., Bastien, P., Ruf, K., 1983, A&A, 128, 279

Beck, S.C., Beckwith, S., 1983, ApJ, 271, 175

Becklin, E.E., Neugebauer, G., 1967, ApJ, 147, 799

Black, J.H., van Dishoeck, E.F., 1991, ApJ, 369, L9

Blake, G.A., Mundy, L.G., Carlstrom, J.E., Padin, S., Scott, S.L., Scoville, N.Z., Woody, D.P., 1996, ApJ, 472, L49

Blake, G.A., Sutton, E.C., Masson, C.R., Phillips, T.G., 1987, ApJ, 315, 621

Bogey, M., Demuynck, C., Destombes, J.L., 1984, Can. J. Phys. 62, 1248

Bohlin, R.C., Savage, B.D., Drake, J.F., 1978, ApJ, 224, 132

Booth, R.S., Delgado, G., Hagstrom, M., et al., 1989, A&A, 216, 315

Castets, A., Duvert, G., Dutrey, A., Bally, J., Langer, W.D., Wilson, R.W., 1990, A&A, 234, 469

Cesaroni, R., Wilson, T.L., 1994, A&A, 281, 209

Chandler, C.J., Moore, T.J.T., Emerson, J.P., 1992, MNRAS, 256, 369

Chandler, C.J., Carlstrom, J.E., 1996, ApJ, 466, 338

Cheung, A.C., Rank, D.M., Townes, C.H., Thornton, D.D., Welch, W.S., 1968, ApJ, 186, L73

Churchwell, E., Felli, M., Woods, D., Massi, M., 1987, ApJ, 321, 516

Crutcher, R.M., Churchwell, E., Ziurys, L.M., 1984, ApJ, 283, 668

Crutcher, R.M., Henkel, C., Wilson, T.L., Johnston, K.J., Bieging, J.H., 1986, ApJ, 307, 302

Dale, R.M., Herman, M., Johns, J.W.C. et al., 1979, Can. J. Phys. 57, 677

Degiacomi, C.G., Schieder, R., Stutzki, J., Winnewisser, G., 1995, Optical Engineering, 34, 2701

Dixon, T.A., Woods, R.C., 1977, J. Chem. Phys. 67, 3956

Dougados, C., Lena, P., 1993, ApJ, 406, 112

Downes, D., 1989, in *Introductory courses in Galaxies*, Springer, p. 1

Draine, B.T., 1978, ApJS, 36, 595

Feckler, J., 1993, diploma thesis, I. Physikalisches Institut, Universität zu Köln

Flower, D.R., Launey, J.M., 1985, MNRAS 214, 271

Fuente, A., Rodríguez-Franco, A., Martín-Pintado, J., 1996, A&A, 312, 599

Garcia-Burillo, S., Combes, F., Gerin, M., 1993, A&A, 274, 144

Gatley, I., Kaifu, N., 1987, in Astrochemistry, Vardya, M.S., Tarafdar, S.P., Eds. (Reidel, Dordrecht, Netherlands), p. 153

Gaume, R.A., Johnston, K.J., Wilson, T.L., 1992, ApJ, 388, 489

Genzel, R., Downes, D., 1977, A&AS, 30, 145

Genzel, R., Downes, D., Ho, P.T.P., Bieging, J.H., 1982, ApJ, 259, L103

Genzel, R., Reid, M.J., Moran, J.M., Downes, D., 1981, ApJ, 244, 884

Genzel, R., Stutzki, J., 1989, ARA&A 27, 41

Gerin, M., Combes, F., Encrenaz, P., et al. 1984, A&A 136, L17

Gierens, K.M., Stutzki, J., Winnewisser, G., 1992, A&A, 259, 271

Goldsmith, P.F., 1988, in *Molecular Clouds in the Milky Way and External Galaxies*, eds. Dickmann, R.L.,

Snell, R.L., Young, J.S., Springer-Verlag, Berlin, p. 1
Gordy, W., Cook, R.L., 1984, Diatomic Molecules
Graf, U.U., Genzel, R., Harris, A.I., Hills, R.E., Russell, A.P.G., Stutzki, J., 1990, ApJ, 358, L49
Graf, U.U., Eckart, A. Genzel, R., Harris, A.I., Poglitsch, A., Russell, A.P.G., Stutzki, J., 1993, ApJ, 405, 249
Greaves, J.S., White, G.J., 1992, MNRAS, 259, 457
Greaves, J.S., Church, S.E., 1996, MNRAS, 283, 1179
Green, S., Chapman, S., 1978, ApJS, 37, 169
Greve, A., Kramer, C., Wild, W., 1997, A&A, submitted
Guilloteau, S., et al., 1992, A&A, 262, 624
Henkel, C., Wilson, T.L., Bieging, J., 1982, A&A, 109, 344
Herrmann, F., Madden, S.C., Nikola, T., Poglitsch, A., Timmermann, R., Geis, N., Townes, C.H., Stacey, G.J., 1997, ApJ, 481, 343
Herzberg, G., 1950, Spectra of Diatomic Molecules
Ho, P.T.P., Barrett, A.H., 1978, ApJ, 224, L23
Ho, P.T.P., Peng, Y., Torrelles, J.M., Gomez, J.F., Rodriguez, L.F., Canto, J., 1993, ApJ, 408, 565
Hogerheijde, M.R., Jansen, D.J., van Dishoeck, E.F., 1995, A&A, 294, 792
IUPAC, 1988, in *Quantities, units and symbols in physical chemistry*, Oxford 1988, p. 91
Jansen, D.J., Spaans. M., Hogerheijde, M.R., van Dishoeck, E.F., 1996, A&A, 303, 541
Jefferts, K.B., Penzias, A.A., Wilson, R.W., 1970, ApJ 161, L87
Kaiser, M.E., Hawkins, I., Wright, E.L., 1991, ApJ, 379, 267
Kistiakowsky, G.B., Gershinowitz, H., 1933, J. Chem. Phys. 1, 432
Kleinmann, D.E., Low, F.J., 1967, ApJ, 149, L1
Köster, B., Störzer, H., Stutzki, J., Sternberg, A., 1994, A&A, 284, 545
KOSMA, 1994, Technischer Bericht Nr. 9, Taktselektbox
Krotz-Vogel, 1984, Ph.D. thesis, I. Physikal. Institut, Universität zu Köln
Kutner, M.L., Evans, N.J., II, Tucker, K.D., 1976, ApJ 209, 452
Kutner, M.L., Ulich, B.L., 1981, ApJ 250, 341
Lada, E.A., Bally, J., Stark, A.A., 1991, ApJ, 368, 432
Langer, W.D., Penzias, A.A., 1990, ApJ, 357, 477
Langer, W.D., Penzias, A.A., 1993, ApJ, 408, 539
Langer, W.D., 1992, in *The Astrochemistry of Cosmic Phenomena*, IAU Symp. n° 150, ed. P.D.Singh, Kluwer Acad. Publ., p. 193
Lis, D.C., Carlstrom, J.E., Phillips, T.G., 1991, ApJ, 370, 583
Maddalena, R.J., Morris, M., Moscowitz, J., Thaddeus, P., 1986, ApJ, 303, 375
Mangum, J.G., Wootten, A., Barsony, M., 1997, in *Low Mass Star Formation – from Infall to Outflow*, poster proceedings of IAU Symp. n° 182, eds. F. Malbet & A. Castets, Kluwer Acad. Publ., p. 18
Marcy, G.W., Butler, R.P., Williams, E., Bildstein, L., Graham, J.R., Chez, A.L., Jernigan, J.G., 1997, ApJ, 481, 926
Masson, C.R., Mundy, L.G., 1988, ApJ, 324, 538
Mauersberger, R., Wilson, T.L., Mezger, P.G., Gaume, R., Johnston, K.J., 1992, A&A, 256, 640
Meyer, D.M, Jura, M., 1985, ApJ 297, 119
Meyer, D.M, Roth, K.C., Hawkins, I., 1989, ApJ 343, L1
Mezger, P.G., Chini, R., Kreysa, E., Wink, J., Salter, C.J., 1988, A&A, 191, 44
Mezger, P.G., Wink, J.E., Zylka, R., 1990, A&A, 228, 95

Mezger, P.G., Sievers, A.W., Haslam, C.G.T., Kreysa, E., Lemke, R., Mauersberger, R., Wilson, T.L., 1992, A&A, 256, 631

Mihalas, D., 1978, "Stellar Atmospheres", 2^{nd} edition, Freeman, San Francisco

Millar, T.J., Farquhar, P.R.A., Willacy, K., 1997, AAS, 121, 139

Moore, T.J.T., Chandler, C.J., Gear, W.K., Mountain, C.M., 1989, MNRAS, 237, 1p

Moore, T.J.T., Chandler, C.J., 1989, MNRAS, 241, 19p

Moore, T.J.T., Yamashita, T., 1995, ApJ, 440, 722

Mundy, L.G., Snell, R.L., Evans II, N.J., Goldsmith, P.F., Bally, J., 1986, apJ, 306, 670

O'Dell, C.R., Wen, Z., Hu, X., 1993, ApJ, 410, 696

Penzias, A.A., Wilson, K.B., 1965, ApJ, 142, 419

Penzias, A.A., Wilson, K.B., Jefferts, R.W., 1974, Phys. Rev. Lett. 32, 701

Plambeck, R.L., Wright, M.C.H., Welch, W.J., et al., 1982, ApJ, 259, 617

Richer, J.S., Hills, R.E., Padman, R., Russell, A.P.G., 1989, MNRAS, 241, 231

Richer, J.S., 1990, MNRAS, 245, 24p

Richer, J.S., Hills, R.E., Padman, R., 1992, MNRAS, 254, 525

Rodríguez-Franco, A., Martín-Pintado, J., Gómez-Gonzales, J., Planesas, P., 1992, A&A, 264, 592

Saleck, A.H., 1995, private communication

Saleck, A.H., 1995, Ph.D. thesis, I. Physikal. Institut, Universität zu Köln

Saleck, A.H., Yamada, K.M.T., Winnewisser, G., 1991, Molec. Physics 72, 1135

Saleck, A.H., Simon, R., Schneider, N., Winnewisser, G., 1993, ApJ, 414, L133

Saleck, A.H., Simon, R., Winnewisser, G., 1994, ApJ, 436, 176

Saleck, A.H., Simon, R., Winnewisser, G., Wouterloot, J.G.A., 1994, Can. J. Phys., 72, 747

Sanders, D.B., Willner, S.P., 1985, ApJ, 293, L39

Scalo, J.M., 1990, in *Physical Processes in Fragmentation and Star Formation*, R. Capuzzo-Dolcetta et al. eds., Kluwer: Dordrecht

Schilke, P., Walmsley, C.M., Pineau des Forêts, G., Roueff, E., Flower, D.R., Guilloteau, S., 1992, A&A, 256, 595

Schmid-Burgk, J., Güsten, R., Mauersberger, R., Schulz, A., Wilson, T.L., 1990, ApJ, 362, L25

Schneider, N., 1995, Ph.D. thesis, I. Physikal. Institut, Universität zu Köln

Schneider, N., Madden, S., Stutzki, J., Block, D., Winnewisser, G., 1995, in: *The Physics and Chemistry of Interstellar Molecular Clouds*, 1995, 2^{nd} Cologne-Zermatt Symposium, eds. G. Winnewisser, G. Pelz, Lecture notes in physics 459, p. 128

Schneider, N., Stutzki, J., Winnewisser, G., Block, D., 1997, A&A, submitted

Schulz, A., Güsten, R., Zylka, R., Serabyn, G., 1991, A&A, 246, 570

Siebertz, L.A., 1995, diploma thesis, I. Physikalisches Institut, Universität zu Köln

Simon, R., 1992, diploma thesis, I. Physikalisches Institut, Universität zu Köln

Simon, R., Stutzki, J., Sternberg, A., Winnewisser, G., 1997, A&A, 327, L9

Skatrud, D.D., De Lucia, F.C., 1983, J. Mol. Spectr. 99, 35

Snell, R.L., Mundy, L.G., Goldsmith, P.F., Evans II, N.J., Erickson, N.R., 1984, ApJ, 276, 625

Sternberg, A., Dalgarno, A., 1989, ApJ, 338, 197

Sternberg, A., Dalgarno, A., 1995, ApJS, 99, 565

Störzer, H., Stutzki, J., Sternberg, A., 1995, A&A, 296, L9

Stutzki, J., Winnewisser, G., 1985, A&A, 144, 13

Stutzki, J., Winnewisser, G., 1985, A&A, 148, 262

Stutzki, J., Genzel, R., Graf, U.U., Harris, A.I., Jaffe, D.T., 1989, ApJ, 340, L37

Subrahmanyan, R., 1992, MNRAS, 254, 719
Sutton, E.C., Blake, G.A., Masson, C.R., Phillips, T.G., 1985, ApJS 58, 341
Tatematsu, K., Umemoto, T., Kameya, O., et al., 1993, ApJ, 404, 643
Tauber, J.A., Tielens, A.G.G.M., Meixner, M., Goldsmith, P.F., 1994, ApJ, 422, 136
Tauber, J.A., Lis, D.C., Keene, J., Schilke, P., Büttgenbach, T.H., 1995, A&A, 297, 567
Thomson, R., Dalby, F.W., 1968, Can. J. Phys. 46, 2815
Tielens, A.G.G.M., Hollenbach, D., 1985a, ApJ, 291, 722
Tielens, A.G.G.M., Hollenbach, D., 1985b, ApJ, 291, 747
Tielens, A.G.G.M., Meixner, M., van der Werf, P.P., et al., 1993, Sci, 262, 86
Tiemann, E., 1982, J. Mol. Spec., 91, 60
Townes, C.H., Schawlow, A.L., 1975, Microwave Spectroscopy
Turner B.E., Gammon., 1974, ApJ
Turner B.E., Thaddeus P., 1977, ApJ 211, 755
Ungerechts H., Bergin E.A., Carpenter J., et al. 1992, in *The Astrochemistry of Cosmic Phenomena*, IAU Symp. n° 150, ed. P.D.Singh, Kluwer Acad. Publ., p. 271
van der Werf, P.P., Stutzki, J., Sternberg, A., Krabbe, A., 1996, A&A 313, 633
van Dishoeck, E.F., Black, J.H., 1988, ApJ, 334, 711
Visser, A.E., Richer, J.S., Chandler, C.J., Carlstrom, J.E., Padman, R., 1996, JCMT Newsletter no. 7
Wannier, P.G., 1980, ARA&A 18, 399
Wannier, P.G., Linke, R.A., Penzias, A.A., 1981, ApJ 247, 522
Watson, J.K.G., 1980, J. Mol. Spectr. 80, 411
Weinreb, S., Barrett, A.A., Meeks, M.S., Henry, J.C., 1963, Nature, 200, 829
Werner, M.W., Gatley, I., Harper, D.A., Becklin, E.E., Loewenstein, R.F.,
White, J.V., 1940, J. Chem. Phys. 8, 79
White, G.J., Padman, R., 1991, Nature, 354, 511
White, G.J., Sandell, G., 1995, A&A, 299, 179
Wiesemeyer, H., Güsten, R., Wink, J.E., Yorke, H.W., 1996, A&A,
Wilson, T.L., Serabyn, E., Henkel, C., Walmsley, C.M., 1986, A&A, 158, L1
Wilson, K.B., Jefferts, R.W., Penzias, A.A., 1970, ApJ, 161, L43
Wilson, K.B., Mehringer, D.M., Dickel, H.R., 1995, A&A, 303, 840
Winnewisser, G., Zimmermann, P., Hernichel, J., et al., 1990, A&A 30, 248
Winnewisser, G., Herbst, E., 1993, Rep. Prog. Phys., 56, 1209
Wynn-Williams, C.G., Genzel, R., Becklin, E.E., Downes, D., 1984, ApJ, 281, 172
Yusef-Zadeh, F., 1990, ApJ, 361, L19
Zuckermann, B., 1973, ApJ, 183, 863

Appendix A. Frequencies

Tables (A.1) to (A.3) contain frequency predictions for CN, ^{13}CN and C^{15}N ground state rotational transitions up to 1 THz. The frequencies have been calculated using the isotopically invariant parameters from Saleck et al. (1994a).

A.1 CN Frequencies

CN $v = 0$: Predicted rotational spectrum up to 1 THz

N'	J'	F'	–	N''	J''	F''	Frequency	σ	E''/cm^{-1}	rel. Int.
1	1/2	1/2		0	1/2	1/2	113123.38	0.06	0.001	0.0121
1	1/2	1/2		0	1/2	3/2	113144.15	0.05	0.000	0.0990
1	1/2	3/2		0	1/2	1/2	113170.51	0.05	0.001	0.0967
1	1/2	3/2		0	1/2	3/2	113191.29	0.05	0.000	0.1255
1	3/2	3/2		0	1/2	1/2	113488.15	0.04	0.001	0.1255
1	3/2	5/2		0	1/2	3/2	113490.98	0.04	0.000	0.3333
1	3/2	1/2		0	1/2	1/2	113499.67	0.04	0.001	0.0990
1	3/2	3/2		0	1/2	3/2	113508.93	0.04	0.000	0.0967
1	3/2	1/2		0	1/2	3/2	113520.44	0.05	0.000	0.0121
2	3/2	3/2		1	3/2	3/2	226314.57	0.10	3.786	0.0116
2	3/2	5/2		1	3/2	5/2	226359.88	0.10	3.786	0.0283
2	3/2	3/2		1	1/2	3/2	226632.21	0.08	3.776	0.0498
2	3/2	5/2		1	1/2	3/2	226659.57	0.08	3.776	0.1661
2	3/2	1/2		1	1/2	1/2	226663.72	0.08	3.774	0.0495
2	3/2	3/2		1	1/2	1/2	226679.35	0.08	3.774	0.0616
2	5/2	5/2		1	3/2	3/2	226874.22	0.08	3.786	0.1683
2	5/2	7/2		1	3/2	5/2	226874.81	0.08	3.786	0.2667
2	5/2	3/2		1	3/2	1/2	226875.94	0.08	3.787	0.1002
2	5/2	3/2		1	3/2	3/2	226887.45	0.08	3.786	0.0319
2	5/2	5/2		1	3/2	5/2	226892.17	0.08	3.786	0.0317
3	5/2	7/2		2	5/2	7/2	339516.65	0.15	11.353	0.0118
3	5/2	5/2		2	3/2	5/2	340008.17	0.12	11.336	0.0215
3	5/2	3/2		2	3/2	3/2	340019.66	0.12	11.335	0.0214
3	5/2	7/2		2	3/2	5/2	340031.58	0.12	11.336	0.1776
3	5/2	3/2		2	3/2	1/2	340035.29	0.12	11.335	0.0667
3	5/2	5/2		2	3/2	3/2	340035.53	0.12	11.335	0.1119
3	7/2	7/2		2	5/2	5/2	340247.65	0.12	11.354	0.1750
3	7/2	9/2		2	5/2	7/2	340247.90	0.12	11.353	0.2381
3	7/2	5/2		2	5/2	3/2	340248.59	0.12	11.354	0.1271
3	7/2	5/2		2	5/2	5/2	340261.82	0.12	11.354	0.0155
3	7/2	7/2		2	5/2	7/2	340265.01	0.12	11.353	0.0155

N'	J'	F'	–	N''	J''	F''	Frequency	σ	E''/cm^{-1}	rel. Int.
4	7/2	7/2		3	5/2	7/2	453368.24	0.16	22.678	0.0117
4	7/2	5/2		3	5/2	5/2	453375.64	0.16	22.678	0.0117
4	7/2	9/2		3	5/2	7/2	453389.96	0.16	22.678	0.1785
4	7/2	5/2		3	5/2	3/2	453391.52	0.16	22.677	0.0952
4	7/2	7/2		3	5/2	5/2	453391.65	0.16	22.678	0.1312
4	9/2	9/2		3	7/2	7/2	453606.59	0.16	22.703	0.1761
4	9/2	11/2		3	7/2	9/2	453606.73	0.16	22.703	0.2222
4	9/2	7/2		3	7/2	5/2	453607.19	0.16	22.704	0.1389
5	9/2	11/2		4	7/2	9/2	566729.94	0.23	37.802	0.1777
5	9/2	7/2		4	7/2	5/2	566730.79	0.23	37.801	0.1111
5	9/2	9/2		4	7/2	7/2	566730.88	0.23	37.801	0.1408
5	11/2	11/2		4	9/2	9/2	566946.86	0.23	37.834	0.1758
5	11/2	13/2		4	9/2	11/2	566946.95	0.23	37.834	0.2121
5	11/2	9/2		4	9/2	7/2	566947.27	0.23	37.835	0.1455
6	11/2	13/2		5	9/2	11/2	680046.87	0.32	56.706	0.1768
6	11/2	9/2		5	9/2	7/2	680047.41	0.32	56.705	0.1212
6	11/2	11/2		5	9/2	9/2	680047.47	0.32	56.705	0.1465
6	13/2	13/2		5	11/2	11/2	680263.95	0.32	56.745	0.1753
6	13/2	15/2		5	11/2	13/2	680264.01	0.32	56.745	0.2051
6	13/2	11/2		5	11/2	9/2	680264.26	0.32	56.746	0.1496
7	13/2	15/2		6	11/2	13/2	793336.12	0.45	79.390	0.1758
7	13/2	11/2		6	11/2	9/2	793336.49	0.45	79.389	0.1282
7	13/2	13/2		6	11/2	11/2	793336.53	0.45	79.389	0.1502
7	15/2	15/2		6	13/2	13/2	793553.31	0.45	79.437	0.1746
7	15/2	17/2		6	13/2	15/2	793553.35	0.45	79.436	0.2000
7	15/2	13/2		6	13/2	11/2	793553.54	0.45	79.437	0.1524
8	15/2	17/2		7	13/2	15/2	906593.07	0.62	105.853	0.1750
8	15/2	13/2		7	13/2	11/2	906593.34	0.62	105.852	0.1333
8	15/2	15/2		7	13/2	13/2	906593.37	0.62	105.852	0.1528
8	17/2	17/2		7	15/2	15/2	906810.33	0.62	105.907	0.1740
8	17/2	19/2		7	15/2	17/2	906810.36	0.62	105.906	0.1961
8	17/2	15/2		7	15/2	13/2	906810.51	0.62	105.907	0.1544

Table *A.1: CN $v = 0$: Predicted rotational spectrum up to 1 THz, calculated with constants from Saleck et al. (1994). Transitions with relative intensities lower than 0.01 have been omitted.*

A.2 ^{13}CN Frequencies

^{13}CN $v = 0$: Predicted rotational spectrum up to 1 THz

N'	J'	F_1'	F'	–	N''	J''	F_1''	F''	Frequency	σ	E''/cm^{-1}	rel. Int.
1	1/2	0	1		0	1/2	1	1	108412.87	0.06	0.019	0.0252
1	1/2	0	1		0	1/2	1	2	108426.90	0.06	0.019	0.0502
1	1/2	1	0		0	1/2	0	1	108631.13	0.04	0.000	0.0254
1	1/2	1	1		0	1/2	0	1	108636.91	0.04	0.000	0.0766
1	3/2	1	1		0	1/2	1	0	108638.19	0.04	0.019	0.0286
1	3/2	1	2		0	1/2	1	1	108643.61	0.04	0.019	0.0339
1	3/2	1	0		0	1/2	1	1	108644.35	0.04	0.019	0.0254
1	3/2	1	1		0	1/2	1	1	108644.95	0.04	0.019	0.0219
1	1/2	1	2		0	1/2	0	1	108651.27	0.04	0.000	0.1299
1	3/2	1	2		0	1/2	1	2	108657.64	0.04	0.019	0.0959
1	3/2	1	1		0	1/2	1	2	108658.98	0.04	0.019	0.0265
1	3/2	2	3		0	1/2	1	2	108780.18	0.04	0.019	0.1944
1	3/2	2	2		0	1/2	1	1	108782.37	0.04	0.019	0.1025
1	3/2	2	1		0	1/2	1	0	108787.00	0.04	0.019	0.0453
1	3/2	2	1		0	1/2	1	1	108793.76	0.04	0.019	0.0354
1	3/2	2	2		0	1/2	1	2	108796.40	0.04	0.019	0.0364
2	3/2	1	2		1	3/2	1	1	217072.84	0.09	3.643	0.0100
2	3/2	1	2		1	3/2	1	2	217074.18	0.09	3.643	0.0251
2	3/2	1	0		1	1/2	0	1	217264.65	0.08	3.635	0.0100
2	3/2	1	1		1	1/2	0	1	217277.69	0.08	3.635	0.0289
2	3/2	2	2		1	1/2	1	2	217286.80	0.08	3.624	0.0201
2	3/2	2	1		1	1/2	1	1	217290.80	0.08	3.624	0.0199
2	3/2	2	1		1	1/2	1	0	217296.59	0.07	3.624	0.0264
2	5/2	2	2		1	3/2	2	2	217298.96	0.08	3.648	0.0125
2	3/2	2	2		1	1/2	1	1	217301.16	0.07	3.624	0.0594
2	3/2	2	3		1	1/2	1	2	217303.16	0.07	3.624	0.1115
2	3/2	1	2		1	1/2	0	1	217304.92	0.08	3.635	0.0441
2	5/2	2	3		1	3/2	2	3	217306.03	0.08	3.647	0.0219
2	5/2	2	3		1	3/2	1	2	217428.57	0.07	3.643	0.0889
2	5/2	2	2		1	3/2	1	1	217436.39	0.07	3.643	0.0488
2	5/2	2	2		1	3/2	1	2	217437.72	0.08	3.643	0.0146
2	5/2	2	1		1	3/2	1	1	217443.35	0.07	3.643	0.0153
2	5/2	2	1		1	3/2	1	0	217443.94	0.07	3.643	0.0216
2	5/2	3	4		1	3/2	2	3	217467.01	0.07	3.647	0.1500
2	5/2	3	3		1	3/2	2	2	217467.37	0.07	3.648	0.1034
2	5/2	3	2		1	3/2	2	1	217469.15	0.07	3.648	0.0698
2	5/2	3	2		1	3/2	2	2	217480.54	0.07	3.648	0.0132
2	5/2	3	3		1	3/2	2	3	217483.58	0.07	3.647	0.0133

N'	J'	F_1'	F'	–	N''	J''	F_1''	F''	Frequency	σ	E''/cm^{-1}	rel. Int.
3	5/2	2	3		2	5/2	2	3	325588.65	0.14	10.896	0.0100
3	5/2	2	2		2	3/2	1	2	325919.69	0.11	10.884	0.0127
3	5/2	2	1		2	3/2	1	1	325932.08	0.11	10.883	0.0126
3	5/2	2	3		2	3/2	1	2	325943.04	0.11	10.884	0.0698
3	5/2	2	1		2	3/2	1	0	325945.13	0.11	10.883	0.0167
3	5/2	2	2		2	3/2	1	1	325946.91	0.11	10.883	0.0374
3	5/2	3	2		2	3/2	2	1	325956.29	0.11	10.872	0.0485
3	5/2	3	3		2	3/2	2	2	325958.41	0.11	10.872	0.0719
3	5/2	3	4		2	3/2	2	3	325959.59	0.11	10.873	0.1042
3	7/2	3	4		2	5/2	2	3	326118.85	0.11	10.896	0.0966
3	7/2	3	3		2	5/2	2	2	326122.08	0.11	10.896	0.0672
3	7/2	3	2		2	5/2	2	1	326125.36	0.11	10.896	0.0454
3	7/2	4	5		2	5/2	3	4	326141.70	0.11	10.901	0.1310
3	7/2	4	4		2	5/2	3	3	326141.79	0.11	10.902	0.1004
3	7/2	4	3		2	5/2	3	2	326142.76	0.11	10.902	0.0764
4	7/2	3	4		3	5/2	2	3	434598.70	0.16	21.756	0.0765
4	7/2	3	2		3	5/2	2	1	434599.75	0.16	21.755	0.0357
4	7/2	3	3		3	5/2	2	2	434600.37	0.16	21.755	0.0529
4	7/2	4	3		3	5/2	3	2	434609.20	0.16	21.745	0.0584
4	7/2	4	4		3	5/2	3	3	434610.41	0.16	21.745	0.0766
4	7/2	4	5		3	5/2	3	4	434610.95	0.16	21.746	0.1000
4	9/2	4	5		3	7/2	3	4	434788.17	0.16	21.774	0.0967
4	9/2	4	4		3	7/2	3	3	434789.74	0.16	21.774	0.0743
4	9/2	4	3		3	7/2	3	2	434791.61	0.16	21.775	0.0566
4	9/2	5	6		3	7/2	4	5	434802.66	0.16	21.780	0.1204
4	9/2	5	5		3	7/2	4	4	434802.68	0.16	21.781	0.0977
4	9/2	5	4		3	7/2	4	3	434803.29	0.16	21.781	0.0792
5	9/2	4	5		4	7/2	3	4	543240.45	0.22	36.253	0.0792
5	9/2	4	3		4	7/2	3	2	543241.09	0.22	36.252	0.0463
5	9/2	4	4		4	7/2	3	3	543241.39	0.22	36.252	0.0608
5	9/2	5	4		4	7/2	4	3	543248.23	0.22	36.242	0.0640
5	9/2	5	5		4	7/2	4	4	543248.97	0.22	36.242	0.0789
5	9/2	5	6		4	7/2	4	5	543249.20	0.22	36.243	0.0972
5	11/2	5	6		4	9/2	4	5	543436.47	0.22	36.277	0.0955
5	11/2	5	5		4	9/2	4	4	543437.32	0.22	36.277	0.0777
5	11/2	5	4		4	9/2	4	3	543438.50	0.22	36.278	0.0629
5	11/2	6	6		4	9/2	5	5	543446.28	0.22	36.284	0.0957
5	11/2	6	7		4	9/2	5	6	543446.28	0.22	36.283	0.1136
5	11/2	6	5		4	9/2	5	4	543446.70	0.22	36.285	0.0806

N'	J'	F_1'	F'	–	N''	J''	F_1''	F''	Frequency	σ	E''/cm^{-1}	rel. Int.
6	11/2	5	6		5	9/2	4	5	651861.81	0.30	54.373	0.0806
6	11/2	5	4		5	9/2	4	3	651862.23	0.30	54.372	0.0530
6	11/2	5	5		5	9/2	4	4	651862.40	0.30	54.373	0.0655
6	11/2	6	5		5	9/2	5	4	651867.66	0.30	54.362	0.0675
6	11/2	6	6		5	9/2	5	5	651868.13	0.30	54.363	0.0802
6	11/2	6	7		5	9/2	5	6	651868.23	0.30	54.363	0.0952
6	13/2	6	7		5	11/2	5	6	652061.51	0.30	54.404	0.0942
6	13/2	6	6		5	11/2	5	5	652062.02	0.30	54.404	0.0794
6	13/2	6	5		5	11/2	5	4	652062.80	0.30	54.405	0.0669
6	13/2	7	7		5	11/2	6	6	652068.52	0.30	54.411	0.0942
6	13/2	7	8		5	11/2	6	7	652068.52	0.30	54.411	0.1090
6	13/2	7	6		5	11/2	6	5	652068.83	0.30	54.412	0.0814
7	13/2	6	7		6	11/2	5	6	760458.02	0.42	76.117	0.0814
7	13/2	6	5		6	11/2	5	4	760458.32	0.42	76.116	0.0577
7	13/2	6	6		6	11/2	5	5	760458.43	0.42	76.117	0.0686
7	13/2	7	6		6	11/2	6	5	760462.53	0.42	76.106	0.0700
7	13/2	7	7		6	11/2	6	6	760462.86	0.42	76.107	0.0810
7	13/2	7	8		6	11/2	6	7	760462.89	0.42	76.107	0.0937
7	15/2	7	8		6	13/2	6	7	760660.00	0.42	76.154	0.0931
7	15/2	7	7		6	13/2	6	6	760660.32	0.42	76.155	0.0805
7	15/2	7	6		6	13/2	6	5	760660.88	0.42	76.155	0.0695
7	15/2	8	8		6	13/2	7	7	760665.23	0.42	76.162	0.0930
7	15/2	8	9		6	13/2	7	8	760665.24	0.42	76.162	0.1056
7	15/2	8	7		6	13/2	7	6	760665.46	0.42	76.163	0.0818
8	15/2	7	8		7	13/2	6	7	869024.68	0.58	101.483	0.0819
8	15/2	7	6		7	13/2	6	5	869024.91	0.58	101.482	0.0611
8	15/2	7	7		7	13/2	6	6	869024.99	0.58	101.483	0.0708
8	15/2	8	7		7	13/2	7	6	869028.26	0.58	101.473	0.0718
8	15/2	8	9		7	13/2	7	8	869028.49	0.58	101.474	0.0926
8	15/2	8	8		7	13/2	7	7	869028.50	0.58	101.473	0.0815
8	17/2	8	9		7	15/2	7	8	869228.17	0.58	101.527	0.0922
8	17/2	8	8		7	15/2	7	7	869228.39	0.58	101.528	0.0812
8	17/2	8	7		7	15/2	7	6	869228.80	0.58	101.528	0.0715
8	17/2	9	9		7	15/2	8	8	869232.21	0.58	101.535	0.0920
8	17/2	9	10		7	15/2	8	9	869232.22	0.58	101.535	0.1029
8	17/2	9	8		7	15/2	8	7	869232.40	0.58	101.536	0.0822

N'	J'	F_1'	F'	–	N''	J''	F_1''	F''	Frequency	σ	E''/cm^{-1}	rel. Int.
9	17/2	8	9		8	15/2	7	8	977557.51	0.78	130.471	0.0822
9	17/2	8	7		8	15/2	7	6	977557.68	0.78	130.470	0.0637
9	17/2	8	8		8	15/2	7	7	977557.74	0.78	130.470	0.0724
9	17/2	9	8		8	15/2	8	7	977560.41	0.78	130.460	0.0732
9	17/2	9	10		8	15/2	8	9	977560.55	0.78	130.461	0.0917
9	17/2	9	9		8	15/2	8	8	977560.58	0.78	130.461	0.0819
9	19/2	9	10		8	17/2	8	9	977762.04	0.78	130.522	0.0914
9	19/2	9	9		8	17/2	8	8	977762.19	0.78	130.522	0.0817
9	19/2	9	8		8	17/2	8	7	977762.50	0.78	130.523	0.0730
9	19/2	10	10		8	17/2	9	9	977765.24	0.78	130.530	0.0912
9	19/2	10	11		8	17/2	9	10	977765.25	0.78	130.529	0.1009
9	19/2	10	9		8	17/2	9	8	977765.39	0.78	130.530	0.0824

Table *A.2: ^{13}CN $v = 0$: Predicted rotational spectrum up to 1 THz, calculated with constants from Saleck et al. (1994). Transitions with relative intensities lower than 0.01 have been omitted.*

A.3 $C^{15}N$ Frequencies

$C^{15}N$ $v = 0$: Predicted rotational spectrum up to 1 THz

N'	J'	F'	–	N''	J''	F''	Frequency	σ	E''/cm^{-1}	rel. Int.
1	1/2	1		0	1/2	1	109689.54	0.05	0.001	0.1648
1	1/2	1		0	1/2	0	109708.97	0.05	0.000	0.0852
1	1/2	0		0	1/2	1	109733.65	0.06	0.001	0.0833
1	3/2	1		0	1/2	1	110004.09	0.05	0.001	0.0852
1	3/2	1		0	1/2	0	110023.52	0.04	0.000	0.1648
1	3/2	2		0	1/2	1	110024.55	0.04	0.001	0.4167
2	3/2	2		1	3/2	2	219387.47	0.10	3.671	0.0372
2	3/2	1		1	3/2	1	219438.29	0.11	3.670	0.0213
2	3/2	1		1	1/2	0	219708.72	0.08	3.661	0.0833
2	3/2	2		1	1/2	1	219722.48	0.08	3.659	0.2088
2	3/2	1		1	1/2	1	219752.84	0.08	3.659	0.0412
2	5/2	2		1	3/2	2	219913.58	0.08	3.671	0.0253
2	5/2	2		1	3/2	1	219934.03	0.08	3.670	0.2247
2	5/2	3		1	3/2	2	219934.90	0.08	3.671	0.3500

N'	J'	F'	–	N''	J''	F''	Frequency	σ	E''/cm^{-1}	rel. Int.
3	5/2	3		2	5/2	3	329078.55	0.16	11.007	0.0158
3	5/2	2		2	5/2	2	329127.55	0.16	11.006	0.0113
3	5/2	2		2	3/2	1	329623.30	0.12	10.990	0.1500
3	5/2	3		2	3/2	2	329625.97	0.12	10.989	0.2335
3	5/2	2		2	3/2	2	329653.65	0.12	10.989	0.0165
3	7/2	3		2	5/2	3	329815.81	0.12	11.007	0.0120
3	7/2	3		2	.007	0.3214				
4	7/2	3		3	5/2	2	439515.19	0.17	21.985	0.1786
4	7/2	4		3	5/2	3	439516.32	0.17	21.984	0.2411
4	9/2	4		3	7/2	3	439727.34	0.17	22.008	0.2430
4	9/2	5		3	7/2	4	439727.68	0.17	22.009	0.3056
5	9/2	4		4	7/2	3	549388.66	0.24	36.645	0.1944
5	9/2	5		4	7/2	4	549389.28	0.24	36.644	0.2445
5	11/2	5		4	9/2	4	549600.24	0.24	36.676	0.2454
5	11/2	6		4	9/2	5	549600.49	0.24	36.677	0.2955
6	11/2	5		5	9/2	4	659240.16	0.32	54.971	0.2045
6	11/2	6		5	9/2	5	659240.55	0.32	54.970	0.2462
6	13/2	6		5	11/2	5	659451.48	0.32	55.009	0.2468
6	13/2	7		5	11/2	6	659451.66	0.32	55.010	0.2885
7	13/2	6		6	11/2	5	769065.53	0.44	76.961	0.2115
7	13/2	7		6	11/2	6	769065.80	0.44	76.960	0.2473
7	15/2	7		6	13/2	6	769276.71	0.44	77.006	0.2476
7	15/2	8		6	13/2	7	769276.85	0.44	77.006	0.2833
8	15/2	7		7	13/2	6	878860.49	0.61	102.614	0.2167
8	15/2	8		7	13/2	7	878860.69	0.61	102.613	0.2479
8	17/2	8		7	15/2	7	879071.59	0.61	102.666	0.2482
8	17/2	9		7	15/2	8	879071.70	0.61	102.667	0.2794
9	17/2	8		8	15/2	7	988620.74	0.82	131.930	0.2206
9	17/2	9		8	15/2	8	988620.89	0.82	131.929	0.2484
9	19/2	9		8	17/2	8	988831.78	0.82	131.989	0.2485
9	19/2	10		8	17/2	9	988831.87	0.82	131.989	0.2763

Table *A.3: $C^{15}N$ $v = 0$: Predicted rotational spectrum up to 1 THz, calculated with constants from Saleck et al. (1994). Transitions with relative intensities lower than 0.01 have been omitted.*

Appendix B. Spectra and maps from different sources

B.1 Orion A

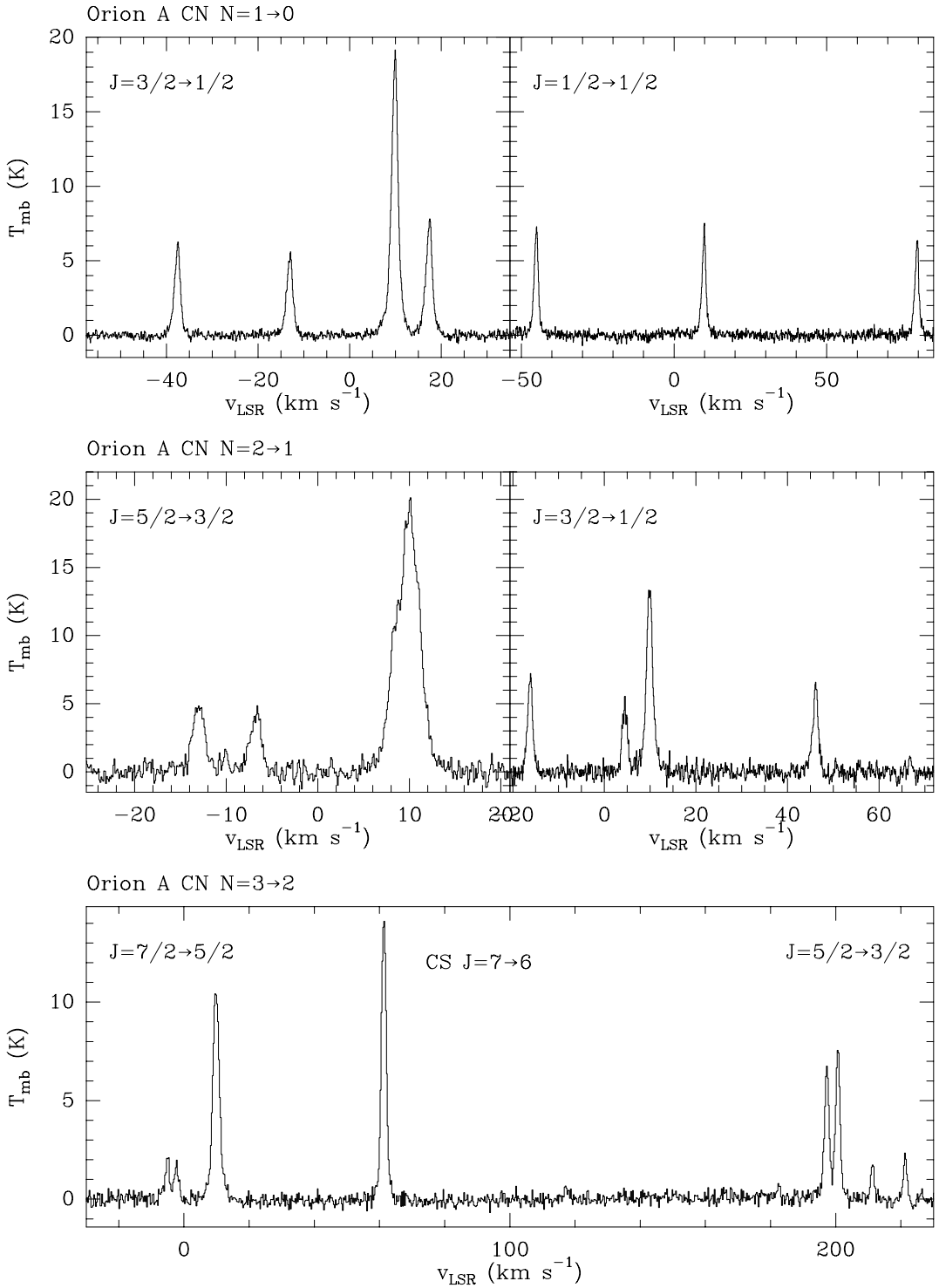

Fig. *B.1: CN N=1→0, N=2→1 (IRAM 30m, two different autocorrelator units for each observed fine structure transition are shown) and N=3→2 (JCMT) observations from OMC-1. Spectra from a* $\sim 1' \times 1'$ *area in the northern part of the ridge have been averaged to enhance the signal to noise.*

B.2 Orion B

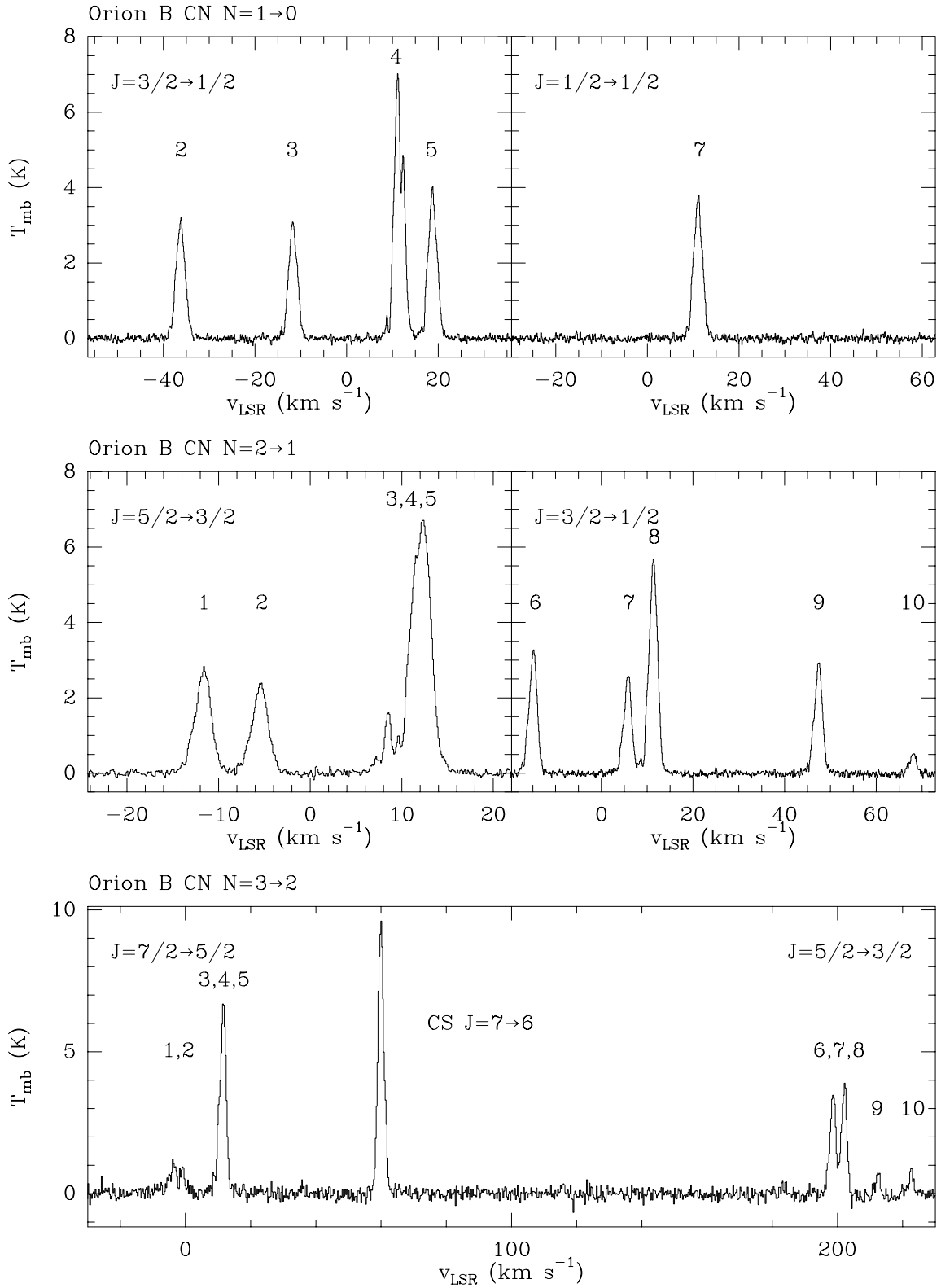

Fig. *B.2: The same as Fig. B.1 for the region around FIR5 in Orion B. The lines are labeled according to the sequence descending in frequency in Table A.1.*

B.3 S106

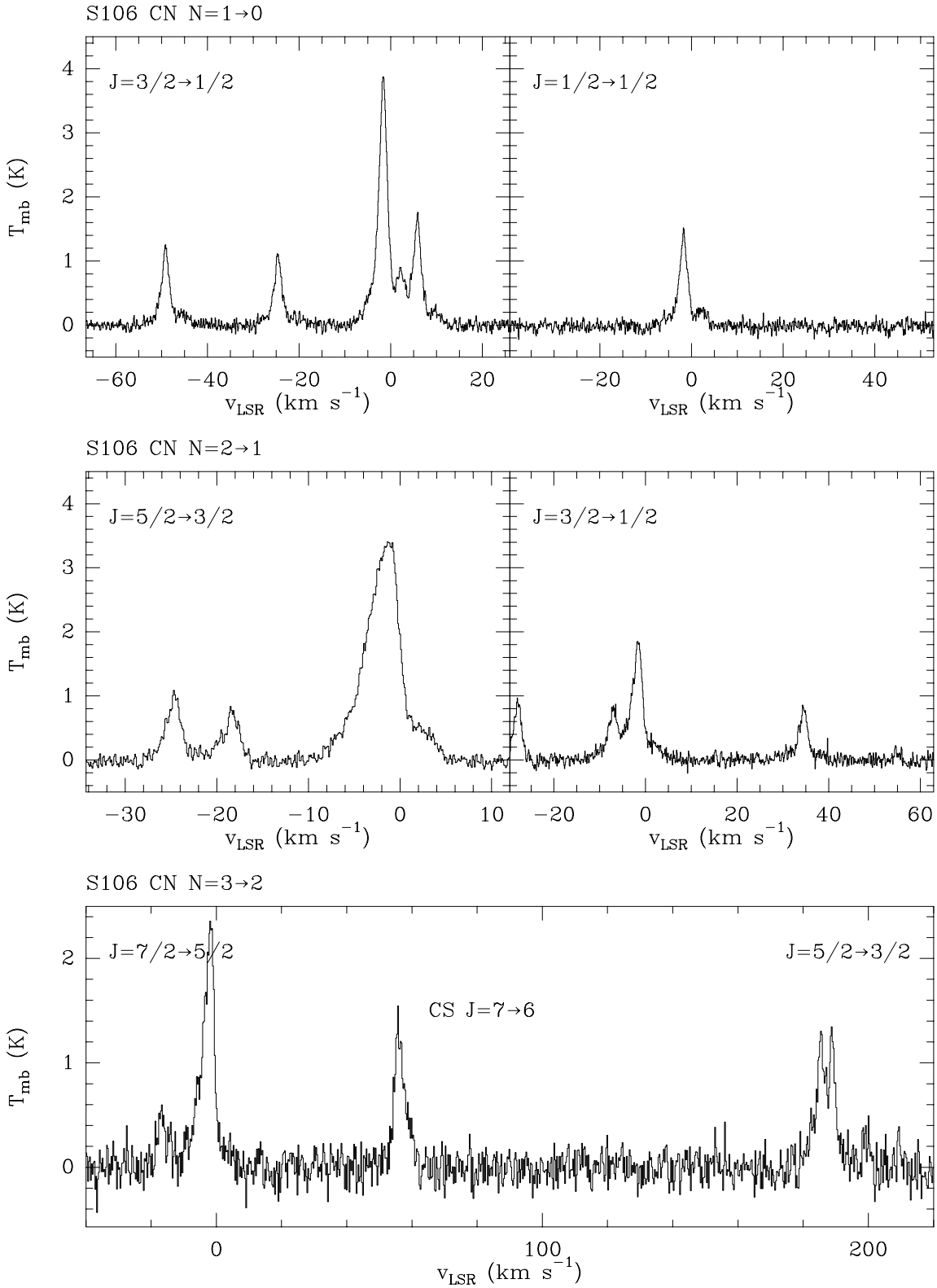

Fig. *B.3: The same as Fig. B.1 for the central region of S106.*

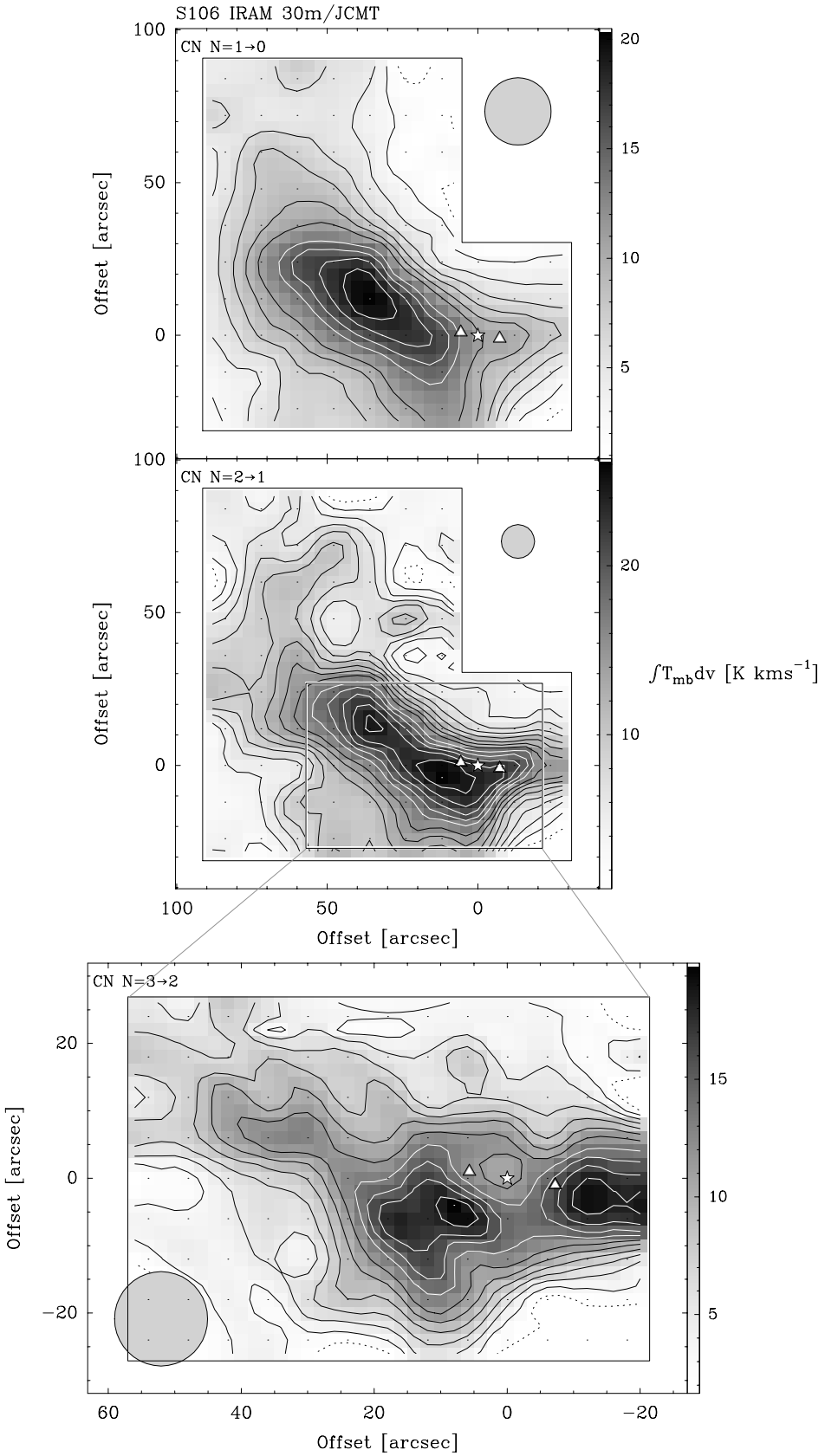

Fig. *B.4: CN intensity integrated over* v_{LSR} *= [-6,13] km* s^{-1} *in S106. Levels are* 3σ *= 0.8(1.6)20.0 K km* s^{-1} *for N=1→0,* 3σ *= 0.9(1.8)26.1 K km* s^{-1} *for N=2→1 and* 3σ *= 1.7(1.7)18.7 K km* s^{-1} *for N=3→2.*

B.4 S140

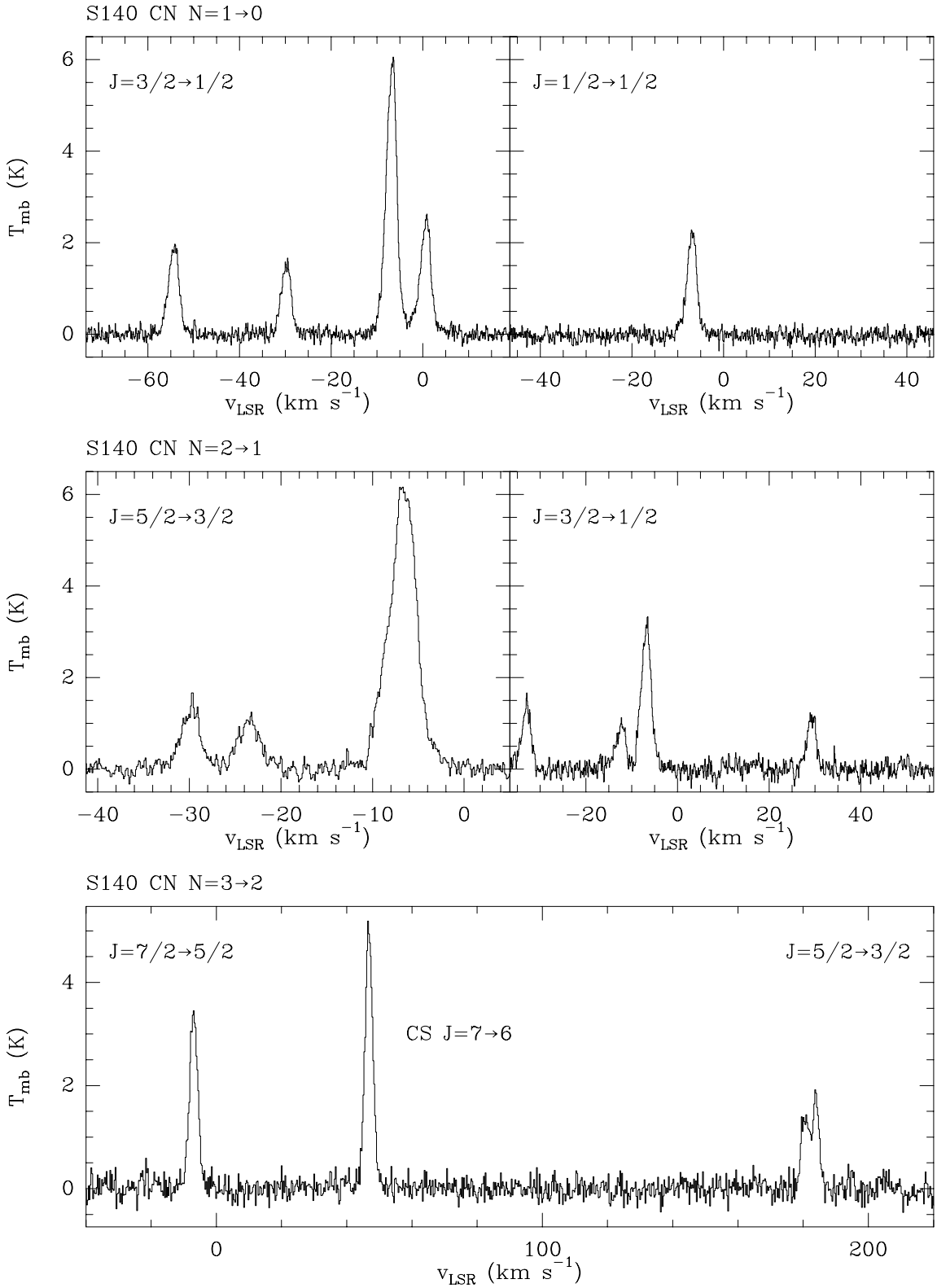

Fig. *B.5: The same as Fig. B.1 for the central region of S140.*

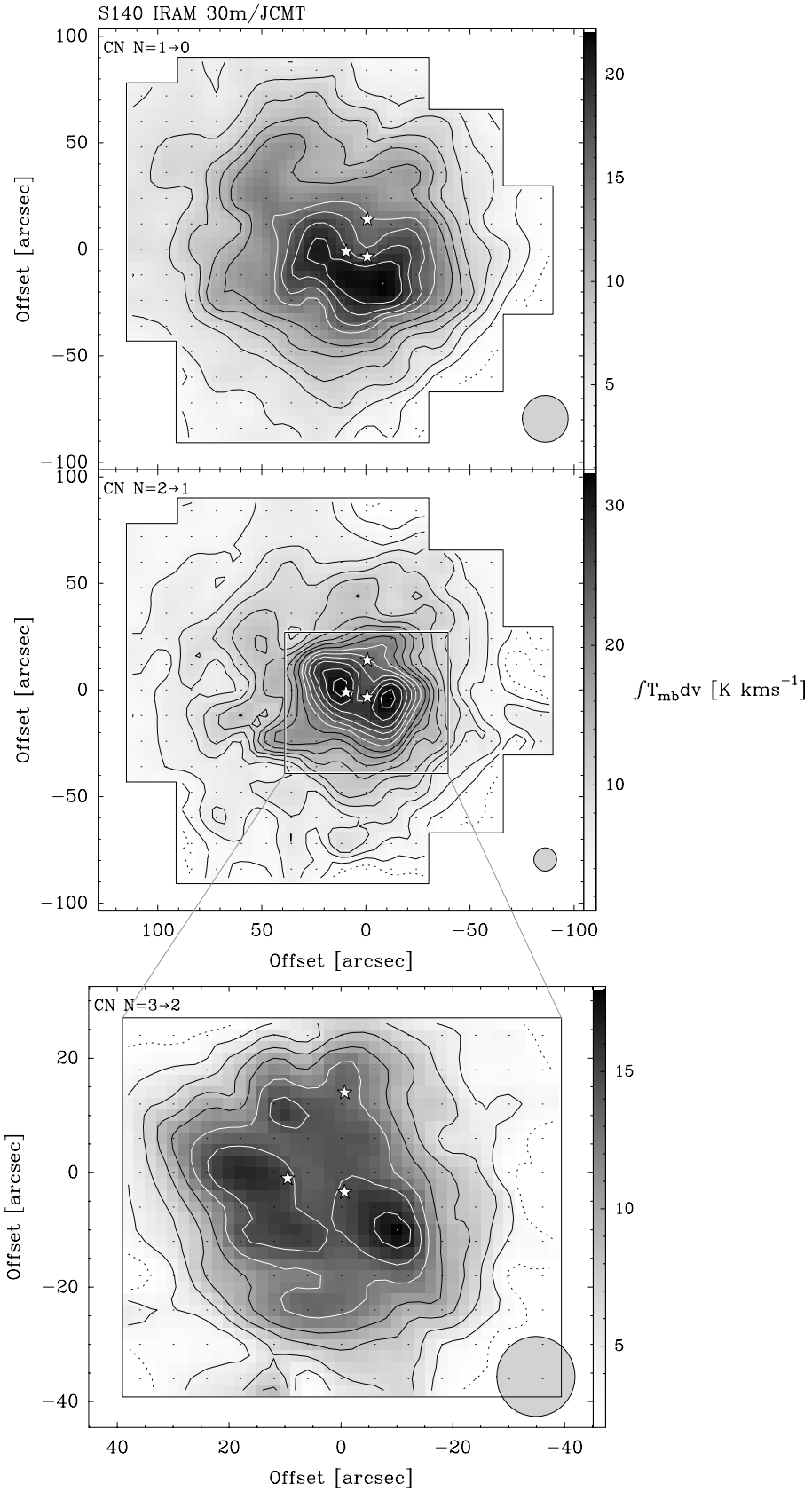

Fig. *B.6: CN intensity integrated over* v_{LSR} *= [-11,-4] km* s^{-1} *in S140. Levels are* 3σ *= 0.9(1.8)20.7 K km* s^{-1} *for N=1→0,* 3σ*=0.9(1.8)31.5 K km* s^{-1} *for N=2→1 and* 3σ*=2.1(2.1)16.8 K km* s^{-1} *for N=3→2.*

B.5 S255

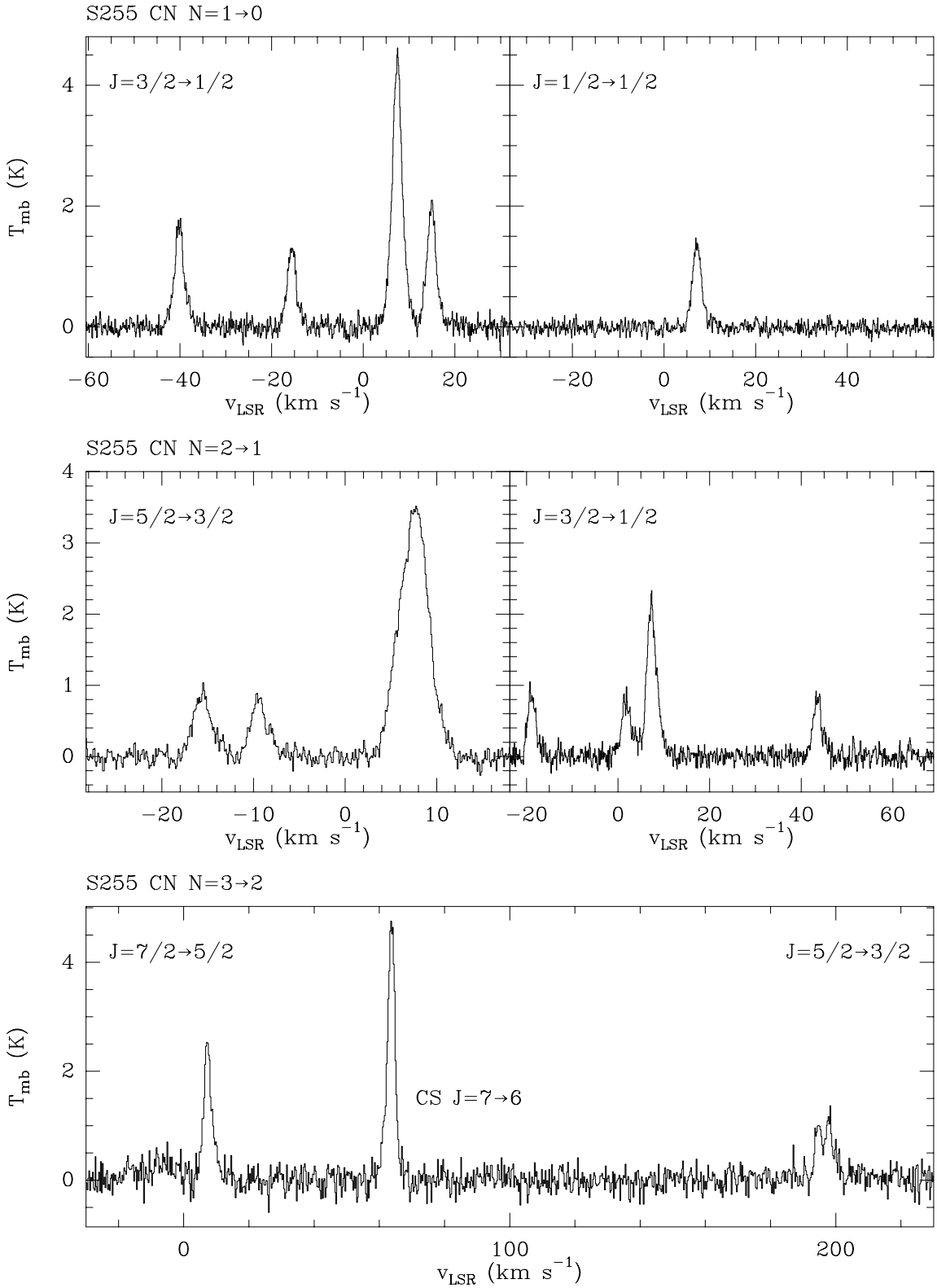

Fig. *B.7: The same as Fig. B.1 for the central region of S255.*

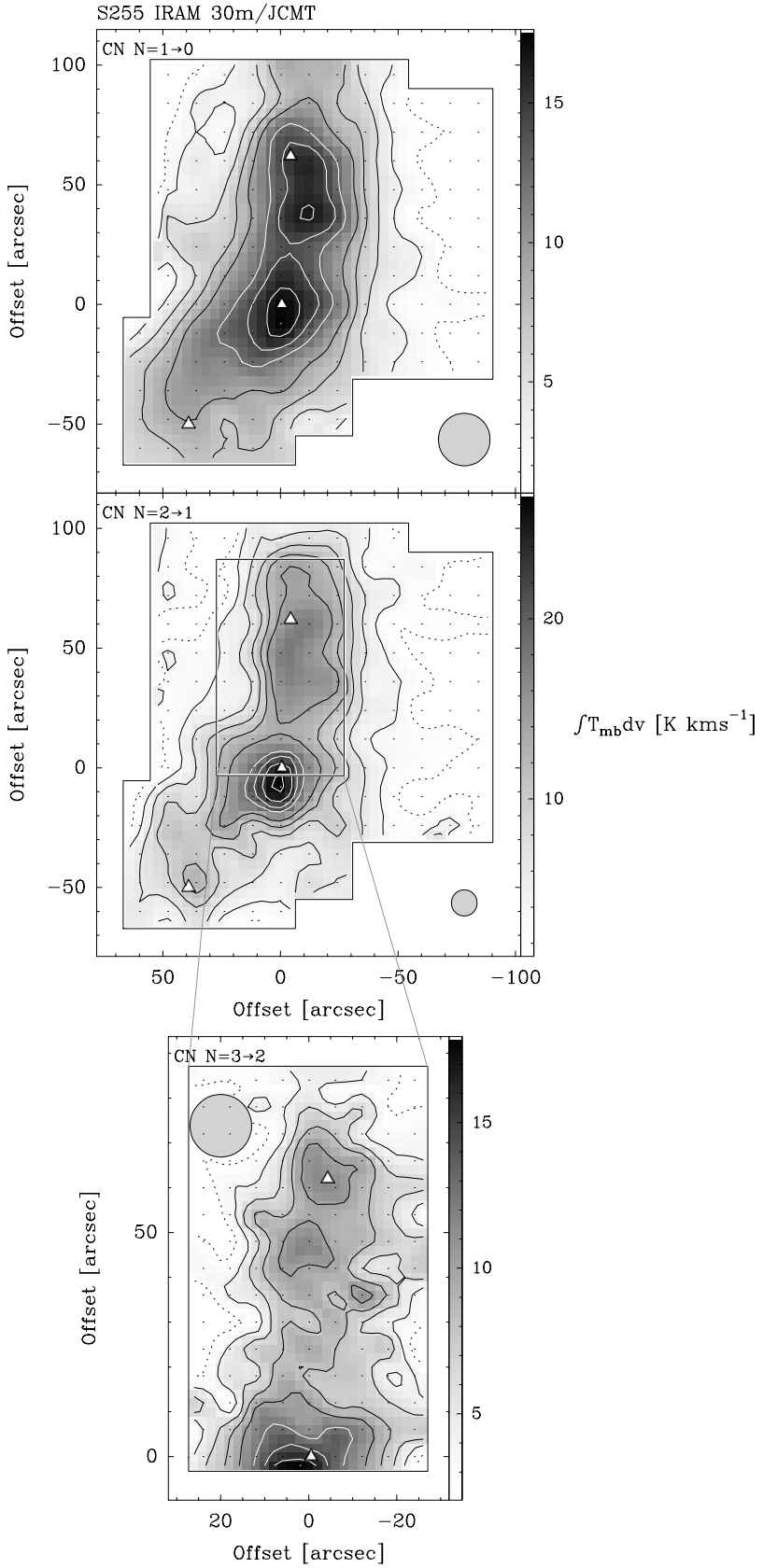

Fig. *B.8: CN intensity integrated over* v_{LSR} *= [4,11] km* s^{-1} *in S255. Levels are* 3σ *= 1.0(2.0)17.0 K km* s^{-1} *for N=1→0,* 3σ*=1.1(2.2)25.3 K km* s^{-1} *for N=2→1 and* 3σ*=2.1(2.1)16.8 K km* s^{-1} *for N=3→2.*

B.6 W49

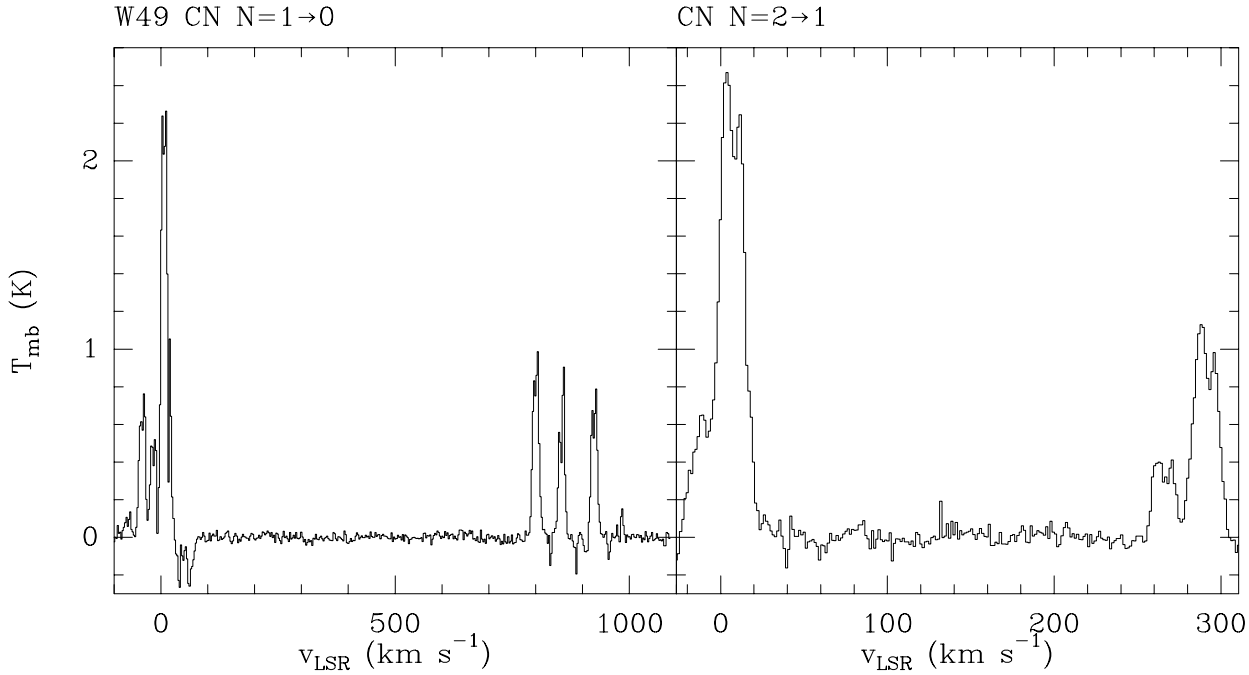

Fig. *B.9: CN N=1→0 and N=2→1 (IRAM 30m, the full 1 MHz resolution filter banks are shown, containing both observed fine structure transitions) observations from W49. Spectra from a* $\sim 1' \times 1'$ *area have been averaged. Note the negative feature in the N=1→0 spectrum is interpreted as to arise from the colder outer envelopes of molecular clouds along the line of sight.*

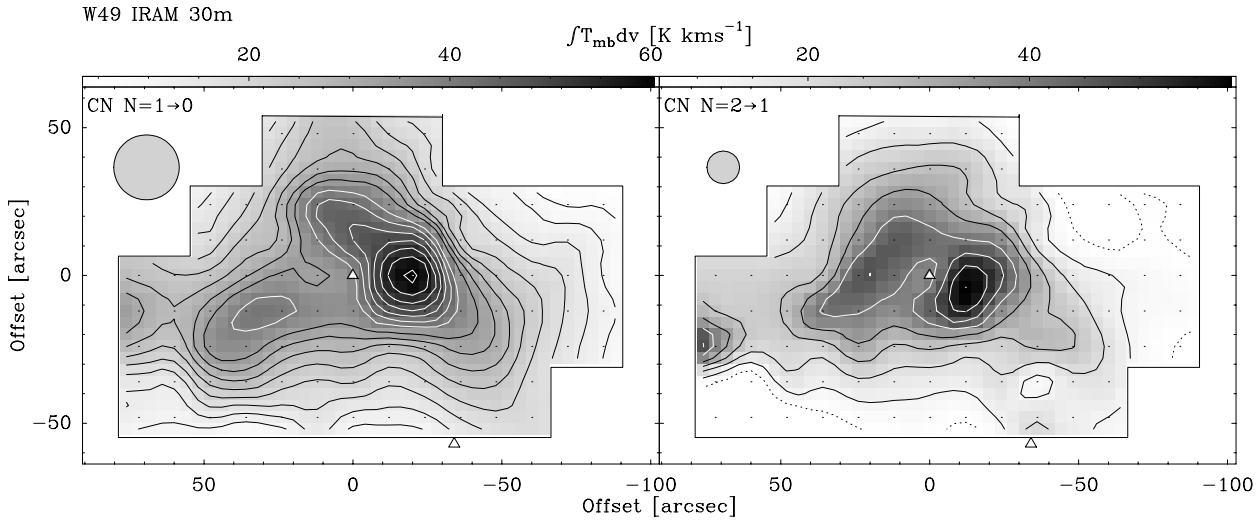

Fig. *B.10: CN intensity integrated over* $v_{\rm LSR}$ *= [-4,25] km* s^{-1} *in W49. Levels are* 3σ *= 3.4(3.4)57.8 K km* s^{-1} *for N=1→0 and* 3σ *= 6.3(6.3)56.7 K km* s^{-1} *for N=2→1.*

B.7 W51

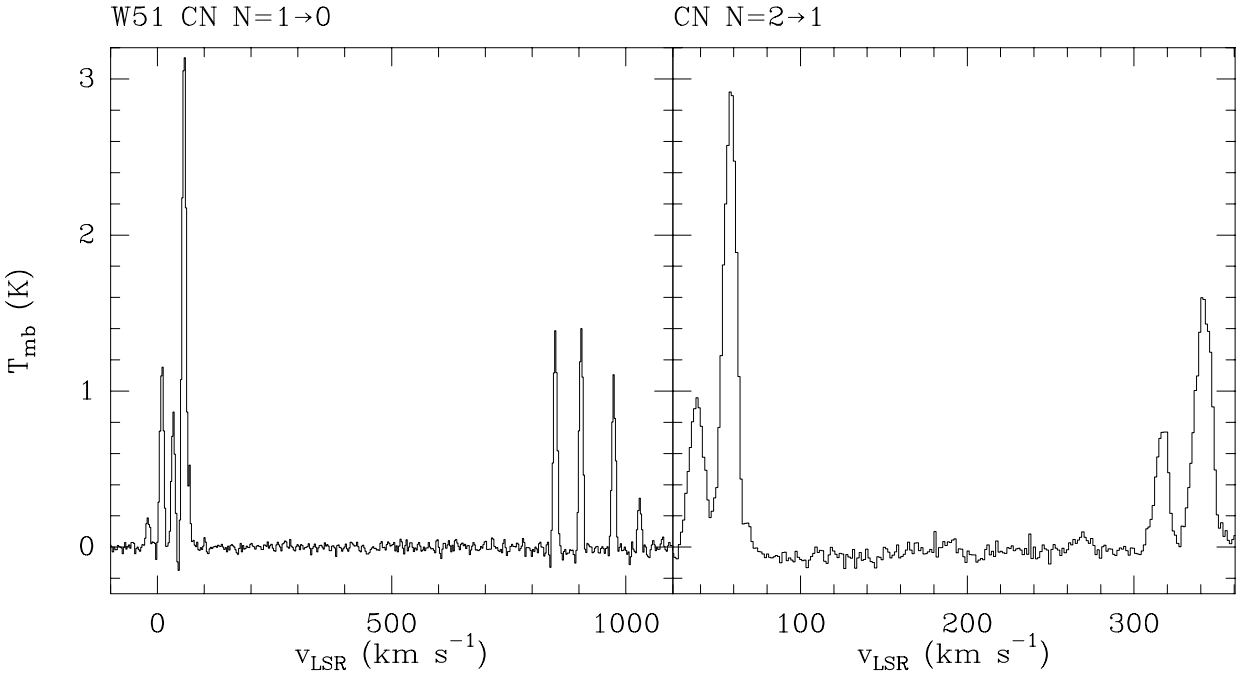

Fig. *B.11: The same as Fig. B.9 for the central region of W51.*

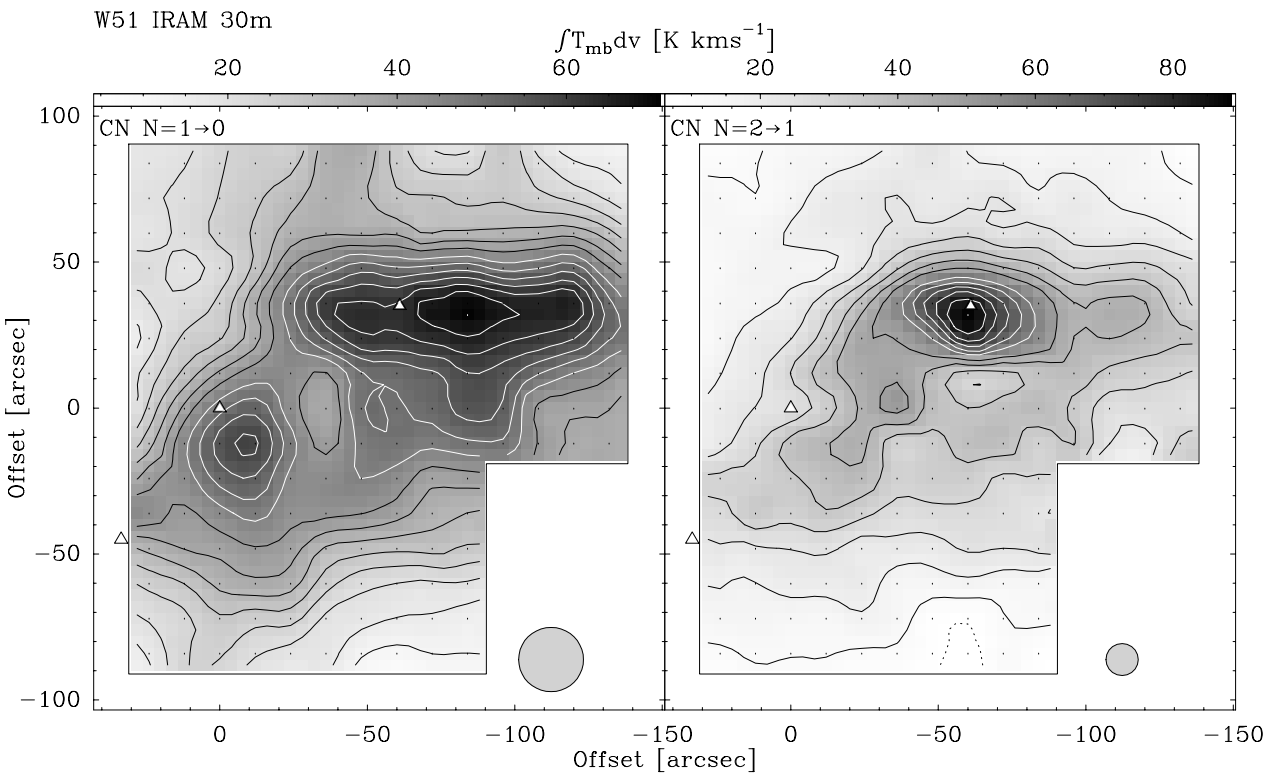

Fig. *B.12: CN intensity integrated over v_{LSR} = [50,75] km s^{-1} in W51. Levels are 3σ = 4.1(4.1)69.7 K km s^{-1} for N=1→0 and 3σ = 5.8(5.8)87.0 K km s^{-1} for N=2→1.*

B.8 OMC-2

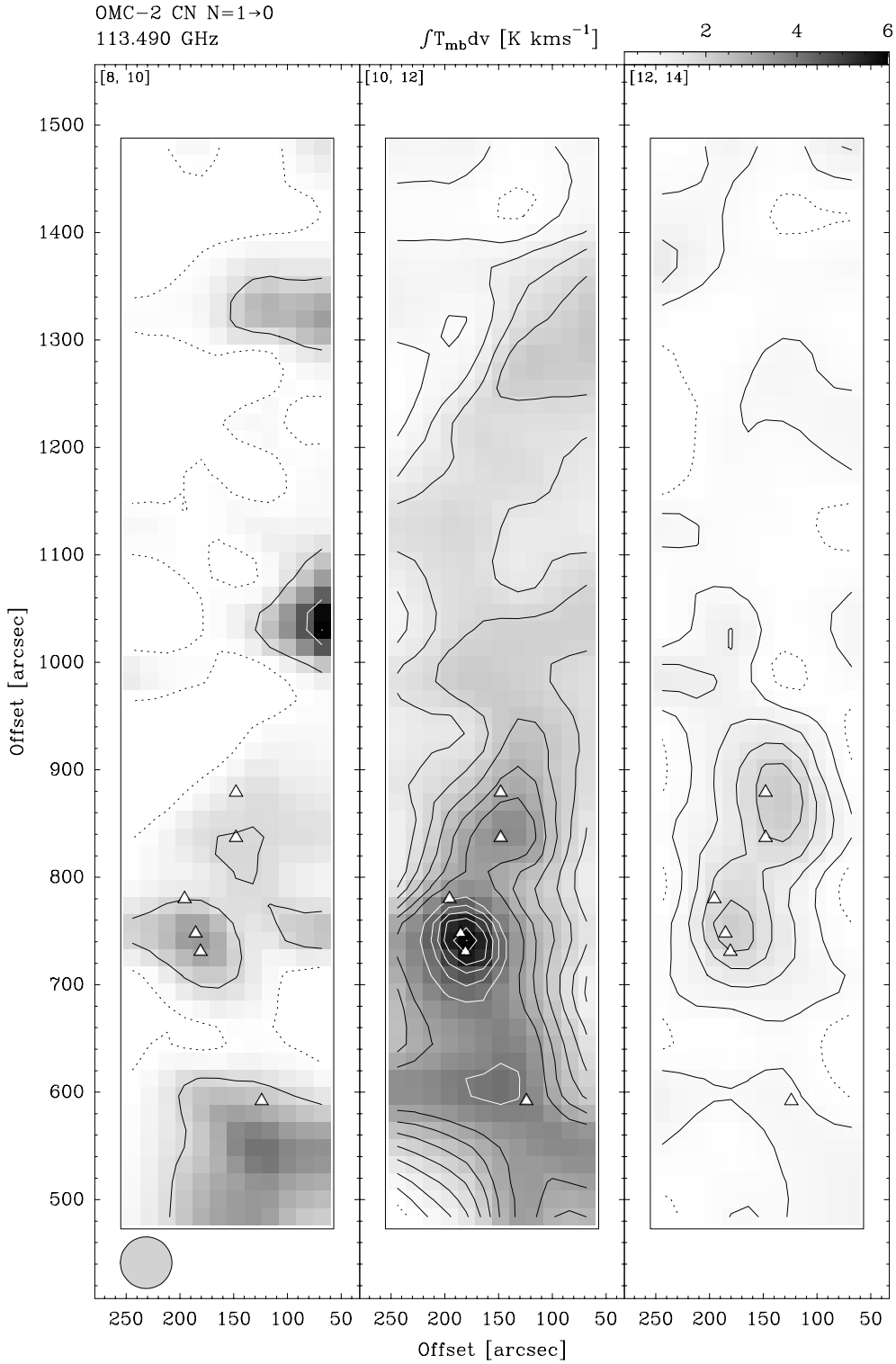

Fig. *B.13: Channel maps of CN N=1→0 in OMC-2 observed with the SEST 15m telescope. The velocity interval in km s^{-1} is given in the top left corner of each panel. Contour levels start at 3σ = 0.21 K km s^{-1} and increase in steps of 6σ to the maximum value given on top of the last panel. The beam size is indicated in the first panel. Note that offsets are relative to BN-KL in OMC-1.*

B.9 ρ Ophiuchus A

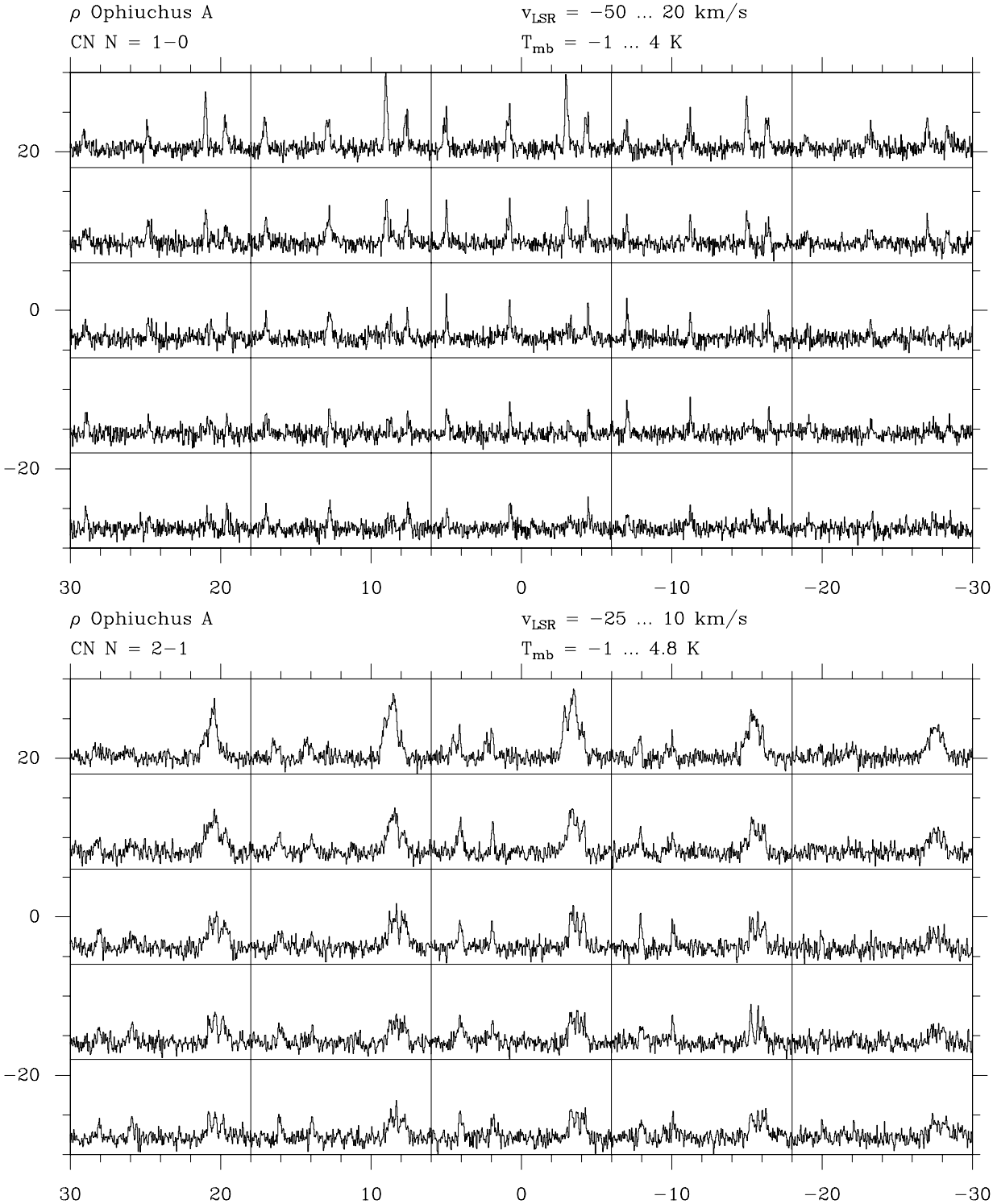

Fig. *B.14: Spectra of the strongest fine structure transition of CN N=1→0 (top) and N=2→1 (bottom) in ρ Ophiuchus A. Note that the strongest N=1→0 hfs component is absorbed almost to the zero level.*

ACKNOWLEDGEMENTS

With the following lines I would like to express my gratitude to those people who, in many different ways, supported me and contributed to this work. Of course, I will not be able to mention all of them here by name, but I would like to start by acknowledging my parents and grandparents for guiding and supporting me during the years of growing up and study. Their permanent interest in my education and work was and still is an invaluable encouragement.

Prof. Gisbert Winnewisser stimulated my interest for more exotic molecules than CO and for the CN radical in particular. He always gave me plenty of rope while keeping a firm eye on the progress I made. Who would have thought that this work, initiated by the very first conversation on a possible CN project, would turn out to be so fruitful. Furthermore, his persistent and successful efforts against the wind mills of bureaucracy and budget curtailment provide the basis without which we all would not have the opportunity to pursue our research interests in such a demanding and challenging field of modern Astronomy.

Prof. Jürgen Stutzki is thanked for his readiness to discuss countless emerging problems and to trigger new ideas. His competent and experienced advice not only pushed this work into the right direction, but also forward at the same time. I owe him a special *thank you* since he has taught me, although sometimes too quick for me in the first iteration, a lot about intuition and solving problems.

I am indebted to Nicola Schneider for her thorough, and sometimes very critical, yet always proficient reading of the manuscript which for me was a constant incentive and led to substantial improvements. I will also remember our hard and, most of the times, fruitful discussions, on both astronomical and non-astronomical topics. Despite some really *hitting* arguments, I believe we both learned a lot from each other and had a great time.

It was a great pleasure to share part of the observing time on Gornergrat, in Spain, and Chile with Axel Saleck, whose enthusiasm and scientific skills have always been a great motivation for me. Together with him I was involved in writing my first papers, an experience that broadened our both horizons. Furthermore, I particularly appreciate his introduction to the Spanish and Latin-american *ars vivendi*, as well as inspiring conversations about the topics that move us and the world.

I have enjoyed working with the other member of the *Orion Bar team*, Friedrich Wyrowski, whose experience and helpful advice provided me with substantial new insights, not only with respect to the GILDAS package. He showed remarkable patience and perseverance concerning my numerous questions and problems connected to the mysteries of interferometry.

Thomas Klaus and I shared the problems related to the final stages of data reduction and writing of our theses which was a helpful motivation and offered the opportunity for countless interesting discussions, many of which were private in nature and helped to experience some healthy distraction.

I thank all members of the KOSMA group for the pleasant atmosphere at the institute and I would like to mention in particular the crew of room 316 and the brave companions at the daily

Mensa: Nicola Schneider, Johannes Frerick, Gabriele Klapper and Thomas Klaus ("*gibts Kaffee?*"), Carsten Kramer, Dirk Krause, Axel Saleck, Oliver Siebertz, Johannes Staguhn, Friedrich Wyrowski, and Prof. Mitsutoshi Tanimoto.
In this context, I should and can not forget all colleagues and friends who helped to make the numerous stays on Gornergrat enjoyable and memorable, especially Nicola Schneider, Frank Boes, Martin Miller, and Thomas Zimmermann, as well as Johannes Staguhn ("*Kelle? Kelle!*") and Jonathan Williams for what he once called "*all the good times on the mountain, snow or shine*".

Carsten Kramer gave helpful comments on an early version of this thesis and I appreciate some interesting discussions with him, in particular on *our* source Orion.
Uwe Corneliussen and Jan Wouterloot are thanked for observing part of the data at the IRAM 30m telescope. Urs Graf made the Orion B CO spectra available to me. Amiel Sternberg kindly provided the code of the chemical PDR model and Uwe Leuenhagen is thanked for his efforts in updating the input for the model.

There is, of course, a life besides work and I would like to mention some of the people who were involved in the numerous activities that helped to focus my thoughts to something different than Astronomy whenever it was necessary. I thank all my friends for their invaluable support over the years, in particular Gereon & Torsten Aßhauer and all others not mentioned here by name for the terrific fun we had, Rolf Kühne and the band for some remarkable sessions, and the Monday Badminton crew. I also enjoyed the hard matches with Urs Müller, and even more the time afterwards which more and more became the real reason for playing and something to look forward to at the end of the week.

Finally, I thank Monika for her patience, support, and encouragement, especially during the time of writing at the end of this work. Beyond doubt, without her the last years would have been harder for me!

Diese Arbeit wurde durch die Deutsche Forschungsgemeinschaft im Rahmen des Sonderforschungsbereiches SFB 301 gefördert.

Das Kölner Observatorium für Millimeter und Submillimeter Astronomie (KOSMA) wird vom I. Physikalischen Institut der Universität zu Köln geleitet und von der Internationalen Stiftung *Hochalpine Forschungsstationen Jungfraujoch und Gornergrat* in Bern verwaltet.

Ich versichere, daß ich die von mir vorgelegte Dissertation selbständig angefertigt, die benutzten Quellen und Hilfsmittel vollständig angegeben und die Stellen der Arbeit – einschließlich Tabellen, Karten und Abbildungen –, die anderen Werken im Wortlaut oder dem Sinn nach entnommen sind, in jedem Einzelfall als Anlehnung kenntlich gemacht habe; daß diese Dissertation noch keiner anderen Fakultät oder Universität zur Prüfung vorgelegen hat; daß sie, abgesehen von unten angegebenen Teilpublikationen, noch nicht veröffentlicht worden ist sowie, daß ich eine solche Veröffentlichung vor Abschluß des Promotionsverfahrens nicht vornehmen werde.

Die Bestimmungen der Promotionsordnung sind mir bekannt. Die von mir vorgelegte Dissertation ist von Herrn Prof. Dr. G. Winnewisser betreut worden.

Teilpublikationen:

Saleck, A.H., Eigler, K., Simon, R., Vowinkel, B., Winnewisser, G.,
Interstellar detection of $C^{13}CH$, 1992, Astron. Ges. Abstr. Ser. 7, 83

Kramer, C., Tigges, A., Simon, R., Wang, T.Y., Wouterloot, J.G.A., Winnewisser, G.,
The Giant Molecular Clouds Orion A and B, 1992, Astron. Ges. Abstr. Ser. 7, 85

Saleck, A.H., Simon, R., Schneider, N., Winnewisser, G.,
Detection of interstellar $C^{15}N$, 1993, ApJ, 414, L133

Saleck, A.H., Simon, R., Winnewisser, G.,
Interstellar CN Rotational Spectra: $C^{15}N$, 1994, ApJ, 436, 176

Saleck, A.H., Simon, R., Winnewisser, G., Wouterloot, J.G.A.,
Detection of interstellar ^{13}CCH and $C^{13}CH$, 1994, Can. J. Phys. 72, 747

Simon, R., Saleck, A.H., Schneider, N., Jacobs, K., Vowinkel, B., Winnewisser, G.,
Observations of interstellar CN, ^{13}CN and $C^{15}N$, in: *The Physics and Chemistry of Interstellar Molecular Clouds*, 1995, 2^{nd} Cologne-Zermatt Symposium, eds. G. Winnewisser, G. Pelz, Lecture notes in physics 459, p. 252

Simon, R., Stutzki, J., Degiacomi, C., Winnewisser, G.,
Millimeter and submillimeter observations of the CN radical, 1995, Astron. Ges. Abstr. Ser. 11, 171

Störzer, H., Simon, R., Stutzki, J., Sternberg, A.,
CO^+ in Photon Dominated Regions in: *CO: Twenty-five years of Millimeterwave Spectroscopy*, eds. S. Radford, W.L. Latter, 1996, IAU Symp. 170

Simon, R., Stutzki, J., Sternberg, A., Winnewisser, G.,
Chemical stratification in the Orion Bar region: CN and CS submillimeter observations, 1997, A&A, 327, L9